Diamant nanostructures fabrication par gravure et de croissance avec des nanoparticules métalliques

Hasan-Al Mehedi

Hasan-Al Mehedi. Diamant nanostructures fabrication par gravure et de croissance avec des nanoparticules métalliques. Physique [physics]. Université de Grenoble, 2012. Français. NNT : 2012GRENT107 . tel-01415964

HAL Id: tel-01415964
https://theses.hal.science/tel-01415964
Submitted on 13 Dec 2016

UNIVERSITÉ DE GRENOBLE

THÈSE

Pour obtenir le grade de

DOCTEUR DE L'UNIVERSITÉ DE GRENOBLE

Spécialité : **Nano Electronique et Nano Technologies**

Arrêté ministériel : 7 août 2006

Présentée par

«Hasan-al MEHEDI»

Thèse dirigée par **« Etienne GHEERAERT »**

préparée au sein du **Laboratoire Institut Néel, CNRS**
dans **l'École Doctorale EEATS: Electronique, Electrotechnique, Automatique & Traitement du Signal**

"Diamond Nanostructure Fabrication by Etching and Growth with Metallic Nanoparticles"

[Diamant nanostructures fabrication par gravure et de croissance avec des nanoparticules métalliques]

Thèse soutenue publiquement le **« 18 Décembre 2012 »**,
devant le jury composé de :

M. Christophe VALLÉE **Président**

Professeur, Université Joseph Fourier

M. Milos NESLADEK **Rapporteur**

Professeur, Universiteit Hasselt

M. Silvère BARRAT **Rapporteur**

Professeur, Université de Lorraine

M. Davy CAROLE **Examinateur**

Maître de Conférences, Université Claude Bernard Lyon 1

M. Etienne GHEERAERT **Directeur de Thèse**

Professeur, Université Joseph Fourier

Université Joseph Fourier / Université Pierre Mendès France /
Université Stendhal / Université de Savoie / Grenoble INP

ACKNOWLEDGEMENTS

The completion of this thesis would never have been possible without the support of a great number of people who have unselfishly given their help and supported me intellectually as well as personally throughout the last three years.

Firstly, I would like to thank Université Joseph Fourier for the financial support without which this work would not have taken place, and Alain Fontaine, and Alain Schuhl for allowing me to work at their laboratory.

I am sincerely and heartily grateful to my supervisor Professor Etienne Gheeraert for selecting me to be a part of this challenging and exciting project, and for providing me with enormous amount of time, encouragement, technical insight, independence and support in the research. Writing of this thesis would not have been possible without his constant guidance. He has also helped me a lot in my life in Grenoble. He is not only a very good advisor but also a nice friend. It was a great pleasure working for and with him.

I would like to thank Professor Milos Nesladek and Professor Silvère Barrat for agreeing to be referees and for their time to review my manuscript. I thank Professor Christophe Vallée for chairing my dissertation defense. I sincerely thank Dr. Davy Carole for being my examiner and also for his assistance in APCVD experiments.

I would like to thank my colleague Clément Hébert for his contribution to this work. I also would like to thank Dr. Jean-Charles Arnault for XPS measurement, Dr. Daniel Araujo and Maripaz for TEM experiment, Pierre Giroux for all the technical assistances throughout the thesis, Dr. David Eon for MPCVD training and NCD growth, Jean-François Motte for FIB, Bruno Fernandez for clean room training, Michel Mermoux and Valérie Reita for Raman Spectroscopy, Sebastien Pairis for SEM training, Vo-Ha for APCVD.

I gratefully acknowledge the members of SC2G group for their professional and personal support. I also appreciate the assistance I received from the administrative staff of Institut Néel.

Finally, I thank my family and friends for their unlimited support and encouragement.

Table of Content

Chapter 4 In Search of Conditions for Diamond Nanowire Growth

Chapter 5 Development of a Catalytic Etching Technique: Results and Discussion

Chapter 6 Catalytic Etching of Diamond: Future Perspective

Résumé

Le diamant est un matériau fascinant avec d'exceptionnelles propriétés physiques. Son application à divers domaines reste limité parce que sa fabrication est difficile et nécessite des substrats et conditions spécifiques. En outre, les dispositifs de diamant tels que les capteurs nécessitent généralement la structuration et l'échelle micro ou nanométrique, et l'inertie chimique du diamant rend ce processus technologique plus difficile que celui des semi-conducteurs réguliers. Il s'agit d'un besoin évident de la recherche fondamentale d'explorer de nouvelles façons de fabriquer des nanostructures de diamant, ce qui permet de nouvelles formes de capteurs et dispositifs. Dans ce contexte, le travail présenté est d'une grande importance pour la communauté de diamant et pour le développement futur de la technologie du diamant.

Le manuscrit est divisé en huit parties: une introduction; 6 chapitres, une conclusion générale. Dans l'introduction le contexte de l'étude est brièvement présenté avec les deux objectifs. Le premier consistait à étudier la croissance des nanofils de diamant et à trouver des conditions appropriées pour obtenir des nanofils de façon reproductible. Le deuxième objectif était la mise au point du procédé de gravure du diamant avec des particules de catalyseur et de l'optimisation des paramètres du procédé pour des applications spécifiques telles que la fabrication de membranes poreuses de diamant pour les bio-capteurs.
Le premier chapitre de ce manuscrit présente tout d'abord l'état de l'art en matière de propriétés et des technologies de croissance du diamant. Puis, dans le deuxième chapitre, en vue de la croissance des nanofils et des études de gravure de nanostructures utilisées catalyseurs métalliques tels que Ni, Pd, Co, ..., la base de l'interaction métal-carbone est présenté. Une attention particulière est consacrée à l'effet de la taille nanométrique du catalyseur, et des résultats récents publiés sur le diamant gravure catalytique sont présentés. Comme la thèse aborde la croissance et la gravure de carbone, il est effectivement important de donner des informations de base sur la croissance du diamant et de l'interaction avec catalyseur métallique, car ceci est la nouveauté principale de ce travail. Il doit être mentionné que la théorie de la croissance du diamant à basse pression (par CVD) est encore en débat, et la plupart des résultats ont été obtenus depuis 30 ans en utilisant le progrès scientifique empirique. En particulier, toutes ces techniques, la forme stable du carbone est le graphite, et l'art de la croissance du diamant est de promouvoir la phase diamant et non graphite.

Le chapitre trois contient l'instrumentation et principe de fonctionnement des techniques expérimentales et analytiques utilisées dans cette étude.

Le chapitre suivant se concentre sur la recherche de conditions favorables à la croissance des nanofils de diamant, d'abord en étudiant en détail un processus signalé en 2005 qui a conduit à la nucléation des nanocristaux sur des nanotubes de carbone, puis la croissance de nanofils. Les conditions de croissance ont été soigneusement reproduites, sans succès reproductible. Il en est déduit déduit que d'un élément non a contribué à la croissance, comme une contamination du catalyseur. La combinaison avec le fait que le processus publiée en 2005 n'a jamais été reproduite, en dépit de son importance technologique élevé, ce qui suggère que la contamination s'est produite également dans cette œuvre originale.. Puis, à partir de cette première observation, l'effet d'un catalyseur a été étudié, et des résultats intéressants ont été obtenus. Les nanofils ont été obtenus de façon reproductible, mais le point important est que les nanofils à base de silicium sont très faciles à cultiver, et qu'un environnement de carbone pur était nécessaire d'étudier la croissance de nanofils de carbone. Dans ces conditions, un continuum allant de diamant de gravure pour la croissance du diamant a été obtenue en fonction de l'apport de carbone, très intéressant pour la technologie du diamant. Dans le cinquième chapitre du mécanisme de gravure de diamant par des particules de catalyseur est explorée. Bien que ce genre de gravure a déjà été signalé, aucune étude systématique n'a été menée à bien comprendre le processus afin de l'utiliser dans un endroit bien contrôlé à sens unique. L'étude minutieuse et approfondie des paramètres du processus nous a conduit à proposer une image claire du processus de gravure et de l'influence des différents paramètres. Sur cette base, la gravure à motifs a été proposé pour la fabrication de nano-ou micro-structures dans le diamant, et il est présenté dans la dernière partie de ce chapitre.

Le chapitre 6 présente deux applications intéressantes du processus de développement. Les premières membranes poreuses préoccupations utilisés comme bio-capteurs, et les nanotubes de carbone second concerne la base neuro-capteurs.

La dernière partie est la conclusion qui indique de manière concise les réalisations de la thèse. Malgré l'étude infructueuse de la croissance du diamant nanofil, le travail fait des progrès significatifs à la science de la croissance matérielle nanocarbone. Et elle a conduit à l'étude approfondie de gravure diamant, qui est également très important pour la technologie.

Introduction

One-dimensional structures with nanometre diameters, such as nanotubes and nanowires, have attracted extensive interest in recent years and form new family of materials that have characteristic of low weight with sometimes exceptional mechanical, electrical and thermal properties. Without any change in chemical composition, fundamental properties of bulk materials can be enhanced at the nanometre scale leading to extraordinary nanodevices. Since a few years, nanowires of different semiconducting materials have been grown. To mention few of these, Si, GaN, SnO, SiC and ZnO nanowires were all successfully demonstrated. However, the growth of diamond nanowires has not yet been demonstrated, despite the strong interest for this material. Bulk diamond combines various exceptional properties for a wide range of applications: Chemical inertness, radiation hardness, biocompatibility, high hole/electron mobility (2000/1000 $cm^2/V/s$), high thermal conductivity (22 W/cm/K), wide bandgap (5.5 eV), and wide electric potential window (3.25 eV H-O evolutions).

Since about 30 years, the growth of diamond thin film is well controlled either as insulator or as semiconductor with p- and n- type dopants. Fabrication of 25x25 mm^2 monocrystalline diamond wafer has already been reported, and two inches wafers are expected in a couple of years demonstrating the growing interest for this material. Among present or short-term applications one can mention alpha-particle detectors, solar-blind UV sensors, high voltage electronic devices, bio-sensors and single photon source. The realization of nanowires should improve the performance of some of these devices and also open a range of new high performance applications.

The stability of 0D (nanocrystals) and 1D (nanowires) diamond nanostructures has been extensively studied using ab initio modelling and indicates that for specific crystallographic orientations clusters of nanometric size are thermodynamically stable. One experimental indication for diamond nanowire growth has been published by Sun *et al.* in 2005, based on nanocrystal nucleation and growth on carbon nanotubes followed by 1D growth. This particular nucleation process on carbon nanotube has furthermore been explained theoretically in 2009. Based on these experimental and theoretical results, the first objective of this thesis was to explore the growth of diamond nanowire and find suitable conditions to obtain nanowires in a reproducible way. A wide range of process conditions were explored, first without any catalyst, then with metallic catalyst in order to promote Vapour-Liquid-Solid (VLS) growth. Although a comprehensive knowledge regarding carbon nanotube stability in hydrogen atmosphere and diamond-catalyst interaction has been obtained and some carbon nanostuctures were grown, no diamond nanowires were obtained in a reproducible way. However, the careful study of the diamond-catalyst interaction revealed a very interesting etching process that could be very useful for the fabrication of diamond nanostructures. A second objective was then defined: development of the etching process for diamond using transition metal as catalyst and optimization of the process parameters for specific applications such as the fabrication of porous diamond membranes for bio-sensors.

The first chapter of this manuscript presents the state-of-the-art regarding diamond properties and growth technologies. Then, in the second chapter as both nanowire growth investigation and nanostructure etching studies used metallic catalysts, such as Ni, Pd, Co, …, the fundamental of metal-carbon interaction is presented. A special attention is dedicated to the effect of the nanometric size of the catalyst, and recent results published on catalytic etching of diamond are presented.

Chapter three contains the instrumentation and working principle of the experimental and analytical techniques used in this study.

The next chapter focuses on the search for suitable conditions for diamond nanowire growth; first studying in details the process reported by Sun *et al.* that led to nanocrystal nucleation on carbon nanotube and subsequent nanowire growth. For that purpose carbon nanotubes were grown by hot filament assisted chemical vapour deposition, and their properties were compared with commercially available nanotubes. Then the stability of nanotubes in hydrogen atmosphere suitable for diamond growth was studied, and different process parameters were explored. The different carbon nanostructures such as nano-spikes, nanocrystals, nanotubes or nanowires are presented. The difficulty in obtaining reproducible results on the growth of nanowires suggested that a contamination could promote the growth in particular conditions, the contamination being due, for example, to residual catalyst that exists in commercial nanotubes. Consequently the second part of the chapter is devoted to nanowire growth activated by metallic catalyst deposited on a well-controlled process. Various catalysts and sources of carbon were studied leading to reproducible results. However, a clear influence of silicon on the growth of nanowires has been observed, and the last part of the chapter presents the results obtained in a pure carbon-catalyst environment using bulk diamond substrates in order to avoid any silicon contamination and promote pure carbon nanostructure growth. In these conditions and depending on the amount of carbon supplied to the gas phase, the effect of catalyst could be tuned from carbon nanowire growth (high carbon concentration), perfect balance between growth and etching (intermediate values) to diamond etching (no carbon supplied). The high potential of the last process led us to focus on it for the last part of this thesis.

The following chapter, chapter 5, explores in details the mechanism of diamond etching by catalyst nanoparticles. Various types of catalysts were studied, as well as process parameters such as gas composition, catalyst thickness, pressure, temperature, diamond microstructure or crystallographic orientation, and process duration. The etched diamond samples were studied by various techniques, including chemical surface analysis, and the gas composition was analyzed during the process. The investigation led us to propose a clear picture of the etching process and the influence of various parameters. Based on this and after the analysis of the thin metallic catalyst behaviour at high temperature, in particular the formation of droplet by dewetting, patterned etching was proposed for the fabrication of nano- or micro-structures in diamond and is presented in the last part of the chapter.

The last chapter, before the conclusion, explores two applications of this etching process. The first application concerns porous membranes used as bio-sensors. The challenge is to fabricate long (> 100 nm) and narrow (< 30 nm) pores in a diamond membrane, which will act as a selective filter for biomolecules. As regular etching techniques such as reactive ion etching fails to fabricate such high aspect ratio patterns, our new process is the key technology for such sensor development. The second application concerns carbon nanotubes based neuro-sensors. The high reactivity of carbon nanotubes enhances the signal measured, but the poor adhesion of nanotubes on the substrate is a concern for reproducibility and also for in vivo applications. The etching process allowed us to anchor the carbon nanotubes deep inside a nanocrystalline diamond substrate, leading to a full carbon electrode with high mechanical stability, high bio-compatibility and high sensitivity. The development of these electrodes, mainly carried out in the framework of another thesis in our research group, is briefly presented to give an overview of the potential of the new etching technology we developed.

The last chapter gathers the main results obtained throughout this thesis, and give a few ideas about future development both on diamond nanowire growth and catalytic etching.

CHAPTER 1

State of the Art

Résumé

Ce chapitre présente brièvement la structure électronique et cristallographique du diamant, ses propriétés matérielles notables, et les applications actuelles et futures de diamant. L'état de l’art des technologies en ce qui concerne la croissance de diamant est également discuté. Enfin, la nécessité d'une nanostructure unidimensionnelle de diamant tels que le diamant nanofil et le progrès dans le développement du diamant nanofil est présentée.

En minéralogie, le diamant est un allotrope métastable de carbone, où les atomes de carbone sont disposés dans une variante de la structure à faces centrées cristalline cubique appelée un réseau de diamant. Le diamant est moins stable que le graphite, mais le taux de conversion du diamant en graphite est négligeable dans les conditions ambiantes. Le diamant est reconnu comme un matériau aux exceptionnelles qualités physiques, dont la plupart proviennent de la forte liaison covalente entre les atomes. En particulier, le diamant a la dureté la plus élevée et la conductivité thermique la plus élevée de tous les matériaux connus. Ces propriétés déterminent l'application industrielle majeure du diamant dans la coupe et le polissage des outils et des applications scientifiques couteaux diamant et les cellules à enclumes de diamants. Le diamant possède de remarquables caractéristiques optiques. En raison de son réseau extrêmement rigide, elle ne peut être contaminée que par très peu d'impuretés, telles que le bore et de l'azote. Le diamant possède également relativement élevé de dispersion optique (capacité à disperser la lumière de couleurs différentes), ce qui entraîne son lustre caractéristique. Par ses excellentes propriétés optiques et mécaniques, sa dureté et sa durabilité inégalée notamment, le diamant est la pierre précieuse la plus populaire.

Malheureusement, il s'est avéré très difficile d'exploiter ces propriétés, en raison à la fois le coût et la rareté des grands diamants naturels, et le fait que le diamant était uniquement disponible sous la forme de pierres ou de gravier. La plupart des diamants naturels sont formés à haute température, dans des conditions similaires à celles régnant dans le manteau terrestre. La connaissance des conditions dans lesquelles le diamant naturel est formé en profondeur a été à la base de la technique de croissance à haute pression et haute température (HPHT), d'abord commercialisé par General Electric. L'inconvénient de la méthode HPHT est qu'il continue de produire du diamant en forme de monocristaux dont la taille du nanomètre au millimètre, ce qui limite la gamme des applications pour lesquelles il peut être utilisé. Le développement de la technique de dépôt chimique en phase vapeur (CVD) a permis de

diversifier les types de diamant produits.. Parmi les différents procédés de dépôt de diamant CVD, le filament chaud CVD (HF-CVD) et le micro-ondes plasma CVD (MP-CVD) se sont révélés être les procédés les plus utilisés de dépôt de diamant dans la réalisation d'un film de diamant de bonne qualité. Au fil des années, il y a eu un grand nombre d'études de la chimie en phase gazeuse et nous commençons maintenant à obtenir une image plus claire des principes importants impliqués. Dans un procédé classique CVD, les gaz de procédé de mélange dans la chambre, puis ils passent à travers une région d'activation (par exemple un filament chaud ou par décharge électrique), qui fournit de l'énergie pour les espèces gazeuses. Cette activation provoque molécules à se fragmenter en des radicaux et des atomes, crée des ions et des électrons, et chauffe le gaz jusqu'à quelques milliers de Kelvin. Au-delà de la zone d'activation, ces fragments réactifs continuent à se mélanger et se soumettre à une série complexe de réactions chimiques jusqu'à ce qu'ils frappent la surface du substrat. A ce stade, les espèces peuvent soit absorber et réagir avec la surface, désorber on revient en phase gazeuse, ou diffuser autour de près de la surface jusqu'à ce qu'un site de réaction appropriée soit trouvée. Si une réaction se produit surface, un des résultats possibles, si toutes les conditions sont appropriées, est la croissance de diamant. De plus la cinétique de croissance du diamant est lente à des températures faibles dépôts, un pré-traitement approprié du substrat, ce qui assure une densité de nucléation homogène et élevée tout au long de la surface du substrat, est l'étape indispensable avant le dépôt. De nombreuses approches ont été utilisées pour améliorer cette densité de nucléation allant de l'abrasion du substrat, l'addition de carbure formant ou contenant des intercalaires, par polarisation de nucléation accrue, à la demande de monocouches de particules de nanodiamant sur la surface pour la croissance ultérieure.

La dernière partie de ce chapitre traite de la nanostructure unidimensionnelle de diamant tels que le diamant nanofil. Avec l'expansion de la nanotechnologie qui entoure les quasi-unidimensionnels nanomatériaux de carbone sp2 liés, la prochaine étape logique dans l'étude de nanocarbone est l'étude des nanofils de diamant (DNWs). La réalisation de nanofils de diamant, ses propriétés uniques, et les dimensions géométriques, devrait améliorer le comportement de certains des dispositifs de diamant, et aussi ouvrir un éventail de nouvelles applications de haute performance tels que le diamant nanofil de photon unique source de traitement de l'information quantique photonique. Cependant, les progrès dans la fabrication de nanofils de diamant a été limitée, en particulier la fabrication de nanofils longs en diamant cristallin. Théoriquement, il a été montré que la stabilité dynamique et structurale des nanofils de diamant dépend de la morphologie de surface, direction cristallographique de l'axe principal et le diamètre des nanofils. Dans le cas d'1D, par exemple, le long de la croissance de nanofils d'orientation [100] sont révélés stables, alors que pour une orientation telle que [110] de la structure de diamant est instable. La croissance de nanofils de diamants a été rapportée par Sun et al. en 2005, où ils ont présenté la croissance de nanofils de diamant en forme de chaîne d'un diamètre de 4-8 nm et des longueurs allant jusqu'à 200 par plasma d'hydrogène très longtemps après le traitement de nanotubes de carbone. Ce processus de croissance, en particulier la nucléation du diamant sur un nanotube de carbone, a ensuite été étudié théoriquement et les résultats suggèrent qu'un site de nucléation pour le diamant existe dans la structure de nanotubes. D'autre part, le succès récent dans le diamant de synthèse de nanofils a suggéré que l'utilisation de métaux de transition comme catalyseurs peut faciliter la croissance unidimensionnelle. Cette situation a incité à reconsidérer le mécasisme vapeur-liquide-solide croissance (VLS) de nanofils de silicium pour la croissance des nanofils de diamant. Toutefois, en ce qui concerne l'aspect critique de diamant nanofil la stabilité, et le manque de connaissances expérimentales sur le mécanisme de formation, il est donc la plus haute importance d'avoir un aperçu plus loin dans l'interaction entre le catalyseur et l'atmosphère du carbone. La nature de l'interaction métal-carbone et les facteurs qui affectent cette interaction a été présenté dans le chapitre 2.

1.1. Bulk Diamond

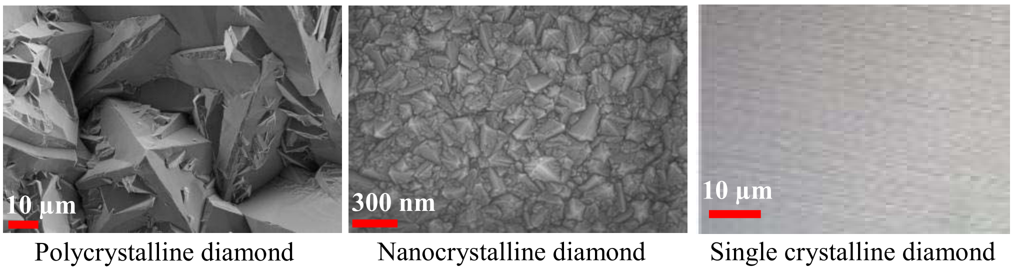

Polycrystalline diamond Nanocrystalline diamond Single crystalline diamond

Figure 1.0. SEM images of conventional diamond microstructures

1.1.1. Structure and Classification

The extensive study of carbon has led to the discovery of a variety of remarkable properties, which have prompted some ingenious inventions, and that have found their way into countless applications (**Barnard, 2000**). The fact that carbon, having atomic number 6, is able to form single, double and triple bonds sets it apart from the other elements. These bonds themselves are described as *sp* bonds, as the bonding involves both σ and π orbitals, and determine the formation of a number of different allotropes (figure 1.1). This is the bonding that determines the properties and applications of different carbon allotropes. For example, the formation of sp^3 bonds (in the case of four-coordinated atoms) produces the hardest known mineral, diamond; whereas the formation of sp^2 bonds (in the case of three coordinated atoms) produces one of the most fragile, graphite.

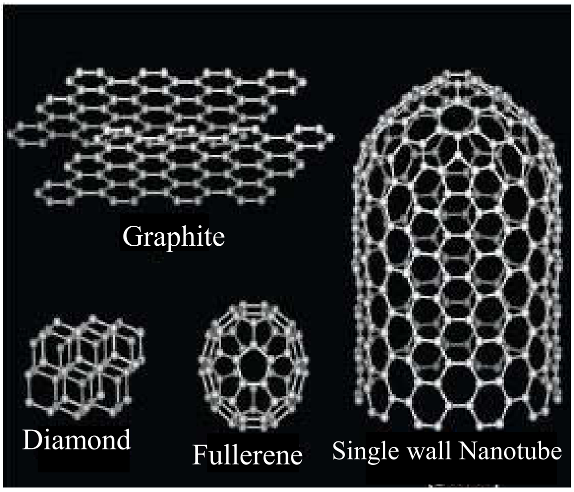

Figure 1.1. Schematic illustration of the principal allotropes of carbon.

In pure natural cubic diamond, carbon atoms are bound to four adjacent atoms placed at the corners of a regular tetrahedron forming single σ bonds, with small bond length of 0.154 nm and high bond energy of 347 kJ/mol (**Guy, 1959**), which result in sp^3-hybridised orbitals in the direction of the cube diagonals. The bonds form equal angles of 109° 28′ to each other as shown in figure 1.2 (a).

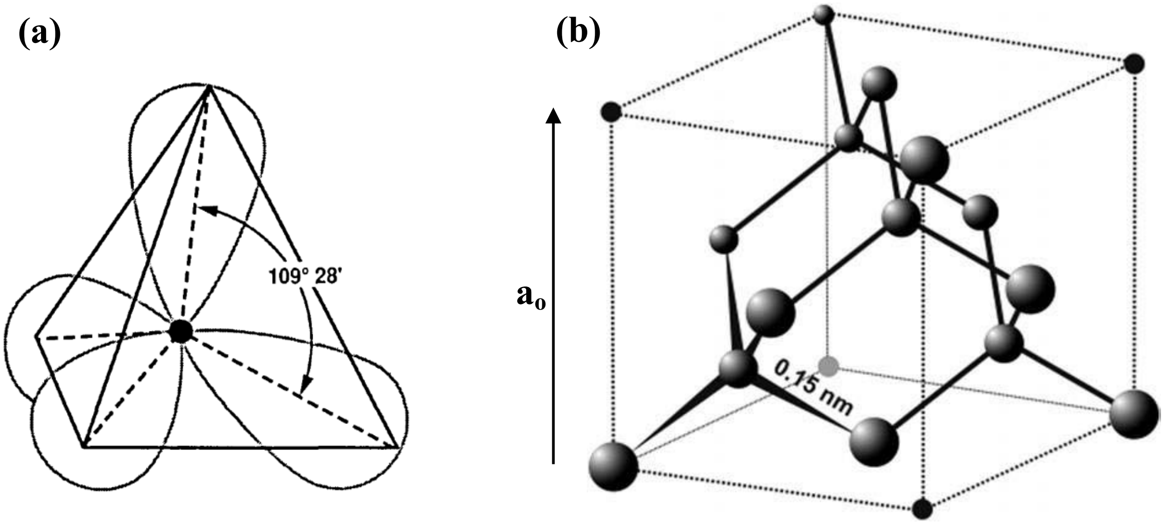

Figure 1.2. (a) The diamond tetrahedron and (b) face-centred cubic structure of diamond, figure is not scaled.

With its fourfold coordinated tetrahedral (sp^3) bonds, the diamond structure is isotropic and, except on the (111) plane, is more compact than graphite (with its sp^2 anisotropic structure and wide interlayer spacing). Consequently, diamond has higher density than graphite (3.515 g/cm^3 vs. 2.26 g/cm^3) and it is predicted to be the highest of any material (**Spear, 1989**). As a result, diamond is the stiffest, hardest and least compressible of all substances.

Diamond is a face-centred cubic (FCC) lattice, with a basis of two identical carbon atoms: one at (0, 0, 0) and the other at (1/4, 1/4, 1/4), where the coordinates are given as fractions along the cube sides. This is the same as two interpenetrating FCC lattices, offset from one another along a body diagonal by one-quarter of its length. The conventional unit cell is cubic (figure 1.2 (b)), with a side length a_o approximately equal to 3.567 Å at room temperature (**Guy, 1959; Cullity, 1956**).

Diamond occurs in several crystal forms (or habits) which include the octahedron, the dodecahedron, and others which are more complicated. The simple crystallographic planes in a cubic crystal ((100), (110), and (111)) correspond to the faces of the three major crystal forms of diamond: the {100} cubic, the {110} dodecahedral and the {111} octahedral (figure 1.3). Both cubic and octahedral surfaces predominate in high-pressure synthetic diamond where they are found alone or in combination to form blocky crystals (**Gardinier, 1988**). In chemical vapor deposited (CVD) diamond, the (111) octahedral and the (100) cubic surfaces predominate and cubo-octahedral crystals combining both of these surfaces are commonly found. Twinning occurs frequently on the (111) surface. Faceted crystals of cut diamonds are predominantly the (111) and (100) surfaces.

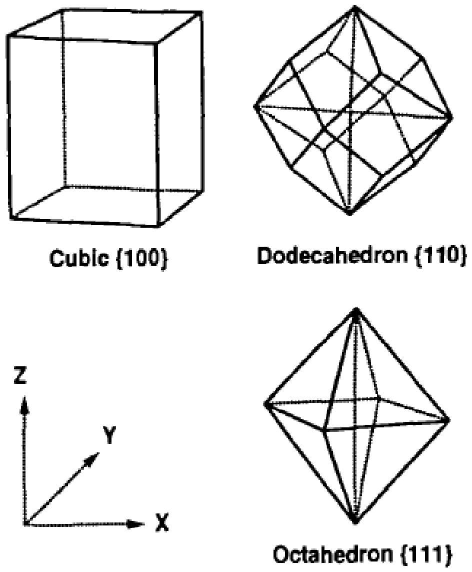

Figure 1.3. Major crystal forms of diamond, adapted from ***Gardinier, 1988****.*

The current classification of diamond is based on one-phonon optical absorption of few impurities /and defects, which are present in both natural and synthetic diamond. The most important of such impurities is nitrogen (N) that is detectable by optical absorption in almost 98% of all natural diamonds. An extensive description of nitrogen in diamond had been given by **Collins** (**1992**) and **Woods** (**1986**). Boron (B) and hydrogen-related defects also play a role in the classification of natural, high pressure-high-temperature (HPHT) and CVD diamond. The presence of such impurities and defects yields very typical features in the absorption spectra making possible to distinguish between different classes of diamond (**Field, 1992; Spear & Dismukes, 1994; Walker, 1979; Woods, 1994**). In particular, the Infrared (IR) region of the absorption spectrum is the most sensitive to extrinsic impurities.

In **1959**, **Kaiser & Bond** identified N as the major impurity in diamond, producing a great number of optical centres through the whole optical range. As a consequence of the high optical activity of nitrogen, diamond classification is primarily based upon nitrogen-related optical absorption.

The most common type Ia contains agglomeration of nitrogen impurities in the amount of ~10^{18} cm^{-3}, where as type Ib contains single nitrogen defects having 200 ppm of nitrogen and commonly used as substrates for epitaxy. The type IIa and IIb are more pure (and more rare in nature), containing extremely low concentrations of impurities. The third type III diamond has a hexagonal structure and is the rarest of all. Type III diamond has the same nearest-neighbour configurations like cubic diamond but hexagonal stacking, and is named lonsdaleite after the English crystallographer Dame Kathleen Lonsdale. There is also a rare form of crystalline carbon called charoite, which is a hexagonal form usually produced in shock metamorphosed graphite, and meteorites. It shares many similarities with graphite, and with hexagonal diamond (**Barnard, 2000**).

1.1.2. Properties and Applications

Properties: The rigid covalent lattice in diamond, with its high atomic number density (**Spear, 1989**), gives diamond some of the most remarkable properties, together in one material. For example, the atoms in diamond can vibrate at unusually high frequencies because of this strong covalent bond (347 $kJmol^{-1}$) and light weight of carbon atoms. The maximum frequency is about 40×10^{12} Hz, compared with 16×10^{12} Hz of silicon (**Gracio *et al.* 2010**). The high frequency of vibration results in the high heat conduction of diamond, which is even larger than in metals: at room temperature diamond conducts heat 4 times better than copper (**Gruen & Buckely-Golder, 1998**). In addition, since the atoms in diamond are strongly bonded, a large amount of energy is required to remove a carbon atom from the diamond lattice, making diamond extremely hard and abrasion-resistant.

It is known that photon absorption in diamond with the creation of only one phonon is forbidden by the inversion symmetry of diamond lattice (**Dolling & Cowley, 1966**). Absorption with the creation of two phonons is observed at photon energies up to about 0.27 μm^{-1}, approximately twice the maximum frequency of lattice vibrations (**Kulda *et al.* 1996**). This leads to a high transparency of diamond to most infrared radiation—it is only slightly opaque in the mid-infrared wavelength between 4 and 5μm, making diamond a promising material for window and detector applications.

Diamond is a wide bandgap material, having bandgap of 5.47 eV and is generally considered as an electrical insulator, since 5.47 eV is much higher than the thermal energy $k_BT \sim 0.025$ eV (where k_B is Boltzmann's constant and T is the absolute temperature) and the probability of thermal excitation of electrons from the valence band to the conduction band is negligible at room temperature. The electric breakdown field is correspondingly high: 2×10^7 Vcm^{-1} for diamond, and only 3×10^5 Vcm^{-1} for Si and 4×10^5 Vcm^{-1} for GaAs (**Gracio *et al.* 2010**). While diamond possesses a wide bandgap, the band structure calculation and experiments demonstrate that the vacuum level lies below the conduction band and diamond (111) surface is known to show a negative electron affinity (NEA) (**Himpsel *et al.* 1979**). This allows the diamond surface to emit electrons to the vacuum with a low applied electric field and opens the door for the use of diamond for cold cathodes and field-emitter displays. Some notable properties of diamond are summarized in Table 1.

Table 1. Notable material properties of diamond

Property and unit	**Value**
Mechanical hardness (GPa)	~ 100
Young modulus (GPa)	1.1×10^3
Compressive modulus (GPa)	4.4×10^2
Friction co-efficient	0.05-0.15
Thermal conductivity at room temperature (RT) (Wcm^{-1}K^{-1})	21.9
Thermal expansion coefficient at RT	8×10^{-7}
Transparency	225 nm to far IR
Refractive index	2.41 at 590 nm
Bandgap (eV)	5.47
Resistivity at RT (Ω cm)	$>10^{16}$ (**Pernot *et al.* 2010**)
Electron mobility at RT (cm^{2}V^{-1}S^{-1})	2400 (**Pernot & Koizumi, 2008**)
Hole mobility at RT (cm^{2}V^{-1}S^{-1})	2000 (**Pernot *et al.* 2010**)
Breakdown field (Vcm^{-1})	2×10^7
Electron affinity	-1 eV to +1 eV depending on diamond surface
Chemical reactivity	Inert below 600 °C

Applications: Tribological applications come naturally as one of the main and well-established diamond application areas. The extreme hardness of diamond, coupled to its wear resistance and chemical inertness, have made it an ideal candidate for use in cutting tools for machining non-ferrous metals, plastics, chip-board and composite materials (**Nebel & Ristein, 1992**). Indeed, HPHT industrial diamond has been used for this purpose since the

1960s, and remains a lucrative commercial process today. CVD diamond is beginning to be used in a similar way. Diamond-based tools can be divided into two main areas: (i) tools fabricated with diamond particles using the conventional powder metallurgy techniques and (ii) CVD diamond coated tools, where a thin diamond film is deposited on the tool surface. Initial tests (**Reineck *et al.* 1996; Karner *et al.* 1996**) indicate that such CVD diamond-coated tools have a longer life, cut faster, and provide a better finish than conventional WC tools. Commercially available diamond-based tools include drill bits, plates, die blanks, grinding and cut-off wheels, blades, chain saws and circular concrete saws (www.idr-online.com). In addition, diamond's high thermal conductivity and thermal oxidation resistance make it a suitable material for high speed and dry machining (**Balmer *et al.* 2009**) and for the moulding industry (**Neto *et al.* 2009**). Diamond's wear resistance, together with the range of high transmittance, also enables the use of various diamond coatings on wear-resistant windows (**Miller *et al.* 1997**), UV mirrors (**Pace *et al.* 2001**), IR (**Klein, 1993; Dore *et al.* 1998**), microwave (**Thumm, 2001**), RF (**Brandon *et al.* 2001**) and optical transmission windows (**Ying *et al.* 2003**) and waveguides (**Hiscocks *et al.* 2008**).

The characteristics wide bandgap, large breakdown field and high hole mobility make diamond a promising material for high-power and high frequency electronic applications. Several diamond-based devices have already been developed, such as transistors operating in the microwave range (**Calvani *et al.* 2009**), high-voltage diode (**Volpe *et al.* 2010**), high-temperature diodes (**Gurbuz *et al.* 2005**), thermistors (**Bade *et al.* 1993**) and transistors (**Pang *et al.* 1997**), laser windows (**Mildren *et al.* 2008**) and solid-state detectors (**Bergonzo *et al.* 2006**). Diamond field emitters and cold cathodes also take advantage of the NEA (**Kang *et al.* 2004**). The excellent thermal properties of diamond are the basis of heat-spreading films for RF devices thermal management (**Seelmann-Eggebert *et al.* 2001**) and, more recently, diamond packages for high-power lasers (**Rotter *et al.* 2008**).

Among all materials, diamond possesses the highest surface acoustic wave (SAW) velocity, which is about 18,000 ms^{-1} in longitudinal elastic wave (**Davis, 1994**). Taking advantage of this feature, together with diamond's high stiffness, diamond-based surface acoustic wave (SAW) devices (**Shikata, 1998**), micromechanical oscillators (**Baldwin *et al.* 2006**) and tweeter components (**Fujimori, 1998**) have also been successfully developed and commercialized.

Although pure (type IIa) diamond is an insulator with a large indirect band-gap of 5.47eV (at 300 K), when doped with boron it forms a p-type semiconductor, with an acceptor level at 0.38 eV above the valence band maximum (**Collins & Lightowlers, 1979; Swain *et al.***

1998). This type of conducting diamond electrodes has been found to have a very large potential window in water (**Martin *et al.* 1995**). This is a great advantage over other electrode materials, such as Pt, which dissociate water at higher electrode potentials resulting in the unwanted evolution of hydrogen and oxygen. For diamond based electrodes, this hydrogen evolution rate is much slower, allowing much higher electrode potentials to be used. This permits the chemistry of redox couples to be studied, which would otherwise be inaccessible (**Bouamrane *et al.* 1996**). Diamond electrodes for electrochemical water treatment are a commercial product readily supplied by several organizations, such as CONDIAS and CSEM. However, there are a number of major problems which still need to be overcome if high performance diamond-based devices are to be achieved. Probably the most difficult problem is that of doping the diamond reliably and reproducibly. p-type doping is relatively straightforward, since addition of a few ppm of a boron-containing gas such as B_2H_6 to the CVD process gas mixture is all that is required to incorporate B into the lattice (**Okushi, 2001; Lagrange *et al.* 1998**). However, the close packing and rigidity of the diamond lattice make doping with atoms larger than C very difficult. This means that dopants which are routinely used to n-dope Si, such as P or As, cannot easily be used for diamond. The development of a successful n-doping process has taken a considerable time and the first evidence of n-type conduction for phosphorus-doped {111}-oriented homoepitaxial layers was obtained at the National Institute for Materials Science (NIMS) laboratories, in Japan (**Koizumi *et al.* 1997**).

Despite these difficulties, diamond-based devices are gradually beginning to appear, and may become the material of choice for electronic applications in few years.

1.1.3. Synthesis of Diamond Thin Films: Historical Background

High Pressure High Temperature (HPHT) synthesis: With wide range of exceptional properties, it is not surprising that diamond has sometimes been referred to as ‘the ultimate engineering material’. Unfortunately, it has proved very difficult to exploit these properties, due both to the cost and scarcity of large natural diamonds, and the fact that diamond was only available in the form of stones or grit. It had been shown by Antoine Lavoisier in 1772 that diamond is composed solely of carbon. Since then, many attempts were made to synthesize diamond artificially using as a starting material another commonly occurring form of carbon, graphite. This proved extremely difficult, mainly because at room temperature and pressure, graphite is the thermodynamically stable allotrope of carbon. In fact, diamond has long been known to be thermodynamically stable with respect to graphite only at high pressure (**Leipunski, 1939**; **Berman & Simon, 1955**). At 298 K and 1 atm pressure, the difference in free energy between diamond and graphite is only 2.9 kJ mol^{-1} (approximately 0.03 eV per atom), which is only on the order of kT (**Angus *et al.* 1993**). Furthermore, there is a very large activation barrier inhibiting the transformation of diamond to graphite. Or perhaps, more significance is the fact that graphite (2.26 g cm^{-3}) is less dense than diamond (3.51 g cm^{-3}). Therefore, as solid carbon precipitates out of a supersaturated carbon gas, the 'first' phase encountered is graphite, not diamond. This is an example of Volmer's rule, which states that the least dense solid phase is the first to crystallize from a supersaturated fluid phase. Once formed, diamond will not spontaneously transform further into graphite because of the high activation barrier between the two phases. Thus, diamond is said to be metastable, that is, kinetically stable but not thermodynamically stable.

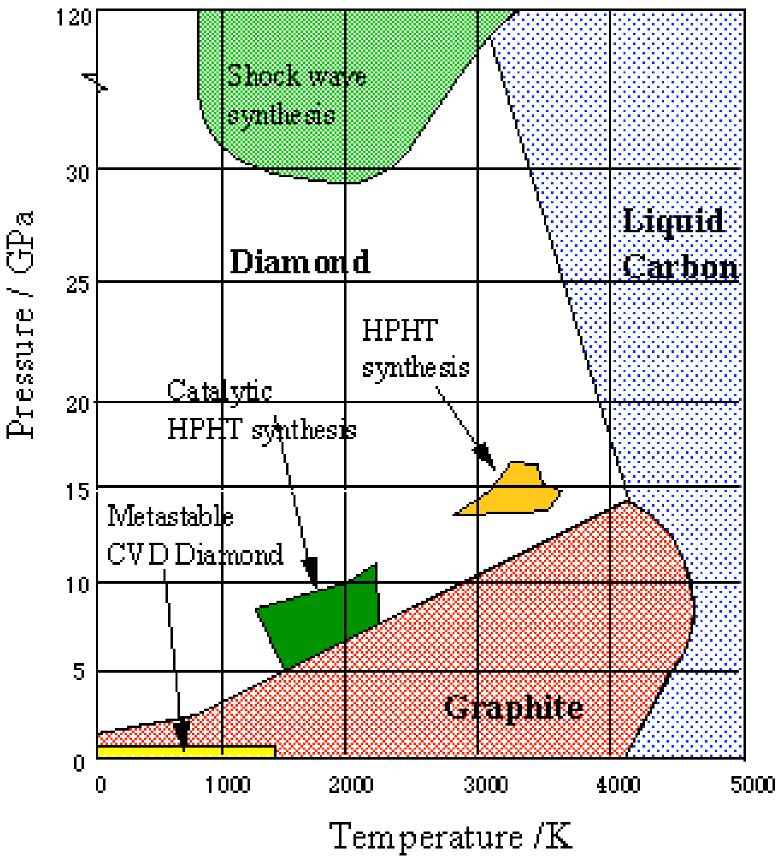

*Figure 1.4. Phase diagram of carbon after **F.H. Bundy (1980)**.*

To overcome these problems, researchers realized that in order to form diamond, conditions are needed where diamond is the more stable phase. The knowledge of the conditions under which natural diamond is formed deep underground suggested that diamond could be formed by heating carbon under extreme pressure. This process forms the basis of the so-called high-pressure high-temperature (HPHT) growth technique (**Field, 1992**), first marketed by General Electric.

Early attempts to make diamonds began in 1878 with the work of **Hannay** (**1880**), followed by Moissan in 1889, Crooks in 1909, **Parsons** in **1918**, and decades of work performed by Bridgman in the early half of the twentieth century (**Bundy *et al.* 1955**). The first successful synthesis of diamond was reported in 1954 by Hall using high pressure high temperature (HPHT) methods (**Hall, 1961**). In this process, graphite is compressed in a hydraulic press to tens of thousands of atmospheres, heated to over 2000 K in the presence of a suitable metal catalyst, and left until diamond crystallizes.

This discovery proved to be the ignition point for what has become a multi-billion dollar industry, with synthetic HPHT diamond crystals being used for a variety of applications (**Barnard, 2000**). However, the drawback of the HPHT method is that it still produces diamond in the form of single crystals ranging in size from nanometres to millimetres, and this limits the range of applications for which it can be used. What is required is a method to produce diamond in a form that can allow many more of its superlative properties to be exploited, in other words, as a diamond thin film and consequently, the development of the chemical vapour deposition (CVD) method has made it possible.

Chemical Vapour Deposition (CVD): Rather than try to duplicate nature's method for creating diamond (as in the HPHT method), diamond could conceivably be produced if carbon atoms could be added one-at-a-time to an initial template, in such a way that a tetrahedrally bonded carbon network results. If this could be accomplished from the gas phase using much lower pressure than in HPHT, there would be an obvious advantage in terms of equipment and energy costs. These ideas were considered to be the motivational point for the development of chemical vapour deposition technique as a successful diamond synthesis method.

The first reported synthesis of diamond using low pressure chemical vapor deposition (CVD) methods was in **1911**, by **W. von Bolton**. This was however generally regarded at the time as an academic experiment for the sake of curiosity, and further interest in the field was not generated until the late 1950s and early 1960s. In 1949 Eversole began work on diamond synthesis, leading to successful growth of thin films on high-surface area powder from methane and carbon monoxide in 1952, and a patent in 1962 (**Eversole, 1962**). This effort was ultimately abandoned after the announcement of the successful growth of diamond at high pressures by General Electric Corporation (**Bundy *et al.* 1955**). Eversole's work was later extended by Angus *et al*. at Case Western Reserve University (**Angus *et al.* 1968, 1971**; **Poferl *et al.* 1973**; **Chauhan *et al.* 1974, 1976**) and by Derjaguin and a large group at the Physical Chemistry Institute in Moscow (**Derjaguin *et al.* 1968, 1970**; **Fedoseev *et al.* 1978, 1979**; **Varnin *et al.* 1977**; **Spitsyn *et al.* 1981**). The Angus group showed the beneficial effect of added hydrogen on diamond yield, developed methods for removing unwanted graphitic carbon using atomic hydrogen, and grew boron-doped diamond by chemical vapor deposition (**Poferl *et al.* 1973**). In their first studies, the Soviet workers reported the growth of filamentary diamond whiskers using a vapor-liquid-solid (VLS) technique with molten iron and nickel (**Deryagin *et al.* 1968, 1970**). Surprisingly, this process has received little attention in subsequent years. From the same group at the Physical Chemistry Institute, **Varnin *et al*.** (**1977**) grew diamond thin films from the gas phase; **Spitsyn**, Bouilov, and Derjaguin (**1981**) reported both diamond films and isolated diamond crystals grown on copper substrates by chemical vapor transport from a graphite source.

Although the early studies showed the feasibility of diamond synthesis by chemical vapor deposition, the growth rates were low. This situation changed dramatically in the mid-1980s. A group at the National Institute for Research in Materials in Tsukuba, Japan, under the leadership of Yoichiro Sato achieved large increase in growth rates by activating the gas phase during growth with a hot filament (**Matsumoto *et al.* 1982a, 1982b**), a microwave discharge (**Kamo *et al.* 1983**), and an RF discharge (**Matsumoto, 1985**; **Matsumoto *et al.* 1987**). Since the mid-1980s, the interest in chemical vapor deposition of diamond has expanded enormously, and it is now used to grow extremely high-quality diamond in many shapes and grain sizes from ultrananocrystalline (**Gruen *et al.* 1994**; **Butler & Sumant, 2008**) and nanocrystalline (**Butler & Sumant, 2008**; **Windischmann & Epps, 1990**) films, through polycrystalline plates and wafers (**Gray & Windischmann, 1999**), to large single crystals (www.e6cvd.com; **Bogdan *et al.* 2006**).

1.1.4. Chemical Vapour Deposition (CVD) of Diamond

CVD systems: The growth of diamond films from the vapour phase on non-diamond substrates at practical rates was accomplished with the development of thermal- and plasma-enhanced CVD methods, in which a hydrocarbon gas (usually methane) mixed in low concentrations with hydrogen is energized thermally or in a plasma, prior to contact with a heated substrate. The first of these enhanced CVD methods was the chemical transport reaction synthesis developed by Soviet workers in the late 1970s (**Derjaguin & Fedoseev, 1975**; **Spitsyn *et al.* 1981**). From that time until the late 1980s, virtually all of the significant developments on CVD systems reported have been due to Japanese work. These include the development of filament-assisted thermal CVD (**Matsumoto *et al.* 1982a**), electron-assisted thermal CVD (**Sawabe & Inuzuka, 1985, 1986**), laser-assisted thermal CVD (**Kitahama *et al.* 1986**), RFplasma CVD (**Matsumoto, 1985**), microwave-plasma CVD (**Kamo *et al.* 1983**), combustion-flame-assisted CVD (**Hirose *et al.* 1989**) and direct-current arc plasma jet CVD (**Kurihara *et al.* 1988**). Detailed reviews of the various methods used for fabricating diamond can be found in the literature (**Dischler & Wild, 1998**; **Gracio *et al.* 2010**).

Among the various diamond deposition processes, the hot filament chemical vapour deposition (HF-CVD) process and the microwave plasma CVD (MP-CVD) method have proven to be the most used diamond deposition processes in achieving a good quality diamond film. However, DC-plasma is still used in specific cases, such as hetero-epitaxy on Ir (**Washiyama *et al.* 2011**).

The hot filament method was the first practical method to produce diamond in a systematic way because of a greater degree of process control (**Matsumoto *et al.* 1982b**). In this method, diamond particles or films are deposited on a heated substrate from a mixture of methane and hydrogen dissociated by hot tungsten or other high-melting-point metal filament placed close to the substrate. The main role of the hot filament is to dissociate molecular hydrogen into atomic hydrogen. Although the HFCVD method is relatively cheap and easy to operate and produces reasonable quality polycrystalline diamond films, it suffers from a number of major disadvantages. The hot filament is particularly sensitive to oxidizing or corrosive gases, and this limits the variety of gas mixtures which can be employed. It is also very difficult to avoid contamination of the diamond film with filament material. Due to the temperature upper limit of the filament material, hot-filament processes operate at significantly lower gas temperatures than plasma processes, and consequently produce less atomic hydrogen. The low gas phase concentrations give relatively low growth rates compared with the plasma methods. Despite these drawbacks, hot-filament assisted deposition has remained popular because of its low capital cost and simplicity. Also, hot-filament reactors are directly scalable to large sizes and can be used to coat complex shapes and internal surfaces.

The microwave plasma CVD method was the next practical method to be developed (**Kamo *et al.* 1983**) and despite being significantly more expensive, are now among the most widely used techniques for diamond growth. In this method, the substrate can be heated by the plasma alone or with a separate heating source. The deposition parameters are similar to those in the hot filament reactor. The role of the plasma is to generate atomic hydrogen and to produce proper carbon precursors for the growth of diamond. Adding oxygen to the feed gas mixture improves the quality of the diamond (**Chiang *et al.* 1988**). Most commercial microwave systems operate at a frequency of 2.45 GHz. The fact that no filament is involved makes MPCVD systems inherently cleaner than HFCVD systems, and so they have become the system of choice for electronic applications. Furthermore, the presence of a significant number of ions within the discharge allows the possibility of deliberately altering the deposition conditions by biasing the substrate (**Stoner *et al.* 1992**). The most important use for this has been in so-called bias-enhanced nucleation (BEN), whereby a negative potential (typically 100–200 V) is applied to the substrate heater for the first few minutes of the deposition process.

While each method differs in detail, they all share a number of features in common. For example, the temperature of the substrate is usually greater than 700 °C to ensure the formation of diamond rather than amorphous carbon. However, the high substrate temperature limits the use of diamond films in many industrially important systems. CVD diamond has a much higher density of structural inhomogeneities (such as grain boundaries) and contaminants than bulk diamond. But, the use of diamond films for thermal applications, for example, requires a high crystallinity, reduced grain boundary network and very low contamination by non-carbon elements. Low temperature deposition eliminates the risk of any Si (for Si wafer) or other substrate material diffusion into the deposited diamond layers. Consequently, a major goal in the diamond research has been to lower the substrate temperature required for diamond growth. Several reviews have been written on the growth of diamond films at low temperatures (**Muranaka *et al.* 1994**; **Das & Sing, 2007**). Numerous reports in the literature show the advantage of the low temperature deposition of diamond film on hard tool materials (**Haubner *et al.* 1993**; **Mallika & Komanduri, 1999**; **Sakamoto & Takaya, 2002**; **Silva *et al.* 2000**), electronics substrates (**Gicquel *et al.* 2001**; **Hiraki, 2001**), and also on optically transparent substrates such as sapphire, zirconia and zinc sulphide used in infrared windows (**Drory & Hutchinson, 1994**; **Ramesham & Roppel, 1992**).

Synthesis of diamond at low temperatures is even more challenging because of the difficulties in the nucleation and growth steps involved in diamond thin film deposition on a variety of substrates. Nucleation is the first and probably the most important step in achieving a good quality diamond film and the nucleation process depends strongly on the processing parameters such as gas composition, concentration of the precursor gases in the mixture, temperature, pressure, and microwave power. Since diamond growth is slow at low deposition temperatures, a suitable pre-treatment of the substrate, which ensures a uniform and high nucleation density throughout the substrate surface, is essential step before deposition. Just like nucleation, growth of diamond film is very much dependent on the deposition parameters. Numerous approaches have been used to enhance this nucleation density ranging from substrate abrasion, the addition of carbide forming or containing interlayers, through bias enhanced nucleation, to the application of monolayers of nano-diamond particles on the surface for subsequent growth (**Das & Singh, 2007**).

Chemistry of CVD diamond: The complex chemical and physical processes which occur during diamond CVD comprise several different but interrelated features, and are illustrated in figure 1.5.

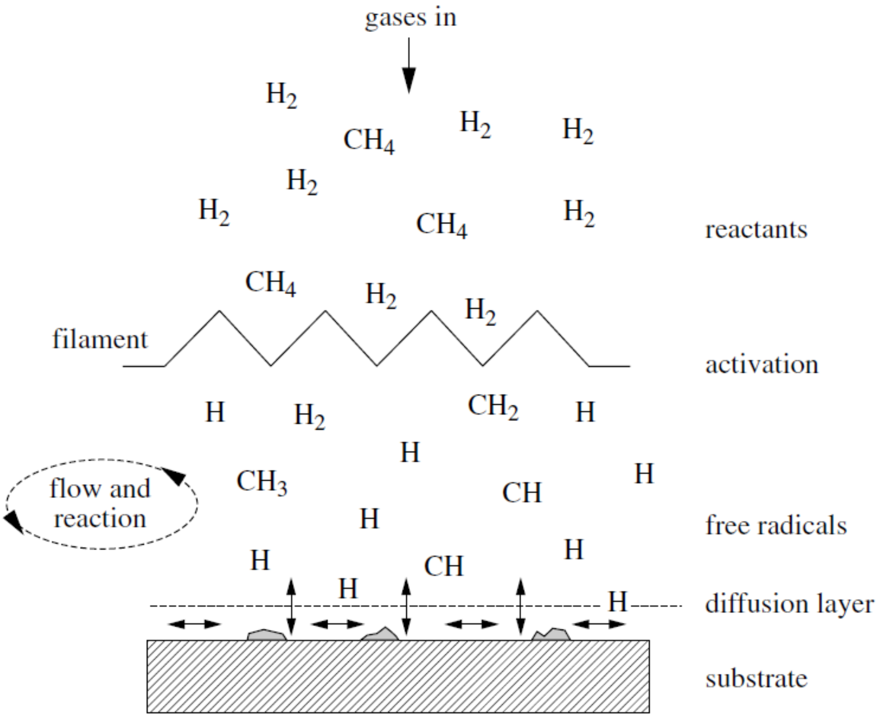

Figure 1.5. A Schematic of the physical and chemical processes occurring during diamond CVD, adapted from ***Ashfold et al. 1994****.*

The process gases first mix in the chamber, then they pass through an activation region (e.g. a hot filament or electric discharge), which provides energy to the gaseous species. This activation causes molecules to fragment into reactive radicals and atoms, creates ions and electrons, and heats the gas up to a few thousand kelvins. Beyond the activation region, these reactive fragments continue to mix and undergo a complex set of chemical reactions until they strike the substrate surface. At this point the species can either adsorb and react with the surface, desorb again back into the gas- phase, or diffuse around close to the surface until an appropriate reaction site is found. If a surface reaction occurs, one possible outcome, if all the conditions are suitable, is diamond.

Over the years, there have been a large number of studies of the gas phase chemistry (**Spear & Dismukes, 1994**; **Rego *et al.* 1996**; **Loh *et al.* 1997**; **Ferreira *et al.* 1998**), and we are now beginning to obtain a clearer picture of the important principles involved. The first clue was obtained from the 'Bachmann triangle diagram' (**Bachmann *et al.* 1991**), which is a C–H–O composition diagram based upon over 70 deposition experiments in different reactors and using different process gases (see figure 1.6). Bachmann found that independent of deposition system or gas mixture, diamond would only grow when the gas composition was close to and just above the CO tie-line. This implied that diamond growth was independent of the nature of the gas phase precursors, and that the gas phase chemistry was so rapid it simply and effectively broke down the constituent gases to smaller, reactive components.

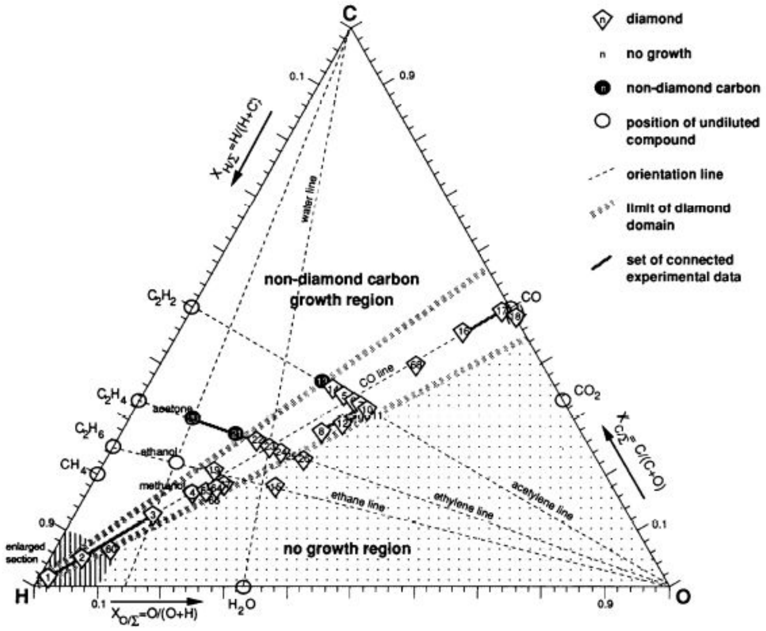

Figure 1.6. A C–H–O phase diagram summarising 70 experiments using different mixtures to deposit diamond by CVD adapted from ***Bachmann et al. 1991****.*

It is now believed that atomic hydrogen is the most critical component in the gas phase mixture, and indeed that it drives the whole chemical system (**Goodwin *et al.* 1997**). In an HF system, atomic hydrogen is produced heterogeneously by thermal decomposition of H_2 on the hot filament surface, while in a plasma system H is created by electron impact dissociation of H_2. The atomic hydrogen, once formed, undergoes several spontaneous, highly exothermic, reactions (Table 2) (**Angus *et al.* 1993**). It can react with neutral species such as CH_4, in the gas phase, abstracting hydrogen to form methyl radicals (CH_3) which can then attach to suitable surface sites. The atomic hydrogen also abstracts hydrogen from the CH surface, providing surface radical sites for carbon containing radicals to adsorb. However, much more frequently these are simply replaced with another hydrogen atom due to the relatively high concentration. It is this turnover of hydrogen atoms that also dehydrogenates the adsorbed carbon species and incorporates them into the lattice. Atomic hydrogen also reacts with *sp* and *sp*^{2} carbon sites on the surface converting them to *sp*^{3} carbon (**Butler *et al.* 2009**). Thus, atomic hydrogen is critical for the CVD growth process and the efficiency of its production is a key parameter in CVD apparatus design.

Table 2. Standard enthalpy and free energy changes of some important reactions during diamond growth adapted from **Angus *et al.* 1993**.

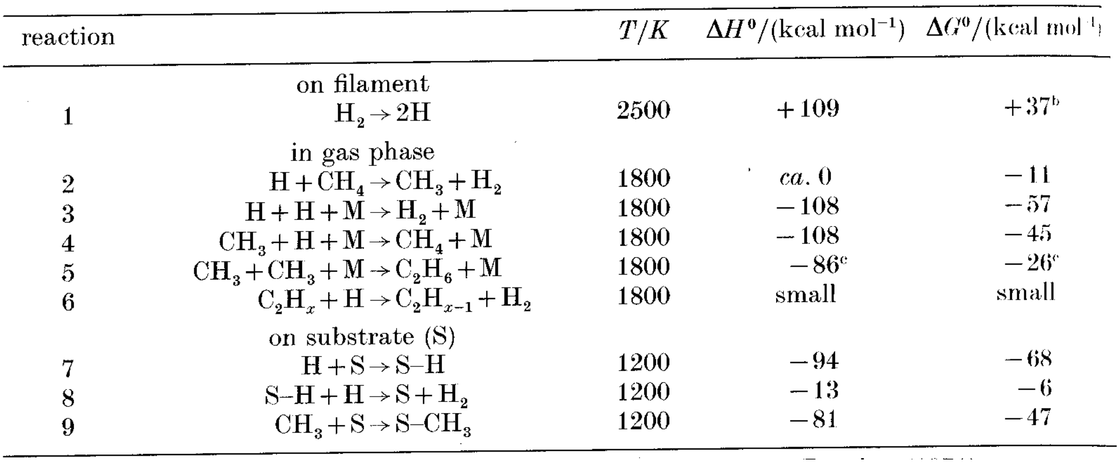

reaction		T/K	$\Delta H^0/(\text{kcal mol}^{-1})$	$\Delta G^0/(\text{kcal mol}^{-1})$ [a]
	on filament			
1	$H_2 \rightarrow 2H$	2500	+109	+37[b]
	in gas phase			
2	$H + CH_4 \rightarrow CH_3 + H_2$	1800	*ca.* 0	−11
3	$H + H + M \rightarrow H_2 + M$	1800	−108	−57
4	$CH_3 + H + M \rightarrow CH_4 + M$	1800	−108	−45
5	$CH_3 + CH_3 + M \rightarrow C_2H_6 + M$	1800	−86[c]	−26[c]
6	$C_2H_x + H \rightarrow C_2H_{x-1} + H_2$	1800	small	small
	on substrate (S)			
7	$H + S \rightarrow S{-}H$	1200	−94	−68
8	$S{-}H + H \rightarrow S + H_2$	1200	−13	−6
9	$CH_3 + S \rightarrow S{-}CH_3$	1200	−81	−47

[a] **Rossini & Jessup** (**1938**); **Stull *et al.*** (**1969**) and **Stull & Prophet** (**1971**).

[b] At 20 Torr and 2500 K, the equilibrium mole fraction of atomic H is 0.16.

[c] Molecular mechanics estimate.

Among the possible diamond growth species (C, CH_3, CH, C_2H, CH_3, C_2H_2, CH^+_3, and diamondoids, such as adamantine), the general consensus is now that the bulk of the evidence supports CH_3 as being the important radical (**Butler & Woodin, 1993**; **Goodwin & Butler, 1997**; **Butler *et al.* 2009**; **Celii *et al.* 1988**; **Ashfold *et al.* 2001**).

It should be emphasized that the picture outlined above is a *very* simplified description of diamond CVD growth. The exact mechanism is dependent upon the gas phase chemistry, the reactor used and even the nature of the diamond crystal surface used (**Goodwin & Butler, 1997**).

1.2. Diamond Nanowires: One-Dimensional (1-D) Nanostructure

One-dimensional structures (1-D) with nanometer diameters, such as nanotubes and nanowires, are new materials, which have characteristics of low weight with sometimes extraordinary mechanical, electrical, thermal and multifunctional properties (**Zheng *et al.* 2005**; **Cui *et al.* 2001**). By creating nanostructures, it is possible to control the fundamental properties of materials without changing their chemical composition. The ability to generate such minuscule structures is essential to much of modern science and technology. It is generally accepted that 1D nanostructures provide a good system to investigate the dependence of electrical and thermal or mechanical properties on dimensionality and size reduction (or quantum confinement).

With the variety of quasi-zero dimensional (0-D) carbon materials available to nanoscience and technology, it comes as no surprise that the attention of many nanotechnologists is focussed around carbon-based nanostructures (**Gogotsi, 2001**; **Shenderova *et al.* 2002**). Nano-size carbon particles such as fullerenes, carbon onions and nanodiamond represent the 0-D analogues of three dimensional sp^2-bonded graphite and sp^3-bonded diamond. At a fundamental level, the study of nanocarbon continues to highlight that at the nanoscale such structures differ from their macroscopic counterparts, possessing unique properties due entirely to their finite size (**Shenderova *et al.* 2002**).

Since the discovery of the quasi-one dimensional sp^2-bonded carbon nanomaterials, so called ‘carbon nanotubes’, there is a speculation that other quasi-one dimensional (1-D) carbon nanostructures may also become important components in nanotechnology. In particular, nanowires are expected to play an integral role in the design and construction of both electronic and optoelectronic nanodevices (**Yang *et al.* 2002**). Significant work has been compiled regarding the growth, structure and properties of carbon nanowires (**Zhang *et al.* 2002**; **Botti *et al.* 2002**; **Liu *et al.* 2002**; **Xia *et al.* 2002**; **Tang *et al.* 1999**).

With the expansion of nanotechnology surrounding CNTs, the next logical step in the study of nanocarbon is the investigation of diamond nanowires (DNWs) and diamond nanorods (DNRs). In addition, diamond-based materials have been proposed as the optimal choice for nano-mechanical designs (**Drexler, 1992**), as they possess unique structural properties such as high elastic modulus and strength-to-weight ratio (**Shenderova *et al.* 2002**), possibly making them ideal for structural applications at the nanoscale. Diamond is also promising choice for the next generation sensor platforms (**Angus *et al.* 2004**; **Swain, 2004**; **Nebel *et al.* 2007**) because of its chemical stability, low background current and wide potential window. Diamond survives in harsh environments in which other materials such as ZnO_2, SnO_2, and Si fail. Diamond is also biocompatible towards large biomolecules, such as DNA (**Yang *et al.* 2002**). The realization of diamond nanowires, its unique properties, and geometrical dimensions, should improve the behavior of some of these devices, and also open a range of new high performance applications such as diamond nanowire single-photon source for photonic and quantum information processing (**Hsu *et al.* 2010**).

Diamond microwires with 25 μm diameter and 400 μm length were synthesized in 1968 using a radiation heating unit developed from a super-high-pressure xenon tube (**Derjaguin *et al.* 1968**). Some top-down approaches employed include reactive ion etching to fabricate diamond nanowires 3-10 nm in length (**Yang *et al.* 2008**) and using porous anodic aluminum oxide as a template to form a diamond nanocylinder array (**Masuda *et al.* 2001**). Post-treatment of carbon species and PECVD techniques have been used to make diamond nanorods of low crystallinity of up to 200 nm in length (**Vlasov *et al.* 2007**; **Shang *et al.* 2009**; **Sun *et al.* 2004**). However, progress in the fabrication of diamond nanowires has been limited, in particular, the fabrication of long, single crystalline diamond nanowires using conventional CVD methods has so far proven elusive, despite the potential benefits. The limited successes in the synthesis of diamond nanowires raise concerns regarding their structural and energetic viability. Are there fundamental problems that prohibit the mass production of stable 1-D sp^3 structures such as diamond nanowires?

A number of theoretical and computational studies have been undertaken, in an attempt to gain some appreciation of the relationship between nanocarbon phases (including phase stability) and to identify factors that may induce structural transformations in 1-D. Ab initio simulations of the structural relaxation of diamond nanowires with octahedral (**Barnard *et al.* 2004a**), dodecahedral (**Barnard et al. 2003a**) and cubic (**Barnard *et al.* 2003a**, **2003b**) surface facets by Barnard *et al.* (**2004b**) found that the energetic and structural stability of diamond nanowires depends on the surface morphology, crystallographic direction of the principle axis and nanowire diameter. In the case of 1D, for example, she showed that nanowires grown along the [100] orientation are stable (figure 1.7). For orientation such as [110] the diamond structure is unstable, the nanowire relaxing by the creation of *sp*^{2} (graphitic) bonding and eventually exfoliation of part of the structure.

A similar investigation by **Malcioğlu & Erkoç** (**2003**) examined these issues using classical methods, while incorporating the effects of temperature. Using a different approach **Shenderova *et al.*** (**2003**), examined the stiffness and fracture force of hydrogenated diamond nano-rods compared with those of single-walled nanotubes and multi-walled nanotubes. It was determined in this study that the mechanical properties of the nano-rods also depend on both the diameter of the nano-rod, and the orientation of the principle axis.

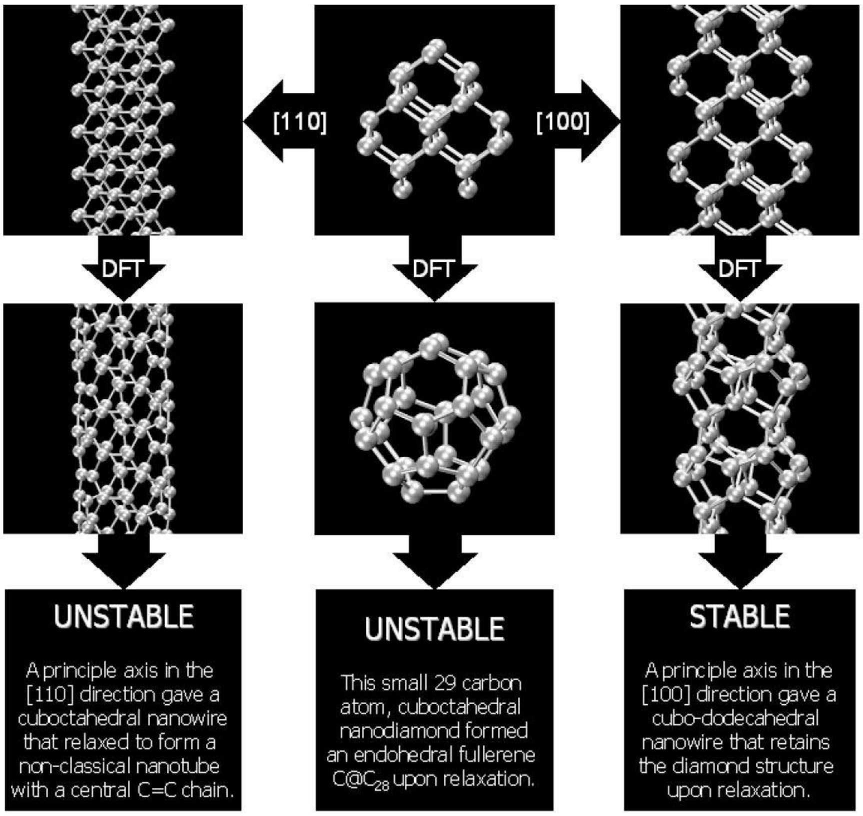

Figure 1.7. The importance of direction of the nanowire principle axis, illustrated by showing the results of relaxing (DFT) two nanowires generated by repeating the same nanodiamond along the [110] (left) and [100] (right) directions. These structures are the C_{96} cuboctahedral nanowire (left) and the C_{63} cylindrical nanowire, as 1-D analogues of the C_{29} nanodiamond (centre) adapted from ***Barnard et al. 2003a, 2003b, 2004b****.*

Although all of these models have begun to establish a framework for the structural stability of DNWs and DNRs as a function of morphology and size, these approaches do not directly address the phase stability of 1-D diamond structures. This question was investigated by **Barnard & Snook** (**2004c**), using a thermodynamic model that had previously been devised to examine the phase stability of 0-D nanocarbon (**Barnard *et al.* 2003c**, **2003d**). Their results indicated that diamond nanowires with C (110) surface facets, and a principle axis in the [100] direction are not only structurally stable, but also almost as energetically favorable as CNTs. The upper limit of DNW stability was also investigated, using estimates for the heat of formation of graphite made with experimental values for the bond energies (**Barnard *et al.* 2004c, 2003c, 2003d**). These results indicated a 'window' of stability for DNWs, between approximately 450 to 870-930 atoms/nm (2.7 nm to 3.7-3.9 nm in diameter). It is important to note that the upper limit of this range (where graphite becomes energetically preferred) is sensitive to the chiral scaling direction, just as the lower limit of the reported range (where SWNTs become energetically preferred) was sensitive to the DNW morphology (**Barnard *et al.* 2004c**).

An empirical thermodynamic model argued that it is possible for a diamond nanowire to grow inside a tubular graphitic enclosure (or carbon nanotube) (**Wang & Yang, 2005**). A key aspect of this argument, independent of the specifics of the model, is that for a small diameter wire a capillary pressure (or so-called Young-Laplace pressure) $\Delta P \approx 2\gamma/r$ (where r is the radius and γ is the surface energy of diamond) can be sufficiently high to allow the diamond phase to exist in the inner core while the outer shell with less equivalent pressure takes on the graphitic phase. Depending on the specific surface and interface energy parameters, within a thick nanotube-like shell of an interior radius around 10-25 nm, or for even smaller dimensions occurring at a defective spot of the nanotube wall, the equivalent pressure could reach the order of 1-5 GPa (**Wang *et al.* 2005**). Similar phenomena were observed experimentally in diamond nucleation inside carbon onion high curvature enclosures (**Banhart & Ajayan, 1996**).

There is only one report for the successful growth of diamond nanowires by CVD. Indeed, Sun et al. reported in 2005 (**Sun *et al.* 2005**) that chain-like diamond nanowires with diameters of 4-8 nm and lengths up to 200 nm were fabricated by hydrogen plasma post-treatment of multiwalled carbon nanotubes (MWCNTs) dispersed on silicon substrate. After 10 hours of annealing, diamond clusters appeared on the surface of nanotubes, with a size of about 10-20 nm. X-ray diffraction and high-resolution transmission electron microscopy (HRTEM) confirm the diamond structure of these clusters. After 20 hours of annealing, nanowires grew from the diamond clusters (figure 1.8 (a)). HRTEM confirms the diamond structure of the core (figure 1.8 (b)), and energy dispersive X-ray analysis indicates that there is no trace of metallic catalyst used for the growth of the nanotubes. The core crystalline wire is sheathed by a 2-4 nm thick amorphous carbon film, with atomically sharp interface.

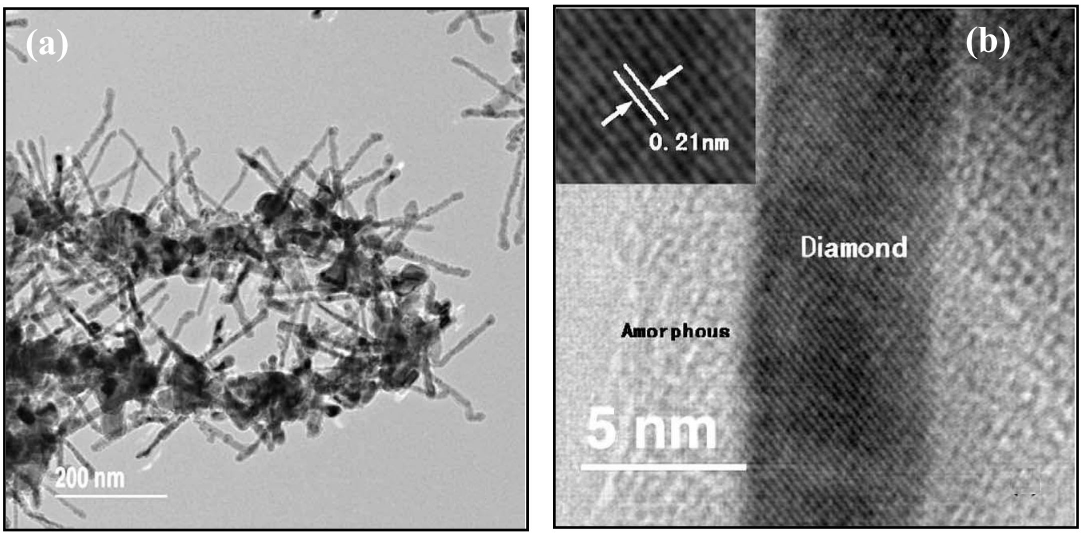

Figure 1.8. (a) TEM image of the single-crystal diamond nanowires (DNWs) from the MWCNTs after treatment in hydrogen plasma at temperature of 1000 K for 20 h; (b) High resolution TEM image shows the structure of single-crystal DNWs with crystalline core and amorphous carbon sheath. The inset is the simulated image of the nanocrystals after image filter processing by Fourier transform. The figure is adapted from ***Sun et al. 2005****.*

This experimental growth of diamond nanowires from MWCNTs (**Sun *et al.* 2005**) was later supported by Muniz et al. (**Muniz *et al.* 2009**) using first-principles density-functional theory calculations and molecular-dynamics simulation. In this theoretical framework it is shown that the structures generated as a result of the intershell C-C bonding of adjacent, concentric graphene walls of MWCNTs can provide seeds for the nucleation of cubic- and hexagonal-diamond nanocrystals and that the chirality and relative alignment of the adjacent MWCNT graphene walls determine the lattice structure of the resulting crystalline phase (figure 1.9). In addition, the formation of diamond nanocrystals is possible over the broadest range of nanotube diameters and through any arrangement of adjacent graphene walls, i.e., for all possible combinations of zigzag, armchair, or chiral graphene wall configurations to within a certain range of the difference in the chiral angles between adjacent graphene walls in the MWCNT.

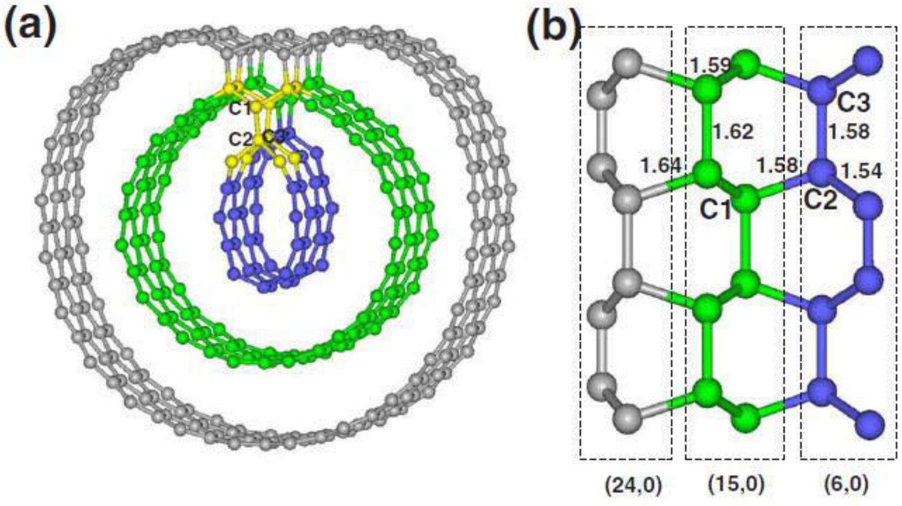

Figure 1.9. Structure resulting from intershell C-C bonding in a MWCNT according to first-principles DFT calculations. Optimized atomic configuration of MWCNT with (6, 0), (15, 0), and (24, 0) concentric inner (colored in blue), middle (colored in green), and outer (colored in gray) nanotubes, respectively, depicting intershell C-C bonding. (a) Top view along the axial direction. (b) Cross-sectional view on the symmetry plane. Blue, green, and yellow spheres denote C atoms. The yellow-colored C atoms highlight the seed unit for the nucleation of a bulk phase of hexagonal diamond (lonsdaleite). The figure is adapted from ***Muniz et al. 2009****.*

Very recently synthesis of diamond nanowires using Atmospheric-Pressure Chemical Vapor Deposition (APCVD) method has been reported by **Hsu *et al.*** (**2010**). In this work, the growth process began with methane and hydrogen flow over an iron catalyst solution dispersed on a silicon substrate (prepared by sol-gel technique) under conventional chemical vapor deposition conditions at 900 °C. Unlike the diamond film growth processes that have been documented, no plasma or energy radiation is used during the CVD growth. After this process was completed, and without pumping the residual methane from the chamber, pure hydrogen was flowed through the quartz tube chamber at the rate of 200 sccm while the temperature was slowly lowered to ambient at the rate of 1.2 °C/min over a period of 12 h.

Diamond nanowires grown in this experiment were straight, thin and long, and uniform in diameter (60-90 nm) over tens of micrometers. Spectroscopic analysis, electron diffraction, and transmission electron microscopy provided confirmation that these nanowires were diamond with high crystallinity and high structural uniformity (figure 1.10). They further revealed that these diamond nanowires are encased within MWCNTs. Although the order of magnitude estimate corresponds well to the experimental findings of the wire diameter and the crystal domain size, the growth direction [110] is found to be inconsistent with theoretical predictions. Also, diamond nanowires were achieved with a relatively low yield (~10%) and so far offer no direct control for the diameter and length.

So, as much as the results reported here (**Hsu *et al.* 2010**) appear to provide a basis for optimism, they themselves are far from optimal.

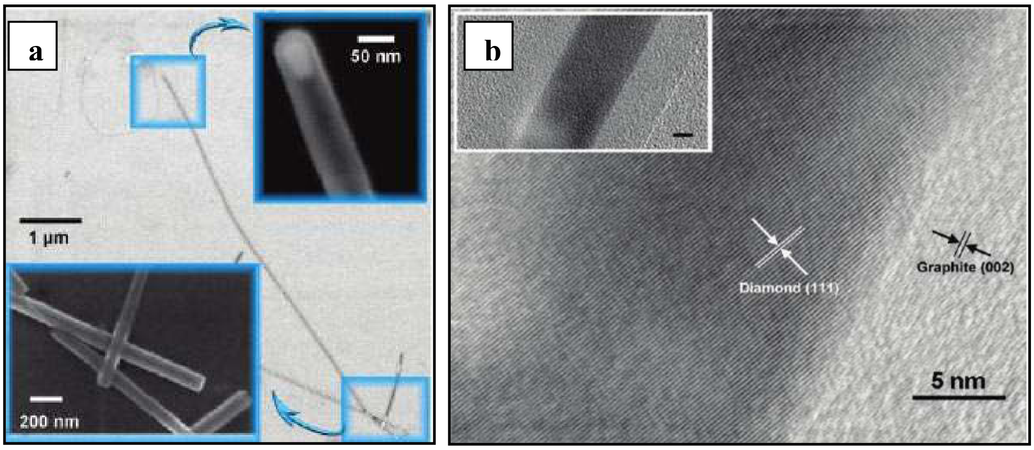

Figure 1.10. Electron microscopy of diamond nanowires encased within a carbon nanotube shell. (a) Diamond core enclosed in a CNT sheath. A magnified SEM image of the nanowire tip in the upper inset shows a catalyst embedded inside the tip of the nanowire. The SEM image in the lower inset shows the straight and uniform nanowires with flat terminations. (B) The transmission electron microscopy (TEM) image shows the diamond core and CNT walls of the nanowire. The diamond (111) lattice (0.21 nm) is enclosed by the outer CNT shell with a graphite (002) surface (0.34 nm) whose surface stress provides a very high effective pressure (on the order of gigapascals) in which the diamond phase is stable. The low-magnification TEM image in the inset shows the core-in-shell wire structure more clearly. The scale bar in the inset is 5 nm. The figure is adapted from ***Hsu et al. 2010****.*

Although the successful synthesis has been limited, and subsequent production of DNWs and DNRs has not yet been realized, the current researches do suggest that a future exists for these nanostructures. The work of experimentalists have shown that a number of possible synthesis routes exist (**Hsu *et al.* 2010**; **Masuda *et al.* 2001**; **Sun *et al.* 2005**; **Baik *et al.* 2000a**, **2000b**; **Ando *et al.* 2004**), depending upon the type of structures required, and that the shape and orientation of these diamond nanomaterials maybe controlled (**Baik *et al.* 2000b**; **Ando *et al.* 2004**).

Still, a great deal of work has yet to be done, in particular, in developing a controlled and reproducible high-yield fabrication process and a good understanding of the growth mechanism. Carbon nanotubes have so far been identified as an effective catalyst /and support to grow diamond nanowires by chemical vapour deposition but the growth mechanism is still not clear, rather contradictory to some extent, to the theoretical predictions. In addition, the recent success in diamond nanowire synthesis (**Hsu *et al.* 2010**) has suggested that using transition metals as catalysts can facilitate the one dimensional growth. This has prompted us to reconsider the vapour-liquid-solid (VLS) growth mechanism of Si nanowires for diamond nanowire growth. Although it was not fully understood, the VLS mechanism was first observed in 1968 (**Derjaguin *et al.* 1968**) in the growth of filamentary diamond crystals on a seed diamond single crystal (substrate) using drops of transition metals (Ni, Fe and Mn). Because of their unique carbon affinity, transition metals (Fe, Ni, Co and Pd) are widely used as catalysts for carbon nanotube growth. They are also known to facilitate the dissociation of hydrogen molecules into atomic hydrogen at significant low hydrogen dissociation barrier (**Gross, 1998**; **Berger *et al.* 1992**). Such atomic hydrogen was demonstrated to locally decompose amorphous and graphitic deposits more quickly than diamond (**Spear, 1989**; **Angus *et al.* 1968**) allowing methane feedstock to grow diamond preferentially (**Chauhan *et al.* 1976**) and thus has been widely applied in the synthetic diamond growth processes. Thus, it can be expected that transition metals might be effective catalysts for diamond nanowire growth. However, concerning the critical aspect of diamond nanowire stability, and the lack of experimental knowledge about its formation mechanism, it is therefore outmost importance to gain further insight into some of the essential questions that arise very often in the case of CNT growth by CVD: what determines whether or not a metal can catalyze the nucleation and growth of CNTs, and in particular, why do Ni, Co, and Fe display the highest catalytic activity; what is the interaction between the catalyst and the released atoms of carbon; and what thermodynamic properties of the carbon source influence the reaction?

Bibliography

Ando, Y., Nishibayashi, Y. & Sawabe, A. **2004** *Diamond Relat. Mater.* 13, 633.

Angus, J. C., Pleskov, Y. V. & Eaton, S. C. **2004** *Semiconduct. Semimet.* 77, 97.

Angus, J. C., Argoitia, A., Gat, R., Li, G., Sunkara, M., Wang, L. & Wang, Y. **1993** *Phil. Trans. R. Soc. Lond. A* 342, 195-208.

Angus, J.C., Poferl, D.J., Gardner, N.C., Chauhan, S., Dyble, T.J. & Sung, P. **1971** *Sint. Almazy.* 3, 30.

Angus, J.C., Will, H.A. & Stanko, W.S. **1968** *J. Appl. Phys*. 39*,* 2915.

Ashfold, M.N.R., May, P.W., Petherbridge, J.R., Rosser, K.N., Smith, J.A., Mankelevich, Y.A., & Suetin, N.V. **2001** *Phys. Chem. Chem. Phys.* 3, 3471.

Ashfold, M.N.R., May, P.W., Rego, C. A. & Everitt, N. M. **1994** *Chem. Soc. Rev*. 23, 21.

Bachmann, P. K., Leers, D. & Lydtin, H. **1991** *Diamond Relat. Mater*. 1, 1.

Bade, J. P., Sahaida, S. R., Stoner, B. R., von Windheim, J. A., Glass, J. T., Miyata, K., Nishimura, K. & Kobashi, K. **1993** *Diamond Relat. Mater.* 2, 816.

Baik, E. –S., Baik, Y. –J. & Jeon, D. **2000a** *J. Mater. Res.* 15, 923.

Baik, E. –S., Baik, Y. –J., Lee, S. W. & Jeon, D. **2000b** *Thin solid Films* 377**,** 295.

Baldwin, J. W., Zalalutdinov, M. K., Feygelson, T., Pate, B. B., Butler, J. E. & Houston, B. H. **2006** *Diamond Relat. Mater.* 15, 2061.

Balmer, R. S. *et al* **2009** *J. Phys.: Condens. Matter.* 21, 364221.

Barnard, A.S., Russo, S.P. & Snook, I.K. **2004a** *J. Nanosci. Nanotechnol.* 4 142.

Barnard, A.S., Russo, S.P. & Snook, I.K. **2004b** *Phil Mag,* 84, 899.

Barnard, A.S. & Snook, I.K. **2004c** *J. Chem. Phys.* 120, 3817.

Barnard, A.S., Russo, S.P. & Snook, I.K. **2003a** *Nano Lett.* 3, 1323.

Barnard, A.S., Russo, S.P. & Snook, I.K. **2003b** *Surf. Sci.* 538, 204.

Barnard, A.S., Russo, S.P. & Snook, I.K. **2003c** *J. Chem. Phys.* 118**,** 5094.

Barnard, A.S., Russo, S.P. & Snook, I.K. **2003d** *Phys. Rev. B* 68, 73406.

Barnard, A.S., Russo, S.P. & Snook, I.K. **2003e** *Phys. Rev. B* 68, 235407.

Barnard, A. S. **2000** *The diamond formula, diamond synthesis: a gemmological perspective*. Butterworth-Heinemann, Oxford.

Banhart, F. & Ajayan, P. M. **1996** *Nature* 382, 433.

Berger, H. F., Grosslinger, E. & Rendulic, K. D. **1992** *Surf. Sci.* 261, 313.

Bergonzo, P., Tromson, D. & Mer, C. **2006** *J. Synchrotron Radiat.* 13, 151.

Berman, R. & Simon, F. **1955** *Z. Elektrochem.* 59, 333.

Bogdan, G., De Corte, K., Deferme, W., Haenen, K. & Nesladek, M. **2006** *Phys. Status Solidi* A. 203, 3063.

Botti, S., Ciardi, R., Terranova, M. L., Piccirillo, S., Sessa, V. & Rossi, M. **2002** *Chem.Phys. Lett.* 355**,** 395.

Bouamrane, F., Adjeddine, A., Butler, J. E., Tenne, R. & Levy-Clement, C. J. **1996** *Electroanal. Chem.* 405, 95.

Brandon, J. R., Coe, S. E., Sussmann, R. S., Sakamoto, K., Spoerl, R., Heidinger, R. & Hanks, S. **2001** *Fusion Eng. Des.* 53, 553.

Bundy, F.H. **1980** *J. Geophys. Res.* 85**,** 6930.

Bundy, F. P., Hall, H. T., Strong, H. M. & Wentorf Jr, R. H. **1955** *Nature* 176**,** 51.

Butler, J.E., Mankelevich, Y.A., Cheesman, A., Ma, J. & Ashfold, M.N.R. **2009** *J. Phys.: Condens. Matter* 21, 364201.

Butler, J. E. & Sumant, A. V. **2008** *Chem. Vapor Depos.* 14, 145.

Butler, J.E. & Woodin, R.L. **1993** *Phil. Trans. R. Soc. Lond. A* 342, 209.

Calvani, P., Corsaro, A., Sinisi, F., Rossi, M. C., Conte, G., Giovine, E., Ciccognani, W. & Limiti, E. **2009** *Microw. Opt. Technol. Lett.* 51, 2786.

Celii, F.G., Pehrsson, P.E., Wang, H.T.& Butler, J.E. **1988** *Appl. Phys. Lett.* 52, 2043.

Chauhan, S.P., Angus, J.C. & Gardner, N.C. **1976** *J. Appl. Phys*. 47, 4746.

Chauhan, S.P., Angus, J.C. & Gardner, N.C. **1974** *J. Vac. Sci. Tech*. 11, 423.

Chiang, C.-P., Flamm, D.L., Ibbotson, D.E. & Mucha, J.A. **1988** *J. Appl. Phys.* 63, 1744.

Collins, A. T. **1992** *Diam. Relat. Mater.* 1, 457.

Collins, A. T. & Lightowlers, E. C. **1979** In *The properties of diamond* (ed. J.E. Field), p. 79. London: Academic.

Cui, Y., Wei, Q.W., Park, H. & Lieber, C.M. **2001** *Science* 293**,** 1289.

Cullity, B. D. **1956** *Elements of X-Ray diffraction.* Addison-Wesley.

Das, D. & Singh, R. N. **2007** *Int. Mater. Rev.* 52, 1.

Davis, F. R. **1994** *Diamond films and coatings: development, properties, and applications*. Noyes.

Derjaguin, B. V. & Fedoseev, D. V. **1975** *Sci. Am.* 233, 102.

Derjaguin, B.V. & Fedoseev, D.V. **1970** *Russ. Chem Rev*. 39, 783.

Derjaguin, B.V., Fedoseev, D.V., Lukyanovich, V.M., Spitsyn, B.V., Ryabov, V.A. & Lavrentiev, A.V. **1968** *J. Cryst. Growth.* 2, 380.

Dischler, B & Wild, C. **1998** *Low-pressure synthetic diamond*. Springer.

Dolling, G. & Cowley, R. A. **1966** *Proc. Phys. Soc. Lond.* 88, 463.

Dore, P., Nucara, A., Cannavò, D., De Marzi, G., Calvani, P., Marcelli, A., Sussmann, R. S. *et al.* **1998** *Appl. Opt.* 37, 5731.

Drexler, K.E. **1992** *Nanosystems: molecular, machinery, manufacturing and computation.* Wiley.

Drory, M. D. & Hutchinson, J. W. **1994** *Science* 263, 1753.

Eversole, W. G. **1962** U.S. Patent Nos. 3,030,187 and 3,030,188.

Fedoseev, D.V., Derjaguin, B.V., Varnin, V.P. & Sokolina, G.K. **1979** *Doklady Akad. Nauk SSSR.* 247, 1201.

Fedoseev, D.V., Uspenskaya, K.S., Varnin, V.P. & Vnukov, S.P. **1978** *Izv. Akad. Nauk SSSR, Seriya Khimicheskaya.* 6, 1252.

Ferreira, N. G., Corat, E. J., Trava-Airoldi, V. J. & Leite, N. F. **1998** *Diamond Relat. Mater.* 7**,** 272.

Field, J. E. (ed.) **1992** *The properties of natural and synthetic diamond*. Academic.

Fujimori, N. **1998** In *Handbook of Industrial Diamond and Diamond Films (*ed. M. A. Prelas, G. Popopvici & L. K. Bigelow), pp. 1129. New York: Marcel Dekker.

Gardinier, C. F. **1988** *Ceramic Bulletin.* 67, 1006.

Gicquel, A., Hassouni, K., Silva, F. & Achard, J. **2001** *Curr. Appl. Phys.* 1, 479.

Gogotsi, Y. **2001** *Cryst. Growth Design* 1, 179.

Goodwin, D. G. & Butler, J. E. **1997** In *Handbook of industrial diamonds and diamond films* (ed. M. A. Prelas, G. Popovici & L. K. Bigelow), ch. 11. New York: Marcel Dekker.

Gracio, J. J., Fan, Q. H. & Madaleno, J. C. **2010** *J. Phys. D: Appl. Phys.* 43, 374017.

Gray, K. J. & Windischmann, H. **1999** *Diamond Relat. Mater.* 8, 903.

Gross, A. **1998** *Appl. Phys. A: Mater. Sci. Process.* 67, 627.

Gruen, D. M. **1999** *Annu. Rev. Mater. Sci.* 29, 211.

Gruen, D. M & Buckely-Golder, I. (eds.) **1998** *MRS Bull.* 23**,** 61-64.

Gruen, D. M., Pan, X. Z., Krauss, A. R., Liu, S. Z., Luo, J. S. & Foster, C. M. **1994** *J. Vac. Sci. Technol. A* 12, 1491.

Gurbuz, Y., Kang, W. P., Davidson, J. L., Kerns, D. V. Jr. & Zhou, Q. **2005** *IEEE Trans. Power Electron.* 20, 1.

Guy, A. G. **1959** *Elements of physical metallurgy.* Addison-Wesley.

Hall, H. T. **1961** *J. Chem. Educ.* 38, 484.

Hannay, J. B. **1880** *Nature* 22, 255.

Haubner, R., Lindlbauer, A. & Lux, B. **1993** *Diamond Relat. Mater.* 73, 137.

Himpsel, F. J., Knapp, J. A., VanVechten, J. A. & Eastman, D. E. **1979** *Phys. Rev.* B 20**,** 624.

Hiraki, A. **2001** *Mater. Chem. Phys.* 72, 196.

Hirose, Y., Ananuma, S., Okada, N. & Komaki, K. **1989** In *Diamond and Diamond-like Films:* 1st Int. Symp. (ed. J. Dismukes), pp. 80. NJ: The Electrochemical Society.

Hiscocks, M. P., Kaalund, C. J., Ladouceur, F., Huntington, S. T., Gibson, B. C., Trpkovski, S., Simpson, D. *et al.* **2008** *Diamond Relat. Mater.* 17**,** 1831.

Hsu, C. –H., Cloutier, S. G., Palefsky, S. & Xu, J. **2010** *Nano Lett.* 10**,** 3272.

Kaiser, W. & Bond, W.L. **1959** *Phys. Rev*. 115, 857.

Kamo, M., Sato, Y., Matsumoto, S. & Setaka, N. **1983** *J. Cryst. Growth* 62, 642.

Kang, W. P., Davidson, J. L., Wisitsora-at, A., Wong, Y. M., Takalkar, R., Holmes, K. & Kerns, D. V. **2004** *DiamondRelated. Mater.* 13**,** 1944.

Karner, J., Pedrazzinni, M., Reineck, I., Sjöstrand, M. E. & Bergmann, E. **1996** *Mater. Sci. Eng.* A 209, 405.

Kitahama, K., Hirata, K., Nakamatsu, H., Kawai, S., Fujumori, N., Imai, T., Yoshino, H. & Doi, A. **1986** *Appl. Phys. Lett.* 49**,** 634.

Klein, C. A. **1993** *Diamond Relat. Mater.* 2, 1024.

Koizumi, S., Kamo, M., Sato, Y., Ozaki, H. & Inuzuka, Y. **1997** *Appl. Phys. Lett.* 71, 1065.

Kulda, J., Dorner, B., Roessli, B., Strener, H., Bauer, R., May, T., Karch, K., Pavone, P. & Strauch, D. **1996** *Solid State Commun.* 99, 799.

Kurihara, K., Dasaki, K., Kawarada, M. & Koshino, N. **1988** *Appl. Phys. Lett.* 52, 437.

Lagrange, J. P., Deneuville, A. & Gheeraert, E. **1998** *Diam. Relat. Mater.* 7, 1390.

Leipunski, O. I. **1939** *Usp. Khim.* 8, 1519.

Liu, R.-M., Ting, J.-M., Huang, J.-C. A. & Liu, C.-P. **2002** *Thin Solid Films*, 420-421**,** 145.

Loh, K. P., Foord, J. S. & Jackman, R. B. **1997** *Diamond Relat. Mater.* 6**,** 219.

Malcioğlu, O. B. & Erkoç, Ş. **2003** *Int. J. Mod. Phys. C* 14, 441.

Mallika, K. & Komanduri, R. **1999** *Wear* 224, 245.

Martin, H. B., Argoitia, A., Angus, J. C., Anderson, A. B. & Uziel, L. **1995** In *Applications of Diamond Films and Related Materials: 3rd Int. Conf. (*ed. A. Feldmann, Y. Tzeng, W. A. Yarbrough, M. Yoshikawa & M. Murakawa), p. 91. Washington, DC: NIST.

Masuda, H., Yanagishita, T., Yasui, K., Nishio, K., Yagi, I., Rao, T. N. & Fujishima, A. **2001** *Adv. Mater.* 13, 247.

Matsui, Y., Matsumoto, S. & Setaka, N. **1983** *J. Mater. Sci. Lett*. 2, 532.

Matsumoto, S. **1985** *J. Mater. Sci. Lett.* 4, 600.

Matsumoto, S., Hino, M. & Kobayashi, T. **1987** *Appl. Phys. Lett.* 51, 737.

Matsumoto, S., Sato, Y., Kamo, M. & Setaka, N. **1982a** *Jpn. J. Appl. Phys.* 21, L183.

Matsumoto, S., Sato, Y., Tsutsumi, M. & Setaka, N. **1982b** *J. Mater. Sci***.** 17, 3106.

Mildren, R. P., Butler, J. E. & Rabeau, J. R. **2008** *Opt. Express* 16**,** 18950.

Miller, A. J., Reece, D. M., Hudson, M. D., Brierley, C. J. & Savage, J. A. **1997** *Diamond Relat. Mater.* 6, 386.

Muniz, A. R., Singh, T., Aydil, E. S. & Maroudas, D. **2009** *Phys. Rev. B* 80, 144105.

Muranaka, Y., Yamashita, H. & Miyadera, H. **1994** *Diamond relat. Mater.* 3, 313.

Nebel, C.E., Rezek, B., Shin, D., Uetsuka, H. & Yang, N. **2007** *J. Phys. D* 40**,** 6443.

Nebel, C. E. & Ristein, J. **1992** *Thin-Film Diamond II*. Elsevier.

Neto, V. F., Vaz, R., Oliveira, M. S. A. & Grácio, J. **2009** *J. Mater. Process. Technol.* 209, 1085.

Okushi, H. **2001** *Diam. Relat. Mater.* 10, 281.

Ong, T. P. & Chang, R. P. H. **1989** *Appl. Phys. Lett.* 55, 2063.

Pace, E., Pini, A., Corti, G., Bogani, F., Vinattieri, A., Pickles, C. S. J.& Sussmann, R. **2001** *Diamond Relat. Mater.* 10, 736.

Pang, L. Y. S., Chan, S. S. M., Johnston, C., Chalker, P. R. & Jackman, R. B. **1997** *Diamond Relat. Mater.* 6, 333.

Parsons, C. A. **1918** *J. Inst. Metals*, 20, 5.

Pernot, J., Volpe, P.N., Omnes, F. & Muret, P. **2010** *Phys. Rev. B* 81, 205203.

Pernot, J. & Koizumi, S. **2008** *Appl. Phys. Lett.* 93, 052105.

Poferl, D.J., Gardner, N.C. & Angus, J.C. **1973** *J. Appl. Phys*. 44, 1428.

Ramesham, R. & Roppel, T. **1992** *J. Mater. Res.* 7, 1144.

Rego, C. A., Tsang, R. S., May, P. W., Henderson, C. R., Ashfold, M. N. R. & Rosser, K. N. **1996** *J. Appl. Phys.*79**,** 7264.

Reineck, I., Sjöstrand, M. E., Karner, J. & Pedrazzinni, M. **1996** *Refract. Metals Hard Mater.* 14, 187.

Rossini, F. D. & Jessup, R. S. **1938** *J. Res. NBS* 21, 491.

Rotter, S. Z. *et al* **2008** *US Patent* 7432132.

Sakamoto, Y. & Takaya, M. **2002** *J. Mater. Process. Technol.* 127**,** 151.

Sawabe, A. & Inuzuka, T. **1986** *Thin Solid Films* 137, 89.

Sawabe, A. & Inuzuka, T. **1985** *Appl. Phys. Lett.* 46, 146.

Seelmann-Eggebert, M., Meisen, P., Schaudel, F., Koidl, P., Vescan, A. & Leier, H. **2001** *Diamond Relat. Mater.* 10, 744.

Shang, N., Papakonstantinou, P., Wang, P., Zakharov, A., Palnitkar, U., Lin, I. N., Chu, M. & Stamboulis, A. **2009** *ACS Nano* 3, 1032.

Shenderova, O. A., Brenner, D. W. & Ruoff, R. S. **2003** *Nano Lett.* 3, 805.

Shenderova, O. A., Zhirnov, V. V. & Brenner, D. W. **2002** *Crit. Rev. Sol. State and mater. Sci.* 27 (3-4), 227.

Shikata, S-I. **1998** In *Low pressure synthetic diamond: manufacturing and applications (*ed B. Dischler & C. Wild), pp. 261. Berlin: Springer.

Silva, F., Gicquel, A., Chiron, A. & Achard, J. **2000** *Diamond Relat. Mater.* 9, 1965.

Spear, K. E. & Dismukes, J. P. **1994** *Synthetic diamond, emerging CVD science and technology.* Wiley.

Spear, K. E. **1989** *J. Am. Ceram. Soc.* 72, 171.

Spitsyn, B.V., Bouilov, L.L. & Deryagin, B.V. **1981** *J. Cryst. Growth.* 52, 219.

Stoner, B. R., Ma, G., Wolter, S. D. & Glass, J. T. **1992** *Phys. Rev. B* 45, 11067.

Stull, D. R. & Prophet, H. **1971** In *JANAF thermochemical tables:* 2nd edn. Washington, DC: National Bureau of Standards.

Stull, D. R., Westrum, E. F. & Sinke, G. C. **1969** *The chemical thermodynamics of organic compounds.* Wiley.

Sun, L.T., Gong, J.L., Zhu, Z.Y., Zhu, D.Z., Wang, Z.X., Zhang, W., Hu, J.G. & Li, Q.T. **2005** *Diamond Relat. Mater.* 14**,** 749.

Sun, L. T., Gong, J. L., Zhu, D. Z., Zhu, Z. Y. & He, S. X. **2004** *Adv. Mater.* 16, 1849.

Suzuki, K., Yasuda, J. & Inuzuka, T. **1987** *Appl. Phys. Lett.* 50, 728.

Swain, G. M. **2004** *Semiconduct. Semimet.* 77, 121.

Swain, G. M., Anderson, A. B. & Angus, J. C. **1998** *MRS Bull.* 23, 56.

Takahashi, K., Illy, S., Heidinger, R., Kasugai, A., Minami, R., Sakamoto, K., Thumm, M. & Imai, T. **2005** *Fusion Eng. Des.* 74, 305.

Tang, Y. H., Wang, N., Zhang, Y. F., Lee, C. S., Bello, I. & Lee, S. T. **1999** *Appl. Phys. Lett.*, 75**,** 2921.

Tennant, S. **1797** *Phil. Trans. R. Soc. Lond A.* 87, 123.

Thumm, M. **2001** *Diamond Relat. Mater.* 10, 1692.

Varnin, V.P., Deryagin, B.V., Fedoseev, D.V., Teremetskaya, I.G. & Khodan, A.N. **1977** *Kristallografiya.* 22, 893–896.

Vlasov, I. L., Lebedev, O. I., Ralchenko, V. G., Goovaerts, E., Bertoni, G., Van Tendeloo, G. & Konov, V. I. **2007** *Adv. Mater.* 19, 4058.

Volpe, P. N., Muret, P., Pernot, J., Omnes, F., Teraji, T., Koide, Y., Jomard, F. *et al.* **2010** *Appl. Phys. Lett.* 97, 223501.

von Bolton, W. **1911** *Elektrochem.* 17, 971.

Walker, J. **1979** *Rep. Prog. Phys.* 42, 1065.

Wang, C. X. & Yang, G. W. 2005 *Mater. Sci. Eng. R* 49, 157.

Wang, C. X., Chen, J., Yang, G. W. & Xu, N. S. **2005** *Angew. Chem., Int. Ed.* 44, 7414.

Wang, W. Y., Moses, T., Linares, R. C., Shigley, J. E., Hall, M. & Butler, J. E. **2003** *Gems Gemol.* 39, 268.

Washiyama, S., Mita, S., Suzuki, K. & Sawabe, A. **2011** *Appl. Phys. Express* 4, 095502.

Windischmann, H. & Epps, G. F. **1990** *J. Appl. Phys.* 68, 5665.

Woods, G. S. **1994** In *Properties and growth of diamond* (ed. G. Davies), p. 88-97. London: INSPEC.

Woods, G. S. **1986** *Proc. Phys. Soc. London* A 470, 219.

Xia, A., Huizhao, Z., Li, Y. & Chengshan, X. **2002** *Appl. Surf. Sci.* 193**,** 87.

Yan, C. S., Vohra, Y. K., Mao, H. K. & Hemley, R. J. **2002** *Proc. Natl Acad. Sci.* 99, 12523.

Yang, N. J., Uetsuka, H. S., Osawa, E. & Nebel, C. E. **2008** *Nano Lett.* 8, 3572.

Yang, P., Wu, Y. & Fan, R. **2002** *Int. J. Nanosci.* 1**,** 1.

Yang, W., Auciello, O., Butler, J. E., Cai, W. *et al.* **2002** Nat. Mater. 1, 253.

Ying, X., Luo, J., Wang, P., Cui, M., Zhao, Y., Li, G. & Zho, P. **2003** *Diamond Relat. Mater.* 12**,** 719.

Zhang, R. Q., Lee, S. T., law, C.-K., Li, W.-K. & Teo, B. K. **2002** *Chem. Phys. Lett.* 364**,** 251.

Zheng, G., Patolsky, F., Cui., Y., Wang, W.U. & Lieber, C.M. **2005** *Nat. biotechnol.* 23**,** 1294.

CHAPTER 2

Carbon-Metal Interaction: Basis of Catalytic Etching

Résumé

Les métaux de transition sont largement utilisés dans la synthèse de matériaux carbonés et en fonction de l'ampleur de l'interaction métal-carbone, les différentes formes de carbone tels que les nanotubes de carbone, nanofils et de nanostructures diamant peuvent être élaborés. L'activité catalytique des métaux de transition se reflète dans leur interaction avec le carbone et dépend de la température, de la taille des particules et de l'état chimique de source de carbone. Dans cette thèse, les deux études sur la croissance des nanofils et sur la gravure de nanostructures utilisent des catalyseurs métalliques tels que Ni, Pd, Co, ..., dont le fondements de l'interaction métal-carbone est discuté dans le chapitre 2. Une attention particulière est consacrée à l'effet de la taille nanométrique du catalyseur, et les résultats publiés récemment sur la gravure catalytique de diamant sont également présentés.

Un métal de transition a tendance à réagir avec le carbone en faisant se chevaucher ses orbitales *d* avec les orbitales *p*. Par conséquent, la réactivité d'un métal de transition avec le carbone est principalement déterminé par son état électronique, en particulier, le nombre d'électrons des orbitales *d*. Ainsi, Cu, avec tous les orbitales *d*, montre peu d'interaction avec le carbone; Fe, avec quatre postes vacants dans orbitales *d*, présente une interaction modérée, et Ti, avec huit postes vacants dans orbitales *d*, manifeste une forte interaction. La réactivité croissante entre le métal et le carbone se reflète également dans l'augmentation de la solubilité du carbone dans le métal, ce qui tend à culminer à métaux du groupe du Fe et ensuite diminuer. L'inverse de la solubilité avec augmentation du nombre de postes vacants *d*-est due à la sur-réaction entre le métal et le carbone. Quand la réactivité dépasse une valeur de seuil, les atomes de carbone commencent à perdre de leur mobilité dans la solution solide formant des carbures métalliques. Ainsi, des éléments tels que Cu, Zn, avec tous les orbitales *d* (pas de *d*-postes vacants), sont relativement inertes au carbone et montrent un degré minimal d'interaction, tandis que des éléments tels que Ti, V, ou Sc, avec beaucoup *d*-postes vacants (sept à neuf), montrent une très forte interaction avec le carbone formant des carbures stables. Mais des éléments tels que Ni, Co ou Fe, avec quelques *d*-postes vacants (deux à quatre), présentent une interaction modérée et une solubilité importante qui donne dans l'excès mène à la formation de carbures métastables. Les solubilités «effectives» de carbone dans les métaux de transition sont les plus élevés lorsque les métaux de transition possèdent environ la même quantité d'électrons de valence et les postes vacants dans leurs orbitales *d*. Toutefois, exception notable est Pd qui montre étonnamment élevé "solubilité effective» de carbone,

malgré l'absence de vacance de ses orbitales *d*. Il est également le seul métal de transition sans *s*-électron. Par conséquent, Pd doit se comporter comme Cu ou Ag avec une solubilité minimale de carbone. Toutefois, cette prédiction est basée sur l'état électronique de Pd métal pur. Quand il y a des atomes de carbone autour, un électron dans l'orbitale *d* de Pd peut entrer dans le vide *s*-orbitaire et en laissant une orbitale *d* vacants. En conséquence, Pd a deux orbitales non satisfaites, à savoir, *s* et *d*, de sorte qu'il peut interagir avec le carbone et la dissolution de ce dernier. L'affinité des atomes de carbone pour les catalyseurs métalliques se traduit également par l'enthalpie de formation des carbures métalliques, les enthalpies croissantes de formation de la liaison carbone-métal, et le point de fusion augmentant de carbures métalliques, le nombre de postes à pourvoir de *d*- les augmentations de métal. Il se retrouve également dans la stabilité des produits intermédiaires de la réaction carbone-métal.

En plus de la structure électronique, la réactivité entre le métal et le carbone est également changée lorsque la taille du métal est réduite à l'échelle du nanomètre en raison d'une augmentation notable du rapport des atomes de surface à des atomes internes. Il en résulte des différences dans les diverses propriétés physiques et chimiques par rapport au matériau massif, par exemple, des températures de fusion plus basses et solubilités élevées de carbone dans les métaux ont été observées. Cet effet de taille est particulièrement sensible pour les petites particules de métal à environ 100 nm. La solubilité du carbone dans du métal est une propriété dépendant de la température, qui augmente lorsque la température augmente. La solubilité du carbone dans les métaux de transition peut également être considérablement augmentée en raison de la petite taille des particules métalliques.

Dans la réalisation de l'activité catalytique d'un métal de transition, une autre propriété importante est l'enthalpie de formation de la source de carbone car il améliore l'activation du catalyseur. En fonction du métal sélectionné et la source de carbone, un choix approprié des paramètres de synthèse répond à la $\Delta G < 0$ et l'état du produit de réaction. Sur la base de cette analyse thermodynamique, C_2H_2 a été observé pour produire plus de changements énergie libre de Gibbs que d'autres sources de carbone qui réagissent avec un même métal. Pour cette raison, C_2H_2 est considérée comme l'une des sources de carbone les plus réactive dans la synthèse catalytique de nanotubes de carbone.

En plus de l'interaction avec les molécules de carbone contenant des métaux de transition également interagir avec la source de carbone solide (allotropes de carbone) et à éliminer le carbone du substrat de carbone sous la forme d'hydrocarbures (essentiellement du méthane), tandis que la réaction est produite dans une atmosphère d'hydrogène. Ce processus est connu sous le nom 'hydrogénation catalytique », et se trouve être dépendant d'un grand nombre de facteurs: la structure de carbone de départ, le type de catalyseurs métalliques, et la méthode de traitement de l'échantillon. En outre, l'hydrogénation catalysée par du diamant et du graphite naturel a également été observée être accompagnée de la formation de canaux (tubes ouverts) à la surface et dans les tunnels du volume de cristaux. Ces observations ont conduit plus tard à la mise au point de la technique de gravure catalytique, qui a été utilisé pour la haute qualité de polissage et le façonnage du diamant CVD. La technique a également été utilisée dans la modification de surface des cristallites de diamant synthétique et de diamant dopé au bore avec des nanoparticules métalliques divers et de l'hydrogène. Le processus est, cependant, loin de l'optimal du point de vue pratique, en raison du manque d'informations sur la vitesse, l'effet de gravure de température, la densité et la morphologie des nanopores, la gravure du diamant nanocristallin et l'évolutivité du processus, qui jouent un rôle pour la mise au point de dispositifs, tels que les diamants, sur la base de capteurs nanopores dans une membrane en diamant pour l'analyse de biomolécules dans des conditions difficiles. Il n'y a aucun consensus sur l'étape limitant de la gravure catalytique du diamant et le mécanisme est encore mal compris. En outre, il est important de noter que dans le cas de capteurs, le processus de fabrication du dispositif comporte une étape de gravure, effectué généralement par lithographie et gravure ionique réactive. Toutefois, dans le cas de capteurs sur la base de nanopores dans une membrane, de la technique de gravure régulière (par exemple, une gravure ionique réactive) ne parvient pas à créer des trous étroits (10 à 50 nm de diamètre) et longs (typiquement de plus de 300 nm) dans la membrane due à la limite de résolution. Ces observations renforcent l’importance de la poursuite du développement de la technique de gravure catalytique du diamant.

Although early attempts of diamond synthesis did not specifically call for using a catalyst, one way or another, these experiments (**Hanny, 1880**; **Moissan, 1893**; **Leipunskii, 1939**; **Liander, 1960**) were associated with the use of iron, the most dominant catalyst that is used today for commercial production of diamond under high pressure. The subsequent research of General Electric scientists led to the discovery that certain molten metals could catalyze the formation of diamond under high pressure. These metals contain at least one of a dozen transition metals (**Bundy *et al.* 1955**). These metals are primarily group VIIIa (iron group) elements (Fe, Co, Ni, Ru, Th, Pd, Os, Ir and Pt), but they also include three other transition metals (Mn, Cr and Ta). Other 'non-catalysts,' such as Cu, Zn and Ge could also be used to grow diamond when the temperature is higher than that for typical diamond synthesis using the conventional catalysts of iron group elements (**Kanda *et al.* 1994**). Thus, it would appear that a 'noncatalyst' could become a catalyst at a higher temperature. Transition metal powders of micrometric scale (Ni of 3 ~ 5 μm in size, Ti, Cu, Fe, etc.) mixed with diamond powders have also been processed as catalysts to enhance the initial nucleation density for diamond film growth by HFCVD (**Chakk *et al.* 1995, 1996**). The catalytic enhancement was explained to result from the dissociative chemisorption of CH_4 at the Ni catalytic sites. On the other hand, the catalytic effect of Ni was illustrated to inhibit CVD diamond nucleation and growth during diamond film growth on ordered Ni (100) surface (**Belton & Schmieg, 1989**). Here, instead of epitaxial growth, diamond deposition was observed on the amorphous carbon or graphitic interlayer initially formed on Ni. Consequently, under a well controlled growing condition, CNT and diamond can be simultaneously and selectively grown on Ni-coated and diamond powder-seeded Si substrates (**Yang *et al.* 2004**). In addition, Ni nanoparticles were suggested to be ideal catalytic seeds for the growth of nanocrystalline diamond film with enhanced nucleation density by HFCVD due to their higher surface to volume ratio, thereby higher catalytic activity, as compared to Ni particles in micron size (**Teng *et al.* 2010**). The above examples illustrate the various degrees of catalytic activity of transition metals in the growth of different carbon allotropes. The catalytic activity of transition metals is, indeed, reflected in their interaction with carbon and is varied with temperature, particle size, and chemical state of carbon source.

2.1. Carbon Solubility in Metals

A transition metal tends to react with carbon by overlapping its *d*-orbitals with carbon's *p*-orbitals (**Menon *et al.* 2000; Sung & Tai, 1996**). Hence, the reactivity of a transition metal toward carbon is primarily determined by its electronic state, specifically, the number of electron vacancy of *d*-orbitals. As a result, the reactivity of transition metals generally decreases in the order of groups: IIIA, IVA, VA, VIA, VIIA, VIIIA, IB and IIB. Thus, Cu, with full *d*-orbitals, shows little interaction with carbon; Fe, with four vacancies in *d*-orbitals, exhibits moderate interaction; and Ti, with eight vacancies in *d*-orbitals, manifests strong interaction.

Table 2.1. Electronic configurations of selected transition metal elements (**Martin & Wiese, 1996**).

Elements	Atomic numbers	Electronic configurations
Ti	22	[Ar] $3d^{2}\,4s^{2}$
Fe	26	[Ar] $3d^{6}\,4s^{2}$
Co	27	[Ar] $3d^{7}\,4s^{2}$
Ni	28	[Ar] $3d^{8}\,4s^{2}$
Cu	29	[Ar] $3d^{10}\,4s^{1}$
Pd	46	[Kr] $4d^{10}\,5s^{0}$
Pt	78	[Xe] $4f^{14}\,5d^{9}\,6s^{1}$

Notes: [Ar] = $1s^{2}\,2s^{2}\,2p^{6}\,3s^{2}\,3p^{6}$; [Kr] = [Ar] $3d^{10}\,4s^{2}\,4p^{6}$; [Xe] = [Kr] $4d^{10}\,5s^{2}\,5p^{6}$

The increasing reactivity between metal and carbon is also reflected in the increasing solubility of carbon in metal, which tends to peak at Fe group metals and then decline (**Sung & Tai, 1996**). The reverse in solubility with further increase of the number of *d*-vacancies is due to the over-reaction between metal and carbon. As the reactivity exceeds a threshold value, carbon atoms begin to lose their mobility in the solid solution forming metal carbides. Thus, elements such as Cu or Zn, with full *d*-orbitals (no *d*-vacancies), are relatively inert to carbon and show a minimal degree of interaction dissolving only a trace amount; while elements such as Ti, V, or Sc, with many *d*-vacancies (seven to nine), show a very strong interaction with carbon forming stable carbides. But elements such as Ni, Co, or Fe, with few *d*-vacancies (two to four), exhibit moderate interaction dissolving a substantial amount of carbon that in excess leads to the formation of metastable carbides.

Eutectic solubilities of carbon in solid and liquid metals are listed in Table 2.2, adapted from (**Sung & Tai, 1996**), along with their corresponding eutectic temperatures. In order to compare these solubilities at the same temperature, e.g. 1000 ^{o}C, 'effective solubilities' as listed in Table 2.2, were obtained (**Sung & Tai, 1996**) by extrapolation of eutectic solubilities. In addition, these effective solubilities are compared in Table 2.3 to understand the possible control of *d*-vacancies on carbon solubilities.

Table 2.2. Carbon solubilities (at.%) in selected metals, adapted from **Sung & Tai, 1996**. M. P. refers to the eutectic point of a metal-carbon system. 'Solid' denotes the maximum carbon solubility in the solid phase that is in equilibrium with the liquid phase at the eutectic point. 'Liquid' means the carbon content at eutectic composition. 'At 1000°C designates the 'effective solubility' of carbon at 1000°C. It is obtained by multiplying the eutectic solubility by 1000/M. P.

Elements	M. P. (^{o}C)	Solid (at.%)	Liquid (at.%	At 1000 (^{o}C)
Ti	1648	3.1	1.96	1.19
Fe	1153	9.1	16.9	14.7
Co	1321	4.5	11.9	9.01
Ni	1327	2.7	6.93	5.22
Pd	1504	9.0	20.3	13.5
Pt	1705	3.0	16.5	9.66
Au	1050	0.01	4.7	4.48

Table 2.3. Effective eutectic solubilities of carbon in molten transition metals at 1000 ^{o}C, adapted from **Sung & Tai, 1996**.

d	3d	C (*A*%)	4d	C (*A*%)	5d	C (*A*%)
2	Ti	1.2	-	-	-	
6	Fe	14.7	-	-	-	
7	Co	9.0	--	-	-	
8	Ni	5.2	Pd	13.5	Pt	9.7
9	-	-	-	-	Au	4.5

According to Table 2.3, the 'effective solubilities' of carbon in transition metals are the highest when transition metals possess about an equal amount of valence electrons and vacancies in their *d*-orbitals. However, notable exception is Pd which shows surprisingly high 'effective solubility' of carbon, despite having no vacancy in its *d*-orbitals. It is also the only transition metal without an *s*-electron ([Kr] $4d^{10}5s^{0}$). Hence, Pd should behave as Cu or Ag with a minimal solubility of carbon. However, this prediction is based on the electronic state of pure Pd metal. When there are carbon atoms around, an electron in the *d*-orbital of Pd may enter the empty *s*-orbital and leaving one *d*-orbital vacant. As a result, Pd has two unfilled orbitals, i.e., *s* and *d* ($4d^{9}\,5s^{1}$), so it can interact with carbon and dissolve the latter (**Sung & Tai, 1996**).

2.2. Formation of Carbides

The extent of the ''carbon affinity'' of transition metals has been widely studied (**Blomberg *et al.* 1992**; **Bent, 1996**; **Zaera, 1995**; **Sheppard, 1988**). The affinity is reflected in the increasing enthalpy of formation of metal carbides (**Meschel & Kleppa, 1997**), the increasing enthalpies of formation of the carbon–metal bond (**Pauson, 1970**; **Drowart *et al.* 1967**), and the increasing melting point of metal carbides (Table 2.4), as the number of d-vacancies of the metal increases. It is also reflected in the stability of the intermediate products of the carbon–metal reaction. Ni, Co, and Fe result in the formation of metastable carbides followed by their decomposition and graphitization (**Sinclair *et al.* 2002**). However, metals such as Ti, Ta, or Mo produce stable carbides which can eventually lead to carbon precipitation once the concentration of carbon on these surfaces reaches a certain saturation value (**Liu & Dandy, 1995**; **Wolter *et al.* 1995**). The energy barrier to diffuse through an interlayer of stable carbide (**Ozturk *et al.* 1982**) is such that, after the formation of a critical thickness, there is no subsequent formation of metal carbide and carbon may eventually precipitate on these surfaces leading to a carbon activity of $a_C = 1$ at the interface between graphite and metal carbide (**Esconjauregui *et al.* 2008**). Under this driving force, the metal carbide becomes unstable and thus decomposes. Detailed thermodynamic calculations for the decarburization of Ni, Co, and Fe have been reported elsewhere (**Bonnet *et al.* 2003**; **de Bokx *et al.* 1985**; **Sinharoy *et al.* 1978**).

Table 2.4. Melting points (^{o}C) of some refractory carbides, adapter from **Pierson, 1996**.

No. of *d*-vacancies	Refractory carbides	Melting points (^{o}C)
4	Fe_3C	1227
5	Mn_7C_3	1340
6	Cr_3C_2	1810
8	TiC	3067

The formation energy of the carbides of the transition metals is shown in figure 2.1 (**Wirth *et al.* 2009**).

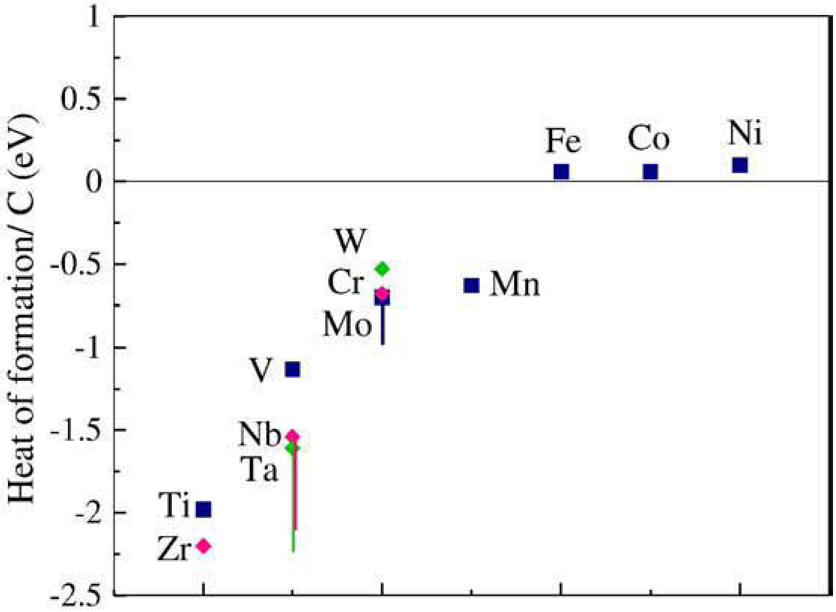

Figure 2.1. Heat of formation of transition metal carbides, per C atoms across the transition metal series, adapted from ***Wirth et al. 2009****.*

2.3. Size Effect

In addition to electronic structure, the reactivity between metal and carbon is also changed when the size of the metal is reduced to nanometer scale due to a notable increase in the ratio of surface atoms to internal atoms. The atoms located on the surface are electronically and coordinatively unsaturated and, thus, are more reactive and mobile. This results in differences in various physical and chemical properties compared to the bulk material, e.g., lower melting temperatures and higher carbon solubilities in metals have been observed. This size effect is particularly noticeable for metal particles smaller than approximately 100 nm (**Buffat & Borel, 1976**).

The melting temperature of a particle (Tc) with a radius r can be approximated by

$$T_c = T_0 - \frac{2T_0}{\Delta H_{fusion}\, \rho_s r} \quad \sigma_{sl} + \quad 1 - \frac{\rho_s}{\rho_l} \; \sigma_l \tag{1}$$

where T_0 is the bulk melting temperature, ΔH_{fusion} is the latent heat of fusion, ρ_s and ρ_l are the densities of solid and liquid metal respectively, σ_{sl} is the solid–liquid interfacial energy and σ_l is the surface energy of the liquid (**Friedlander, 2000**). The melting temperature of iron, nickel, gold and silver as a function of particle diameter according to equation (1) is presented in figure 2.2 (**Moisala *et al.* 2003**). It is clearly seen that the melting temperature is reduced from the bulk value for particles with diameters below 100 nm and a remarkable decrease is observed below 10 nm. On the basis of the presented calculation (**Moisala *et al.* 2000**), the 1–3 nm metal particles would, without any doubt, be in liquid form. In addition to the size effect, the melting point of a metal is also depressed by forming a eutectic with carbon (**Wirth *et al.* 2009**).

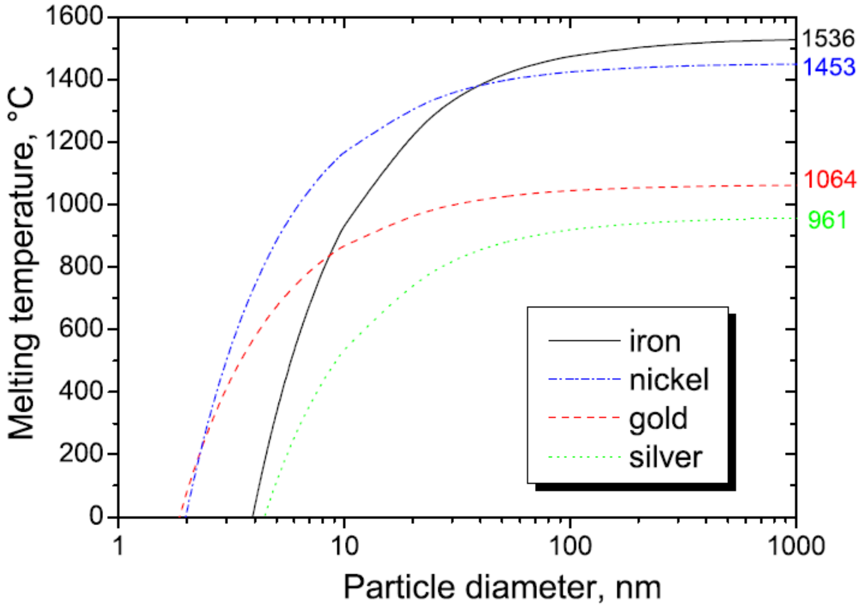

Figure 2.2. Melting temperature of selected metals as a function of particle diameter, adapted from ***Moisala et al. 2000****.*

The solubility of carbon in metal is a temperature-dependent property, which increases with increasing temperature. The solubility of carbon in transition metals can also be significantly increased due to the small size of the metal particles. The effect of particle size on the solubility of carbon in metal particles can be estimated as

$$S = S_0 \exp \frac{2\sigma V}{kTr} \tag{2}$$

where S and S_0 are solubilities in the particle and bulk material respectively, defined as the ratio of the amounts of solute and solvent (**Hochella, 2002**). The size-dependent solubilities of carbon in nickel and iron at the metal melting temperatures are shown in figure 2.3 (**Moisala *et al.* 2003**), where the solubility is presented as the atomic percentage. The bulk solubility of carbon in nickel is 10.7 and in iron 20.2 at.%. According to figure 2.3, the solubility of carbon in iron and nickel increases for metal particles with a diameter of less than approximately 10 nm. For 1 nm diameter iron and nickel particles over 80% carbon solubility is observed, which implies that more than 4 mol of carbon can be dissolved in 1 mol of iron.

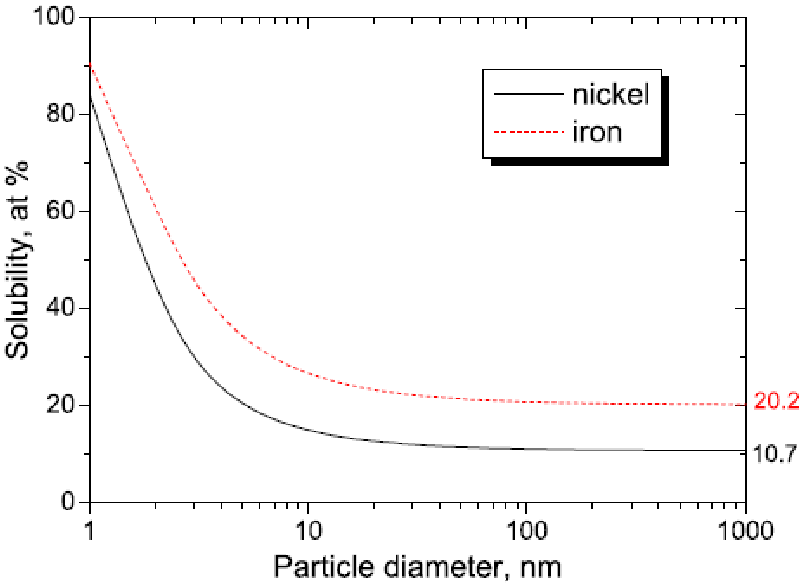

Figure 2.3. Solubility of carbon in iron and nickel at the metal melting temperature as a function of particle diameter, adapted from ***Moisala et al. 2003****.*

The diffusion mechanism of carbon on transition metal particles has been studied (**Hofmann *et al.* 2005**; **Teschner *et al.* 2006**; **Vass *et al.* 2008**; **Gracia *et al.* 2005**) and it has turned out that subsurface incorporation and diffusion of C in transition metals is more general. A surface site has fewer bonds than a bulk interstitial site, but it requires the volume expansion. These leads to the optimum site being a subsurface interstitial, which is fully bonded, but which allows some relaxation by pushing up the surface layer above it.

2.4. Influence of Carbon Source

In realizing the catalytic activity of a transition metal, another property of significance is the enthalpy of formation of the carbon source because it enhances the activation of the catalyst. This can be explained by the thermodynamics of the following metal-carbon reaction:

$$\mathrm{zM} + \mathrm{C_xH_y} \rightarrow \mathrm{M_zC_x} + \frac{1}{2}\mathrm{yH_z}$$

where M denotes a metal, C_xH_y a carbon source and M_zC_x the corresponding metal carbide. The Gibbs free energy of the reaction (ΔG) is:

$$\Delta G = \Delta H - T_r \Delta S \tag{3}$$

where ΔH is enthalpy, T_r is reaction temperature, and ΔS is entropy. When the catalyst is a pure metal, the enthalpy of the reaction has two components:

$$\Delta H = \Delta_f H^0_{M_zC_x} - \Delta_f H^0_{C_xH_y} \tag{4}$$

where $\Delta_f H^0_{M_zC_x}$ is the standard enthalpy of formation of the metal carbide and $\Delta_f H^0_{C_xH_y}$is the standard enthalpy of formation of the carbon source. For a selected metal, $\Delta_f H^0_{M_zC_x}$ is constant and the thermodynamic property that controls ΔH of the reaction is the enthalpy of formation of the carbon source ($\Delta_f H^0_{C_xH_y}$). The lowest energy pathway takes place when the formation of the metal carbide is an endothermic process ($\Delta_f H^0_{M_zC_x}$) and the decomposition of the carbon source is an exothermic process ($\Delta_f H^0_{C_xH_y} < 0$), or vice versa. Depending on the selected metal and carbon source, appropriate choice of the synthesis parameters satisfies the $\Delta G < 0$ condition and the reaction proceeds. On the basis of this thermodynamic analysis, C_2H_2 has been observed to produce higher changes of Gibbs free energy than other carbon sources reacting with same metal (**Lide, 2001-2002**; **Meschel & Kleppa, 1997**). For this reason, C_2H_2 is considered as one of the most reactive carbon sources in catalytic synthesis of carbon nanotubes.

In addition to the interaction with carbon containing molecules (e.g. CH_4, C_2H_2 etc.), transition metals also interact with solid carbon source (carbon allotropes) and remove carbon from the carbon substrate in the form of hydrocarbons (mainly methane), while the reaction is occurred in hydrogen atmosphere. This process is known as 'catalytic hydrogenation', and is found to be dependent on a great number of factors: the structure of starting carbon, the type of metal catalysts, the method of sample treatment (**Randall & Mohammad, 1929**; **Tomita & Tamai, 1972**, **1974**; **Tomita *et al.* 1974**; **McKee, 1974**; **Rewick *et al.* 1974**; **Tamai *et al.* 1977**; **Baker *et al.* 1980**; **Santiesteban *et al.* 1982**).
Tomita and co-workers in particular, have made the major contributions to the understanding of the reaction through a systematic investigation of transition metals activity on an active carbon (AC), a carbon black (HAFn2) and a graphite scale (GS) under atmospheric pressure of hydrogen (**Tomita & Tamai, 1972**). Their studies revealed that methane formation occurred in several stages depending on the kind of catalyst, carbon and the preparative method of metal-carbon mixtures. For example, they observed the formation of methane from an active carbon at temperature below 200 °C when the most active metal was used, and the carbon was completely gasified upon heating up to 1050 °C. On the other hand, without catalyst, only 10% of carbon were observed to be gasified under the same condition. Based on these observations they found the following sequence of activities of transition metals in hydrogenation of carbon under hydrogen atmosphere: $Rh \geq Ru \geq Ir > Pt > Ni >> Pd \geq Co \geq Fe$ (**Tomita & Tamai, 1972**).

2.5. Hydrogen etching

Furthermore, the catalyzed hydrogenation of graphite and natural diamond was also observed to be accompanied by the formation of channels (open tubes) at the surface and tunnels in the volume of crystals (**Tomita & Tamai, 1972**, **1974**; **Tomita *et al.* 1974**; **McKee, 1974**; **Grigor'ev *et al.* 1977**). Both platinum and iridium were found to be active catalysts for this reaction, with the latter exhibiting the higher reactivity (**Tomita & Tamai, 1972**). **Rewick *et al.*** (**1974**) derived an activation energy of 55 ± 3 Kcal mol^{-1} for platinum-catalyzed hydrogenation of different carbon substrates. They interpreted the catalytic effect according to a mechanism involving hydrogen dissociation on the metal surface, followed by surface diffusion across metal/carbon interface and finally reaction with carbon. This conclusion was also shared by Tomita and Tamai (**Tomita & Tamai, 1972**), but in the opinion of Russian workers (**Grigor'ev *et al.* 1977**) the reaction proceeds via dissolution of carbon in the metal, followed by methane formation, according to a solid-solid-gas mechanism.

Such observations have later led to the development of the catalytic etching technique (**Jin *et al.* 1993a**, **1993b**; **McCormack *et al.* 1994**), which has been used for high quality polishing and shaping of CVD diamond, utilizing molten rare earth metals (e.g., Ce or La near 900 ^{o}C) (**Jin *et al.* 1993a**, **1993b**), or rare earth alloys (e.g., La-Ni eutectic near 700 ^{o}C) (**McCormack *et al.* 1994**). The technique has also been employed in the surface modification of synthetic diamond crystallites and boron-doped diamond with various metal nanoparticles and hydrogen (**Lee *et al.* 1995**; **Konishi *et al.* 2006**; **Takasu *et al.* 2006**; **Ohashi *et al.* 2006**). On the other hand, **Ralchenko *et al.*** (**1993**) dealt with diamond etching for the patterning of diamond surface in hydrogen atmosphere through the thin solid metal layer such as Fe, Ni, and Pt. Recently, **Smirnov *et al.*** (**2010**) reported the catalytic formation of nanochannels and nanoholes in microcrystalline and single crystalline diamond using molten Ni particles. According to their observations, the catalytic etching of diamond was based on two steps: (i) the formation of self-assembled Ni nanoparticles from the initially deposited Ni film on a diamond substrate and (ii) the subsequent use of these particles to etch diamond catalytically. After annealing at 1000 ^{o}C for about 1:30 h, they observed the formation of inverse pyramidal shaped etch pits on [100] oriented diamond crystals, elongated etching channels on [110], and etching pits with equilateral triangles and hexagons on [111] oriented crystals (figure 2.4), revealing [111] oriented diamond plane being the slowest-etching plane.

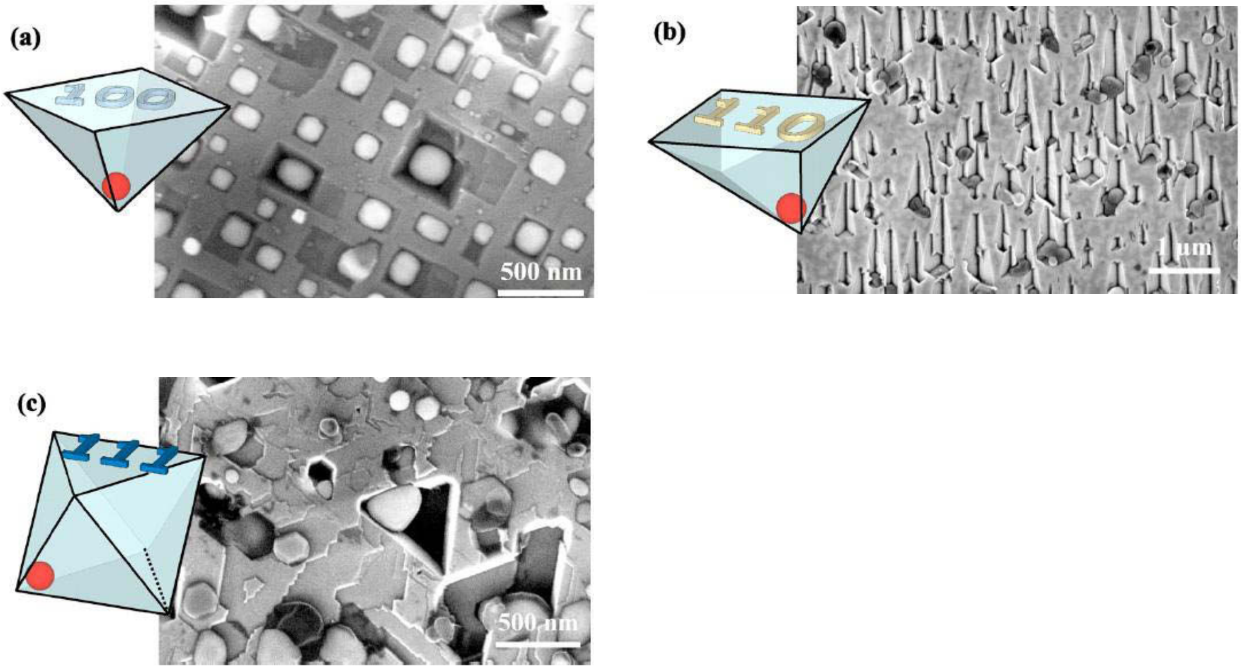

Figure 2.4. SEM micrograph of observed pitting and channelling of (a) [100], (b) [110], and (c) [111] directed and etched single-crystal diamonds, adapted from **Smirnov *et al.* 2010**. *The inset is a modeled octahedron which reflects symmetries of [111] oriented planes with indicated planes. Circles indicate Ni particles.*

Such anisotropy in diamond etching was also observed in etching of synthetic diamond crystallites with small Co particles (**Konishi *et al.* 2006**) and single crystal diamond with dispersed Fe catalyst (**Sonin *et al.* 2003**). In contrast, **Jin *et al.*** (**1994**) found [111] oriented diamond plane to be the easiest-etching plane in etching of single crystal diamond by molten Ce and they tentatively attributed this diamond etching anisotropy to the orientation-dependent difference in the energy required to break the bonds on each atomic plane. Moreover, catalyzed hydrogenation of natural diamonds (**Chepurov *et al.* 1995**) reveals that the anisotropy in diamond etching might also depend on the presence and number of defects in the form of dislocations.

There is no general opinion about the limiting stage of catalytic etching of diamond, though it was found that breaking of C—C bonds in diamond during its dissolution in the metal-catalyst is the limiting stage of the process. The mechanism is still not well understood. In addition, the process is far from the optimal from the practical point of view due to the lack of information about the etching rate, effect of temperature, density and morphology of nanopores, etching of nanocrystalline diamond and scalability of the process, which are instrumental for the development of diamond devices, such as, sensors based on nanopores in a diamond membrane for analyzing biomolecules in harsh conditions. It is important to note that in the case of sensors, the device fabrication process involves an etching step, carried out usually by lithography and reactive ion etching (**Hausmann *et al.* 2010**; **Janssen *et al.* 2011**). However, in the case of sensors based on nanopores in a membrane (**Li *et al.* 2003**; **Storm *et al.* 2003**; **Yamaguchi *et al.* 2004**), regular etching technique (e.g., Reactive ion etching) fails to create narrow (10 to 50 nm in diameter) and long (typically longer than 300 nm) holes in the membrane due to the resolution limitation, and thereby inhibiting the use of diamond. These observations demand the further development of the catalytic etching technique to a well-controlled etching method.

2.6. Carbon-Metal Binary Phase Diagram analysis

The binary carbon phase diagrams of nickel, iron, and cobalt (figure 2.5, 2.6) all of which were found to be effective in catalyzing the growth of carbon materials, in particular carbon nanotubes (CNTs), were found to have distinct similarities not found with other elements. All exhibited some carbon solubility (0.5–1.0 wt.% carbon) in the solid solution within the temperature ranges of 800–900 °C. At the solid solution solubility limit with iron, for example, a stable carbide (Fe_3C) is produced. In view of carbon nanotube growth with Fe catalyst, once the Fe_3C phase is completely saturated with carbon (at 6.67 wt.% C), graphite forms and, when nanoscale catalyst particles are used, this graphite will be produced with a nanotube structure (**Ding *et al.* 2004**; **Kuznetsov**, **2003**). The rapid diffusion of carbon in iron allows for rapid carbide formation and quick graphite precipitation. With cobalt and nickel, meta-stable carbides (Co_3C, Co_2C, and Ni_3C (**Baker**, **1992**)) form immediately following saturation of carbon in the solid solution, and as additional carbon diffuses into the catalyst, graphite precipitates out, forming a nanotube.

This type of carbon–metal phase behavior is not observed in any of the other metals (such as Cu, figure 2.6) within the temperature ranges (800-900 °C). Unsuccessful catalysts for CNT synthesis typically fell into two categories: either there is no significant solubility of carbon in the metal or numerous stable carbides formed at higher carbon concentrations. In the carbon–copper, carbon–zinc, carbon–gadolinium, and carbon–cadmium systems studied, the solubility limit of carbon in the metals is extremely low (for example, only 0.0001 wt.% C in Cu at 1100 °C, which is above the melting point of Cu) (**Hansen, 1958**). Carbon cannot diffuse in significant quantities into the nanoscale catalyst particles, and therefore, these particles cannot act as nucleation sites for the formation of carbon nanotubes.

With other potential metal catalysts, sufficient carbon solubility is observed in the solid solution; however, multiple carbides readily formed at compositions of $M_{23}C_6$, M_5C_2, M_7C_3, and M_3C_2 inhibiting precipitation of carbon and thereby preventing further growth of carbon materials. These carbides are observed in the chromium and manganese systems as well as in the vanadium (VC, V_3C_2, V_2C) titanium (TiC), zirconium (ZrC), and lanthanum (La_2C_3 and LaC_2) systems (**Baker, 1992**; **Hansen, 1958**).

Some metals in the platinum group, such as Pd (figure 2.7), do not show similar phase equilibria and solubility limits similar to Fe, Co, and Ni; however, they could act as catalysts when initially in the carbide form or at elevated temperatures (where carbon diffusion would be more rapid) (**Saito *et al.* 1996**; **Seraphin, 1995**).

For metals (such as Ti, figure 2.8), where carbide formation inhibits growth from the pure metal, carbides could be used as potential catalysts to encourage precipitation, provided the carbide particles were appropriately sized and carbon diffusion was sufficiently fast (**Sinnot *et al.* 1999**). It is suggested that for optimal growth in typical chemical vapor deposition procedures, metal catalysts (e.g. Fe, Ni or Co) need to exhibit sufficient carbon solubility, rapid carbon diffusion, and limited carbide formation (**Sinnott *et al.* 1999**; **Baker, 1989**; **Baker & Harris, 1978**).

Ni-C

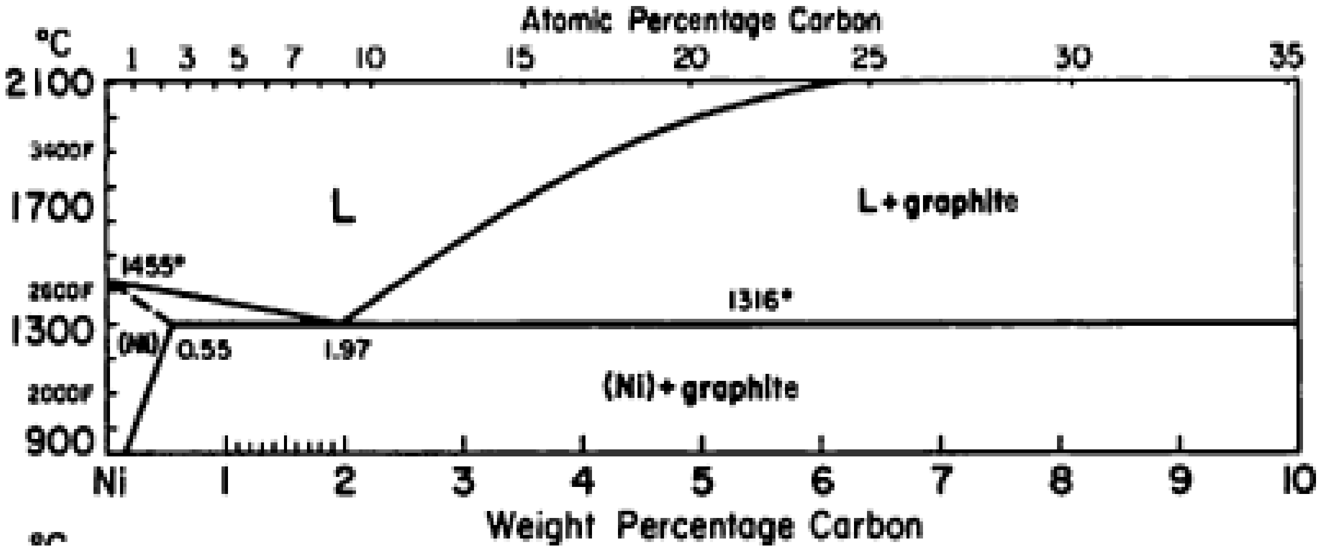

Co-C

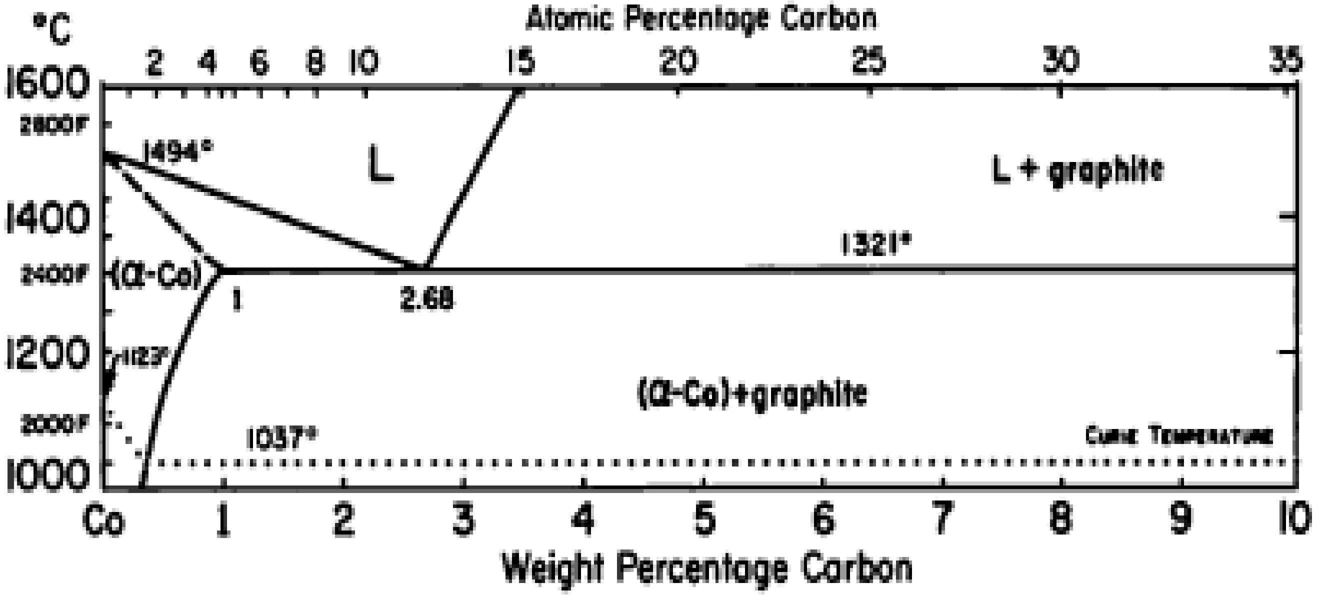

*Figure 2.5. Nickel-Carbon and Cobal-Carbon binary phase diagrams adapted from **American Society for Metals, 1973**.*

Fe-C

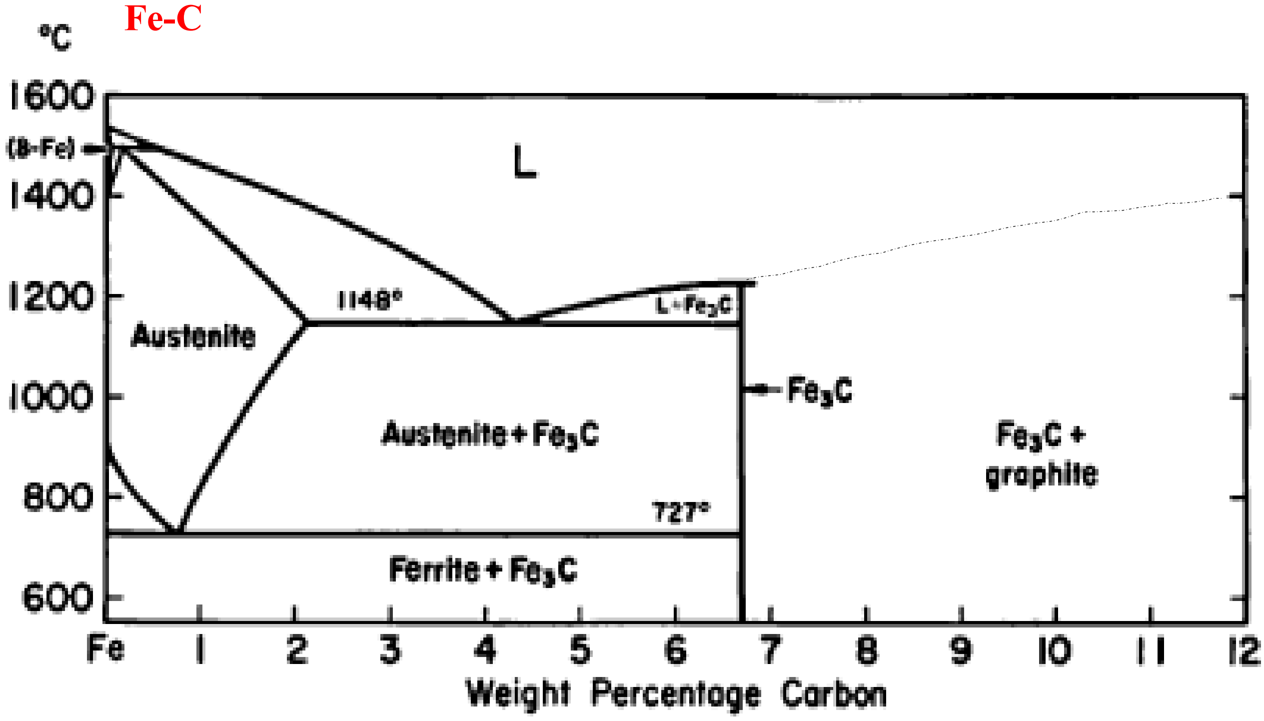

Cu-C

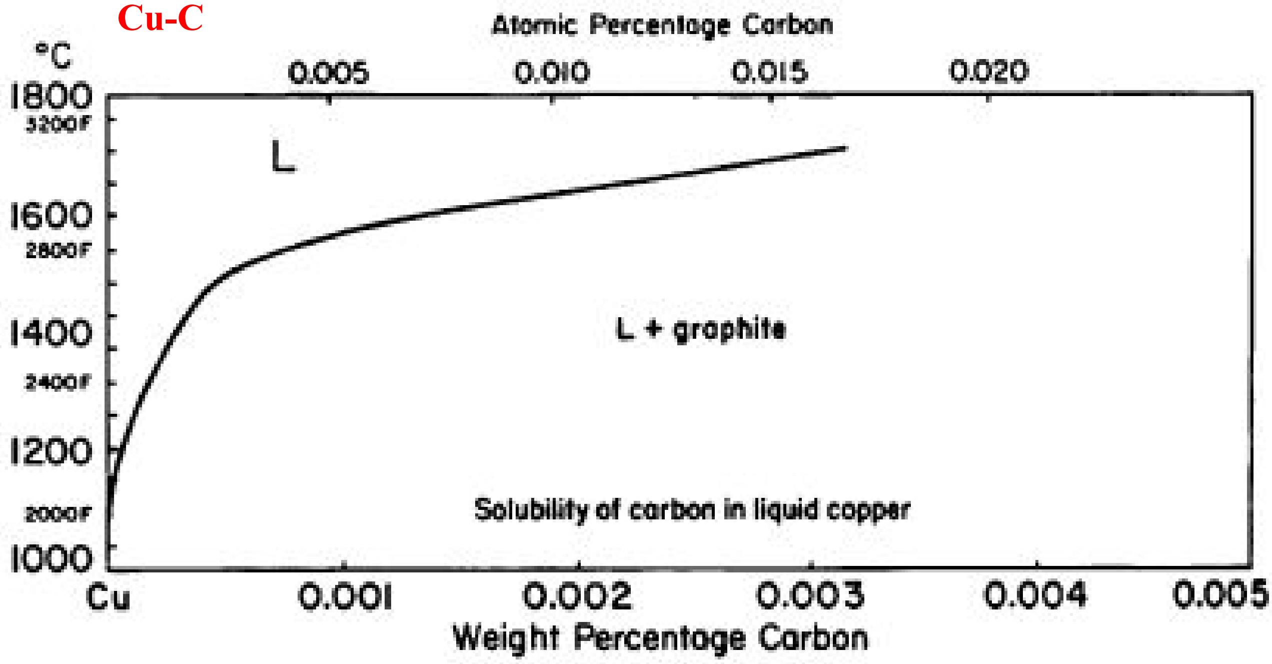

Figure 2.6. Iron-Carbon and Cupper-Carbon binary phase diagrams adapted from ***American Society for Metals, 1973****.*

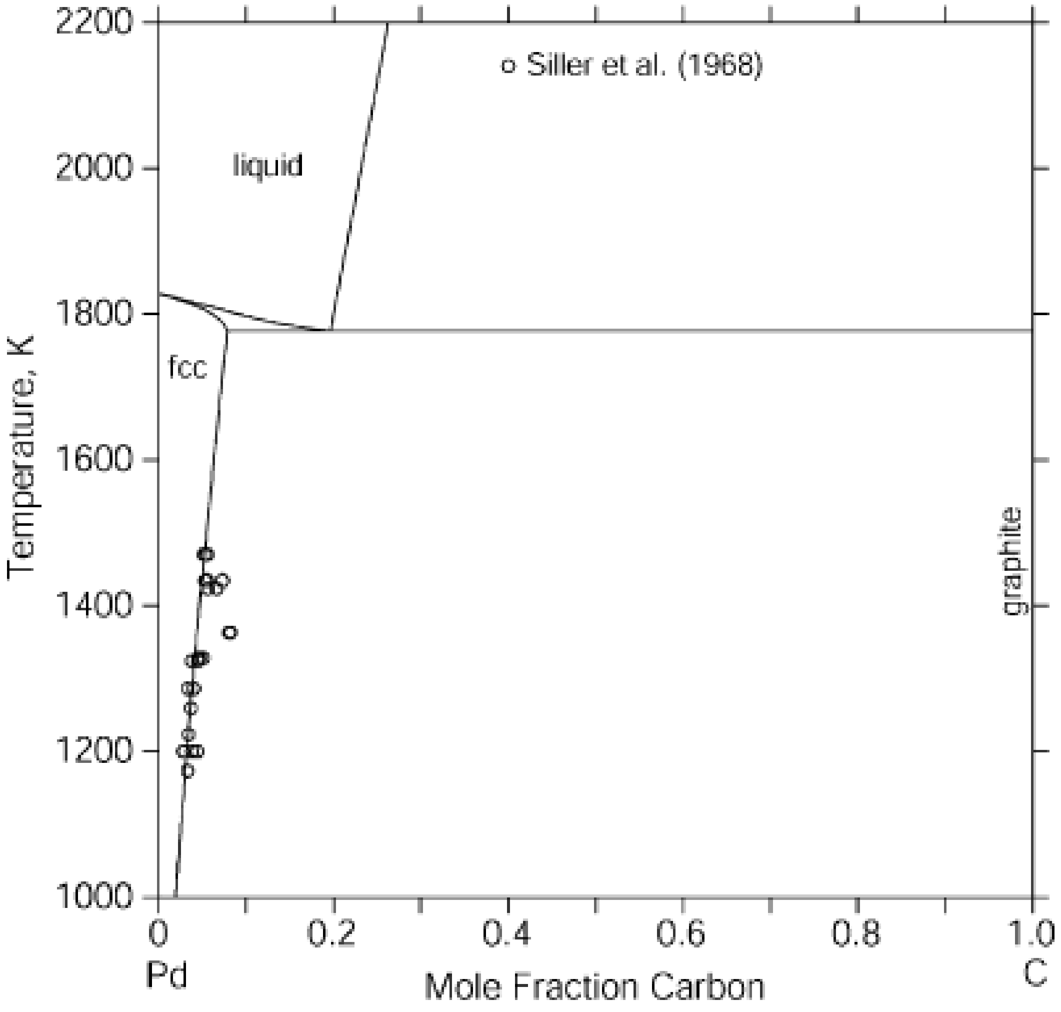

*Figure 2.7. Pd–C phase diagram calculated by the present thermodynamic description and comparison with the experimental data measured by **Siller et al. (1968)**. The figure is adapted from **Du et al. 2006**.*

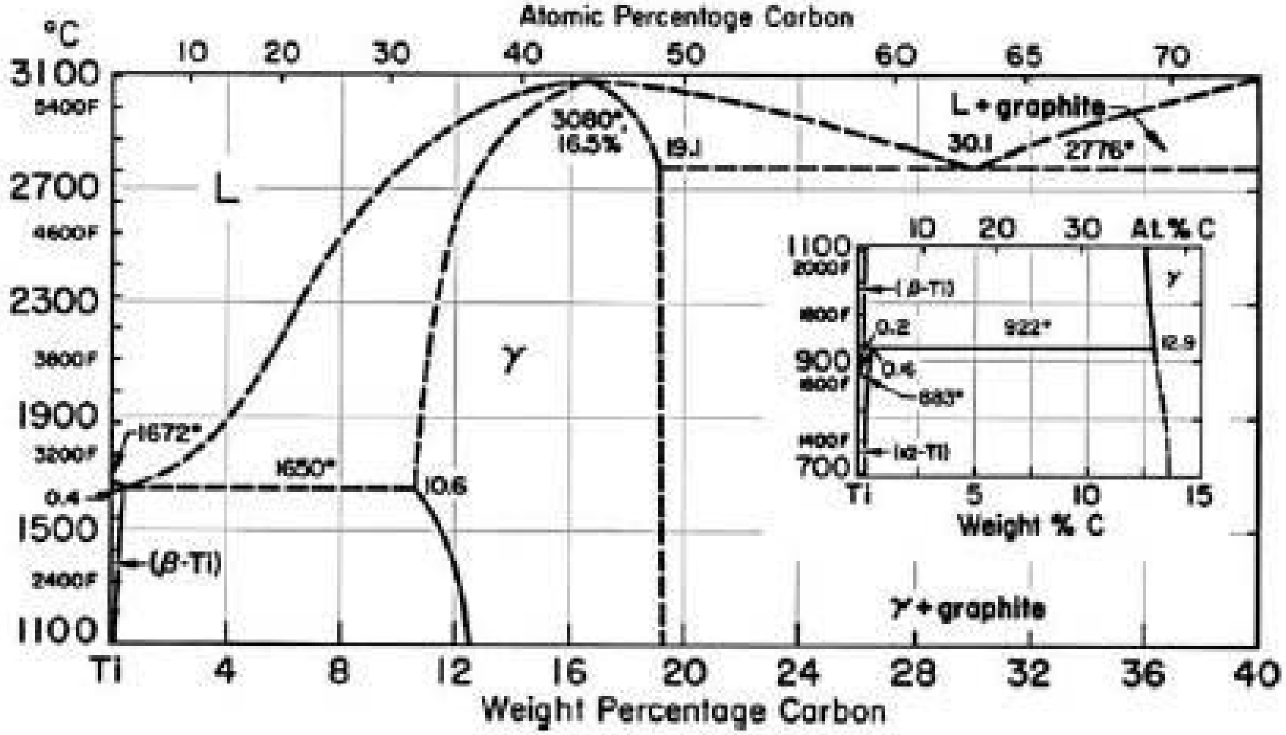

Figure 2.8. Titanium-Carbon binary phase diagrams adapted from ***American Society for Metals, 1973****.*

Bibliography

Agarwala, B. K., Singh, B. P. & Singhal, S. K. **1986** *J. Cryst. Growth* 74, 77.

Baker, H. **1992** Alloy phase diagrams. ASM International.

Baker, R. T. K. **1989** *Carbon* 27, 315.

Baker, R. T. K., Sherwood, R. D. & Dumesic, J. A. **1980** *J. Catal.* 62, 221.

Baker, R. T. K. & Harris, P. S. **1978** In *The formation of filamentous carbon*. (eds. Walker P. L, Thrower P. A.). p. 83. NewYork: Marcel Dekker.

Belton, D. N. & Schmieg, S. J. **1989** *J. Appl. Phys.* 66, 9.

Bent, B. E. **1996** *Chem. Rev.* 96, 1361.

Blomberg, M. R. A., Siegbahn, P. E. M. & Svensson M. **1992** *J. Phys. Chem.* 96, 9794.

Bonnet, F., Ropital, F., Berthier, Y. & Marcus, P. **2003** *Mater. Corr.* 54, 870.

Bundy, F. P., Hall, H. T., Strong, H. M. & Wentorf Jr, R. H. **1955** *Nature* 176**,** 51.

Chakk, Y., Brener, R. & Hoffman, A. **1996** *Diamond Relat. Mater.* 5, 3–5.

Chakk, Y., Brener, R. & Hoffman, A. **1995** *Appl. Phys. Lett.* 66, 21.

Chepurov, A. I., Sonin, V. M., Shamaev, P. P., Yelisseyev, A. P. & Fedorov, I. I. **2002** *Diamond Relat. Mater.* 11, 1592.

de Bokx, P. K., Kock, A. J. H. M., Boellaard, E., Klop, W. & Geus, J. W. **1985** *J. Catal*. 96, 454.

Ding, F., Rose, A. & Bolton, K. **2004** *J. Chem. Phys.* 121, 2775.

Drowart, J., Pattoret, A. & Smoes, S. **1967** *Proc. Brit. Ceram. Soc.* 8, 67.

Du, Z., Guo, C., Yang, X. & Liu, T. **2006** *Intermetallics* 14, 560.

Esconjauregui, S., Whelan, C. M. & Maex, K. **2008** *Nanotechnology* 19, 135306.

Friedlander, S. K. **2000** *Smoke, Dust, and Haze.* 2nd edn. p. 407. New York: Oxford University Press.

Gracia, L., Catatayud, M., Minot, J. A. C. & Salmeron, M. **2005** *Phys. Rev. B* 71, 033407.

Grigor'ev, A. P., Lifshits, S. K. & Shamaev, P. P. **1977** *Kinet. Katal.* 18, 948 (in Russian).

Hannay, J. B. **1880** *Nature* 22*,* 255.

Hansen, M. **1958** Constitution of binary alloys. 2nd ed. New York: McGraw-Hill.

Hausmann, B. M., Khan, M., Zhang, Y., Babinec, T. M., Martinick, K., McCutcheon, M., Hemmer, P. R. & Lončar, M. 2010 *Diamond Relat. Mater.* 19, 621.

Hochella, M. F. Jr. **2002** *Geochim. Cosmochim. Acta* 66, 735.

Hofmann, S., Cantoro, M., B. Kleinsorge, B., Casiraghi, C., Parvez, A., Robertson, J. & C. Ducati, C. **2005** *J. Appl. Phys.* 98, 034308.

Kanda, H., Akaishi, M. & Yamaoka, S. **1994** *Appl. Phys. Lett.* 65, 784.

Kang, W. P., Davidson, J. L., Wisitsora-at, A., Wong, Y. M., Takalkar, R., Holmes, K. & Kerns, D. V. **2004** *Diamond Relat.. Mater.* 13**,** 1944.

Konishi, S., Sugimoto, W., Murakami, Y. & Takasu, Y. **2006** *Carbon* 44, 2338.

Kuznetsov, V. **2003** In *NATO-advance study institute ASI nanoengineered nanofibrous materials*. (eds. Guceri S. I, Gogotsi, Y. and Kuzentsov, V), p. 19. Antalya, Turkey: Kluwer Academic Book.

Janssen, W., Faby, S. & Gheeraert, E. **2011** *Diamond Relat. Mater.* 20, 779.

Jin, S., Graebner, J. E., McCormack, M., Tiefel, T. H., Katz, A. & Dautremont-smith, W. C. **1993** *Nature* 362, 822.

Jin, S., Graebner, J. E., Kammlott, G. M., Tiefel, T. H., Kosinski, S. G., L. H. Chen, L. H. & Fastnacht, R. A. **1992** *Appl. Phys. Lett*. 60, 1948.

Li, J. L., Gershow, M., Stein, D., Brandin, E. & Golovchenko, J. A. **2003** *Nature Mater.* 2, 611.

Lee, W-S., Baik, Y-J., Eun, K. Y. & Yoon, D-Y. **1995** *Diamond Relat. Mater*. 4, 989.

Leipunskii, 0. I. **1939** *Uspekhii Khimii* 8, 1519.

Liander, H. & Lundblad, E. **1960** *Arkiv för Kemi* 16, 139.

Lide, D. R. **2001-2002** *CRC handbook of chemistry and physics*. Boca Raton, FL: CRC Press.

Liu, H. & Dandy, D. S. **1995** *Diamond chemical vapor deposition: nucleation and early stage growth stages*. NJ: Noyes.

Martin, W. C. & Wiese, W. L. **1996** In *Atomic, molecular, and optical physics handbook* (ed. G.W.F. Drake), ch. 11. NY: AIP.

McCormack, M., Jin, S., Graebner, J. E., Tiefel, T. H. & Kammlott, G. W. **1994** *Diamond Relat. Mater*. 3, 254.

McKee, D. W. **1974** *Carbon* 12, 453.

Menon, M., Andriotis, A. N. & Froudakis, G. E. **2000** *Chem. Phys. Lett.* 320, 425.

Meschel, S. V. & Kleppa, O. J. **1997** *J. Alloys Compd.* 257, 227.

Metallography, structures and phase diagrams. 1973 Metals Park, OH: American Society for Metals.

Moisala, A., Albert G Nasibulin, A. G. & Esko I Kauppinen, E. I. **2003** *J. Phys.: Condens. Matter* 15, S3011.

Moissan, H. **1893** *Comptes Rendus* 116, 218.

Naka, S., Horii, K., Takeda, Y. & Hanawa, T. **1976** *Nature* 259, 38.

Ohashi, T., Sugimoto, W. & Takasu, Y. **2011** *Diamond Relat. Mater.* 20, 1165.

Onodera, A., Higashi, K. & Irie, Y. **1988** *J. Mater. Sci.* 23, 422.

Ozturk, B., Fearing, V. L., Ruth, J. A. & Simkovich G. **1982** *Metall. Mater. Trans. A* 13, 1871

Parsons, C. A. **1919** *Phil. Trans. Proc. R. Sot. A* 220, 66.

Pauson, P. L. **1970** *Organometallic chemistry.* Moscow: Mir.

Pierson, H. O. **1996** *Handbook of refractory carbides & nitrides: properties, characteristics, processing and apps*. (ed. William Andrew), pp. 340. Noyes.

Pippel, E., Woltersdorf, J. & Schneider, R. **1998** *Mater. Corr.* 49, 309.

Ralchenko, V. G., Kononenko, T. V., Pimenov, S. M., Chernenko, N. V., Loubnin, E. N., Armeyev, V. Yu. & Zlobin, A. Yu. **1993** *Diamond Relat. Mater*. 2, 904.

Rewick, R. J., Wentrcek, P. R. & Wise, H. **1974** *Fuel* 53, 274.

Saito, Y., Nishikubo, K., Kawabata, K. & Matsumoto, T. **1996** *J. Appl. Phys*. 80, 3062.

Satoru, H. **1984** *Mater. Res. Bull.* 19, 479.

Seraphin, S. **1995** *J. Electrochem. Soc*. 142, 290.

Sheppard, N. **1988** *Ann. Rev. Phys. Chem.* 39, 589.

Siller, R. H., Oates, W. A. & Mclellan, R. B. **1968** *J. Less Common Metals* 16, 71.

Sinclair, R., Itoh, T. & Chin, R. **2002** *Micros. Microanal.* 8, 288.

Sinharoy, S. & Levenson, L. L. **1978** *Thin Solid Films* 53, 31.

Sinharoy, S., Smith, M. A. & Levenson, L. L. **1978** *Surf. Sci.* 72, 710.

Sinnott, S. B., Andrew, S. R., Qian, D., Rao, A. M., Mao, Z., Dickey, E. C. et al. **1999** *Chem. Phys. Lett*. 315, 25.

Sonin, V. M., Chepurov, A. I. & Fedorov, I. I. **2003** *Diamond Relat. Mater.* 12, 1559.

Smirnov, W., Hees, J. J., Brink, D., Muller-Sebert, W., Kriele, A., Williams, O. A. & Nebel, C. E. **2010** *Appl. Phys. Lett***.** 97, 073117.

Solozhenko, V. L., Turkevich, V. Z. & O.O. Kurakevych, O. O. **2002** *J. Phys. Chem. B* 106, 6634.

Storm, A. J., Chen, J. H., Ling, X. S., Zandbergen, H. W. & Dekker, C. **2003** *Nature Mater.* 2 537

Sun, L. & Wu, Q. **1999** *J. Mater. Res.* 14-3, 631.

Sung, J. **2000** *J. Mater. Sci.* 35, 6041.

Sung, C. M. & Tai, M. F. **1997** *Int. J. Refract. Met. Hard Mater.* 15, 237.

Takasu, Y., Konishi, S., Sugimoto, W. & Murakami, Y. **2006** *Electrochem. Solid-State Lett.* 9, C114.

Tamai, A., Watanabe, H. & Tomita, A. **1977** *Carbon* 15, 103.

Teng, C-C., Ku, F-C., Sung, C-M., Deng, J-P., Chien, S-F., Song, S-M. & Lin, C-T. **2010** *J. Nanomater.* 2010, 365614.

Tomita, A. & Tamai, Y. **1974** *J. Phys. Chem.* 78, 2254.

Tomita, A. & **Tamai**, Y. **1972** *J. Catal.* 27, 293.

Vass, E. M., Havecker, M., Zafeiratos, Z., Teschner, D., Knop-Gericke, A. & Schlogl, R. **2008** *J. Phys. Condens. Matter* 20, 1.

Wei, Q., Pippel, E., Woltersdorf, J. & Grabke, H. J. **1999** *Mater. Corr.* 50, 628.

Wirth, C. T., Hofmann, S. & Robertson, J. **2009** *Diamond Relat. Mater.* 18, 940.

Wang, J.B. & G.W. Yang, G. W. **1999** *J. Phys. Condens. Matter* 11, 7089.

Wolter, S. D., Glass, J. T. & Stoner, B. R. **1995** *J. Appl. Phys.* 77, 5119.

Yamaguchi, A., Uejo, F., Uchida, T., Tanamura, Y., Yamashita, T. & Teramae, N. **2004** *Nature Mater.* 3, 337.

Yang, Q., Xiao, C., Chen, W. & Hirose, A. **2004** *Diamond Relat. Mater.* 13, 433.

Yang, Q. H., Bai, S., Fournier, T., Li, F., Wang, G., Cheng, H. M. & Bai, J. B. **2003** *Chem. Phys. Lett.* 370**,** 274.

Zaera, F. **1995** *Chem. Rev.* 95, 2651.

CHAPTER 3

Growth and Analytical Technique:

Technique and Theory

Résumé

Ce chapitre décrit brièvement les principes et les procédures de travail de la technique expérimentale et techniques qui ont été utilisées dans cette étude. Filament chaud et micro-plasma CVD ont été utilisés pour synthétiser des nanomatériaux à base de carbone comme les nanotubes de carbone, des nanofibres, des films de diamant nanocristallin. L'évaporation par faisceau d'électrons (e-beam) a été utilisé pour déposer des couches métalliques différentes. Microscopie électronique à balayage (MEB) a été utilisé pour étudier la morphologie des échantillons. La chimie de surface a été étudiée par microscopie photo-électrons X-ray. Spectroscopie de masse quadripolaire a été utilisé pour analyser la composition du gaz pendant le fonctionnement CVD. En outre, pour nanostructuration de diamant, certaines approches bottom-up telles que la photolithographie ont été utilisés.

3.1. Physical Vapor Deposition: E-Beam Evaporation

Transition metals, such as Fe, Ni, Co, Pt, Pd and Au with different thickness are evaporated on diamond substrates by using Electron Beam Physical Vapour Deposition (EBPVD) technique. A schematic of the deposition system (PlASSYS MEB 550S) used for these experiments is shown in figure 3.1.

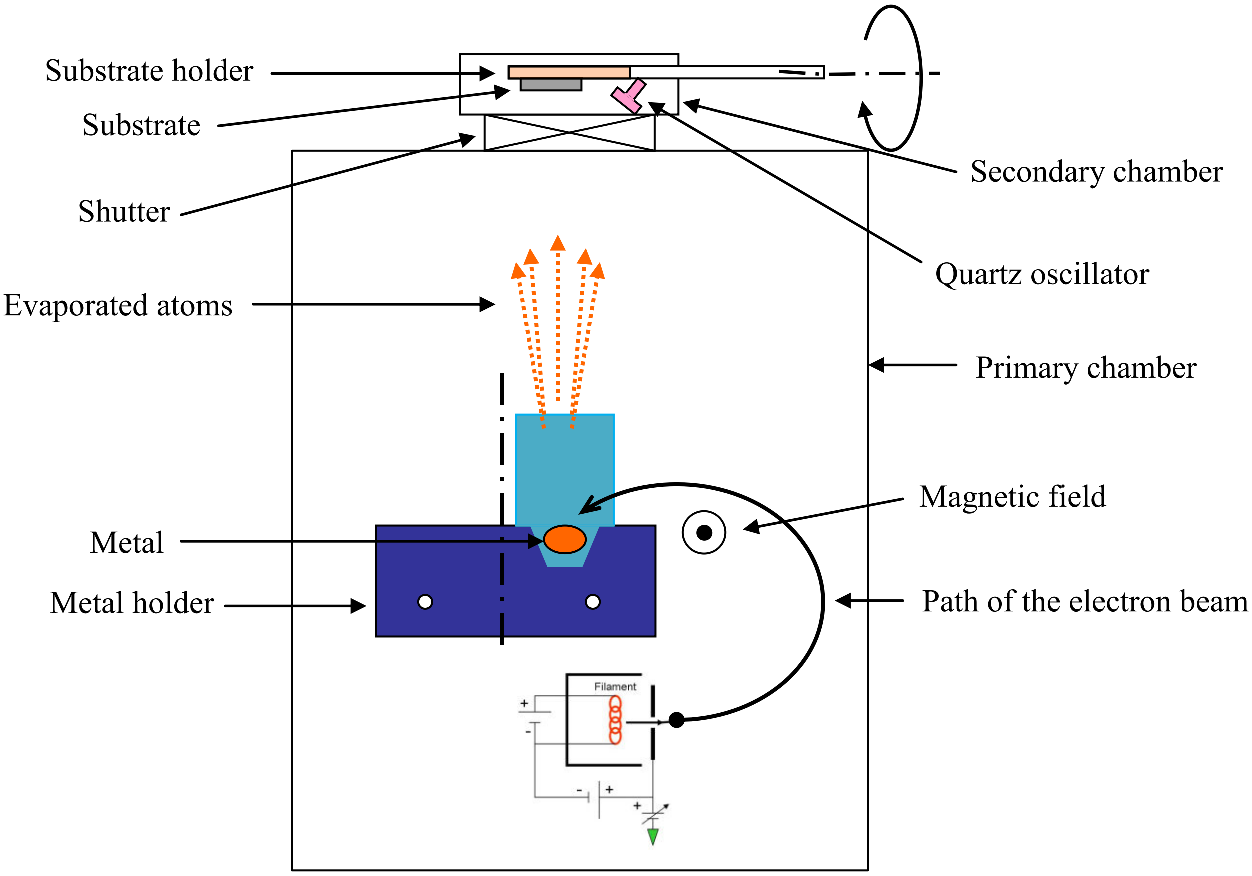

Figure 3.1. Schematic representation of the electron beam physical vapour deposition system (EBPVD). The evaporation material is held at a positive potential relative to the filament. To avoid chemical interactions between the filament and the evaporation material, the filament is kept out of sight. A magnetic field is employed to direct the electron beam from its source to the material location.

The deposition system consists of two vacuum compartments, primary and secondary, separated by an automated shutter. The diamond substrate on which the film deposition takes place is ultrasonically cleaned and fastened to the substrate holder in the secondary compartment. The substrate holder is attached to the manipulator shaft. The shaft rotates the holder to adjust the distance between the metal source and the substrate and turns it upside down.

When the pressure in the secondary compartment reaches to < 9 × 10^{-5} Torr, the automated shutter is opened to connect the primary compartment where the metal source is located. The metal deposition starts after the pressure in the primary compartment reaches to about 1 × 10^{-8} Torr. The electron beam generated thermionically is accelerated to a high kinetic energy and directed towards the evaporation material. Upon striking the evaporation material, the kinetic energy of the electrons is converted into the thermal energy that heats up the evaporation material causing it to melt or sublimate. The resulting vapor is then used to coat the substrate surface. The rate of the film deposition we used varied from 0.05 to 0.2 nm/sec. The thickness of the deposited film is measured by a quartz oscillator. The deposition process is software controlled.

3.2. Chemical Vapour Deposition (CVD)

3.2.1. Hot-Filament Chemical Vapour Deposition (HFCVD)

A home built hot-filament chemical vapour deposition (HFCVD) system, usually dedicated to diamond growth, has been used to (i) grow carbon nanotubes on silicon and diamond substrates, (ii) study the stability of carbon nanotubes dispersed on silicon substrates under hot-filament and hydrogen environment without the addition of methane in the gas phase, (iii) anneal diamond films of different microstructure with metal layers deposited on the surface, in hydrogen atmosphere only, no hot-filament and methane being used.

The deposition system consists of a water cooled vacuum chamber that is made of stainless steel and around 30 cm in diameter. Substrate is placed on a Mo-holder positioned in the center of the chamber. A tungsten (W) filament of 0.25 mm diameter is placed, on two metal electrodes, in parallel and ~ 6-10 mm above the substrate. Both filament and Mo-holder are heated resistively. A thermocouple is connected to Mo-holder to measure the temperature of the substrate and an infrared pyrometer is used to measure the temperature of the filament. In the case of annealing experiments the pyrometer has been used to measure the surface temperature of the substrate. The reaction chamber is connected to a pump system underneath, consisting of a primary pump and a turbo pump molecular pump. While the primary pump is used for the circulation of the gas mixture, the secondary pump ensures a base pressure below 10^{-5} Torr before introduction of the gas mixture and therefore prevents incorporation of other impurities. A picture of the deposition system and a schematic of the reactor are shown in figure 3.2.

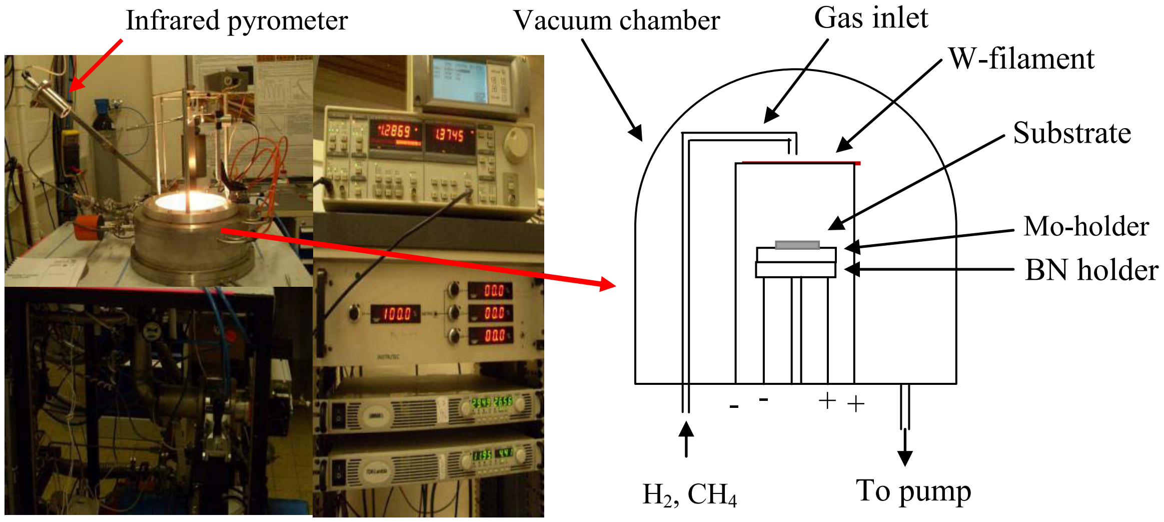

Figure 3.2. A picture of the home built HFCVD system (left) and a schematic of the main reaction chamber.

Role of Hot-Filament: The main role of the hot-filament is to dissociate molecular hydrogen into atomic hydrogen. At higher pressures (20-30 Torr) the dissociation occurs mainly near the filament (without adsorption and desorption) due to the high gas temperature. At lower pressures the filament surface acts as a catalyst for adsorption of molecular hydrogen and desorption atomic hydrogen. The dissociation equilibrium is governed by thermodynamics.

Besides the original role of the tungsten filament, it was discovered that during diamond and nanotube growth the tungsten filament reacts with methane and undergoes carburization. This results in the consumption of carbon from the methane, and thus a specific incubation time is needed for the nucleation of diamond films, in particular. The high temperature radial gradient also induces a gradient in species concentration. Typically in HFCVD, the filament is heated to 2317 °C, and a temperature of 850 °C is maintained at the substrate ~6-10 mm from the filament. Experimentally, large temperature drops are found at the filament-gas and gas-substrate interfaces. A fairly slow decrease in gas temperature is observed as one traverses the filament-substrate gap, and the temperature in this region is typically 1127-1727 °C (**Harris *et al.* 1988**), see figure 3.3.

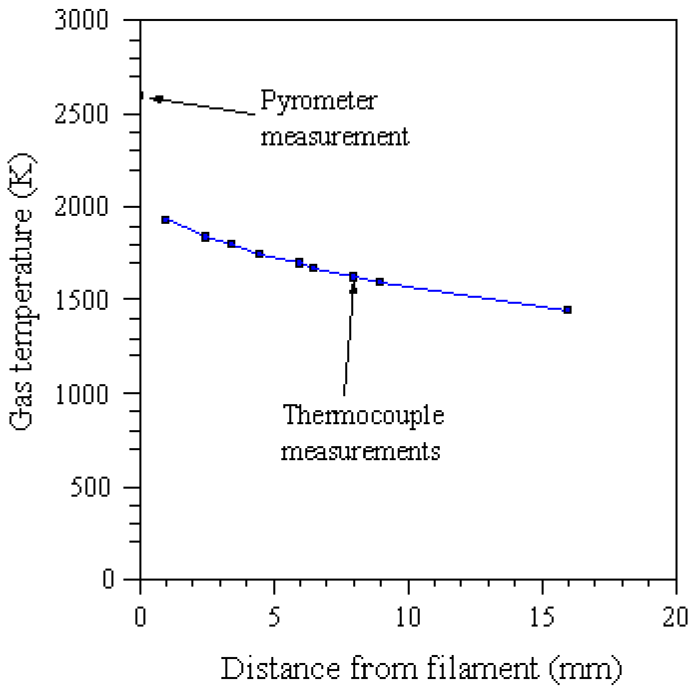

*Figure 3.3. Gas temperature profile measured in a hot filament reactor at 20 Torr by **Harris et al.** (adapted from **Wahl et al. 1996**).*

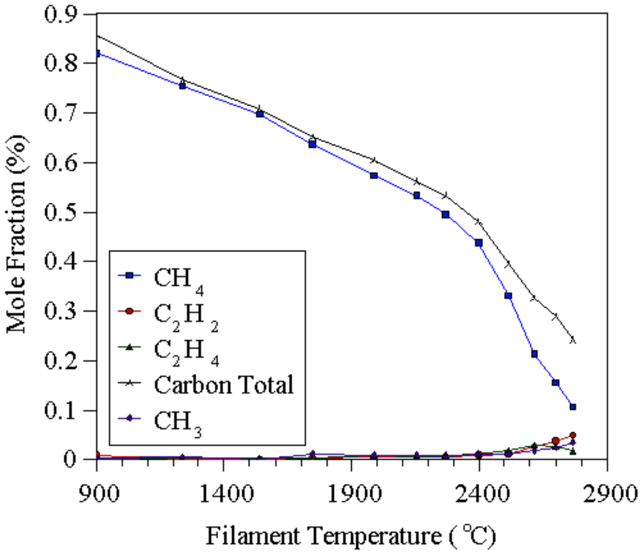

*Figure 3.4. MBMS results of Tsang, showing the effect of thermal diffusion on species concentration measurements during HFCVD. The total measured carbon is less than the 1% CH_4 input at elevated temperatures (adapted from **Tsang, 1997**).*

An important temperature related effect has been noted by *in situ* detection methods. In the region of the hot filament the total measured carbon is less than the total input carbon, see figure 3.4 (**Tsang, 1997**). In the cool regions far from the filament these totals are equal, as expected. It is believed that such observations are the result of *thermal diffusion* (Soret effect) (**Corat & Good, 1993**; **Wu *et al.* 1990**; **Harris *et al.* 1989**; **DebRoy *et al.* 1990**). In the presence of a significant temperature gradient, mass dependent diffusion effects occur, whereby heavier species preferentially diffuse away from hot regions. This explains the under abundance of heavy (*i.e.* hydrocarbon) species in the high temperature region close to the filament, compared with the lighter components (*i.e.* H_2, H). Thus, the resistance of the filament should be monitored and adjustments to the supplied voltage and current made in order to keep the temperature of the filament constant.

Due to the temperature upper limit of the filament material, hot-filament processes operate at significantly lower gas temperatures than plasma processes, and consequently produce less atomic hydrogen.

3.2.2. Microwave Plasma Chemical Vapour Deposition (MPCVD)

Two MPCVD systems have been used to (i) study the stability of carbon nanotubes dispersed on silicon substrates under hydrogen and plasma environment, no methane has been added in the gas phase, (ii) investigate the VLS growth mechanism for diamond nanowire growth using methane as the main carbon containing precursors and transition metals as catalyst and (iii) grow nanocrystalline diamond films (NCD) on silicon substrates through bias enhanced nucleation (**Barrat *et al.* 1998**).

Stability Study of Carbon Nanotubes: The main objective was to investigate the growth mechanism of diamond nanowires on carbon nanotubes originally proposed by **Sun *et al.*** (**2005**). The MPCVD reactor used for this study was built up by E. Gheeraert (**1992)**, see figure 3.5, principally based on the model of a Japanese reactor used at NIRIM (National Institute for Research on Inorganic Materials, actually called NIMIS). The CVD system consists of an inner and an outer fused silica (quartz) tube forming a reaction chamber. The sample holder is placed on the top of the inner quartz tube at the intersection with the waveguide. Microwaves are emitted by a generator (maximum power 2 kW) at a frequency of 2.45 GHz in the transverse electric mode (TE) through an insulator, preventing the reflected wave to return to the generator power, tuner for minimizing reflected power and an applicator, which are all connected with wave guides (**Teraji, 2008**).

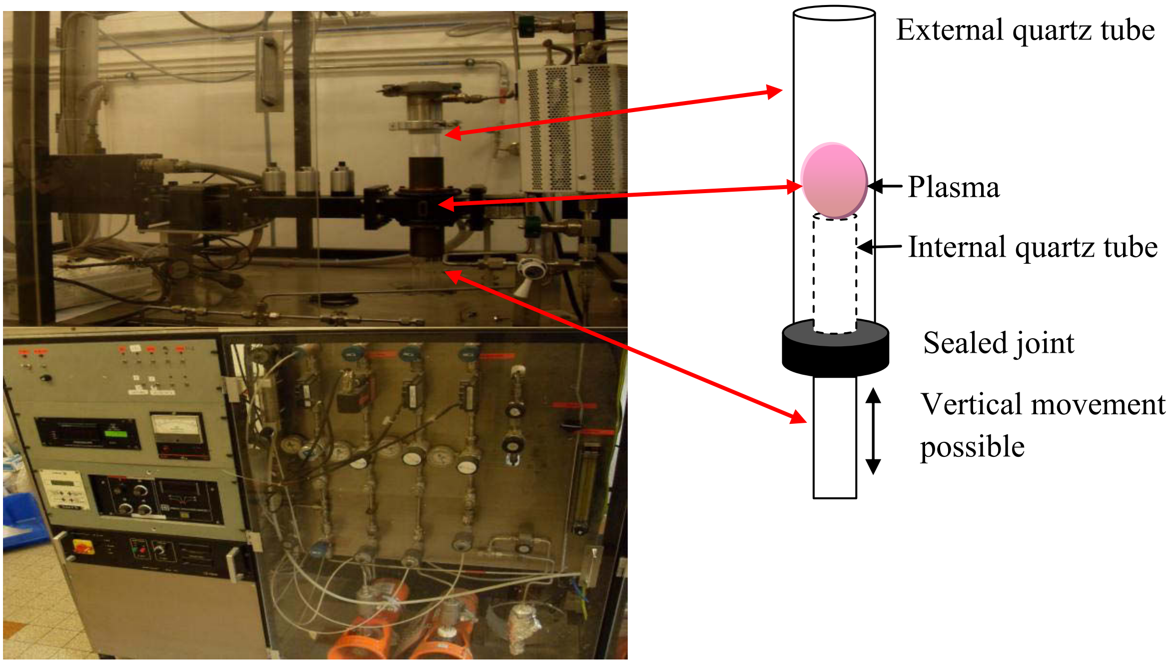

Figure 3.5. A Picture and a schematic of a NIRIM type MPCVD reactor.

The reaction chamber is connected to a pump system underneath, consisting of a primary pump and a turbo pump molecular pump. A quartz tube is commonly used as a reaction chamber because it is transparent and is exchangeable. Moreover, it offers small dielectric power loss of microwave. However, atomic hydrogen in plasma can etch the quartz wall and grown films could consequently be contaminated with etched silicon. Purified hydrogen (6N purity) with 100 sccm (sccm denotes standard cubic centimeter per minute at STP) has been used as main etching agent. Hydrogen purification is effective to improve diamond purity, especially in the case of diamond deposition under very low methane concentration, because the impurities in hydrogen gas dominate residuals of the total feed gas. A constant pressure of 30 Torr has been maintained during the etching experiments. The substrate temperature has been monitored using non-contact optical measurement with a pyrometer. The effect of the plasma radiation must be considered for precise evaluation and control of the substrate temperature.

Theory of Plasma: A plasma may be defined as a partially ionized gas containing equal volume concentrations of positively and negatively charged species (mostly ions and electrons, respectively) and different concentrations of ground state and excited species.

Supplying a sufficiently high energy to a gas generates plasma. This energy may be supplied by subjecting the gas to very high temperatures or very strong electric or magnetic fields. Plasma constantly loses energy in the form of heat and electromagnetic radiation and to retain the plasma state of a gas, energy has to be supplied continuously.

Degree of ionization: Degree of ionization is the fraction of original neutral species that have been ionized in the plasma. The degree of ionization depends on several factors such as power input, gas pressure, electric field distribution, gas composition and so on. Generally, the energy of the electrons in the plasma is believed to be a Maxwellian distribution given by

$$f(E) = \{2(e)^{1/2}/(\pi^{1/2}\, kT^{3/2})\}\exp(-E/kT) \tag{3}$$

where f(E) is the fraction of electrons with energy between E and E + dE, and T is the electron temperature. The average energy of the electron is

$$\int E\, f(E)\, dE = 3/2\, kT \tag{4}$$

Debye shielding: When a substrate is immersed into a plasma the surface of the substrate becomes negatively charged due to the current of electrons to the substrate. This is due to the relatively high average velocities of the electrons compared to the positive ions due to a large difference in their masses. This leads to the formation of a sheath with a voltage drop across its length, around any object inserted in the plasma. Hence substrates immersed in a plasma are always subject to positive ion bombardment and localized heating due to the formation of a Debye sheath (**Chapman, 1980**). Therefore, the external process control parameters such as the gas pressures, composition, and gas temperatures are significantly different from the localized process conditions on the nucleation and growth front. Plasma parameters such as ion temperature, electron temperature, ion density, are strongly interdependent, vary across the substrate area during the deposition, and are difficult to measure, control, and reproduce across reactors. Since a constant flow of energy is provided to maintain the plasma, thermal equilibrium can never be reached. Consequently, epitaxy during PECVD is very challenging. In a typical high density microwave plasma, electron temperatures are about 20000-40000°C, ion temperatures about 1000-2000°C, substrate temperatures about 400-800°C (**Lieberman & Lichtenberg, 1994**). In our plasma system (Seki Technotron.), electron and ion temperatures were estimated by simulation to be about 11227 and 1827 °C respectively. The temperature imbalance between electrons and neutrals can exist because the electrons have such low mass that they cannot efficiently transfer energy to the gas. Most of the knowledge gained about the relationships between process parameters and film properties during diamond film deposition has been empirical.

Investigation of VLS Process and NCD growth: ASTEX 5200 plasma enhanced chemical vapour deposition system (figure 3.6) has been used for the investigation of VLS process, no biasing of the substrate being employed. The detail experimental conditions and the proceduces have been discussed in Chapter 4 at the relevant section. The reactor has also been used to grow NCD on silicon substrate through bias enhanced nucleation (BEN) using the developed NCD growth condition in our lab. Note that no elaborate study of the BEN process and the effect of process parameters involved in the NCD deposition have been carried out. In some particular cases, the reactor has been used to treat thermally NCD with thin metal layers in hydrogen atmosphere without plasma and methane.

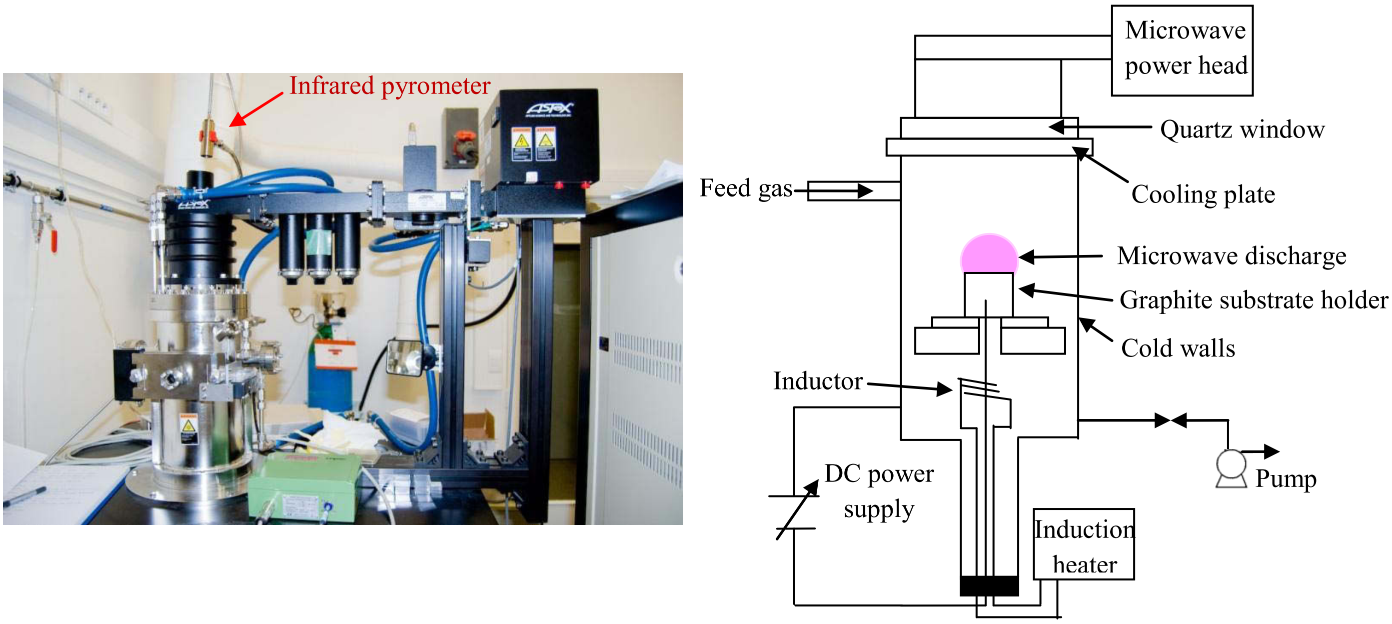

Figure 3.6. A picture (left) and a schematic of the ASTEX 5200 MPCVD system (right).

The reactive vessel is constituted of a water-cooled stainless-steel cavity having an inner diameter of 15 cm and a length of 33 cm. It is surmounted by a quartz window ensuring tightness and crossing of the microwave wave. A graphite substrate holder is located inside the microwave cavity and is surmounted by an additional substrate holder which sustains the silicon wafer and whose dimensions can be modified (diameter varying between 13 and 30 mm). The substrate temperature is reached by direct heating via the microwave and the bias plasma. This temperature can be indirectly increased by using a HF inductor connected to a generator having a nominal power of 3000 W. The substrate surface temperature is measured by an infrared pyrometer placed few cm above the reactor, see figure 3.6.

The microwave discharge is initiated by interaction between the plasma-producing gas mixture injected downstream from the quartz window and the microwave wave generated by an ultra-high-frequency generator (2.45 GHz, 1500 W) and conveyed by a symmetric plasma coupler. The negative bias of the substrate holder, which thereby constitutes a cathode, is carried out with respect to the reactor walls and is obtained with a dc generator whose voltage can be adjusted between 0 and –400 V.

For NCD growth, in the nucleation step, a –280 V voltage is applied on <100> silicon substrates that are heated at about 700 °C. The microwave power is held at 1400W with a methane concentration of 5% in H_2. The duration of the nucleation step is fixed to 7 min. The growth step follows the nucleation step without any bias and significantly lower methane concentration (e.g. 0.4 vol.% CH_4 in H_2) with 30 gas pressure at about 900 °C. Oriented diamond films are formed by the growth and coalescence of the nuclei formed by BEN provided the process parameters are suitable.

Thermodynamics of heterogeneous nucleation: Diamond growth on diamond is relatively well understood and controlled. Diamond growth on non-diamond surfaces requires a nucleation step that is much less understood and relies largely on trial and error. To understand the diamond nucleation process, let us consider a nucleus forming on a substrate from the gas phase during the heterogeneous nucleation. The substrate-nucleus system tries to minimize the energy to the lowest value possible. The thermodynamic equilibrium angle (θ) a diamond nucleus forms with the substrate surface (figure 3.7a) is given by

$$\mathrm{Cos}\ \theta = (\gamma_{sa}-\gamma_{ds}) / \gamma_{da},$$

where γ_{ds} is the diamond-substrate interfacial energy, γ_{sa} is the substrate-air interfacial energy and γ_{da} is the diamond air interfacial energy. Considering the energy balance equation, three modes of nucleation of thin films (figure 6b) have been described: (1) Frank van der Merwe (FM) mode, (2) Volmer–Weber (VW) mode, and (3) Stranski-Krastanov (SK) mode (**Matthews, 1975**).

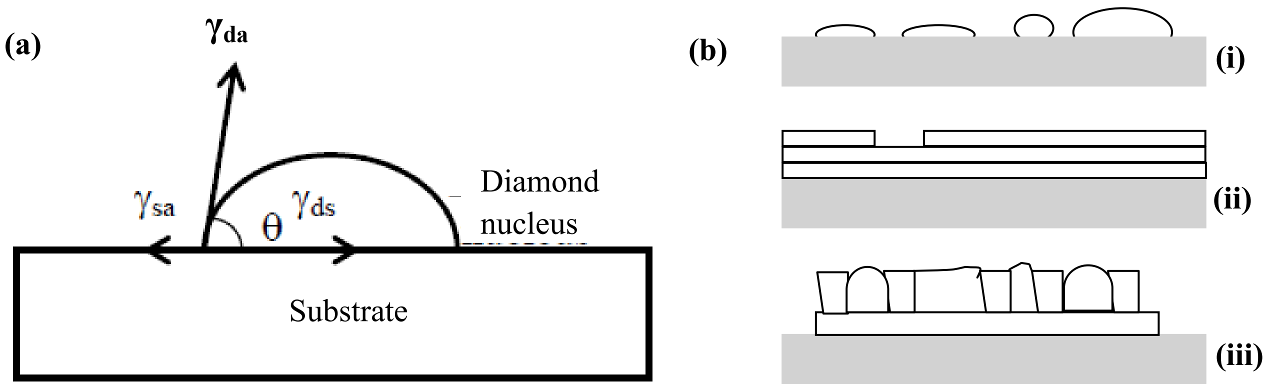

Figure 3.7. (a) Equilibrium wetting angle of a nucleus on a substrate during heterogeneous nucleation, and (b) schematic of the (i) VW, (ii) FM and (iii) SK modes of epitaxial growth based on the interface bond energy.

For epitaxial growth, strong wetting is desired, and θ has to be close to zero. Nuclei formed in these cases are 2D and layer by layer growth occurs. This is described by the FM mode and since diamond has very high surface energy, the substrate's surface energy and the interface energy have to be very high. For diamond growth the VW mode is the most commonly observed with high values of θ, particularly for relatively low surface energy substrates like Silicon and Silicon Carbide. 3-D nucleation occurs followed by growth and coalescence to form a continuous film. Substrate selection to lower the θ values becomes critical for successful epitaxial growth.

3.3. Characterization Techniques

3.3.1. Scanning Electron Microscopy (SEM)

The scanning electron microscope (SEM) uses a focused beam of high-energy electrons to generate a variety of signals at the surface of solid specimens by scanning them in a raster scan pattern. The signals that derive from electron-sample interactions reveal information about the sample including external morphology (texture), chemical composition, and crystalline structure and orientation of materials making up the sample. In most applications, data are collected over a selected area of the surface of the sample, and a 2-dimensional image is generated that displays spatial variations in these properties.

A picture and a schematic diagram of the Field Emission Scanning Electron Microscope used in this study are shown in figure 3.8 (a) and (b) respectively.

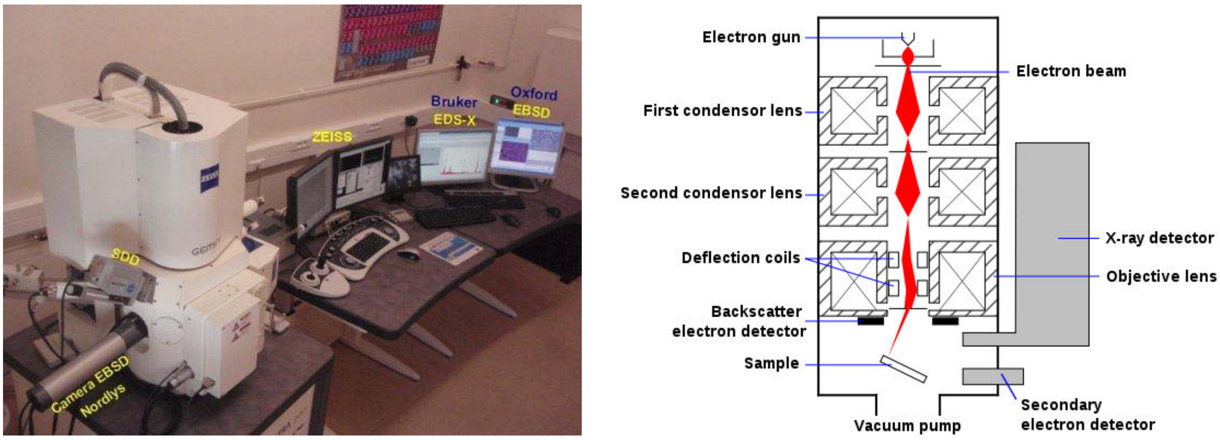

Figure 3.8. (a) A typical FESEM instrument, showing the electron column, sample chamber, EDS detector, electronics console, and visual display monitors. (b) a schematic of the microscope.

In the SEM, the electron beam emitted thermionically from a field emission gun typically has an energy ranging from 0.2 keV to 40 keV and is focused by one or two condenser lenses to a spot about 0.4 nm to 5 nm in diameter. The beam passes through pairs of scanning coils or pairs of deflector plates in the electron column, typically in the final lens, which deflect the beam in the x and y axes so that it scans in a raster fashion over a rectangular area of the sample surface.

When the primary electron beam interacts with the sample, the electrons lose energy by repeated random scattering and absorption within a teardrop-shaped volume of the specimen known as the interaction volume (figure 3.9), which extends from less than 100 nm to around 5 µm into the surface.

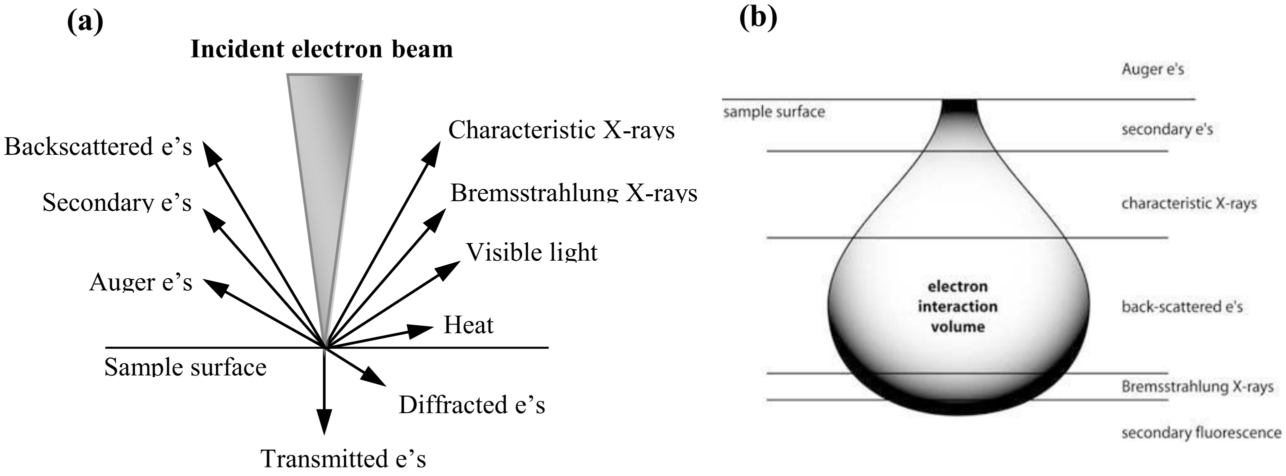

Figure 3.9. (a) Types of interactions between electrons and a sample, (b) electron interaction volume within a sample.

The size of the interaction volume depends on the electron's landing energy, the atomic number of the specimen and the specimen's density. The energy exchange between the electron beam and the sample results in the reflection of high-energy electrons (backscattered electrons) by elastic scattering, emission of secondary electrons by inelastic scattering and the emission of electromagnetic radiation, each of which can be detected by specialized detectors. The beam current absorbed by the specimen can also be detected and used to create images of the distribution of specimen current. Electronic amplifiers of various types are used to amplify the signals, which are displayed as variations in brightness on a computer monitor. Each of the signals produced from different electron interaction volumes has different imaging or analytical resolution. Auger and Secondary images have the best imaging resolution, being generated in the smallest volume near the surface of the sample. Backscattered electrons are generated over a larger volume resulting in images of intermediate resolution. Cathodoluminescence is generated over the largest volume, even larger than Bremsstrahlung radiation, resulting in images with the poorest resolution.

3.3.2. X-ray Photoelectron Spectroscopy (XPS)

XPS, also known as ESCA (Electron Spectroscopy for Chemical Analysis), is the most widely used surface analysis technique because of its relative simplicity in use and data interpretation. The sample is irradiated in an ultra high vacuum environment with mono-energetic x-rays causing the ejection of core-level electrons from sample atoms. An electron energy analyzer determines the binding energy of the photoelectrons. From the binding energy and intensity of a photoelectron peak, the elemental identity, chemical state, and quantity of an element are determined.

X-ray photoelectron spectroscopy was developed in the mid- 1960's by Kai Siegbahn (Nobel Prize 1981) and his research group at the University of Uppsala, Sweden. The phenomenon is based on the photoelectric effect outlined by Einstein in 1905 (Nobel Prize 1921) where the concept of the photon was used to describe the ejection of electrons from a surface when photons impinge upon it. In the photoemission process (figure 3.10), if an electron within some material absorbs the energy of one photon and acquires more energy than the work function (the electron binding energy) of the material, it is ejected. Because the energy of an X-ray with particular wavelength is known, the electron binding energy of each of the emitted electrons can be determined by using an equation that is based on the work of Ernest Rutherford (1914):

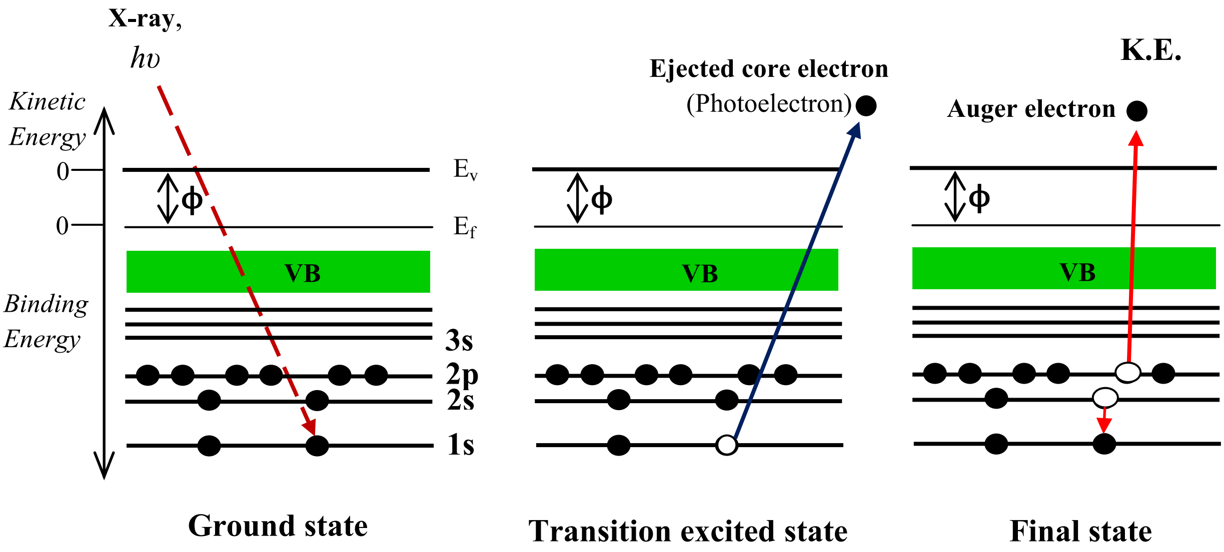

Figure 3.10. Schematic of the photoemission process.

$$E_{\text{binding}} = E_{\text{photon}} - (E_{\text{kinetic}} + \phi)$$

where E_{binding} is the binding energy (BE) of the electron, E_{photon} is the energy of the X-ray photons being used, E_{kinetic} is the kinetic energy of the electron as measured by the instrument and ϕ is the work function of the spectrometer (not the material). Energy analysis of the emitted photoelectrons is the primary data used for XPS.

When the core electron is ejected by the incident x-ray, an outer electron fills the core hole (figure 10). The energy of this transition is balanced by the emission of an Auger electron or a characteristic x-ray. Analysis of Auger electrons can be used in XPS, in addition to emitted photoelectrons.

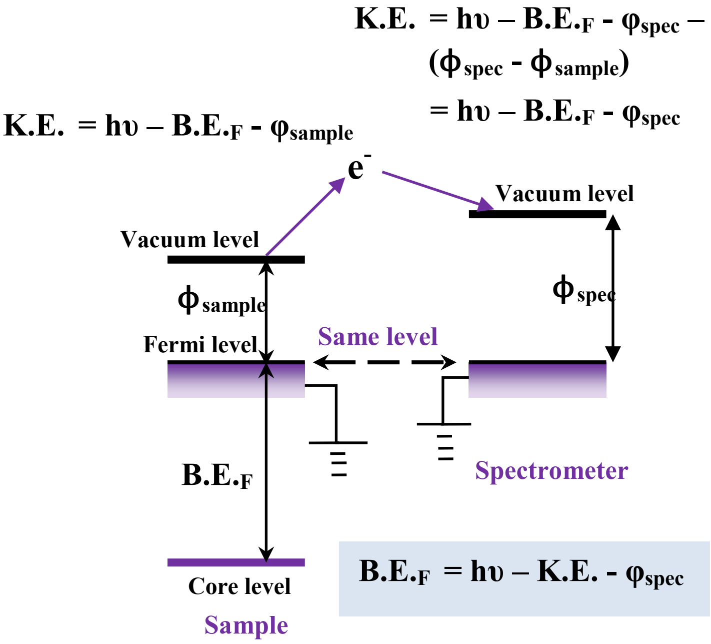

Figure 3.11. Schematic of the calculation of binding energy.

The basic mechanism behind an XPS instrument is illustrated in Figure 3.12.

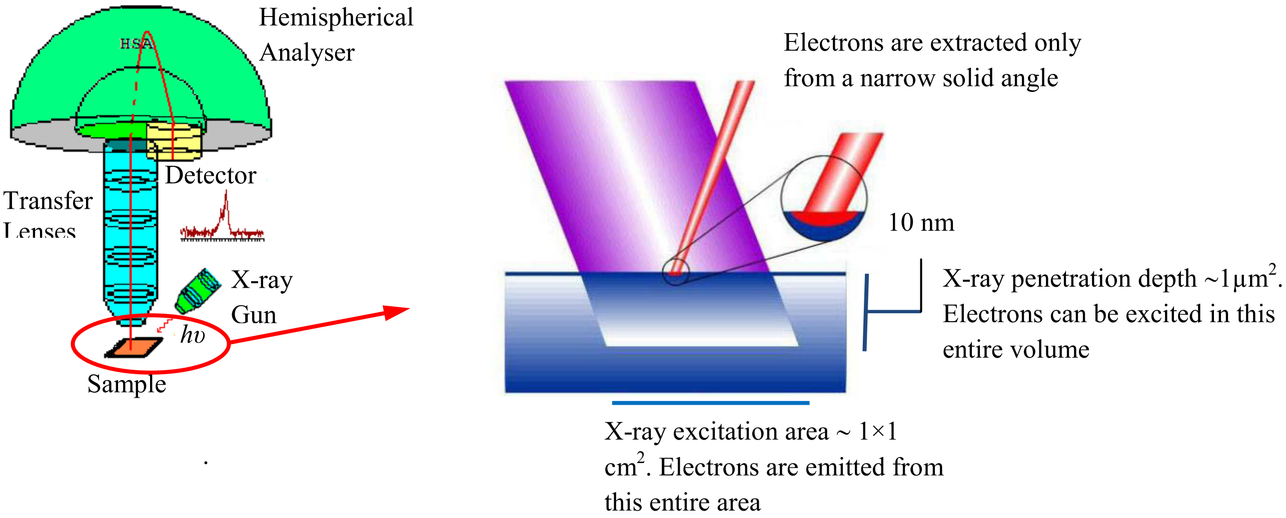

Figure 3.12. Schematic representation of XPS system.

Photons of a specific energy (MgKα: $h\upsilon = 1253.6$ eV; or AlKα: $h\upsilon = 1486.6$ eV) are used to excite the electronic states of atoms below the surface of the sample. Electrons ejected from the surface are energy filtered via a hemispherical analyser (HSA) before the intensity for a defined energy is recorded by a detector. Since core level electrons in solid-state atoms are quantized, the resulting energy spectra exhibit resonance peaks characteristic of the electronic structure for atoms at the sample surface. While the x-rays may penetrate deep into the sample, the escape depth of the ejected electrons is limited. That is, for energies around 1400 eV, ejected electrons from depths greater than 10 nm have a low probability of leaving the surface without undergoing an energy loss event, and therefore contribute to the background signal rather than well defined primary photoelectric peaks.

A typical XPS spectrum is a plot of the number of electrons detected (sometimes per unit time) (Y-axis, ordinate) versus the binding energy (X-axis, abscissa). Each element produces a characteristic set of XPS peaks at characteristic binding energy values that directly identify each element that exist in or on the surface of the material being analyzed. These characteristic peaks correspond to the electron configuration of the electrons within the atoms, e.g. 1s, 2s, 2p, 3s, etc. The number of detected electrons in each of the characteristic peaks is directly related to the amount of element within the area (volume) irradiated. To generate atomic percentage values, each raw XPS signal must be corrected by dividing its signal intensity (number of electrons detected) by a "relative sensitivity factor" (RSF) and normalized over all of the elements detected. The area under a peak in the spectrum is a measure of the relative amount of the element represented by that peak. The peak shape and precise position indicates the chemical state for the element. For p, d and f peaks, two peaks are observed. The separation between the two peaks is named spin orbital splitting. The values of spin orbital splitting of a core level of an element in different compounds are nearly the same. The peak area ratios of a core level of an element in different compounds are also nearly the same. Spin orbital splitting and peak area ratios assist in element identifications.

Note that, to count the number of electrons at each kinetic energy value, with the minimum of error, XPS must be performed under ultra-high vacuum (UHV) conditions because electron counting detectors in XPS instruments are typically one meter away from the material irradiated with X-rays. Detection limits for most of the elements are in the parts per thousand range. Detection limits of parts per million (ppm) are possible, but require special conditions: concentration at top surface or very long collection time (overnight). For most applications, it is, in effect, a non-destructive technique that measures the surface chemistry of any material.

3.3.3. Raman Spectroscopy

Introduction: Raman spectroscopy is a non-destructive and non-contact spectroscopic technique based on inelastic scattering of monochromatic light, usually from a laser source. Inelastic scattering means that the frequency of photons in monochromatic light changes upon interaction with a sample. Photons of the laser light are absorbed by the sample and then reemitted. Frequency of the reemitted photons is shifted up or down in comparison with original monochromatic frequency, which is called the Raman effect. This shift provides information about vibrational, rotational and other low frequency transitions in molecules. Raman spectroscopy is extremely information rich, (useful for chemical identification, characterization of molecular structures, effects of bonding, environment and stress on a sample).

Theory of Raman Spectroscopy: The Raman effect is based on molecular deformations in electric field E determined by molecular polarizability α. The laser beam can be considered as an oscillating electromagnetic wave with electrical vector E. Upon interaction with the sample it induces electric dipole moment $P = \alpha E$ which deforms molecules. Because of periodical deformation, molecules start vibrating with characteristic frequency υ_m. Amplitude of vibration is called a nuclear displacement. In other words, monochromatic laser light with frequency υ_0 excites molecules and transforms them into oscillating dipoles. Such oscillating dipoles emit light of three different frequencies (figure 3.13) when:

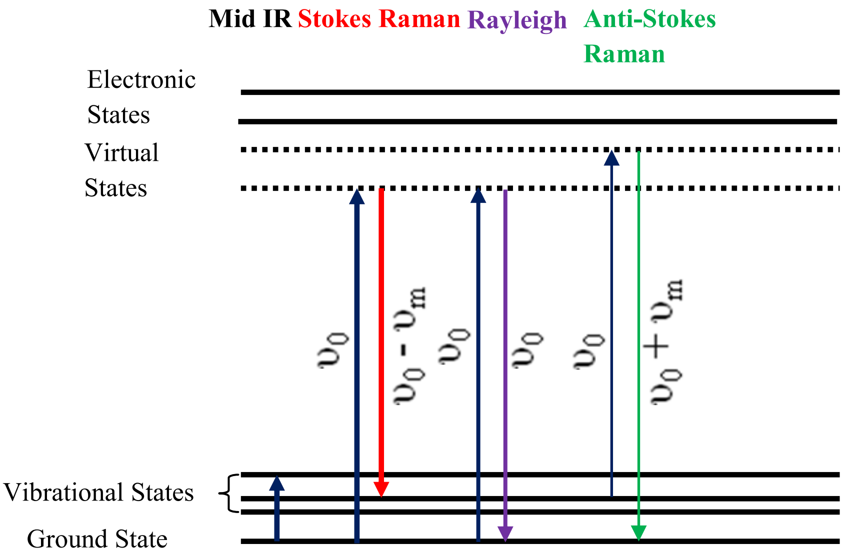

Figure 3.13. Energy level diagram showing the states involved in Raman signal. The line thickness is roughly proportional to the signal strength from the different transitions.

1. A molecule with no Raman-active modes absorbs a photon with the frequency υ_0. The excited molecule returns back to the same basic vibrational state and emits light with the same frequency υ_0 as an excitation source. This type of interaction is called an elastic Rayleigh scattering.
2. A photon with frequency υ_0 is absorbed by Raman-active molecule which at the time of interaction is in the basic vibrational state. Part of the photon's energy is transferred to the Raman-active mode with frequency υ_m and the resulting frequency of scattered light is reduced to $\upsilon_0 - \upsilon_m$. This Raman frequency is called Stokes frequency, or just "Stokes".
3. A photon with frequency υ_0 is absorbed by a Raman-active molecule, which, at the time of interaction, is already in the excited vibrational state. Excessive energy of excited Raman active mode is released, molecule returns to the basic vibrational state and the resulting frequency of scattered light goes up to $\upsilon_0 + \upsilon_m$. This Raman frequency is called AntiStokes frequency, or just "Anti-Stokes".

The incident photons will thus interact with the present molecule, and the amount of energy change (either lost or gained) by a photon is characteristic of the nature of each bond (vibration) present. Not all vibrations will be observable with Raman spectroscopy (depending upon the symmetry of the molecule.) but sufficient information is usually present to enable a very precise characterization of the molecular structure.

Note that about 99.999% of all incident photons in spontaneous Raman undergo elastic Rayleigh scattering. This type of signal is useless for practical purposes of molecular characterization. Only about 0.001% of the incident light produces inelastic Raman signal with frequencies $\upsilon_0 \pm \upsilon_m$. Spontaneous Raman scattering is very weak and special measures should be taken to distinguish it from the predominant Rayleigh scattering. Instruments such as notch filters, tunable filters, laser stop apertures, double and triple spectrometric systems are used to reduce Rayleigh scattering and obtain high-quality Raman spectra.

Instrumentation: A Raman system typically consists of four major components:

1. Excitation source (Laser).
2. Sample illumination system and light collection optics.
3. Wavelength selector (Filter or Spectrophotometer).

4. Detector (Photodiode array, CCD or PMT).

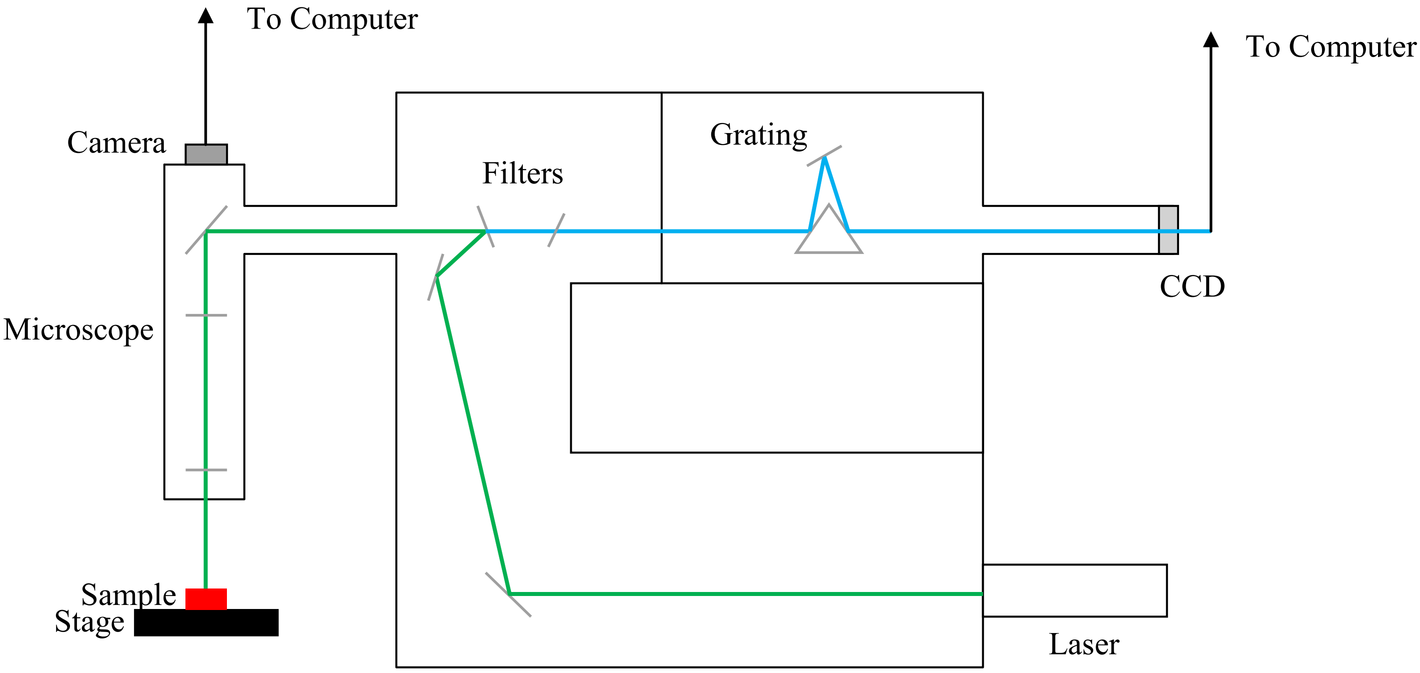

Figure 3.14. A typical Raman Spectrometer scheme.

A sample is normally illuminated with a laser beam in the ultraviolet (UV), visible (Vis) or near infrared (NIR) range. Scattered light is collected with a lens and is sent through interference filter or spectrophotometer to obtain Raman spectrum of a sample. Since spontaneous Raman scattering is very weak the main difficulty of Raman spectroscopy is separating it from the intense Rayleigh scattering. More precisely, the major problem here is not the Rayleigh scattering itself, but the fact that the intensity of stray light from the Rayleigh scattering may greatly exceed the intensity of the useful Raman signal in the close proximity to the laser wavelength. In many cases the problem is resolved by simply cutting off the spectral range close to the laser line where the stray light has the most prominent effect. People use commercially available interference (notch) filters which cut-off spectral range of ± 80-120 cm^{-1} from the laser line. This method is efficient in stray light elimination but it does not allow detection of low-frequency Raman modes in the range below 100 cm^{-1}. Stray light is generated in the spectrometer mainly upon light dispersion on gratings and strongly depends on grating quality. Raman spectrometers typically use holographic gratings which normally have much less manufacturing defects in their structure then the ruled once. Stray light produced by holographic gratings is about an order of magnitude less intense then from ruled gratings of the same groove density.

3.3.4. Quadrupole Mass Spectrometer

The mass spectrometer allows you to identify the masses of individual atoms and molecules that have been converted to ions from a given sample. This technique is unique in that it provides a fingerprint identification for the structural and chemical properties of these molecules. The quadrupole mass spectrometer is one of a specialized subset of mass spectrometers that measure background gases in an existing vacuum chamber. The spectrometer, AMETEK Dycor Dymaxion DM 100, used in this study is shown in figure 3.15.

A mass spectrometer consists of the following components:

- Sampling System
- Mass spectrometer
- Hardware Data System

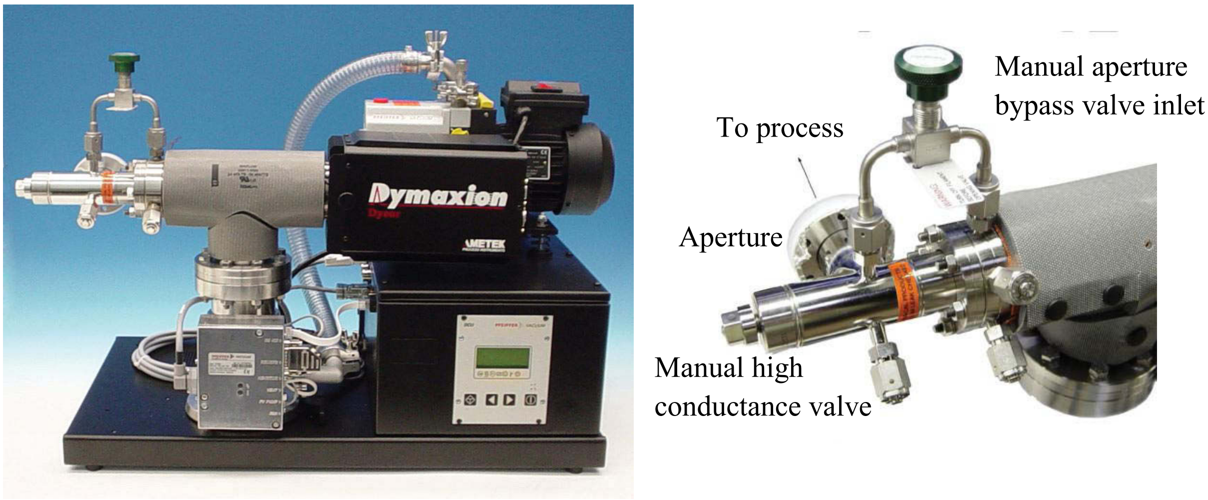

Figure 3.15. AMETEK Dycor Dymaxion Mass Spectrometer (DM 100).

Sampling System: The Sampling System serves as a connection between the outside sample environment and the vacuum environment of 10^{-4} to 10^{-9} Torr required by the mass spectrometer. If a sample is at the same operating pressure as the mass spectrometer, the spectrometer can be directly fitted into the sampling environment without an inlet with a differential pumping system. However, when the sample environment pressure is greater than

10^{-4} Torr, a pressure reduction sampling system is required. For these applications, a high conductance inlet (figure 3.15) can be fitted to the sample chamber. When the pressure in the sampling chamber is greater than 10^{-4} Torr (but below atmospheric pressure), the high conductance valve is closed tightly and the aperture inlet is opened. The aperture inlet consists of a small aperture within a valve that connects the sampling system to the vacuum environment of the mass spectrometer. The pressure in the test chamber, the diameter of the aperture, and the pumping speed determine the pressure of the Dymaxion.

Mass Spectrometer Hardware: Once the sample reaches the mass spectrometer hardware, three processes take place:

- Ionization
- Separation
- Detection

Ionization: During ionization, sample molecules are turned into ions which are then focused towards the quadrupole to be detected. The process occurs in the ionizer which consists of a filament, filament electron repeller, ionizer body, ion volume and two focusing lenses. Electron Ionization (EI) is the most common ionization technique. The electrons used for ionization are produced by passing a current through the filament (figure 3.16).

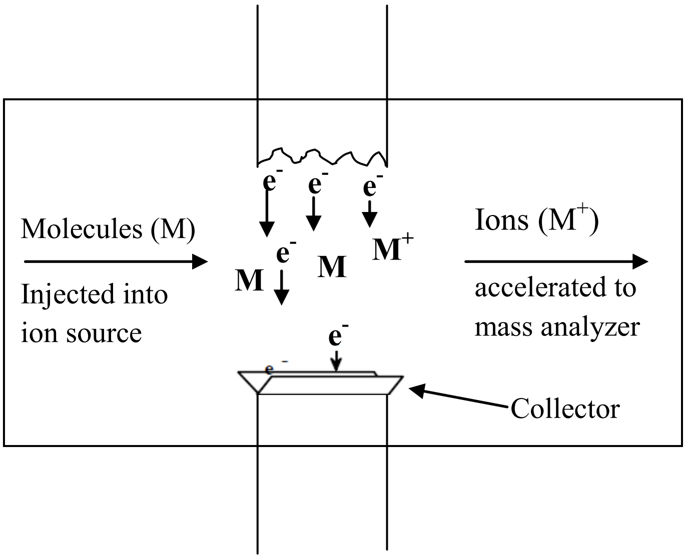

Figure 3.16. Electron ionization source.

The amount of current controls the number of electrons emitted by the filament. An electric field accelerates these electrons across the source region to produce a beam of high energy electrons. When an analyte molecule passes through this electron beam, a valence shell electron can be removed from the molecule to produce an ion. Ionization does not occur by electron capture, which is highly dependent upon molecular structure. Instead, EI produces positive ions by knocking a valence electron off the analyte molecule (figure 3.17).

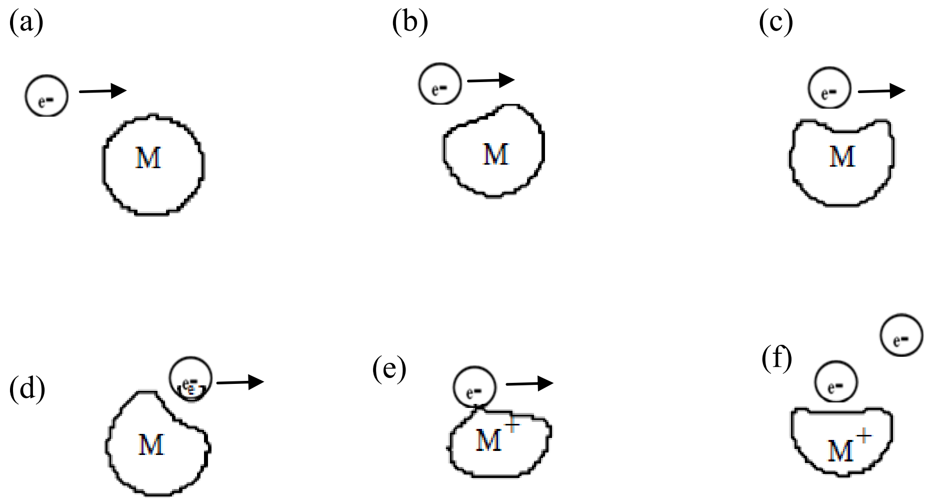

Figure 3.17. Electron Ionization Process. a) Ionizing electron approaches the electron cloud of a molecule, b) Electron cloud distorted by ionizing electron, c) Electron cloud further distorted by ionizing electron, d) Ionizing electron passes by the molecule, e) Electron cloud of molecule ejecting an electron, f) Molecular ion and ejected electron.

As the electron passes close to the molecule the negative charge of the electron repels and distorts the electron cloud surrounding the molecule. This distortion transfers kinetic energy from the fast-moving electron to the electron cloud of the molecule. If enough energy is transferred by the process, the molecule will eject a valence electron and form a radical cation (M^+).

Separation: Once the ions reach the quadrupole mass filter, they are filtered according to their mass-to-charge (m/z) ratio. Each ion has an identifiable mass. The quadrupole mass filter is constructed of four electrically-conducting, parallel cylindrical rods. The m/z value transmitted by the quadrupole is determined by the Radio Frequency (RF) and Direct Current (DC) voltages applied to the electrodes. These voltages produce an oscillating electric field that functions as a bandpass filter to transmit the selected m/z value. The RF voltage rejects or transmits ions according to their m/z value by alternately focusing them in different planes (figure 3.18).

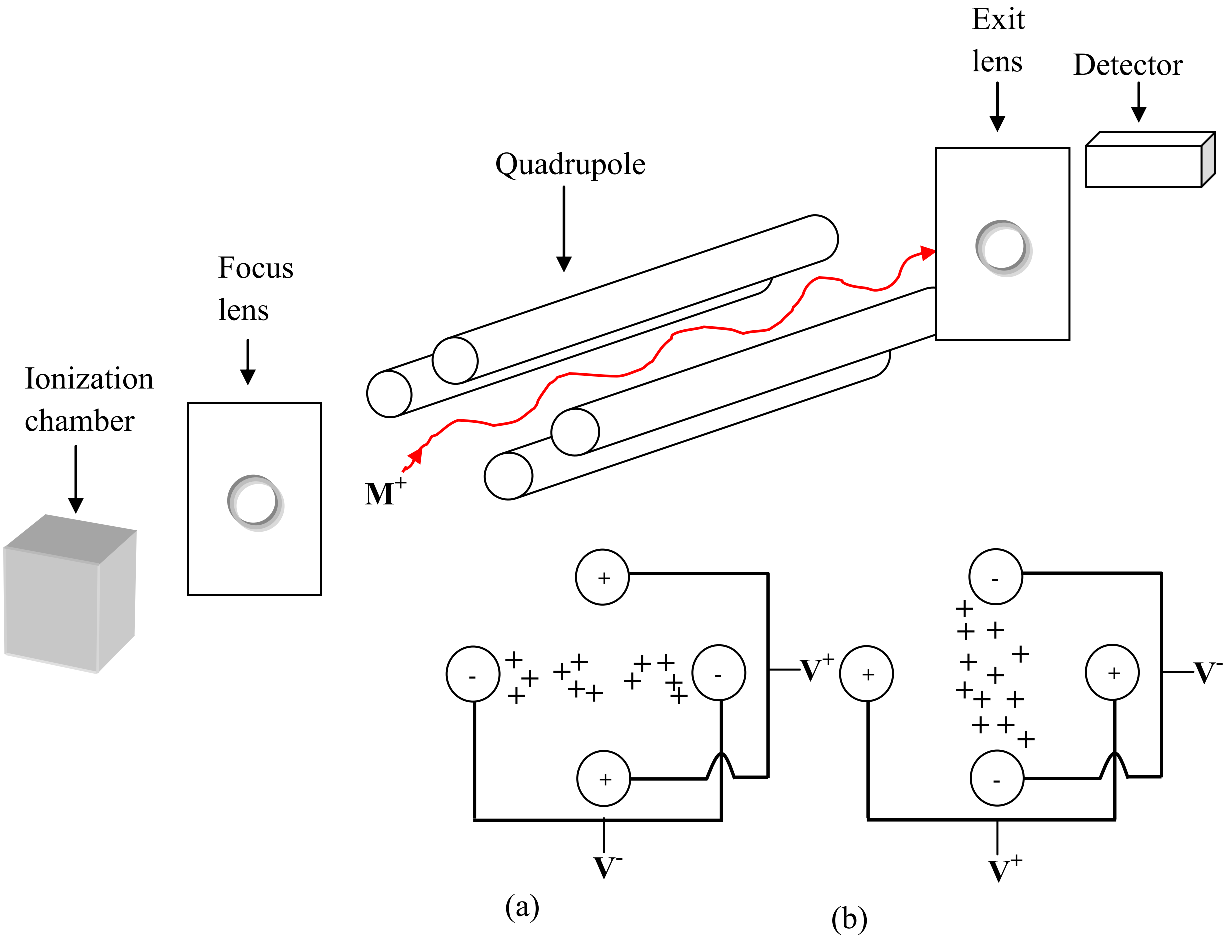

Figure 3.18. Quadrupole mass filter. (a) Ion focusing during first half of RF cycle, (b) Ion focusing during second half of RF cycle.

The four electrodes are connected in pairs and the RF potential is applied between these two pairs of electrodes. During the first part of the RF cycle the top and bottom rods are at a positive potential and the left and right rods are at a negative potential. This squeezes positive ions into the horizontal plane. During the second half of the RF cycle the polarity of the rods is reversed. This changes the electric field and focuses the ions in the vertical plane. The quadrupole field continues to alternate as the ions travel through the mass analyzer. This causes the ions to undergo a complex set of motions that produces a three-dimensional wave. The quadrupole field transmits selected ions because the amplitude of this three dimensional wave depends upon the m/z value of the ion, the potentials applied, and the RF frequency. By selecting an appropriate RF frequency and potential, the quadrupole acts like a high pass filter, transmitting high m/z ions and rejecting low m/z ions. The low m/z ions have a larger acceleration rate so the wave for these ions has larger amplitude. If this amplitude is great enough the ions will collide with the electrodes and can not reach the detector. The low m/z value cutoff of the quadrupole is changed by adjusting the RF potential or the RF frequency. Any ions with a m/z greater than this cutoff are transmitted by the quadrupole.

A DC voltage is also applied across the rods of the analyzer. This potential combined with the RF potential acts like a low pass filter to reject high m/z ions. Because they respond quickly to the changing RF field the motion of the low m/z ions is dominated by the RF potential. This motion stabilizes their trajectory by refocusing each time the RF potential changes polarity. Because low m/z ions are quickly refocused, the DC potential does not affect these ions. High m/z ions, however, do not refocus as quickly during the RF cycle. The DC potential has a greater influence on their trajectory and they slowly drift away from the center of the quadrupole. At the end of the analyzer, they are too far off-axis to strike the detector. The combination of high and low pass filters produced by the RF and DC potentials is adjusted to only transmit the selected m/z value. All ions above or below the set m/z value are rejected by the quadrupole filter. The RF and DC fields are scanned (either by potential or frequency) to collect a complete mass spectrum. Quadrupole mass analyzers are often called mass filters because of the similarity between m/z selection by a quadrupole and wavelength selection by an optical filter or frequency selection by an electronic filter.

Detection: The simplest detection setup consists of a Faraday cup detector. An electron multiplier is used for amplified sensitivity.

A Faraday cup detector is a closed structure except for an opening that allows the ions to enter. As the positive ions exit the quadrupole mass filter, they strike the detector, creating a current. This current is then sent to the preamplifier for amplification and then to the data system for display. When an electron multiplier is used, the ions are attracted to the multiplier because of its negative charge. As the ions strike the multiplier, secondary electrons are emitted. This creates a cascading effect as each secondary electron generates more secondary electrons as they move down the multiplier wall, amplifying the signal by approximately one thousand.

Data system: Overall control of the system, acquisition of data, and access to collected data is accomplished through the Dycor Process 2000 software. Adjustment of all instrument parameters that affect sampling, ionization, separation and detection are software controlled. All data acquisition parameters are also set using the software.

3.4. Patterning Technique: Photolithography

Photolithography uses light to transfer a geometric pattern from a photomask to a light-sensitive chemical "photoresist", or simply "resist," on the substrate. A series of chemical treatments then either engraves the exposure pattern into, or enables deposition of a new material in the desired pattern upon, the material underneath the photoresist. The steps involved in the photolithographic process are wafer cleaning, photoresist application, soft baking, mask alignment, exposure and development.

Cleaning and Photoresist application: In the first step, the wafers are chemically cleaned to remove particulate matter on the surface as well as any traces of organic, ionic, and metallic impurities. The wafer is then covered with positive photoresist (Microposit 1818) by spin coating. A viscous, liquid solution of photoresist is dispensed onto the wafer, and the wafer is spun rapidly to produce a uniformly thick layer. The spin coating typically runs at 6000 rpm for 30 seconds, and produces a layer of about 2.5 micrometres thick. The spin coating process results in a uniform thin layer, usually with uniformity of within 5 to 10 nanometres. This uniformity can be explained by detailed fluid-mechanical modelling, which shows that the resist moves much faster at the top of the layer than at the bottom, where viscous forces bind the resist to the wafer surface. Thus, the top layer of resist is quickly ejected from the wafer's edge while the bottom layer still creeps slowly radially along the wafer. In this way, any 'bump' or 'ridge' of resist is removed, leaving a very flat layer.

There are two types of photoresist: positive and negative. For positive resists, the resist is exposed with UV light wherever the underlying material is to be removed. Positive resists are sensitizer cross-linked within the resin. During exposition, the energy from the UV light dissociates the sensitizer and breaks down the cross-links and the resist therefore becomes more soluble in the developer. The exposed resist is then washed away by the developer solution, leaving windows of the bare underlying material (figure 3.19). In other words, "whatever shows, goes." The mask, therefore, contains an exact copy of the pattern which is to remain on the wafer.

Negative resists behave in just the opposite manner. Exposure to the UV light causes the negative resist to become polymerized, and more difficult to dissolve. Therefore, the negative resist remains on the surface wherever it is exposed, and the developer solution removes only the unexposed portions. Masks used for negative photoresists, therefore, contain the inverse (or photographic "negative") of the pattern to be transferred.

After depositing photoresist the wafer is prebaked to drive off excess photoresist solvent, typically at 90 to 100 °C for 30 to 60 seconds on a hotplate. Prebaking (Soft-baking) is the step during which almost all of the solvents are removed from the photoresist coating. Soft-baking plays a very critical role in photo-imaging. The photoresist coatings become photosensitive, or imageable, only after soft-baking. Over soft-baking will degrade the photosensitivity of resists by either reducing the developer solubility or actually destroying a portion of the sensitizer. Under soft-baking will prevent light from reaching the sensitizer. Positive resists are incompletely exposed if considerable solvent remains in the coating. This undersoft-baked positive resists is then readily attacked by the developer in both exposed and unexposed areas, causing less etching resistance.

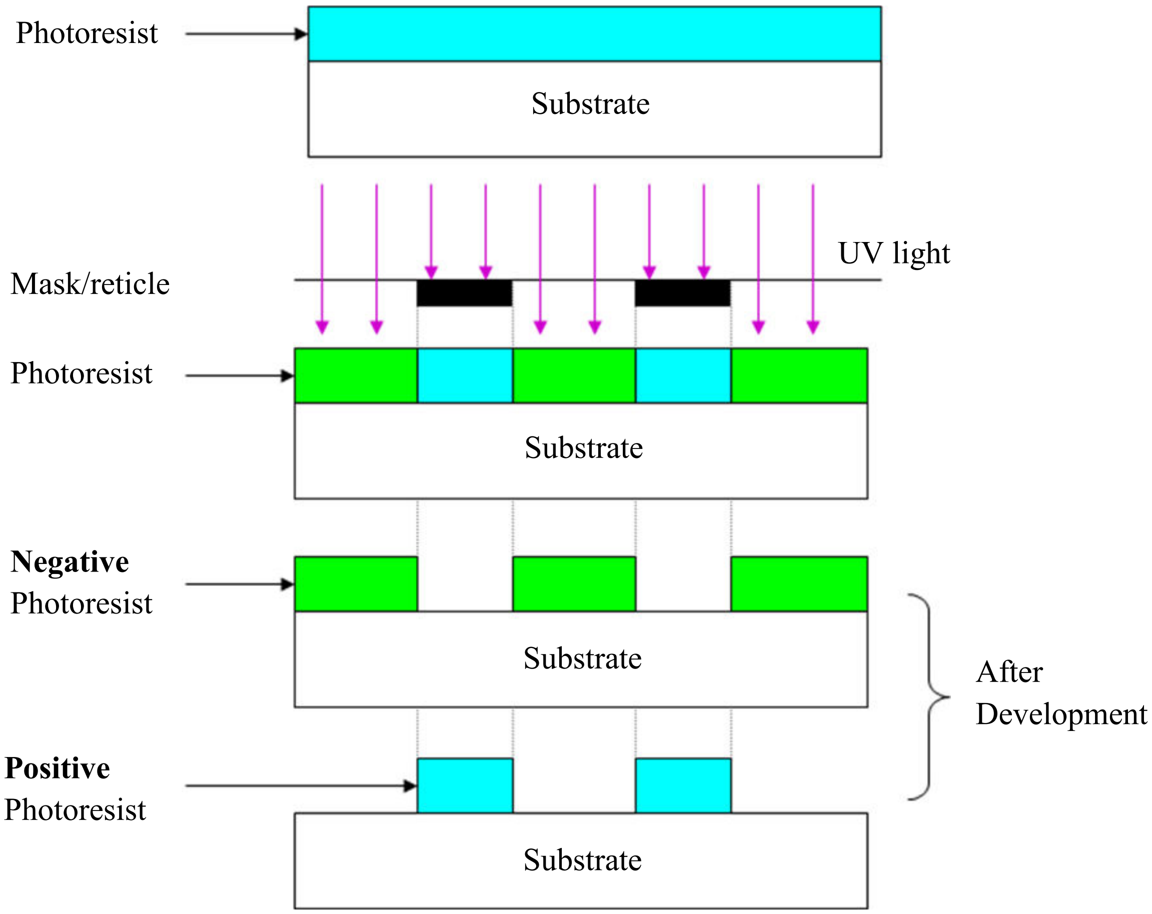

Figure 3.19. The main processes in the photolithography.

Mask alignment, Exposure and Development: One of the most important steps in the photolithography process is mask alignment. A mask or "photomask" is a square glass plate with a patterned emulsion of metal film on one side. The mask is aligned with the wafer, so that the pattern can be transferred onto the wafer surface. Each mask after the first one must be aligned to the previous pattern. Once the mask has been accurately aligned with the pattern on the wafer's surface, the photoresist is exposed through the pattern on the mask with a high intensity ultraviolet light. There are three primary exposure methods: contact, proximity, and projection. They are shown in the figure below.

Contact printing: The photoresist is exposed with UV light while the wafer is in contact position with the mask. Because of the contact between the resist and mask, very high resolution is possible in contact printing (e.g. 1-micron features in 0.5 microns of positive resist). The problem with contact printing is that debris, trapped between the resist and the mask, can damage the mask and cause defects in the pattern.

Proximity printing: The proximity exposure method is similar to contact printing except that a small gap, 10 to 25 microns wide, is maintained between the wafer and the mask during exposure. This gap minimizes (but may not eliminate) mask damage. Approximately 1- to 4-micron resolution is possible with proximity printing.

Projection printing: Projection printing avoids mask damage entirely. An image of the patterns on the mask is projected onto the resist-coated wafer, which is many centimeters away. In order to achieve high resolution, only a small portion of the mask is imaged. This small image field is scanned or stepped over the surface of the wafer. Projection printers that step the mask image over the wafer surface are called step-and-repeat systems. Step-and-repeat projection printers are capable of approximately 0.2- to 1-micron resolution.

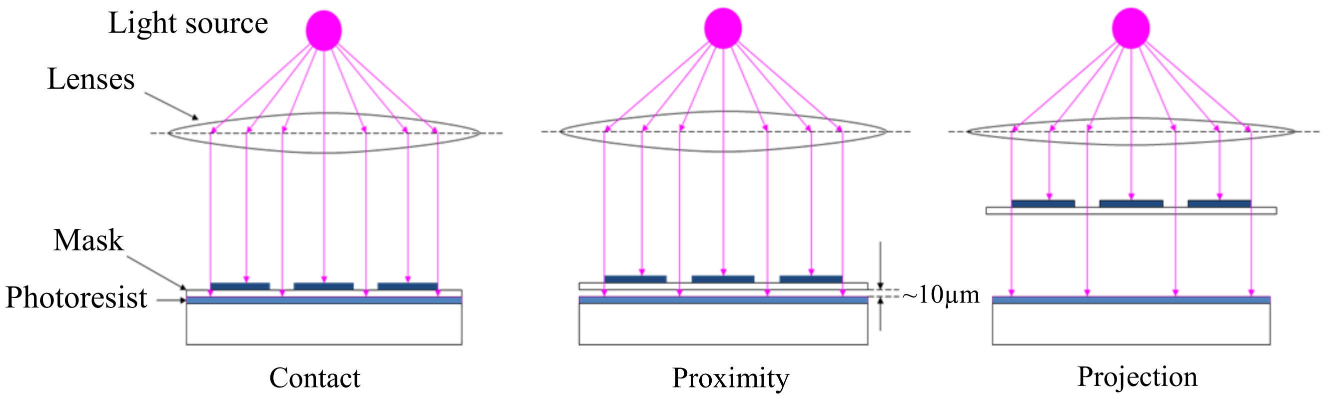

Figure 3.20. Primary exposure methods in photolithography.

For proximity and contact printing

Resolution = $\sqrt{\{\lambda(\text{gap between mask and resist + resist thickness})\}}$

where λ is the wavelength of the illuminating radiation.

For projection printing

Resolution = $(Ka \times \lambda) / NA$; Depth of focus = $(Kb \times \lambda) / (NA)^2$

where Ka is a process constant ~ 0.75, Kb is a process constant ~ 0.5,

NA is the numerical aperture of the optical system.

One of the last steps in the photolithographic process is development. The exposure to light causes a chemical change that allows some of the photoresist to be removed by developer solution. Positive photoresist, the most common type, becomes soluble in the developer when exposed; with negative photoresist, unexposed regions are soluble in the developer. Mostly metal-ion-free developers such as tetramethylammonium hydroxide (TMAH) are used.

Bibliography

Barrat, S., Saada, S., Dieguez, I. & Bauer-Grosse, E. **1998** *J. Appl. Phys.* 84, 1870.

Corat, E. J. & Goodwin, D. G. **1993** *J. Appl. Phys.*, 74, 2021.

DebRoy, T., Tankala, K., Yarbrough, W. A. & Messier, R. **1990** *J. Appl. Phys.*, 68, 2424.

Gheeraert, E. **1992**, Ph.D. thesis, Université Joseph Fourier, Grenoble, France.

Harris, S. J., Belton, D. N., Weiner, A. M. & Schmieg, S. J. **1989** *J. Appl. Phys.*, 66, 5353.

Harris, S. J., Weiner, A. M. & Perry, T. A. **1988** *Appl. Phys. Lett.*, 53, 1605.

Lieberman, M. A. & Lichtenberg, **1994** *Principles of Plasma Discharges and Materials Processing*. Wiley.

Matthews, J. W. **1975** *Epitaxial growth*. Academic.

Teraji, T. 2008 *Physics and applications of CVD diamond*. Wiley.

Tsang, R. S. **1997** Ph.D. Thesis, University of Bristol, United Kingdom.

Wahl, E. H., Owano, T. G., Kruger, C. G., Zalicki, P., Ma, Y. & Zare, R. N. **1996** *Diamond Relat. Mater.* 5, 373.

Wu, C. –H., Tamor, M. A., Potter, T. J. & Kaiser, E. W. **1990** *J. Appl. Phys.*, 68, 4825.

CHAPTER 4

In Search of Conditions for Diamond Nanowire Growth

Résumé

Le premier objectif de cette thèse était d'obtenir un état reproductible pour la croissance des nanofils de diamant. Les voies qui ont été explorées à cet effet peuvent être résumées comme suit:

1. Filament chaud et un traitement au plasma de nanotubes de carbone dispersés,

2. Traitement à chaud de filaments de nanotubes de carbone dispersés de catalyseur,

3. Enquête de croissance mécanisme vapeur-liquide-solide en utilisant comme précurseur de carbone du méthane et du Ni en tant que catalyseur,

4. Enquête sur les mécanismes de croissance solide-liquide-solide en utilisant des substrats de diamant en vrac comme seule source de carbone et d'Ni en tant que catalyseur.

Ce chapitre présente les résultats et la discussion de l'enquête sur toutes les routes de croissance mentionnés ci-dessus.

Pour la croissance des nanofils de diamant nous avons commencé à étudier le processus proposé par Sun *et al.* en 2005 pour la croissance de nanofils de diamant par un plasma d'hydrogène après le traitement de nanotubes de carbone multiparoies sans catalyseur métallique. Afin de promouvoir la nucléation du diamant sur les nanotubes, notre objectif était d'utiliser des conditions qui induisent une attaque faible, voire négligeable de nanotubes, c'est à dire, les conditions pour lesquelles la croissance de nanotubes est en équilibre avec la gravure de formes de carbone sp^2 par l'hydrogène atomique. Cela augmente la concentration de charbon actif à la surface des nanotubes et favorise la nucléation des agrégats de carbone. Pendant le traitement de la nucléation de carbone sp^2 serait supprimée par l'hydrogène atomique, et la gravure de nanotubes serait réduit par les conditions expérimentales appropriées, permettant la nucléation de diamant lent à se produire. Afin de réduire nucléation spontanée pas de méthane a été ajouté; carbone adsorbé devrait venir du nanotube lui-même.

Pour l'enquête, les nanotubes de carbone purifiés commerciaux ont été dispersés sur des substrats de silicium puis, leur stabilité sous filament chaud ainsi que l'environnement de plasma a été étudié de manière approfondie. Des expériences ont été réalisées sous atmosphère d'hydrogène en un filament chaud CVD assistée plasma micro-ondes et d'un réacteur CVD assisté à l'aide conventionnelle température de croissance du diamant et de la pression. À partir de l'étude de filament chaud, une fenêtre de stabilité pour des nanotubes a été identifié en fonction de la température du filament (T_f):

- T_f = 1900-2000 ° C: gravure très élevée des nanotubes, la quasi-totalité des nanotubes disparu du substrat après 1 heure de traitement,
- 2000 ° C $<T_f \leq$ 2200 ° C: gravure Peu ou pas de nanotubes,
- 2300 ° C-2400 ° C: tendance très élevé de conversion de nanotubes de matériau polycristallin.

Le comportement de gravure de nanotubes de plasma micro-ondes était plus ou moins similaire à celle dans le traitement filament chaud: à basse température (700-800 ° C), plus la gravure et vice-versa.

Étude plus approfondie dans la plage de températures, T_f: 2100-2200 ° C, conduit à la croissance de plusieurs nano-objets sur / et à partir de nanotubes, comme nanocristaux, des nanofils et nanospikes. La densité extrêmement faible et très faible reproductibilité de ces nano-objets en leur caractérisation très difficile et, par conséquent, leur nature exacte et l'origine n'a pas été possible d'identifier. En outre, un objet de forme ronde a été observée au bout de nanofils suggérant catalyseur assistée par la croissance des nanofils. Comme aucun catalyseur métallique a été ajouté dans le procédé, la source de ce catalyseur peut être des contaminants présents dans les nanotubes commerciaux ou le filament de tungstène utilisé au cours du processus. Nous avons donc mis l'accent sur catalyseur traitement assisté par des nanotubes, où un film mince de Ni a été déposé intentionnellement sur les nanotubes, et elle a entraîné la croissance des nanofils. Toutefois, l'analyse Raman a montré que des pics caractéristiques des matériaux de Si suggérant contamination de Si dans le processus. Hot-filament traitement des nanotubes dans un environnement exempt Si, nanotubes étant dispersés sur des substrats de diamant en vrac, n'a montré aucune croissance des nanofils ce qui suggère que la contamination Si pourrait jouer un rôle important dans la croissance des nanofils.

Afin de promouvoir la croissance des nanofils de diamant, le méthane a été ajouté au cours du processus de catalyseur au nickel sur le diamant dans un environnement exempt de silicium, créant les conditions d'un mécanisme de croissance vapeur-liquide-solide. Avec les conditions les plus favorables, en utilisant 2 vol.% et 1% vol. CH_4 consécutivement à une course unique disposition, la croissance des nanofils longs, emmêlés et très dense a été observé sur le substrat de diamant. Microscopie électronique à transmission montre une forme tubulaire des nanofils avec une épaisseur de paroi d'environ 50 nm, et une sélection de modèles de diffraction d'électrons région de révéler la structure graphitique des nanofils. Aucune phase cristalline du diamant a été observée, même si une partie des nanofils ont été identifiés comme du carbone sp3. La conclusion est que dans les conditions expérimentales étudiées, avec ou sans catalyseur, aucun nanofil diamant ne peut être élaboré. Nous n'avons pas réussi à la reproduction de la démarche proposée par Sun *et al.* en 2005, de même qu'aucun autre groupe de recherche.

D'autre part, en l'absence de méthane ajouté dans la phase gazeuse, la gravure de diamant par des nanoparticules métalliques générés à partir du film de métal évaporé initialement été observée. En raison de l'importance de ce processus technologique dans des applications à base de diamant, le deuxième objectif de cette thèse, qui sont présentés dans le chapitre 4 était alors d'explorer ce phénomène gravure intéressant pour développer une technique de gravure simple, rapide et rentable pour la fabrication de nanostructures orientées (nanopores) dans les membranes de diamant.

4.1. Investigation of the Growth Mechanism Proposed by Sun *et al.*

At the start of our study the only experimental work available for diamond nanowire growth by chemical vapour deposition was reported by **Sun *et al.*** (**2005**). Aiming at synthesizing diamond nanowires (DNWs), we primarily investigated their proposed mechanism for diamond nanowire growth.

As discussed in Chapter 1, Section 1.2, Sun *et al.* successfully synthesized chain-like DNWs with ultrahigh equivalent diamond nucleation density ($>10^{11}/cm^2$) and single-crystal DNWs with diameters of 4-8 nm and with lengths up to 200 nm by hydrogen plasma post-treatment of mutiwalled carbon nanotubes (MWCNTs), no catalyst being used. The diamond nanowires were identified to have a core-sheath structure with the inner core being diamond crystal and outer shell being amorphous carbon. To explain the growth mechanism they proposed a four-step process: clustering, crystallization, growth and faceting, and nanowire growth, which is similar to that proposed by **Singh** (**1994**) for the diamond nucleation, crystallization and growth from amorphous carbon precursor. The proposed model is shown schematically in figure 4.1.

i. clustering
ii. crystallization
iii. growth and faceting
iv. nanowire growth

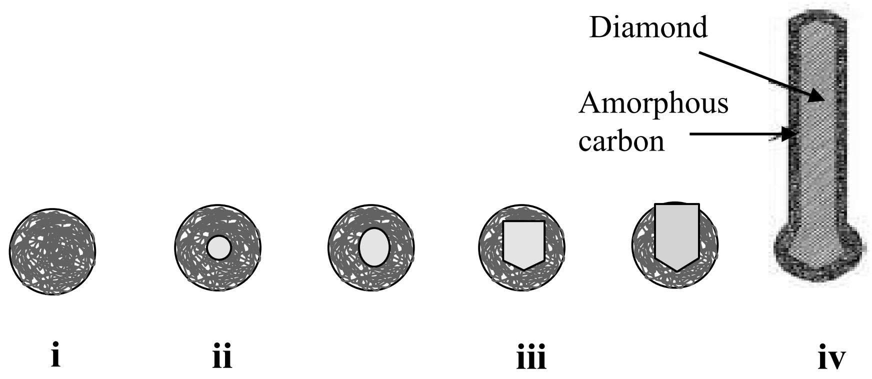

*Figure 4.1. The proposed model for the formation of nanodiamonds, and the growth of diamond nanowires under hydrogen plasma irradiation of MWCNTs at high temperatures. Amorphous carbon clusters are formed in step i. The crystallization of diamond begins in the core of the carbon clusters (step ii), followed by the diamond growth and faceting stage (step iii). After the diamond nanocrystallites are faceted, diamond nanowires begin to grow at the nanodiamond tips (step iv). (**Sun et al. 2005**).*

According to the model, during hydrogen plasma treatment of MWCNTs at high temperature, hydrogen atoms attack nanotubes preferably at the defective sites where there are graphite edges and form reactive hydrocarbons in the vicinity of the surface of the original nanotube framework. The hydrocarbons are again deposited back to the original sites to generate amorphous carbon clusters. The crystallization subsequently occurs, which is mediated by the insertion of hydrogen atoms into the loosely bound amorphous carbon matrix or strained C–C bonds as the hydrogen atoms diffuse through the amorphous carbon similar to the crystallization in amorphous silicon (**Wagner & Ellis, 1996**). The hydrogen termination plays an important role in the diamond crystallization and growth. (**Menon *et al.* 2000**) Once the diamond crystallites reach the critical size, diamond grows via a surface growth mechanism (**Angus & Hayman, 1998**), whereas the sp^2 phase is etched by atomic hydrogen and the buried crystallites expose themselves for further diamond nanowire growth through growth and faceting stage. This means that diamond nanowires actually undergo a vapour-solid growth process, although no additional hydrocarbon gas is introduced into the reaction chamber. At the same time, the size effect at the tip of nanowires makes the tip more reactive and enhances atomic absorption, diffusion, deposition and reconstruction (**Lee *et al.* 2000**), thus favoring the growth of diamond nanowires along one dimension and in a favorable crystalline orientation. On the other hand, the amorphous carbon matrix which sheathes the diamond nanoparticles favors the formation of a layer of a stable graphite sp^2 structure in one dimensional growth. However, the competition between the formation of sp^2 structure and diamond nucleation under hydrogen plasma irradiation forms and stabilizes the precipitation-induced outer amorphous carbon sheath ultimately to prevent further lateral growth of diamond.

From the proposed model it is obvious that both diamond nuclei and amorphous carbon networks, which sheath both the diamond nanoparticles and nanowires preventing the lateral growth of diamond, are very important for the growth of diamond nanowires. Carbon nanotubes provide an easy way to achieve high-density diamond nanoparticles embedded in an amorphous matrix. The amorphous carbon matrix provides the carbon source for the growth of diamond nanowires. Since there was no additional carbon source in the experiment, it seems to imply that less carbon source is needed to grow diamond nanowires than that needed to grow diamond films by chemical vapor deposition. The high substrate temperature should also be an important factor in the formation of diamond particles. Theoretical modeling and computation showed (**Gamarnik, 1996**) that the critical size of diamond decreases with increasing substrate temperature, thus a high substrate temperature has been shown to favor diamond formation. The experimental results and theoretical analysis on the transformation of graphite to diamond under intense electron beam irradiation (**Zaiser *et al.* 2000**) also showed that a high sample temperature is needed to perform the transformation, otherwise, amorphous carbon nanorods would form (**Chen *et al.* 2001**).

In order to investigate the growth model discussed above, we treated both home-grown and commercial MWCNTs under hot-filament as well as plasma environment. For the selection of CNTs important parameters were the density, homogeneity and spurious phase concentration (catalyst and other forms of carbon). Experiments were performed under hydrogen atmosphere in a Hot-Filament assisted CVD (HFCVD) and a Microwave Plasma assisted CVD (MPCVD) system using conventional diamond growth temperature and pressure. In order to promote diamond nucleation on carbon nanotubes, the idea is to search for conditions that induce a weak or no etching of nanotubes, i.e. conditions for which the growth of carbon nanotubes is balanced with the etching of sp^2 by atomic hydrogen. If the activated carbon concentration at the surface of nanotubes is high enough diamond nucleation will occur. During the treatment the nucleation of sp^2 forms of carbon will be suppressed by atomic hydrogen, and the etching of nanotubes will be reduced by the appropriate experimental conditions, allowing slow nucleation of diamond to occur. In order to reduce spontaneous nucleation no methane will be added; adsorbed carbon will have to come from the nanotube itself.

4.1.1. Home-Grown CNTs: Growth and Treatment

Various MWCNTs differing in dimensions and distributions were grown on silicon substrates. Key parameters for the growth process were the filament temperature, substrate temperature, methane concentration in hydrogen, pressure and filament-substrate distance (typically 10-12 mm).

The process consists of four stages: catalyst evaporation, annealing, carbonization, and deposition. The heating cycle of the HFCVD process is shown schematically in figure 4.2.

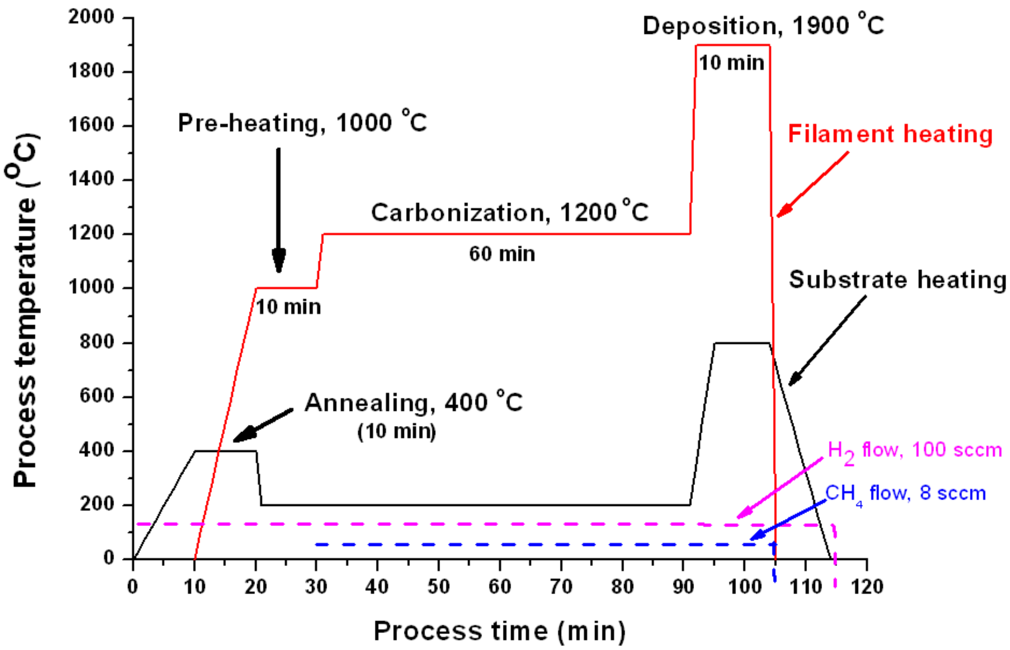

Figure 4.2. A schematic of the heating cycle of HFCVD for CNT growth.

By varying catalyst type and thickness, we were able to grow MWCNTs of different forms: nanotube forest (vertically aligned, very high density), uniform (horizontal growth) and relatively dense, and non-uniform and less dense (figure 4.3). Following an optimization period the following parameters were chosen (Table 4.1).

Table 4.1. Experimental parameters for CNT deposition

Type	Filament Temp, (°C)	Substrate Temp, (°C)	CH_4 flow rate (sccm)	H_2 flow rate (sccm)	Deposition Time (min)	Catalyst Type and Thickness
Forest	1920	800	8	100	15	Ti 0.5 nm,Co 0.5 nm*[1]
High density	1920	800	8	100	15	Co 3 nm
Low density	1920	800	8	100	15	Ni 1 nm,Co 2 nm*[2]

*[1] *Ti evaporation was followed by Co evaporation;* *[2] *Ni evaporation was followed by Co evaporation*

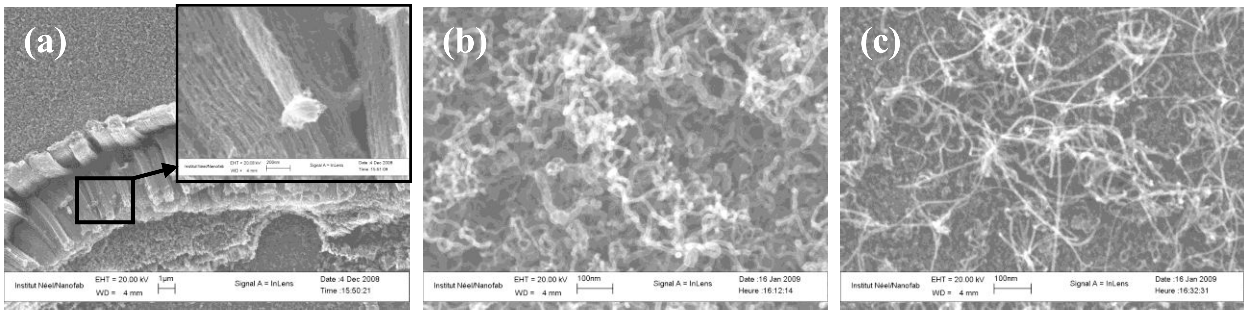

Figure 4.3. SEM images of carbon nanotubes of (a) forest type, (b) uniformly distributed and highly dense and (c) non-uniform and less dense, grown on mirror polished Si substrates by HFCVD.

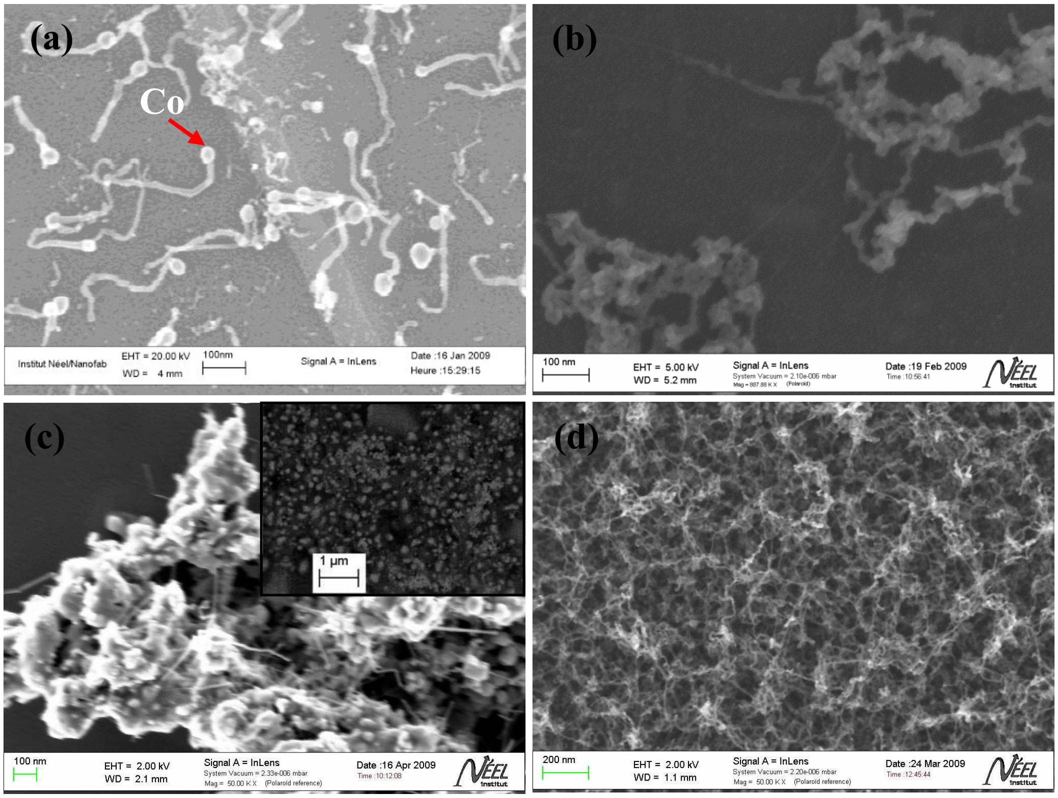

Figure 4.4. SEM images of hot-filament treated home-grown CNTs after 60 min of treatment; (a, b) non-uniform and less dense CNTs treated at 1900 and 1950 °C respectively, (c, d) uniform and highly dense CNTs treated at 1900 and 1950 °C respectively. The inset of (c) is a SEM image recorded by In-lens energy and angle selective backscatter detector (EsB), showing the presence of metal catalyst (Co) used for growth of CNTs. For all cases, substrate temperature was 800 °C.

However, nanotube forest was not suitable for further treatment as it was assumed that the high nanotube density could make the hydrogen diffusion inside the forest very low. On the other hand, the results obtained from first few treatment experiments of horizontal nanotubes of different density, as shown in figure 4.4, were not encouraging for further treatment as the catalyst remaining on the surface was too high that could induce a very complicated chemistry during hydrogen treatment. It was then assumed that the use of commercial purified carbon nanotubes as dispersed on silicon substrates could solve the problem to a large extent.

4.1.2. Dispersed CNTs: Specification and Dispersion

Two types of MWCNTs with different length, diameter and purity (Table 4.2), were purchased from Sigma-Aldrich. The nanotubes were dispersed onto the clean mirror polished Si (100) substrates. For dispersion nanotubes were first put into a solvent (dicholoro ethylene) and then ultrasonification was performed for 15 minutes at room temperature with 40 Watt ultrasonic power. Then a droplet containing nanotubes was added onto a silicon substrate by using pipette and kept the substrate to be dried out itself for 5-10 min.

Table 4.2. Specification of MWCNTs purchased from Sigma-Aldrich.

Specification	CNT-1	CNT-2
Growth method	**CVD**	**CVD**
Diameter (nm)	**O.D*: 110-170**	**O.D*: 6-13**
Length (µm)	**5-9**	**2.5-20**
Purity (%)	**90+**	**> 99**

**O.D: Outer diameter*

Generally carbon nanotubes are strong and flexible but very cohesive. They are difficult to disperse into liquids such as water, ethanol, oil, polymer or epoxy resin. Ultrasound is an effective method to obtain discrete, single and dispersed carbon nanotubes. The liquid jet streams resulting from ultrasonic cavitation, overcome the bonding forces between the nanotubes, and separate the tubes.

The solvent, dichloro ethylene (DCE), was found to be more effective for nanotube dispersion than other solvents such as water, dichloro ethane, dichloro ether etc.

The dispersion of carbon nanotubes was performed in clean room with good care in order to avoid possible contaminations from atmosphere and other solvents. To determine the dispersion quality (uniformity, and number of CNTs), samples were observed by the field emission gun scanning electron microscope (FESEM), figure 4.5.

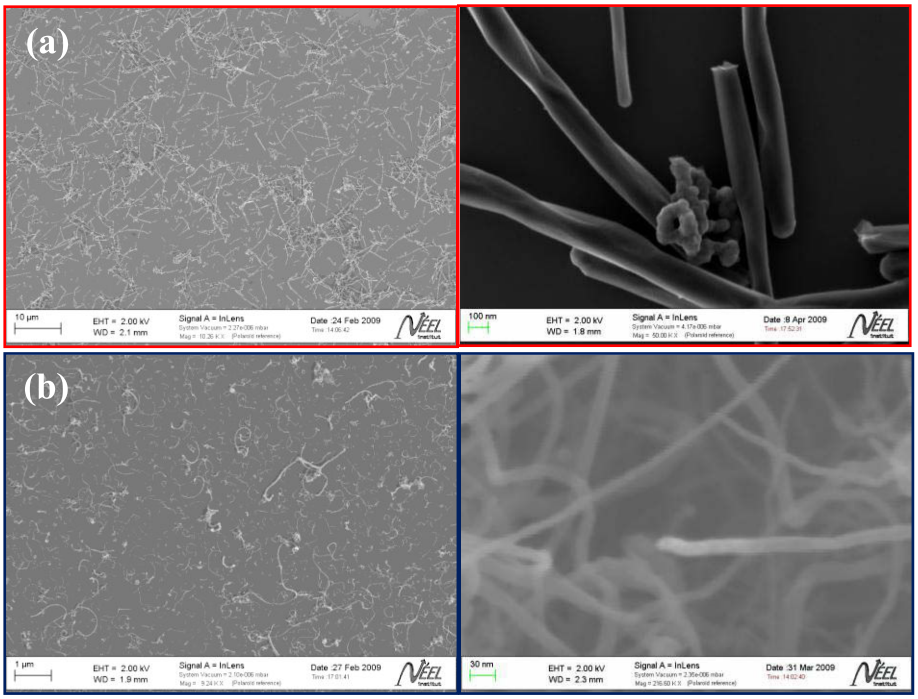

Figure 4.5. SEM images of dispersed (a) CNT-1 and (b) CNT-2 on Si; right panels are the enlarged images of the corresponding panels.

4.1.3. Hot-Filament Treatment of Dispersed CNTs

The dispersed samples (CNT-1, CNT-2) were treated under hot-filament and hydrogen environment in the HFCVD reactor with following parameters: 1900-2400 ^{o}C filament temperature (T_f); 850 ^{o}C substrate temperature (T_s); 30 Torr hydrogen pressure (P_{H2}); 1-4 hours treatment time. A schematic of the process is shown in figure 4.6.

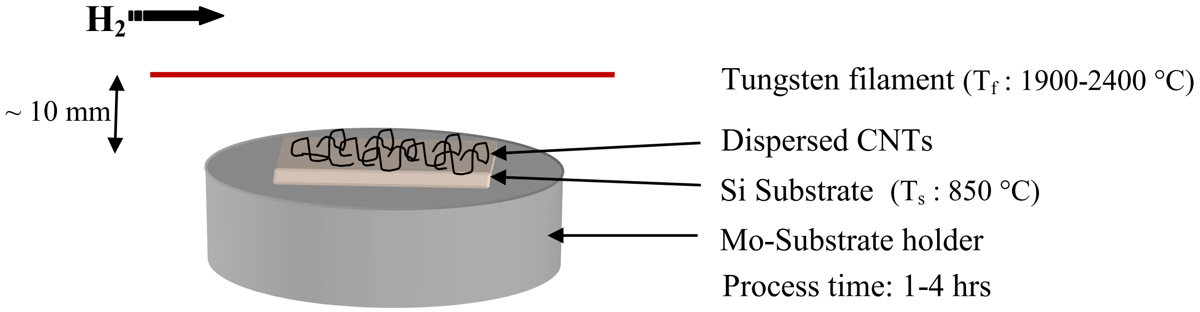

Figure 4.6. Schematic of the hot-filament treatment process of the dispersed CNTs.

Before the treatment, high vacuum (<10^{-6} Torr) was generated inside the reactor by pumping out the residual gases. Hydrogen was then introduced into the reactor with 100 sccm flow (sccm denotes standard cubic centimeter per minute at STP). The treatment process started with the heating of the substrate at 200 °C for 10 min in order to remove any contaminant such as water, organic substances etc. present on the substrate holder and/ substrate. The filament was also cleaned through heating it at 1000 °C for 10 min. Finally, both the filament and the substrate temperature were increased in together to the treatment conditions. After treatment samples were cooled down in flowing hydrogen for 30 min. The heating cycle of the process is shown schematically in figure 4.7.

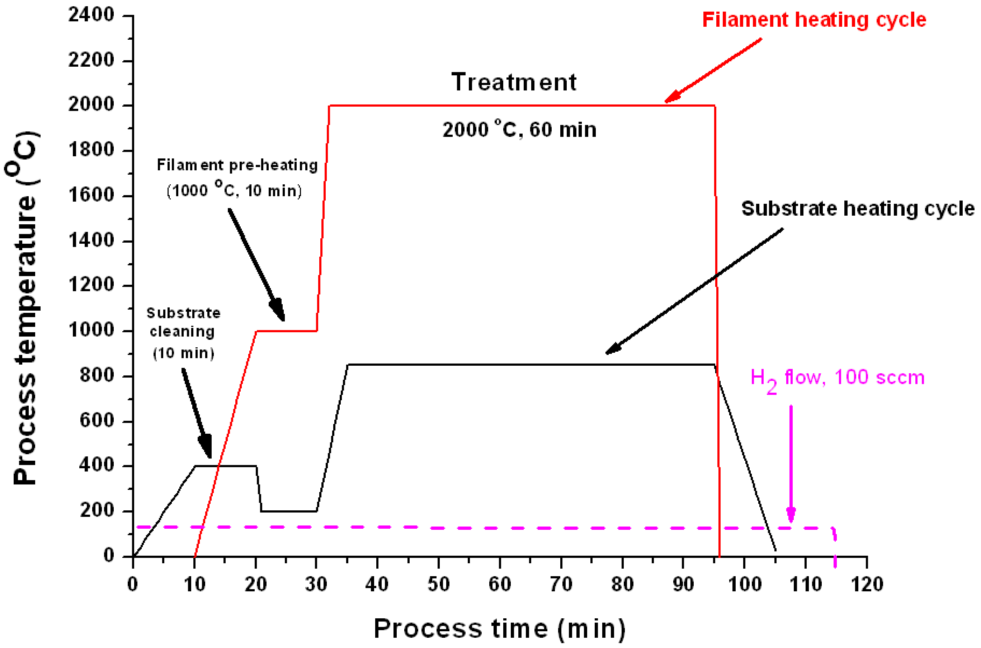

Figure 4.7. A schematic of the heating cycle of HFCVD used for the treatment of dispersed CNTs.

Treated samples were characterized by scanning electron microscope (SEM), Raman Spectroscopy and cathodoluminescence.

4.1.3.1. Hot-filament activity: Results and discussion

Low filament temperature (1900-1950 °C): Figures 4.8 and 4.9 show the effect of low filament temperature (1900-1950 °C) on CNT-1 and CNT-2 samples respectively.

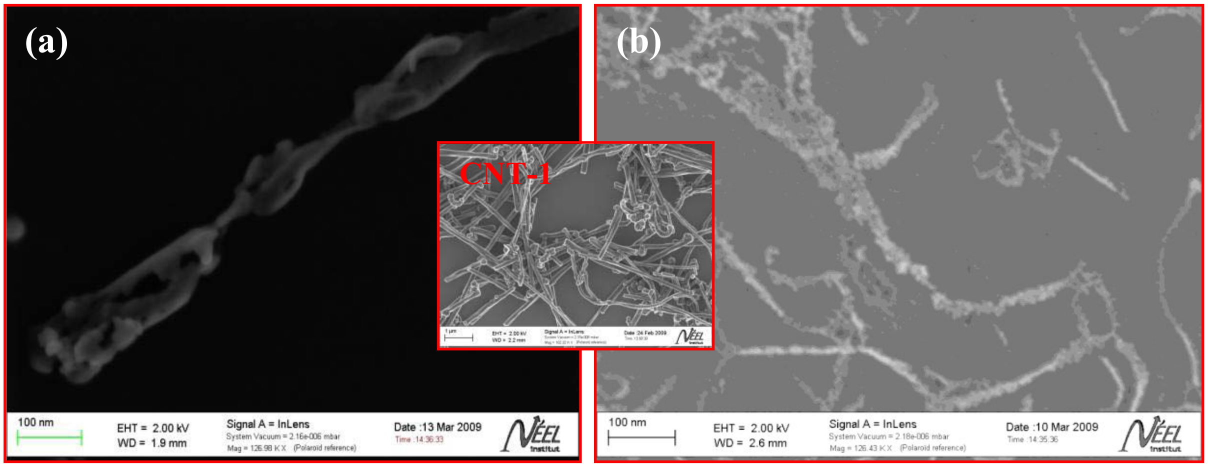

Figure 4.8. SEM images of CNT-1 samples after 60 min treatment at filament temperature of (a) 1900 °C and (b) 1950 °C, (Ts:850 °C, P_{H2}: 30 Torr); the inset is the SEM image of CNT-1 before treatment.

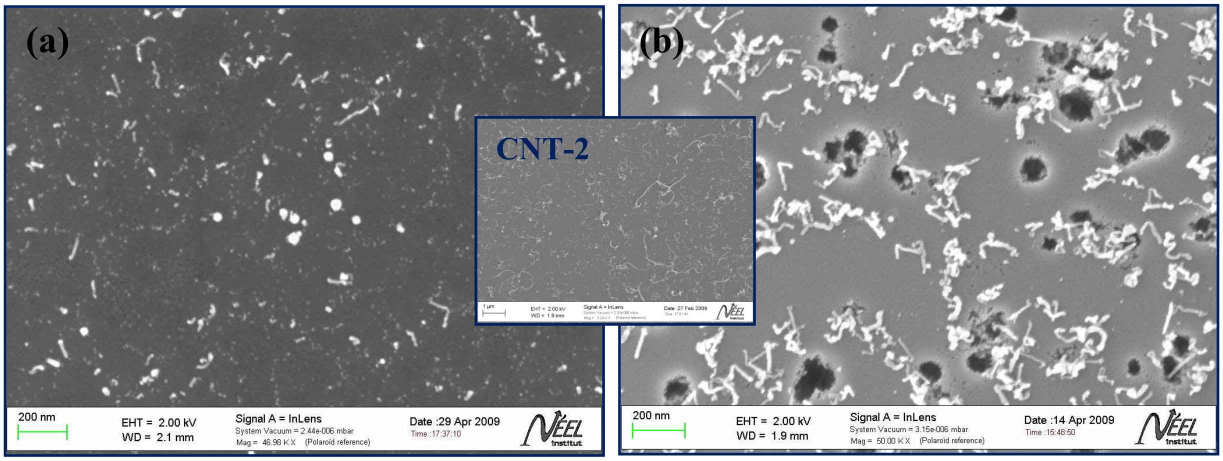

Figure 4.9. SEM images of CNT-2 samples after 60 min treatment at filament temperature of (a) 1900 °C and (b) 1950 °C, (Ts:850 °C, P_{H2}: 30 Torr); the inset is the SEM image of CNT-2 before treatment.

After 60 min treatment at filament temperatures of 1900 and 1950 °C original nanotubes disappeared and only amorphous carbon /and carbon nanoparticles were observed on the Si substrates. The observation suggests that the etching of CNTs is very strong at this temperature range.

High filament temperature (2000-2400 °C): Figures 4.10 and 4.11 show the effect of high filament temperature on CNT-1 and CNT-2 samples respectively.

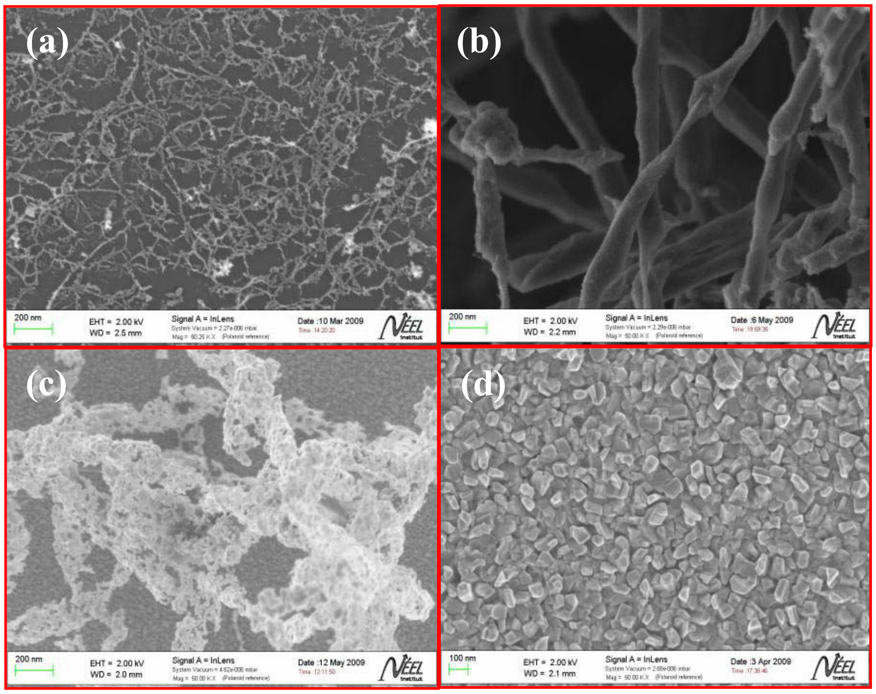

Figure 4.10. SEM images of CNT-1 samples after 60 min treatment at filament temperature of (a) 2000 °C, (b) 2100 °C, (c) 2200 °C and (d) 2400 °C, (T_s: 850 °C, P_{H2}: 30 Torr).

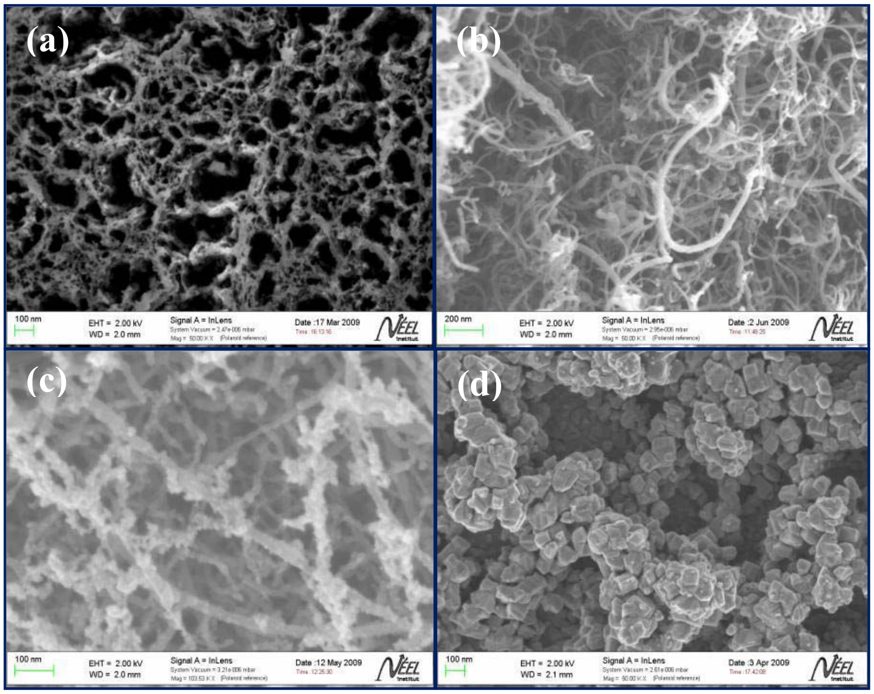

Figure 4.11. SEM images of CNT-2 samples after 60 min treatment at filament temperature of (a) 2000 °C, (b) 2100 °C, (c) 2200 °C and (d) 2400 °C, (T_s: 850 °C, P_{H2}: 30 Torr).

Similar to low filament temperatures, very high etching of nanotubes was observed for both CNT-1 and CNT-2 samples at 2000 °C filament temperature (figures 4.10 (a) and 4.11 (a) respectively). Less etching for CNT-1 (figure 4.10 (b)) and almost no etching for CNT-2 (figure 4.11 (b)) occurred at 2100 °C. At 2200 °C nanotubes started to transform (figure 4.10 (c) and 4.11 (c)) and a complete conversion to polycrystalline material was observed at 2400 °C (figure 4.10 (d) and 4.11 (d)). The polycrystalline material was later characterized by Raman Spectroscopy with 632 nm excitation. On the spectrum two bands centered at around 1350 and 1580 cm^{-1} (figure 4.12) were attributed to microcrystalline graphite.

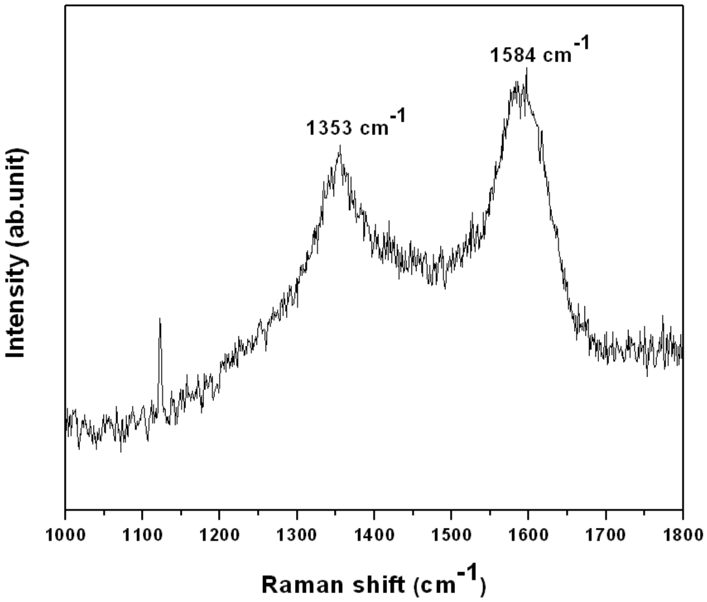

Figure 4.12. Raman spectra of hot-filament treated CNT-1 at 2400 °C for 60 min. The SEM image of this sample is shown in figure 4.10 (d).

The quality of nanotube dispersion on silicon substrates was found to influence the hot-filament activity at both low and high filament temperatures, in particular, in the range of 1950-2200 °C. Here, “quality” means the homogeneity and density of CNTs on the substrate. An example of the dispersion effect is shown in figure 4.13 where two samples containing CNT-1 with different degree of dispersion were treated for 60 min at 2000 °C filament temperature, (T_s: 850 °C, P_{H2}: 30 Torr). Poorly dispersed CNTs generate big and thick nanotube clusters (figure 4.13 (c)), that therefore limit the hydrogen diffusion inside the clusters and consequently only exposed nanotubes to atomic hydrogen are etched away (figure 4.13 (d)).

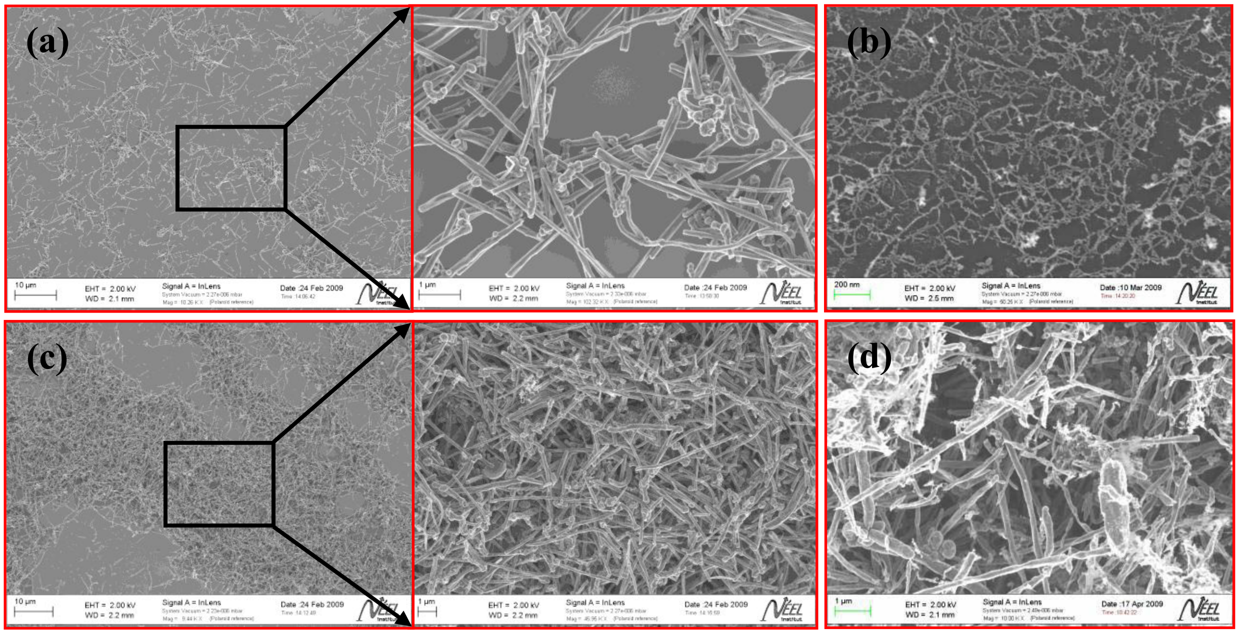

Figure 4.13. SEM images of (a) well dispersed CNT-1 before treatment, (b) after treatment and (c) poorly dispersed CNT-1 before treatment, (d) after treatment; (T_f: 2000 °C, T_s: 850 °C, 60 min, P_{H2}: 30 Torr).

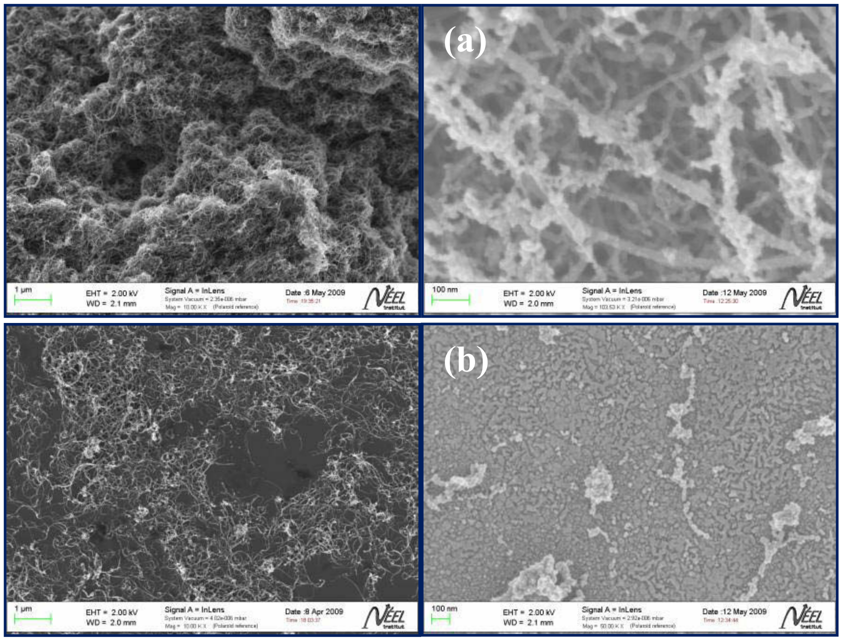

Figure 4.14. SEM images of hot-filament treated CNT-1 in the case of (a) poorly dispersed and (b) well dispersed nanotubes, (T_f: 2200 °C, T_s: 850 °C, 60 min, P_{H2}: 30 Torr). The left panels of (a) and (b) shows the corresponding dispersed CNT-1 before treatment.

Due to smaller diameter and wider length distribution (Table 4.2) the homogeneous dispersion (uniform, no cluster) of CNT-2 was always more difficult than that of CNT-1, thereby CNT-2 showed inconsistency in their treatment under hot-filament. For example, at 2200 °C, nanotubes present only on the outer side of the clusters were either etched or transformed in the case of poor dispersion (figure 4.14 (a)), whereas most well dispersed nanotubes were etched and/ transformed (figure 4.14 (b)). In some cases, treatment of poorly dispersed CNT-2 resulted in the formation of some strange objects such as spikes possibly made of carbon (figure 4.15) (T_f: 1950 °C, T_s: 850 °C, 60 min, P_{H2}: 30 Torr).

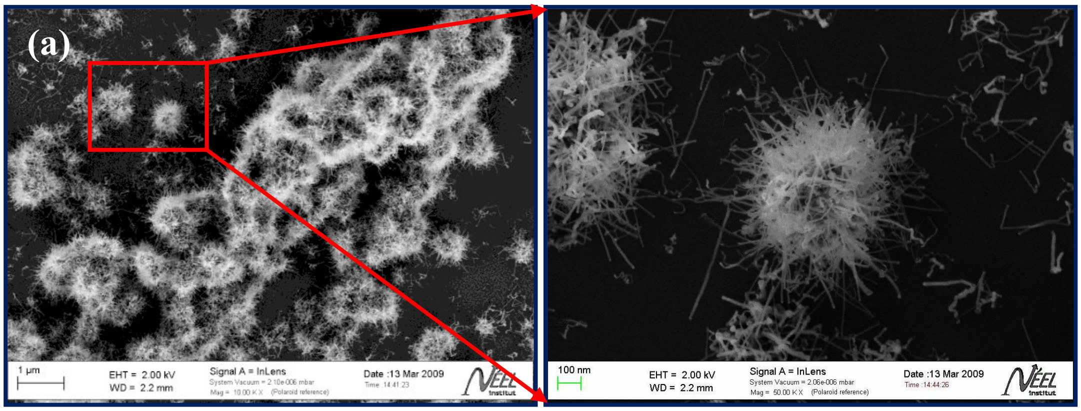

Figure 4.15. SEM images of poorly dispersed CNT-1 sample after 60 min treatment at the filament temperature of 1950 °C, (T_s: 850 °C, P_{H2}: 30 Torr).

As these spikes were electrically insulating deduced from the charging effect in the SEM, and contained oxygen deduced by EDX analysis, the materials are attributed tentatively to carbon polymers. The oxygen may originate from residual solvent trapped with nanotubes. The exact reason for the formation of spikes is not clear.

Although both nanotubes (CNT-1 and CNT-2) are highly purified, they contain a trace amount of amorphous carbon. Solubility of these nanotubes in dichloroethylene is very limited. As a result ultrasonic agitation has only a limited effect, which makes seeding difficult. Several other solvents, such as dichloro ether, dichloro ethane, water, ethanol, Toluol, were also tried but they showed dispersion characteristics similar to that of dichloroethylene.

The hot-filament activities at different filament temperatures are summarized in figure 4.16, where nanotube stability is expressed as the percentage of an individual nanotube remaining on the substrate after 60 min of treatment in hydrogen. Number of nanotubes was estimated before and after treatment by the analysis of the SEM pictures. Values are not very accurate, but allow displaying on one drawing the evolution of nanotube etching under hot-filament.

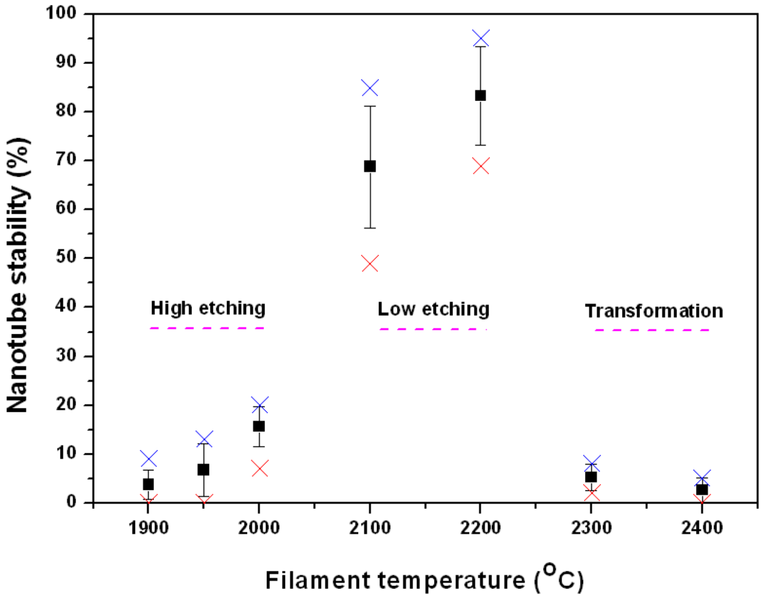

Figure 4.16. Stability of carbon nanotubes after 60 min treatment estimated for well dispersed CNT-1, (T_s: 850 °C, P_{H2}: 30 Torr). Red and blue cross refer to minimum and maximum respectively; the filled square represents mean and whiskers refer to standard deviation. Stability was estimated by the analysis of the SEM pictures.

Three different regions clearly appear, depending on the filament temperature (T_f):

1. T_f = 1900-2000 °C: Very high etching of nanotubes; at 1900 °C etching is not influenced by nanotube dispersion,
2. 2000°C < $T_f \leq$ 2200°C: Low or no etching of nanotubes depending on nanotube dispersion,
3. 2300 °C-2400°C: Very high tendency of nanotube conversion to polycrystalline material.

The observed behavior of dispersed CNTs under hot-filament environment at temperatures in the range of 1900-2400 ^{o}C can be explained as follows:

Based on energetic balance analysis of the filament (electrical power absorbed, thermal and dissociation losses), it has been deduced that hydrogen dissociation starts for a filament temperature of about 1700°C, and increases above (**Gheeraert, 1992**). At 1900°C the filament is therefore dissociating hydrogen, but at a low rate compared to higher temperatures. Then, the atomic H attacks CNTs at some defective places on the structure. The source of these defects could be the presence of many curved surfaces on CNTs. It is found that the carbon structure is easily etched by atomic hydrogen at the defective places and end caps in the temperature range of 1900-2000 °C, because of their instability in structure and higher energy (**Behr *et al.* 2010**). This phenomenon leads to breaking of CNTs in these places and carbon is etched out by hydrogen forming different carbon-hydrogen radicals (e.g. C-H) in gas phase. The possibility of conversion of these radicals into C and H, and also deposition of C into the original places is low at these temperatures (2000 ^{o}C or lower than that). Rather, the radicals are evacuated from the chamber. Also, due to the surface reconstruction it would be difficult for carbon atoms to sit onto the dangling bonds.

On the other hand, the possible explanation for the low etching rate at high temperature (e.g. 2100 ^{o}C) could be the conversion of radicals into carbon and hydrogen due to high temperature, high local carbon concentration, less possibility of surface reconstruction, and high driving force for deposition of carbon into the original places. At higher temperatures (2200-2400 ^{o}C) transformation of CNTs to graphite /and carbon nanoparticles occurs due to the extreme filament activity that satisfies the localized energy conditions required for nanotube conversion.

We can also explain the observed etching behavior of CNTs thermodynamically. Thermodynamic requirement for diamond deposition is that the carbon in the gas phase should be supersaturated with respect to the precipitation of diamond. In other words, the chemical potential of carbon in the gas phase should be higher than that in diamond. This condition is satisfied when the activity of carbon in the gas phase is higher than that in diamond. If the gases in the CVD reactor follow the ideal gas law, the partial pressure of carbon in the gas phase should be higher than the equilibrium vapor pressure of diamond at the given temperature. When this condition is satisfied, the carbon in the gas phase is also supersaturated with respect to precipitation of graphite because the equilibrium vapor pressure of graphite is always lower than that of diamond in a low pressure CVD process;

graphite is more stable than diamond. Thus, when carbon in the gas phase is supersaturated with respect to precipitation of diamond, the formation of graphite as well as diamond is thermodynamically possible. The two processes are kinetically parallel. Since graphite is more stable than diamond, the driving force for precipitation of graphite is higher than that of diamond. However, the higher driving force does not guarantee the dominant precipitation; the kinetic barrier will be a determining factor. Thus, kinetic requirement for diamond deposition is that the kinetic barrier of diamond precipitation from the gas phase should be smaller than that of graphite.

4.1.4. Microwave Plasma Treatment of Dispersed CNTs: Results and Discussion

A hot-filament system relies only upon thermal energy and catalytic H_2 dissociation on the filament surface to initiate the gas phase chemistry, whereas for a microwave system, in addition to thermal excitation, there are plasma activation processes e.g. direct electron excitation and ionizations, and reactions between molecules, ions and excited atoms. The plasma activation is responsible for the presence of many species including H^+, CH_3, C_2H, C_2H_2, in addition to C_2, and several of these species could in principal participate in the diamond growth process. The electric field frequency being too high to allow ions to move, no kinetic energy is transferred to the ions. Only electrons are moving in the field.

A schematic of the plasma treatment process for dispersed CNTs is shown in figure 4.17.

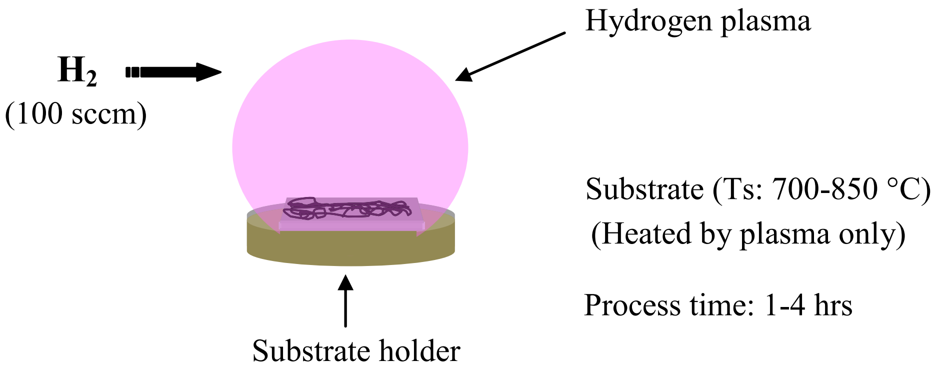

Figure 4.17. Schematic representation of the plasma assisted treatment of dispersed CNTs performed in a Microwave Plasma CVD (MPCVD) diamond growth reactor.

Dispersed MWCNTs (CNT-1 and CNT-2) were treated under microwave plasma at different substrate temperatures (700-850 ^{o}C) and time (1- 4 hrs) in 100 sccm flowing H_2. Only plasma heated the substrate and microwave power was adjusted accordingly; no external heating was employed. The substrate temperature was measured by an optical pyrometer. For all experiments the chamber pressure was maintained at 30 Torr. Treated samples were characterized morphologically by scanning electron microscope (SEM).

Figure 4.18 shows the effect of substrate temperature observed for CNT-1.

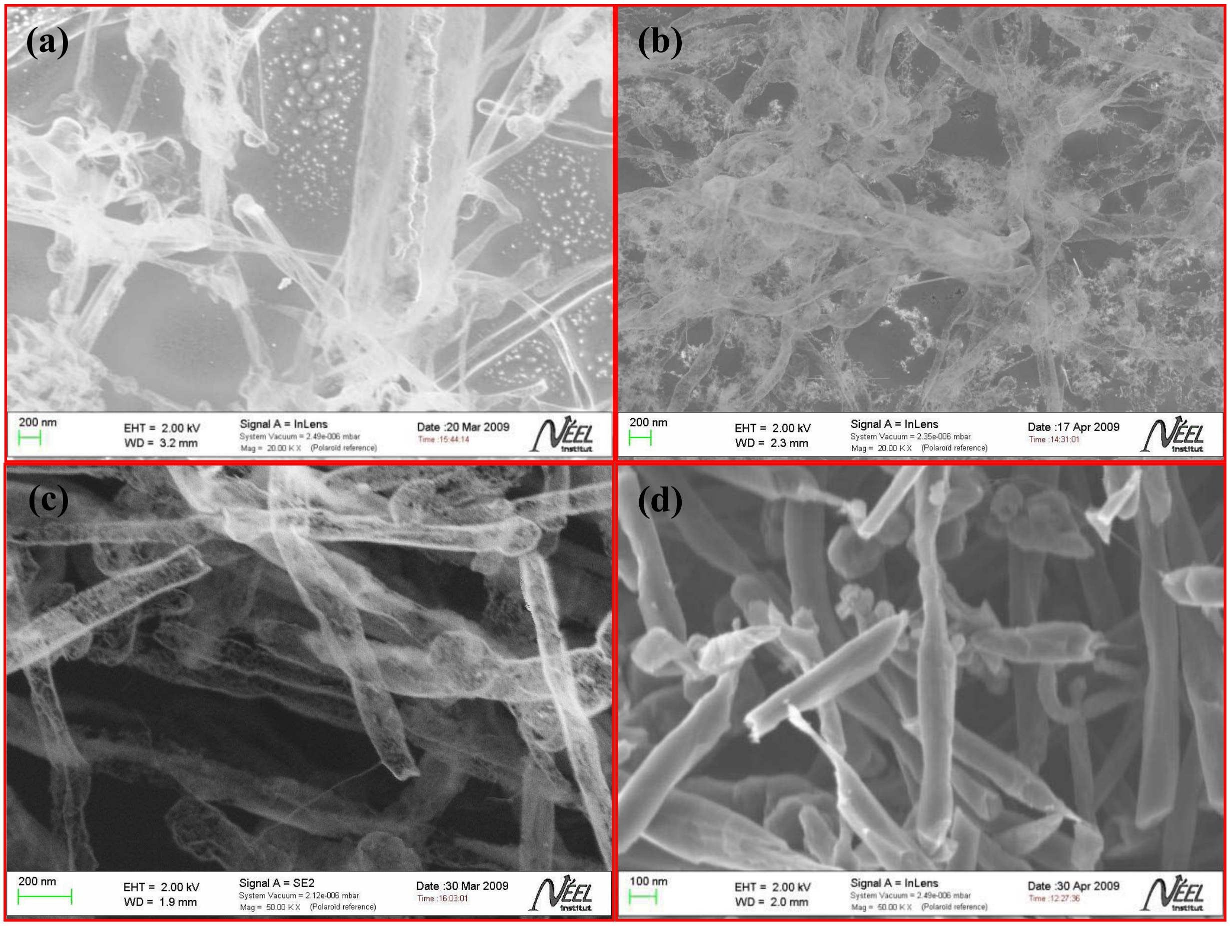

Figure 4.18. SEM images of plasma treated CNT-1 at (a) 700 °C, (b) 750 °C, (c) 800 °C and (d) 850 °C for 60 min, (P_{H2}: 30 Torr).

Strong etching of CNT-1 was observed after 60 min treatment at substrate temperature in the range of 700-800 °C (figure 4.18 (a)-(c)), whereas etching was decreased significantly at 850 °C (figure 4.18 (d)). Treatment of CNT-2 at 700-850 °C (figure 4.19) showed etching characteristics similar to that of CNT-1 with some exceptions, for example, CNT-1 treatment resulted in transparent carbon network with original nanotube frame whereas no framework of original nanotube was left on the substrate and nanoparticles were generated instead from treated CNT-2 (figure 4.19 (c)).

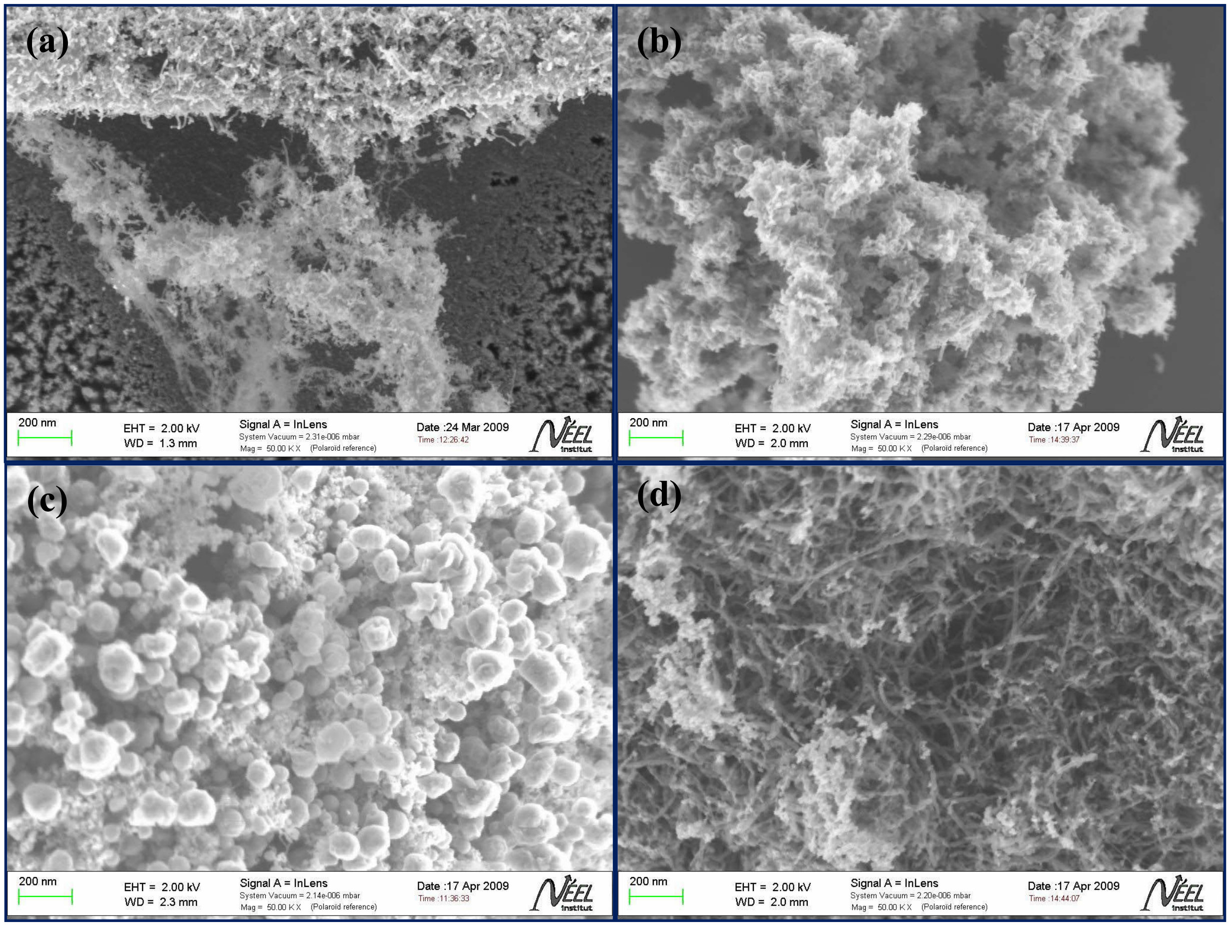

Figure 4.19. SEM images of plasma treated CNT-2 for 60 min at (a) 700 °C, (b) 750 °C, (c) 800 °C and (d) 850 °C, (P_{H2}: 30 Torr).

On the other hand, after prolonged processing (4 hours treatment) of CNT-1 at 750 and 800 °C, the transparent carbon network, as shown in figure 4.18, were crystallized into bad quality diamond and spherically shaped carbon nanoparticles (figure 4.20), where carbon matrix acted as nucleation site for growth.

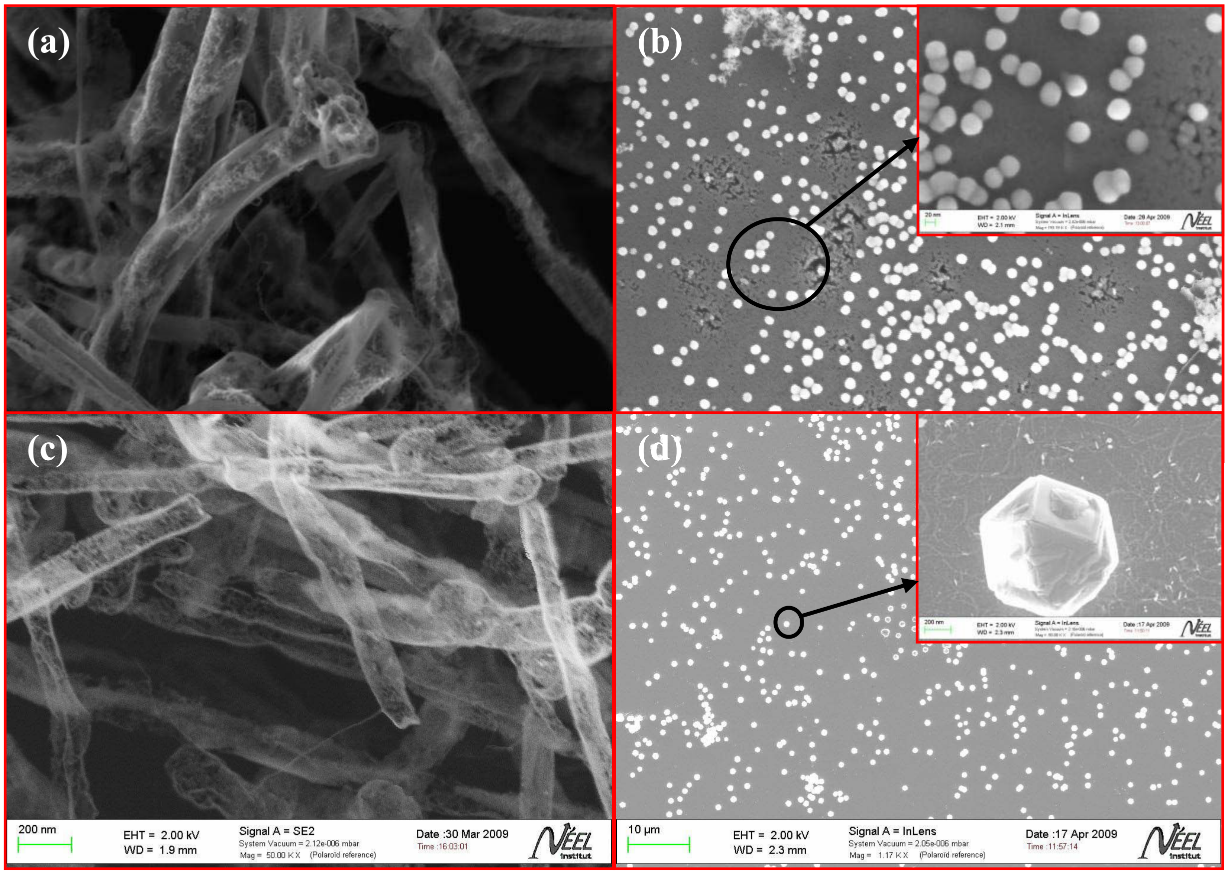

Figure 4.20. SEM images of plasma treated CNT-1. At 750 °C for (a) 1 hour and (b) 4 hours; at 800 °C for (c) 1 hour and (b) 4 hours, (P_{H2}: 30 Torr).

The mechanism of carbon nanotube etching in microwave plasma is complicated and still less understood. The etching behavior of nanotubes in plasma is more or less similar to that in hot filament treatment: low temperature higher etching and vice versa. At low temperature, etching of nanotubes may dominate over growth of new nanotubes, whereas at high temperature growth of new nanotubes may be the dominating factor. This can be due to the higher diffusion rate of carbon towards the etched portion of the original nanotubes leading to the growth of new nanotubes. At low temperature, diffusion of carbon and other species responsible for nanotube growth may be low and instead of depositing they prefer to be evacuated from the chamber.

4.1.5. Growth of Nano-Objects

The hot-filament study of CNT-1 and CNT-2 suggests that there exists a condition where the balance between etching and growth can be achieved depending on the quality of nanotube dispersion. For example, the filament temperature in the range of 2100-2300 ^{o}C could allow a good stability of nanotubes and provide favorable conditions for diamond growth. Focusing in this temperature range, growth of several nano-objects was observed.

4.1.5.1. Nanospikes

Nanospike growth with low reproducibility was observed particularly in the treatment of poorly dispersed CNT-2 at filament temperature of 2000-2100 °C. Figure 4.21 shows nanospikes formed at 2100 °C after 60 min.

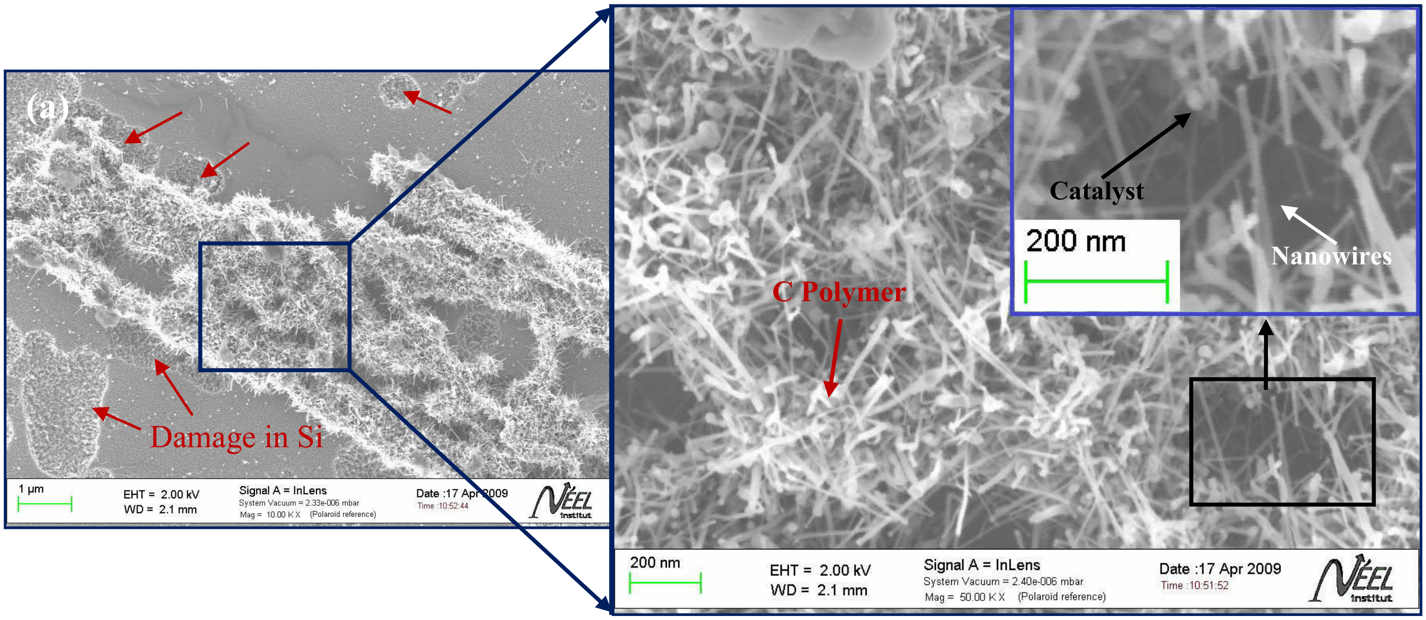

Figure 4.21. SEM images of poorly dispersed CNT-2 after 60 min treatment at 2100 °C filament temperature, (T_s: 850 °C, P_{H2}: 30 Torr).

Nanospikes on the surface of the clusters (bright in contrast) were electrically insulating deduced from the charging effect in the SEM, and contained oxygen deduced by EDX analysis. They are attributed to carbon polymers. The oxygen may originate from residual solvent trapped within nanotube cluster. On the other hand, the spikes just beneath carbon polymer contained round object at their end similar to nanowires that are discussed in the previous section. Nanospike formation was accompanied by the damage in Si substrate near to the spike formation and interestingly no original nanotubes from the dispersed CNT-2 remained on the substrate. Si surface (substrate surface) was not fully covered by CNT-2 due to its poor dispersion and the uncovered areas were exposed to atomic hydrogen. It was reported that hot-tungsten filament generated atomic hydrogen could etch amorphous, microcrystalline and polycrystalline Si (**Wanka & Schubert, 1997**). The sputtered Si atoms could assist to spike and nanowire formation. Indeed, the nanowires could be Si or SiC nanowires. No signal was observed by Raman spectroscopy and glazing incidence X-ray diffraction (XRD), because of the low volume of the material observed.

4.1.5.2. Nanocrystals/Nanoparticles on nanotubes

Growth of nanocrystals/nanoparticles on nanotube surface was observed for treated CNT-1 and CNT-2 at 2200 ^{o}C for 60 min (figure 4.22), in the case of poor nanotube dispersion.

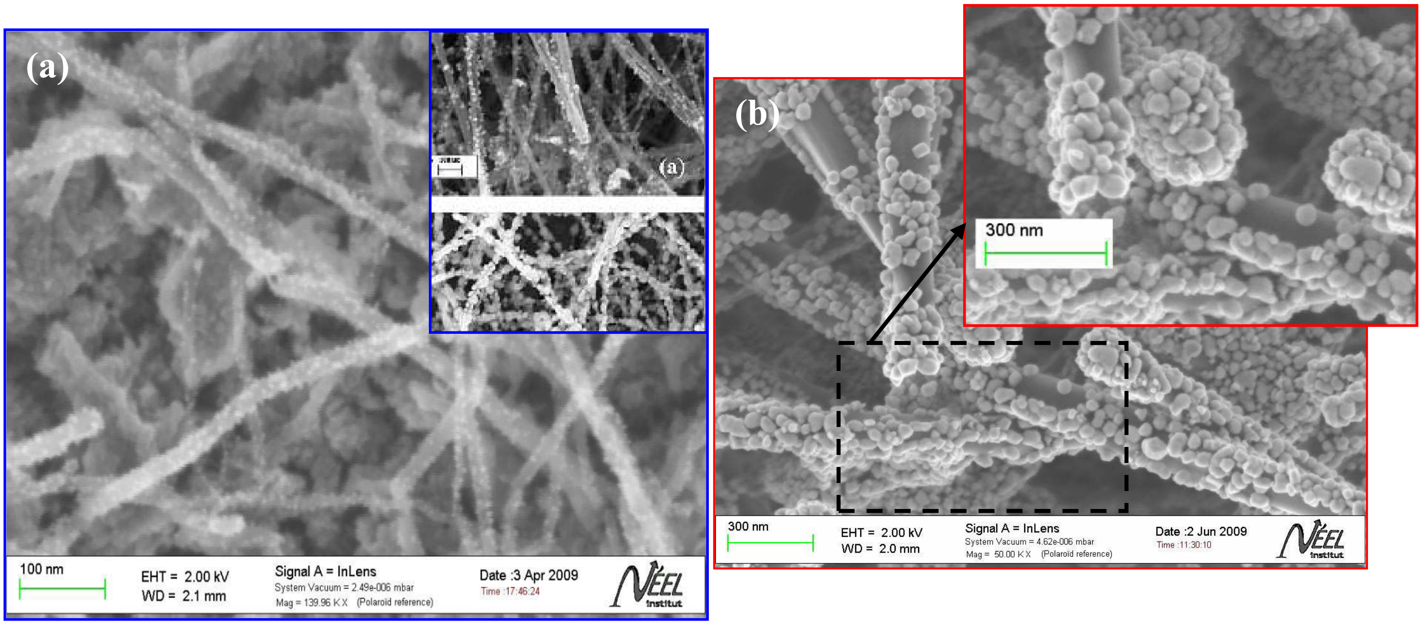

Figure 4.22. SEM images of hot-filament treated (a) CNT-2 and (b) CNT-1 at 2200 ^{o}C for 60 min, (T_s: 850 °C, P_{H2}: 30 Torr). The inset of the panel (a) is a SEM picture taken from the reference (Sun et al. 2005) showing diamond nanocrystals on MWCNTs.

Nanocrystals are of about 5-10 nm and 10-30 nm in diameter for CNT-2 (figure 4.22 (a)) and CNT-1 (figure 4.22 (b)) respectively. The exact shape, and the occurrence of facets, is difficult to estimate from the SEM picture. Note that nanocrystals were observed on a tiny portion of the sample (area of the nanocrystal containing portion of the sample is around 50 μm^2, being estimated from SEM picture of CNT-2) and they were not reproducible, that made their characterization very difficult. Raman spectroscopy of the sample (shown in figure 4.22 (a)) is presented in figure 4.23.

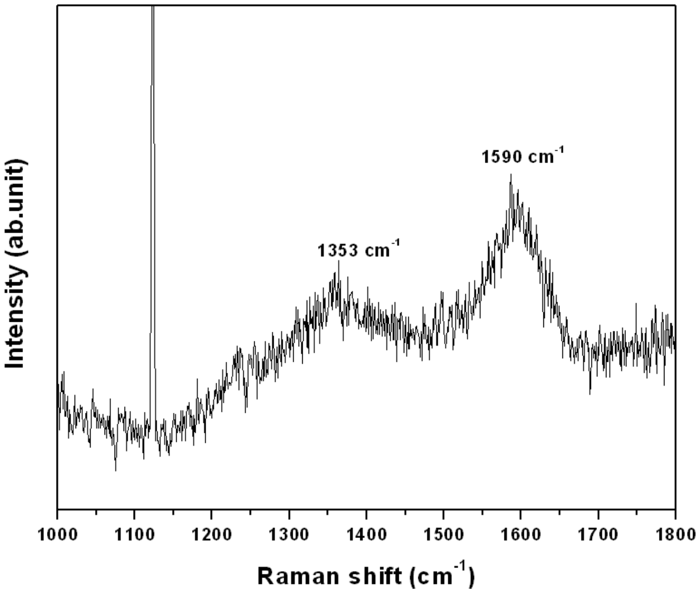

Figure 4.23. Raman spectroscopy of treated CNT-2 at 2200 °C for 60 min; SEM image of this sample is shown in figure 4.22 (a).

In the spectrum the bands centered at around 1353 cm^{-1} and 1590 cm^{-1} are attributed to microcrystalline graphite. It was assumed that the nanocrystals due to their very low quantity contributed very less to the overall signal whereas polycrystalline material (microcrystalline graphite) present beneath the nanocrystal containing nanotubes were the responsible for the raman signal at 1350-1590 cm^{-1}. Nanocrystals were later characterized by cathodoluminescence (CL). The CL experiment was performed in a JEOL JSM 35 C SEM equipped for maximum versatility and sensitivity with Oxford Instruments liquid helium (LHe) cryogenic stages, and an Oxford Instruments Mono CL2 cathodoluminescence imaging and spectral analysis. The CL was excited using a continuous electron beam (E_o = 15 keV, I_B = 10 nA) at normal incidence, and measured using a retractable parabolic mirror collector. Spectra measured over the wavelength range 300-850 nm with a 5 nm bandpass were collected by photon counting using a Hamamatsu R943-02 Peltier cooled high-sensitivity photomultiplier tube (HSPMT) with a 1200 lines per mm grating, blazed at 500 nm. The CL spectra, collected as a function of wavelength λ (nm), were not corrected for total instrument response, as the diamond emissions of interest for imaging were well resolved. Figure 4.24 shows the CL spectrum measure at 5 K for nanocrystals containing CNT-2 sample (figure 4.22 (a)).

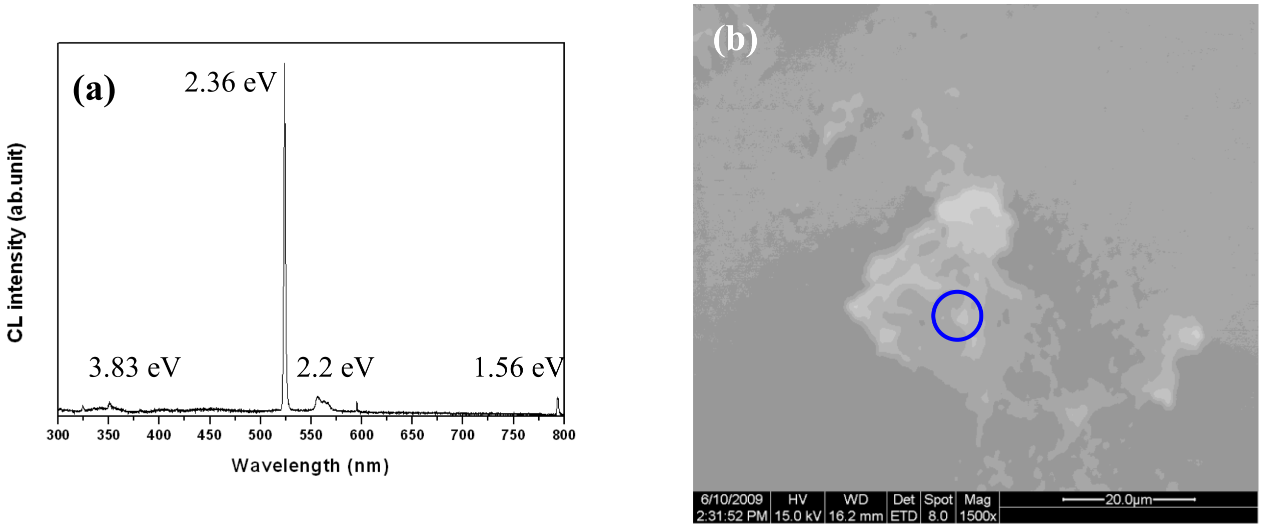

Figure 4.24. (a) The CL spectrum observed at 5 K with 15 keV electron beam energy for treated CNT-2 at 2200 °C for 60 min (T_s: 850 °C, P_{H2}: 30 Torr), (b) corresponding CL image showing the focused area for CL indicated by blue circle.

Signal was very clear at low temperature (5K). The CL spectrum shows several peaks at 351 nm (3.83 eV), 523 nm (2.36 eV), 560 nm (2.2 eV) and 793 nm (1.55 eV). The peaks at 523.7 nm and 560 nm are usually observed for diamond containing Si and Co impurities (**Ruan *et al.* 1991**), or Co alone (**Lawson *et al.* 1996**; **Kanda** & **Watanabe**, **1997**). The weak peak at 793 nm was also observed for Co doped diamond monocrystals, together with 523.7 nm peak (The spectrum is not shown here). However, the spectrum (figure 4.24) is not conclusive for the characterization of the nanocrystals as diamond since some other characteristic peaks for diamond (**Lawson *et al.* 1996**) are missing in the spectrum. So, the nanocrystals could be diamond but it is not conclusive. It is rather assumed that they could be either diamond or SiC or a mixture of the both.

4.1.5.3. Nanowires on nanotubes

At the condition of nanocrystal growth on CNTs (T_f: 2200 °C, T_s: 850 °C, P_{H2}: 30 Torr), nanowire growth was observed in the case of relatively long processing (3 hours treatment) of CNT-2 sample (figure 4.25 (a)). Again nanowire with extremely low in quantity appeared only on a tiny part of the sample (area of the nanowire containing portion of the sample is around 30 μm^2, being estimated from SEM picture), and they were not reproducible. Figure 4.25 (b) represents the nanostructure present on most part of the treated CNT-2 sample.

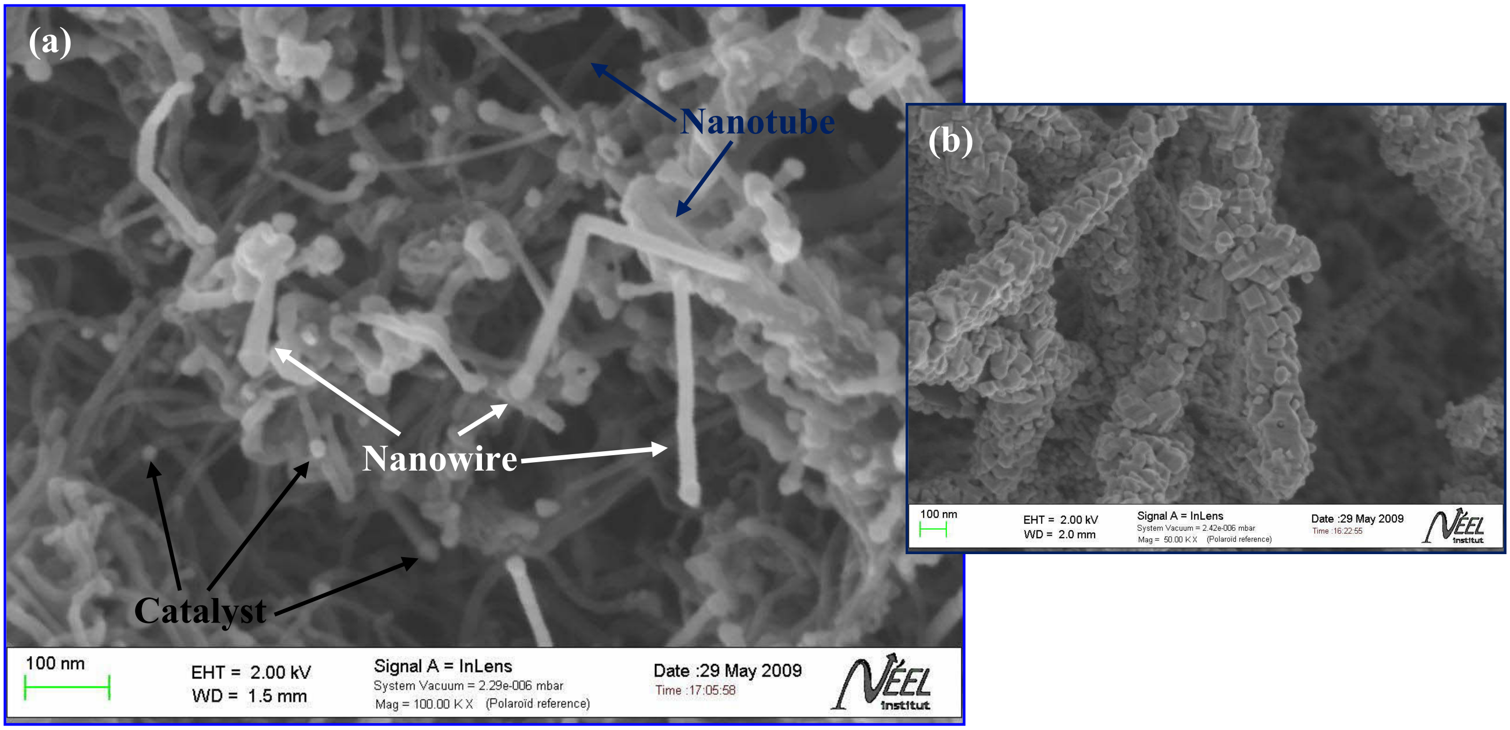

Figure 4.25. SEM images of (a) nanowires grown on a tiny portion of the sample and (b) nanostructure grown on the rest of the sample, after 3 hours treatment of CNT-2 at 2200 °C filament temperature, (T_s: 850 °C, P_{H2}: 30 Torr).

Nanowires are around 10-30 nm in diameter and 100-500 nm in length. At the end of each nanowire there appears a round shape object with a slightly different SEM contrast. The observation could suggest the round object as the catalytic particle that stabilized the structure and favored the 1D growth. No metal catalyst was added to the process and original nanotubes (CNT-2) were purified. The only source of this catalytic particle could possibly be the tungsten filament. It was reported that in the carbon atmosphere tungsten carbide (W_2C) is formed on the surface of the hot-tungsten filament (> 2000 ^oC) due to the high reactivity of the metal surface (**Moustakas, 1989**; **Zeiler *et al.* 2002**). The carbide layers could later be peeled off from the surface due to the high stress developed in the layers and deposit to the substrate.

Another tentative explanation for the contrast between the nanowire and its tip is that as only carbon and hydrogen are present in the chamber, the contrast could originate from two different allotropic forms of carbon, such as diamond and graphite, or diamond and amorphous carbon, as their atomic density are different. Moreover, no charging effect is observed for these objects by SEM, and no oxygen appears by EDX. This observation is relatively consistent with that of **Sun *et al.*** (**2005**), in which diamond nanowires grew from initially nucleated diamond nanocrystals after 20 hours of plasma treatment of dispersed MWCNTs. We could therefore attribute these objects to carbon or diamond nanowires, although it is not conclusive. It was not possible to identify the exact nature of these nanowires due to their extremely low density, the difficulty of locating them on the sample during characterization by Raman, CL or TEM and not being reproducible.

4.1.6. Catalyst Assisted Treatment of Dispersed CNTs: Results and Discussion

Nanowire growth on CNT-2 (figure 4.25) suggests that there could exist a Vapor-Liquid-Solid (VLS) growth mechanism (**Wagner & Ellis**, **1964**) where metal catalyst is used to enhance the 1D crystal growth. In addition, transition metals are known to facilitate the dissociation of hydrogen molecules into atomic hydrogen at significant low hydrogen dissociation barrier (**Gross, 1998**; **Berger, 1992**). In order to investigate the growth condition (figure 4.25) in presence of metal catalyst, Ni layers with thickness of 3 nm were evaporated on dispersed CNTs. Ni was used because of its effectiveness in carbon material synthesis.

4.1.6.1. CNT-2 dispersed on Si substrate

CNT-2 was first dispersed on a Si substrate (P-type, <100>) and 3 nm Ni layers were then evaporated on the sample. A schematic of the sample and the treatment process is shown in figure 4.26. After 3 hours treatment mostly straight and relatively long nanowires were observed (figure 4.27). They are randomly oriented but pointing away from the substrate surface. The average diameter of the nanowires is about 65 nm and the length ranges from a few hundred nanometers to micrometers based on the SEM analysis. Spherically shaped Ni nanoparticles appear at the nanowire tips depicting the catalyst-assisted growth.

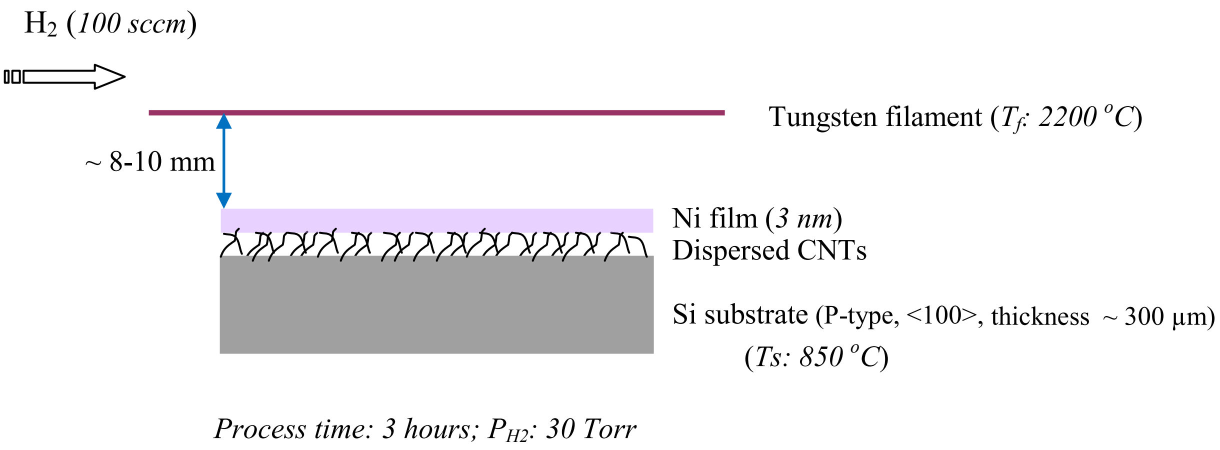

Figure 4.26. Schematic of the hot-filament treatment of the dispersed CNT-2 at nanowire growth condition (indicated in the scheme) in presence of Ni as catalyst.

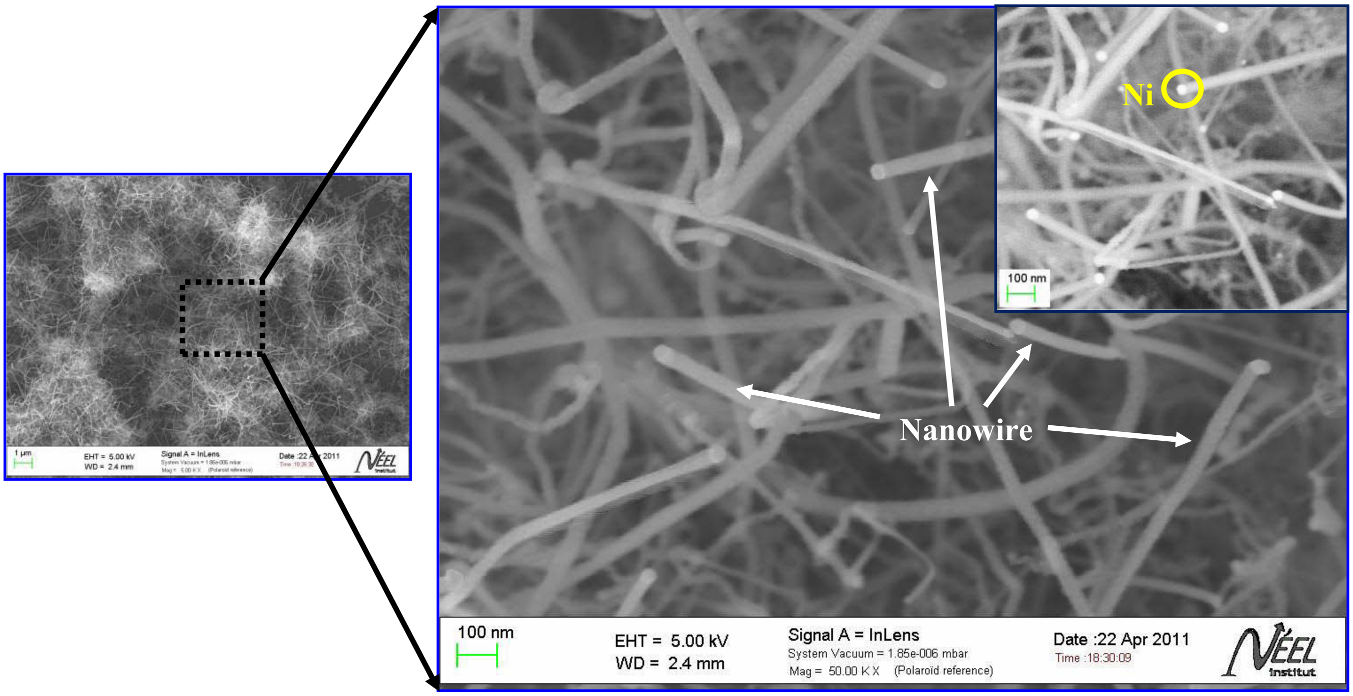

Figure 4.27. SEM images of hot-filament treated CNT-2 with 3 nm Ni layers at 2200 °C for 3 hours, (Ts: 850 °C: P_{H2}: 30 Torr), inset is a secondary electron detected image.

The sample was analyzed using a WITec Raman spectrometer with 632.8 nm excitation (HeNe laser). The resolution of the laser spot was ~ 1 μm and the sampling depth was estimated to be around a few μm depending on the transparency and clarity of the sample. Figure 4.28 shows a series of Raman spectra taken at different locations in the sample.

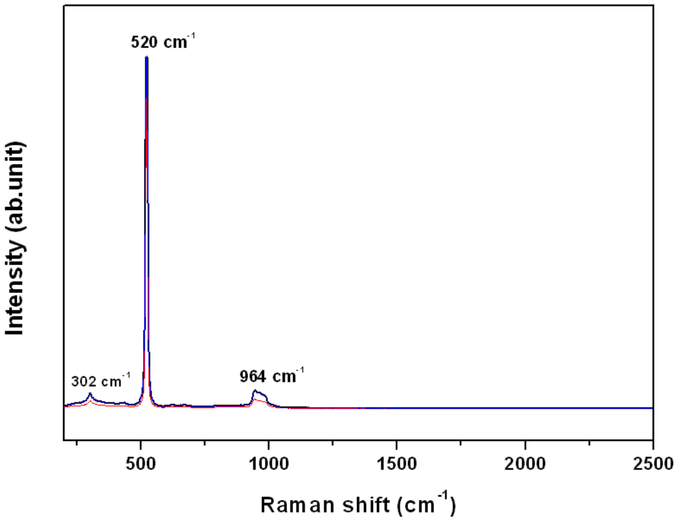

Figure 4.28. Raman spectra of the sample shown in figure 4.27 at 3 random locations taken with 632.8 nm excitation.

The spectra show few peaks located at 302, 520 and 964 cm^{-1}. The sharp and intense peak at 520 cm^{-1} is commonly observed for bulk crystalline silicon (c-Si). This is ascribed to the scattering of the first-order optical phonon of c-Si. In addition, two broad peaks at 302 and 964 cm^{-1} are the second-order peaks observed for bulk Si and they are assigned to the overtones of transverse-acoustic (TA(X)) and transverse-optic (TO(L)) respectively. No peaks in the range of 1000-2000 cm^{-1}, in particular D and G bands, appeared in the spectra suggesting the absence of diamond and graphitic carbon on the substrate. On the other hand, the peaks that are characteristics for Si or SiC nanowires (**May *et al.* 2007**; **Sundaresan *et al.* 2007**) were not also observed. One possible explanation for the appearance of fewer peaks in the Raman spectra is as follows: the SEM observation (figure 4.27) shows that nanowires are less dense and formed only at the places where the original CNT-2 was present as aggregates before the treatment. The nanowires are therefore not distributed homogeneously over the substrate. **May *et al.*** (**2007**) reported that for films < 1 µm, the spectrum is dominated by peaks from the Si substrate in the case of 632.8 nm excitation. This phenomenon could be applicable for the present observation (figure 4.28).

Although the origin of these nanowires is not fully understood, it is assumed that the Si substrate, in particular, Si contamination from the substrate could mediate the nanowire growth and further growth experiment in a Si free environment could give clear insight into the nanowire growth.

4.1.6.2. Dispersed CNT-2 on nanocrystalline diamond film grown on Si substrate

In order to reduce substrate effects (silicon contamination) in the treatment process, a thin nanocrystalline diamond film with about 300 nm thickness and 100 nm average grain size was deposited on a Si substrate in a microwave plasma-enhanced CVD reactor (Seki Technotron ASTEX-5200) with bias enhanced nucleation approach (BEN) (chapter 3, figure). CNT-2 was dispersed on the diamond surface and 3 nm Ni layers were then evaporated on the surface. The sample was treated for 3 hours at 2200 °C (filament temperature). The process is shown schematically in figure 4.28b. The morphology of the deposited NCD film is displayed in a SEM image shown in figure 4.29.

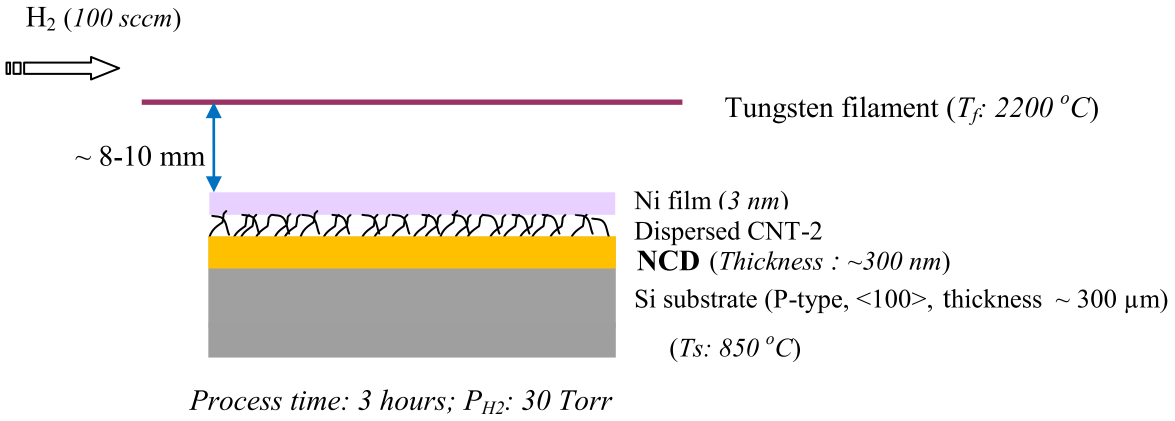

Figure 4.28b. Schematic of the hot-filament treatment of CNT-2 dispersed on a nanocrystalline diamond film (NCD) at nanowire growth condition (indicated in the scheme) in presence of Ni as catalyst.

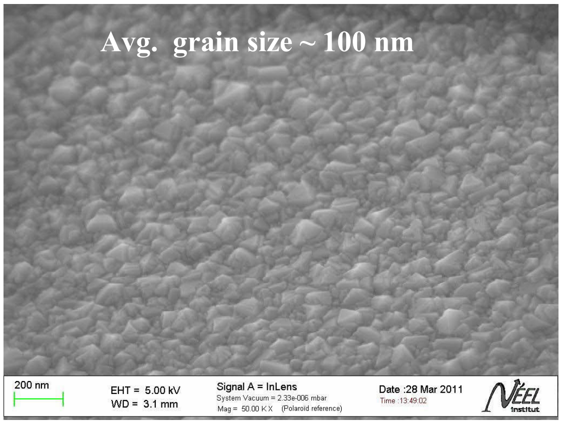

Figure 4.29. SEM image of nanocrystalline diamond film with about 300 nm thickness grown on silicon substrate in a microwave plasma enhanced CVD reactor using bias enhanced nucleation approach.

Again nanowire growth was observed but only near the sample border, close to the exposed Si region (figure 4.30). Inhomogeneity in the NCD film along the border resulted in this exposed region. The nanowires are randomly oriented, and Ni nanoparticles are encapsulated in their tips. The observed nanowires are shorter in length and less dense than that were observed in the case of dispersed CNT-2 on Si substrates shown in figure 4.29. The nanowire density was decreased significantly away from the border area and about 500 µm from the border, around the sample center, almost no nanowire was found, instead, Ni nanoparticles and few CNT-2 (mostly being etched away) were observed (figure 4.30 (c)). Such distribution of these nanowires on the substrate suggests that Si contamination could be responsible for their growth.

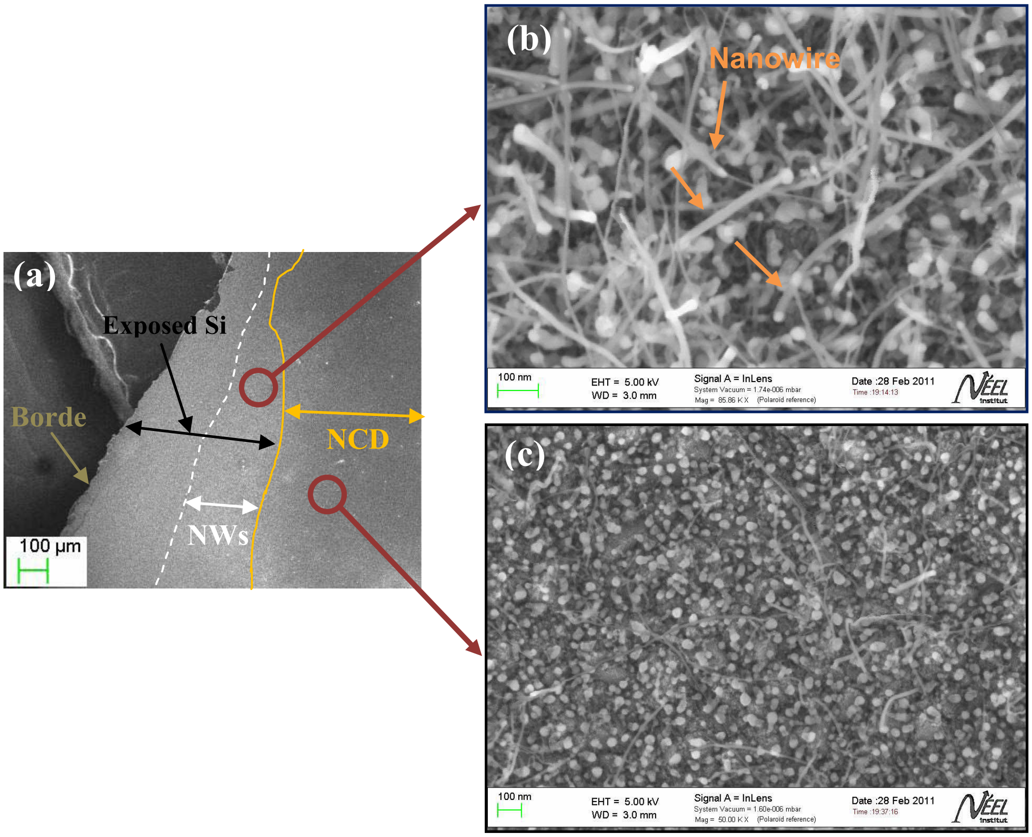

Figure 4.30. SEM images of hot-filament treated CNT-2 with 3 nm Ni layers at 2200 ^{o}*C for 3 hours, (Ts: 850* ^{o}*C:* P_{H2}*: 30 Torr); (a) a portion of the sample at low magnification, (b) nanowires near the border, close to the exposed Si region and (c) Ni nanoparticles and few etched CNT-2 on the diamond surface, about 500 µm away from the border.*

4.1.6.3. Dispersed CNT-2 on polycrystalline diamond substrate

In order to rule out completely the Si substrate effects in the treatment process, CNT-2 was dispersed on a polycrystalline diamond substrate and treated with 3 nm layers at 2200 °C for 3 hours (figure 4.31). The diamond substrates purchased from Element Six are electrochemical grade boron doped CVD diamond with average grain size of about 50 µm (figure 4.32).

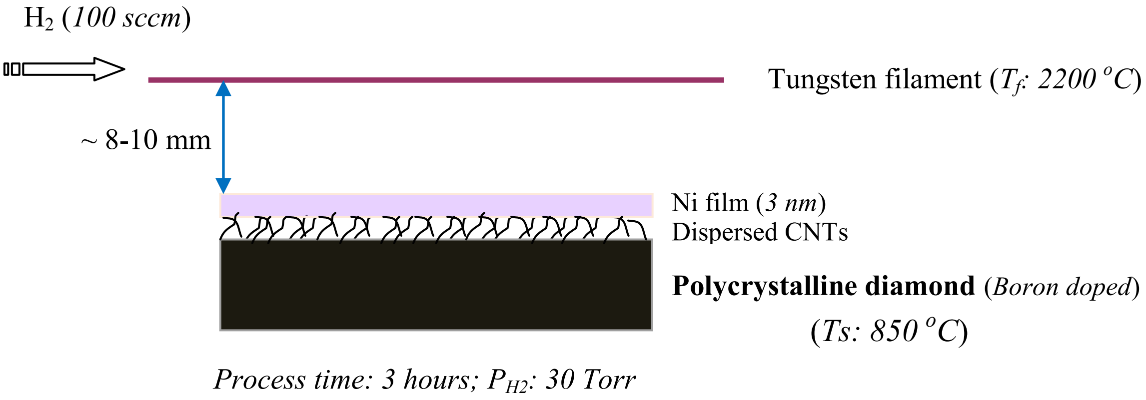

Figure 4.31. Schematic of the hot-filament treatment of dispersed CNT-2 on polycrystalline diamond substrate at nanowire growth condition (indicated in the scheme) in presence of 3nm Ni layers as catalyst.

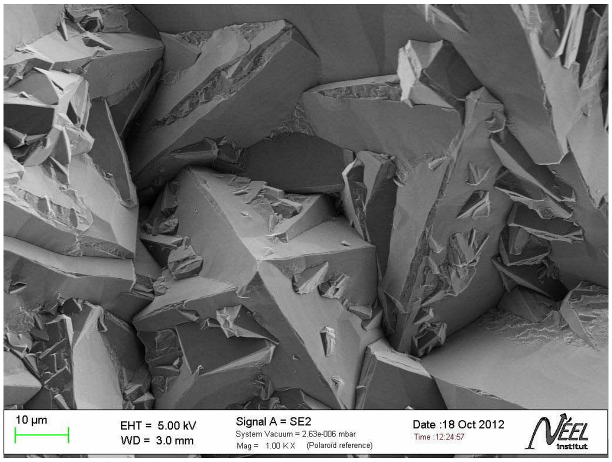

Figure 4.32. SEM image of an electrochemical grade boron doped CVD polycrystalline diamond with average grain size of about 50 µm, obtained from Element Six.

Figure 4.33 shows the morphology of the treated samples. Unlike the treatment of nanotubes on Si substrates with catalyst, neither nanowire nor nanocrystal growth was observed on the diamond substrates. Well dispersed CNT-2 was etched away after 3 hours of treatment and highly dense Ni nanoparticles together with some very short nanotubes were found on the substrate (figure 4.33 (b)). For poorly dispersed CNT-2, nanotubes only around the surface area of the CNT-2 clusters were attacked by atomic hydrogen and etched, and no nanotube transformation was observed (figure 4.33 (a)), unlike to that was observed for CNT-2 treatment on Si substrates without catalyst (figure 4.14 (b)). Ni nanoparticles formed aggregates on the CNT-2 clusters (inset of panel (a)). The observation (figure 4.33) suggests that nanowire growth requires the presence of Si and a metal catalyst; no silicon no nanowire.

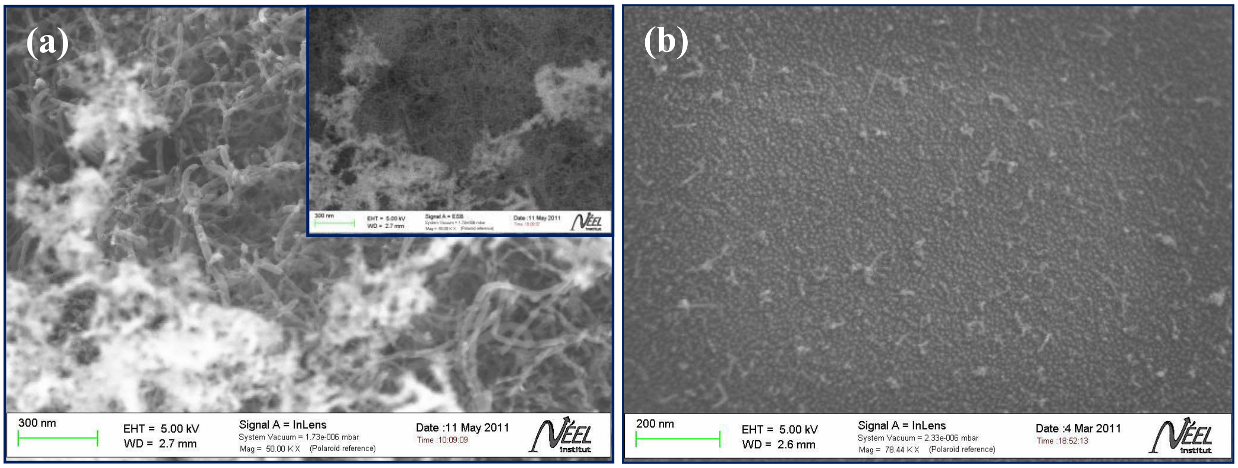

Figure 4.33. SEM images of hot-filament treated (a) poorly dispersed and (b) well dispersed CNT-2 on polycrystalline diamond at 2200 °C for 3 hours, (T_s: 850 °C, P_{H2}: 30 Torr). The inset of panel (a) is a EsB detector recorded SEM image, where the bright contrast corresponds to aggregated Ni nanoparticles.

4.2. Investigation of the VLS Growth Mechanism

Nanowires are a result of anisotropic, 1D crystal growth on a nanometer scale. Therefore, the key issue related to the growth of nanowires is how to induce 1D crystal growth in a controlled manner. Regarding this, many approaches have been studied, including the use of the metal-catalyst-assisted vapor-liquid-solid (VLS) mechanism, the vapor-solid (VS) mechanism, and the template-assisted

(TA) mechanism. Among these, the VLS mechanism is the most widely used owing to its simplicity and versatility when applied in many semiconductor systems. Together with other semiconductor nanowires (Si, Ge, ZnO etc.) the VLS mechanism has been studied extensively for the growth of carbon nanotubes (**Baker *et al.* 1972**; **Kukovitsky *et al.* 1999**; **Page *et al.* 2010**) and carbon filaments (**Baker *et al.* 1972**). On the other hand, the mechanism has yet to be investigated for the growth of diamond nanowires. Note that the high pressure induced by the nanometer-size droplet can favour the formation of diamond phase upon precipitation, and not the graphitic phase. The objective of our study was to investigate the VLS mechanism for diamond nanowire growth by using HFCVD and MPCVD techniques. Polycrystalline diamond (electrochemical grade boron doped CVD diamond) (figure 4.32) was used as the substrate and 3nm Ni layers were evaporated on the substrate surface as catalyst. Methane (CH_4) was used as the main carbon containing precursor and experiments were performed at diamond growth conditions dedicated to the respective CVD methods.

Although the study of the VLS growth of diamond is extremely limited, the VLS mechanism of carbon nanotube could be adopted for diamond nanowire considering the comparability between a carbon nanotube and a diamond nanowire. In the VLS model for nanotube growth, it was assumed that the formation of a single-wall carbon nanotube (SWCNT) started with co-condensation of carbon and metal atoms from the vapor to form liquid metal carbide (**Page *et al.* 2010**). Once the liquid reached supersaturation, the solid pahse carbon nanotubes began to grow. The growth process was divided into three distinct stages: nucleation of a carbon “cap-precursor”, “cap-to-tube” transformation, and continued SWCNT growth. It was reported that particles in the liquid state were the active sites in the process of catalytic carbon nanotube growth from the observed catalyst particle shapes (**Kukovitsky *et al.* 1999**). The interfacial energy contribution to the total free energy of nanoparticles was assumed to be responsible for the significant lowering of the melting temperature of the catalyst particles. The VLS model often included a temperature gradient (TG) across the catalyst metal particle (**Ding *et al.* 2004**). Later, it was confirmed that a TG was only important for the growth of carbon species from large metal particles.

4.2.1. VLS Mechanism: Fundamental Aspects

The VLS mechanism is a 1D crystal growth mechanism that is assisted by a metal catalyst. The mechanism was first proposed for the growth of single crystal silicon whiskers 100 nm to hundreds of microns in diameter (**Wagner & Ellis, 1964**). Figure 4.34 shows a schematic of the VLS mechanism. In this mechanism, the metal catalyst forms liquid alloy droplets at a high temperature by adsorbing vapor components. For some reason, e.g., temperature or vapor pressure fluctuation, the alloy is further supersaturated; i.e., it becomes a solution in which the actual concentration of the components is higher than the equilibrium concentration. Upon supersaturation, a nucleation event generates a solid precipitate of the source material. This seed serves as a preferred site for further deposition of material at the interface of the liquid droplet, promoting the elongation of the seed into a nanowire or a whisker, and suppressing further nucleation events on the same catalyst. Since the liquid droplet catalyzes the incorporation of material from the gas source to the growing crystal, the deposit grows anisotropically as a whisker whose diameter is dictated by the diameter of the liquid alloy droplet. The nanowires thus obtained are of high purity, except for the end containing the solidified catalyst as an alloy particle.

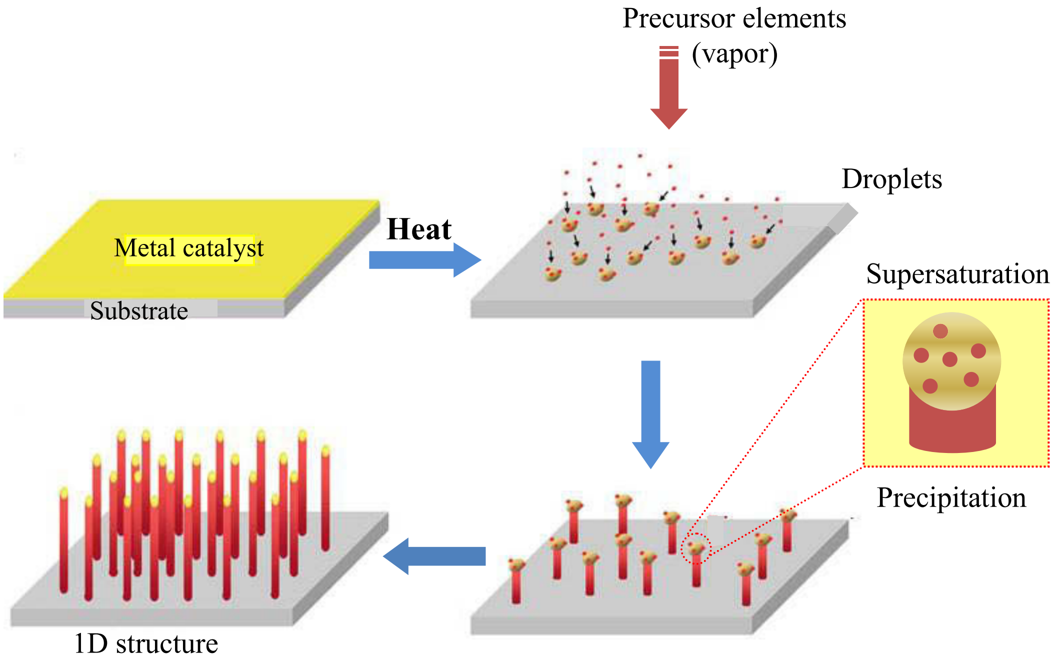

Figure 4.34. Schematic representation of the growth of 1D structures by VLS mechanism.

Because vapor (carries solid components), liquid (catalyst alloy), and solid (precipitated one-dimensional structures) phases are involved, it is known as the VLS mechanism. A direct observation of VLS nanowire growth has been reported using TEM by **Wu *et al.*** (**2001**).

Three phases (gas, liquid, and solid) and two interfaces (gas/solid and liquid/solid) are therefore involved in the VLS mechanism. In these complex system, the kinetics of the VLS mechanism consists of four steps: (1) mass transport in the gas phase; (2) chemical reaction at the vapor-liquid interface; (3) diffusion in the liquid phase; and (4) incorporation of atoms in a crystal lattice (Figure 4.35) (**Givargozov, 1975**; **Kamins *et al.* 2001**; **Lew & Redwing, 2003**; **Kikkawa *et al.* 2005**). Identification of the rate-determining step of the VLS mechanism is therefore complicated as three phases, two interfaces, and chemical reactions are involved (**Givargozov, 1975**). In general, step (4), incorporation of atoms in a crystal lattice is considered as the rate determining step.

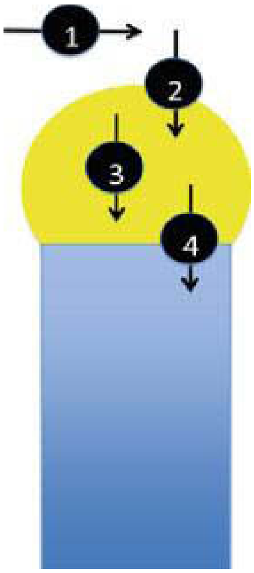

Figure 4.35. Schematic of the kinetic steps in VLS mechanism: (1) mass transport in the gas phase; (2) chemical reaction on the vapor-liquid interface; (3) diffusion in the liquid phase; and (4) in corporation of atoms in a crystal lattice.

It should be noted that the rate-determining step can be changed by the materials involved in the kinetics and by the processing conditions. Therefore, it should be carefully postulated by as many experimental results and data as possible.

VLS requires a metal catalyst can either be self-assembled from a thin film by dewetting, or purchased in colloidal form and deposited on a substrate. The size and position of the catalyst are related to the diameter and position of the 1D structures, as the liquid phase is confined to the area of the precipitated solid phase. The requirements that a metal needs to fulfill to be an effective catalyst are as follows: (1) It must form a liquid solution with a component of the solid phase. (2) The solubility limit of the catalyst component in the liquid phase must be much higher than that in the solid phase (i.e., $K = C_s/C_l < 1$, where C_s is the solubility limit in the solid phase and C_l is the solubility limit in the liquid phase). Under this condition, the catalyst easily leads to the formulation of the liquid alloy with little contamination in the solid phase. (3) The vapor pressure (V_p) of the catalyst component over the liquid alloy should be small. Otherwise, the catalyst will evaporate and eventually disappear in the course of growth. (4) It must be inert to chemical reactions. Otherwise, a reaction could deprive it of its catalytic function. (5) It must not make an intermediate solid. Otherwise, the intermediate solid will also deprive it of its catalytic function (**Wagner & Ellis, 1964**).

The mechanism works at a high temperature at which the metal catalyst forms a liquid alloy. Therefore, chemical processes that occur at high temperatures, such as chemical vapor deposition (CVD), molecular beam epitaxy (MBE), laser ablation (LA) and carbothermal reduction (CR), are generally used in conjunction with the mechanism. Occasionally, metal catalysts sometimes work in a solid state in a vapor or liquid phase environment in a process termed the VSS (vapor-solid-solid) or LSS (liquid-solid-solid) mechanism.

4.2.2. Investigation by HFCVD Method

In the HFCVD process for diamond deposition the gas phase is activated by hot filament or hot surface. In contrast to excitation with electromagnetic waves or by direct current, the gas reaches only temperatures of about 2027 to 2627 °C (**Gat & Angus, 1994**). Using this temperature and the classic thermodynamic ideal gas equation it can be shown, that the internal energy is factor 100 lower than the ionization energy. Since the chemical and thermal reaction close to the filament is not well understood, the heated zone near the filament is described by an approximation, which assumes a constant temperature and chemical composition. As a clue for the approximation, the temperature of the gas near the filament can be determined by thermocouples (**Harris *et al.* 1988**) or laser scattering and is about 1727 °C. However, the filament temperature itself can only be measured through a pyrometer and amounts to about 2227 °C. The distance between the filament and the substrate is normally 5 mm (**May *et al.* 2006**), 5 to 6 mm (**Chattopadhyay *et al.* 2008**), or 7 mm (**Rakha *et al.* 2010**). In individual cases, this amount can vary up to 20 mm (**Nørgård & Matthews, 1996**). The energy transport from the filament to the substrate is dominated by conduction and transport of atomic hydrogen recombination. The mass flux is mainly generated by molecular diffusion. Gas phase recombination of atomic hydrogen is significantly influenced by the reaction: $H+CH_4 = H_2+CH_3$.

Through the distance between filament and substrate, and a substrate temperature around 727 and 927 °C, the temperature gradient and chemical conversion, which depends on convection and thermal conductivity of the gas, can be set. A schematic of the HFCVD deposition process is shown in figure 4.36.

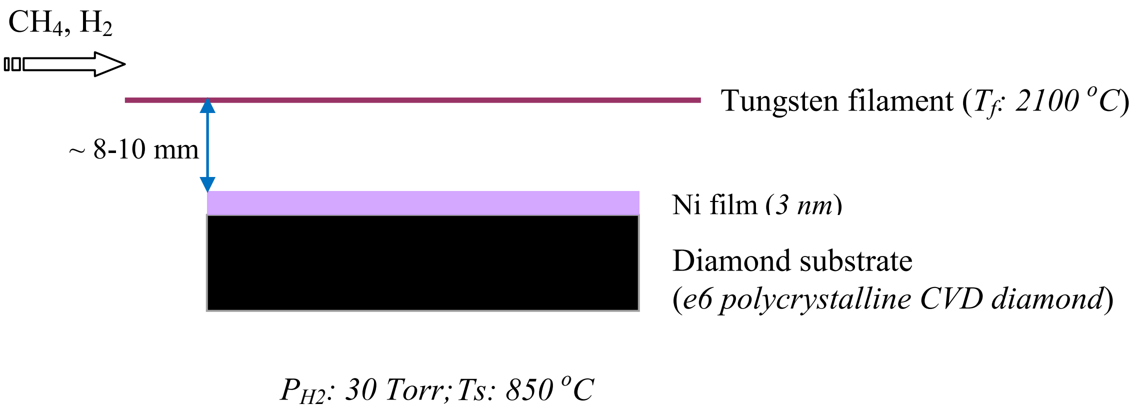

Figure 4.36. Schematic representation of the HFCVD process used in the study for the investigation of VLS mechanism for diamond nanowire growth.

The process started with the annealing of substrate at 400 °C in flowing hydrogen (100 sccm) in order to remove residual contaminants from the substrate and its holder, followed by pre-carburization of the filament at 1200 °C in presence of CH_4 flow in order to reduce filament carbon consumption during deposition and finally the deposition at 2100 °C filament, and 850 °C substrate temperature. The heating cycle of the process has been shown earlier in this chapter schematically in figure 4.2. High filament temperature (typically 2100-2200 °C) is necessary for diamond deposition in the conventional HFCVD process (non-catalytic growth) and no deposition was observed when the filament was kept at a temperature lower than 1727 °C (**Bonnot, 1990**). Other typical deposition parameters are CH_4 concentration in the range of 0.1-3 vol.% in 100 sccm H_2 flow, a pressure of 20-30 Torr and a deposition time of 1-3 hours. Local carbon concentration (near substrate surface) that is difficult to estimate, is very critical for diamond deposition in the process (non-catalytic growth) as various carbon species can be formed with a slight change in the concentration keeping other deposition parameters are constant (**Bonnot, 1990**). In the case of VLS process local carbon (carbon depositing on the catalyst droplet) could also play the similar role and at the diamond growth temperature and pressure, this concentration can be correlated to that of CH_4 in the gas mixture. Figure 4.37 shows the behavior of CH_4 precursor of different concentration in the HFCVD process at diamond growth condition in presence of 3 nm Ni layers deposited on the surface of polycrystalline diamond. Instead of diamond nanowires, carbon nanotube growth was observed where the VLS process could be operative.

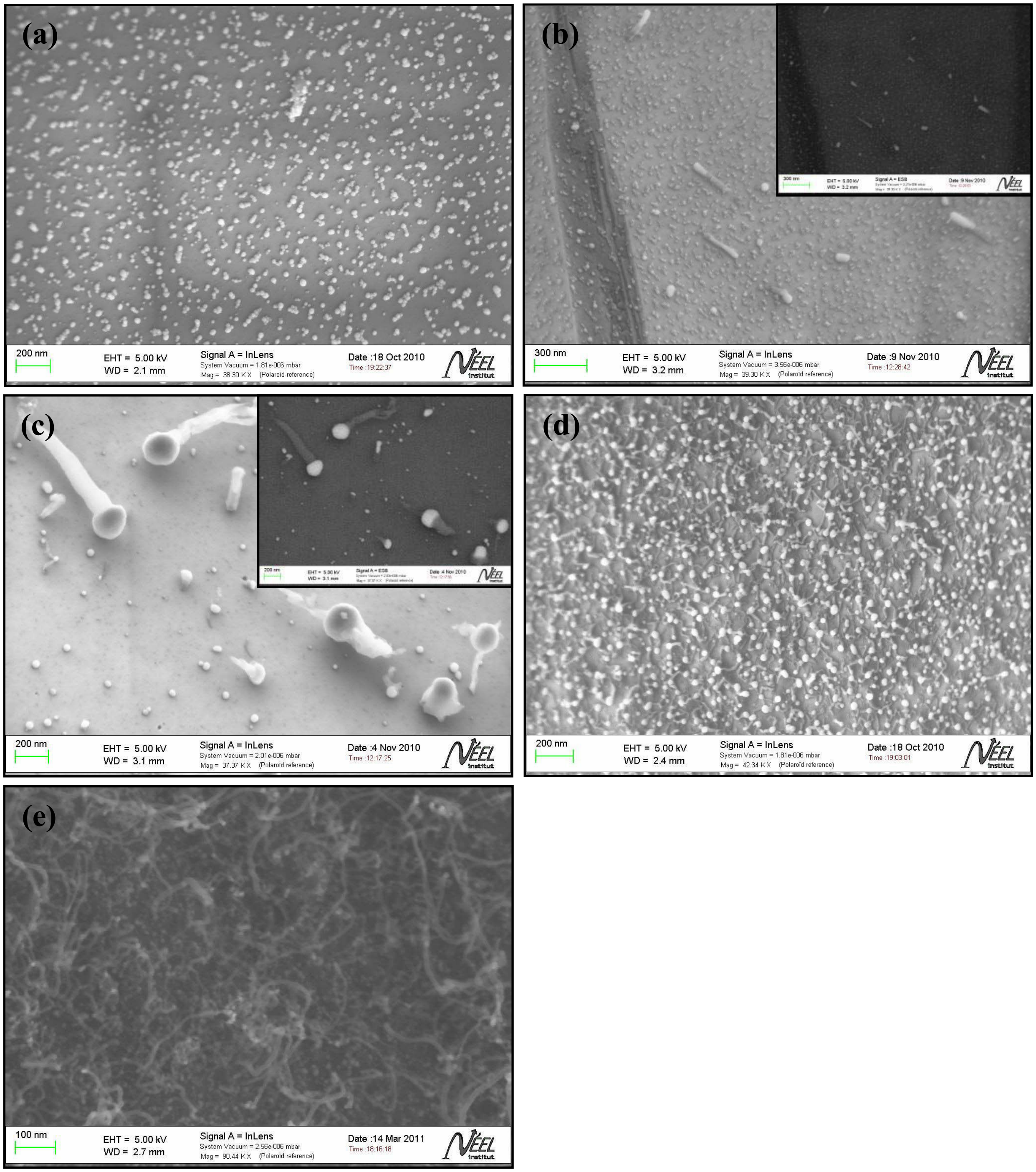

Figure 4.37. SEM images of HFCVD grown samples for 2 hours with (a) 1 vol.%, (b) 2 vol.%, (c) 3 vol.%, (d) 4 vol.% and (e) 6 vol.% CH_4 in 100 sccm H_2, (T_f: 2100 °C, T_s: 850 °C, P_{H2}: 30 Torr). The insets of panels (b) and (c) are corresponding, ESB detected SEM images.

After 2 hours of the HFCVD process only Ni nanoparticles were observed on the substrate surface for 1 vol.% CH_4 (figure 4.37 (a)). The result suggests that local carbon concentration was below the solubility limit of carbon in Ni nanoparticles. The nanoparticles were generated from the initially evaporated 3 nm Ni layers in order to minimize the surface energy. This effect is well known and related to the melting point lowering effect of thin metal films and hydrogen diffusion into the metal (**Gladkich *et al.* 1966**; **Buffet & Borel, 1976**; **Yang *et al.* 1998**; **Pundt, 2004**). With 2 vol.% CH_4, nanoparticles was just supersaturated with carbon and the excess carbon started to precipitate (figure 4.37 (b)). The precipitated carbon encapsulated the nanoparticles forming tubular structures in the case of 3 vol.% CH_4 (figure 4.37 (c)). Further increase in CH_4 concentration continued the growth of these tubes to carbon nanotubes encapsulating Ni nanoparticles at their tips (figure 4.37 (d) and (e)). Due to the limitation in the mass flow controller for CH_4 in the HFCVD system, it was not possible to reduce CH_4 concentration below 1 vol.%.

The observation (figure 4.37) could be correlated to the VLS model proposed for carbon nanotube growth (**Page *et al.* 2010**), where three distinctive stages were identified. Panel (b) of figure 4.37 corresponds to the first stage of the model, nucleation of carbon “cap-precursor”, (c) represents the second stage, “cap-to-tube transformation”, and (d) and (e) are related to the final stage, “continued growth of carbon nanotubes”.

No sign of diamond growth was observed even for 1 vol.% CH_4 which is usually the ideal concentration used in conventional diamond deposition (non-catalytic growth) on non-diamond substrates by using nucleation enhancement methods. This result suggests that hot-filament could absorb most of the carbon very quickly from CH_4 precursor depleting the local carbon concentration required for diamond deposition. It is well known that at 2100 °C hot-filament produces lot of hydrogen atoms that etch non-diamond phase (*sp*^{2} carbon). The appearance of *sp*^{2} phase (carbon nanoube) at higher CH_4 concentration in this temperature could also indicate that the filament activity was reduced due to the fast carburization that could lower the atomic hydrogen concentration. On the other hand, higher deposition time (> 2 hours) and filament temperature (> 2100 °C) was not achieved due to the limited stability of the tungsten filament in carbon atmosphere. In addition, during deposition filament bent into hemisphere in order to accommodate the stress developed due to absorption of carbon. The increased or decreased in the distance between filament and substrate could, indeed, alter the gas chemistry occurred during deposition. It was therefore assumed that the hot-filament could induce a very complicated chemistry and thereby, the HFCVD process would not be ideal for further investigation of the VLS mechanism for diamond nanowire growth.

4.2.3. Investigation by MPCVD Method

Plasma-assisted deposition techniques are very popular methods for growing CVD diamond. Plasma systems offer uniform films over larger substrate areas than hot filament CVD growth. The plasma in the microwave system is detached from any reactor surface hence no impurities from reactor construction materials enter the film bulk during deposition.

The gas phase of the microwave plasma system is not very different from that encountered during HFCVD (**Butler & Woodin, 1993**) – indeed the two techniques operate under similar conditions, producing films with comparable quality film and growth rate. However, the plasma must contain electrons and ionic species which will provide extra chemical reactions not available in the hot-filament system. The investigation of the VLS mechanism for diamond nanowire growth was conducted in a 1.5 KW, 2.45 GHz microwave CVD system (Seki-technotron. Corp. AX-5200) using gas mixture of hydrogen (6N) and methane (4N). A resonant electromagnetic field pattern (mode), created by the microwaves is supported in the chamber and the reactant gases are heated and excited to form a plasma ball. The substrate sits ~1 mm below the visible edge of the plasma ball, on top of molybdenum substrate holder. A schematic of the process is shown in figure 4.38.

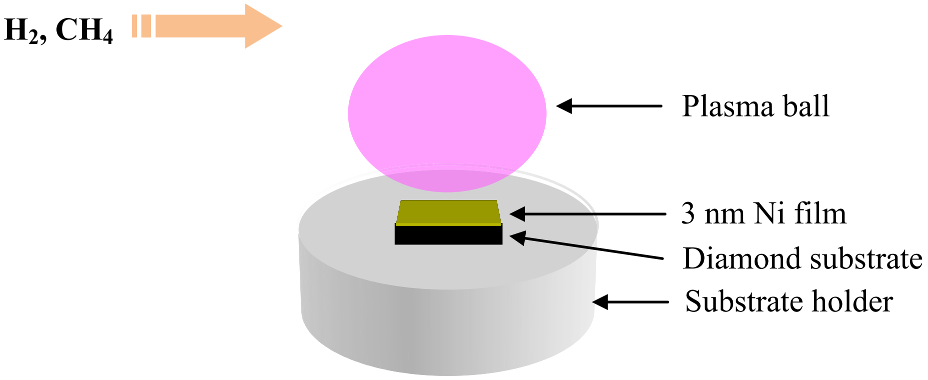

Figure 4.38. Schematic of the plasma enhanced CVD process.

Substrates were electrochemical grade boron doped CVD polycrystalline diamond (figure 4.32) purchased from Element Six. Prior to the CVD process, the substrates were cleaned with isopropanol in an ultrasonic bath and 3 nm Ni layers were then evaporated on the substrate surfaces by e-beam evaporation. During the process, the substrate temperature was measured using an optical pyrometer. Note that no pre-treatment of the substrate surface to enhance diamond nucleation was performed.

After 1 hour of deposition with 1 vol.% CH_4, growth of nanocrystalline diamond covering the substrate surface was observed. At few locations, where carbonaceous balls (**Bonnot, 1990**) were formed, in the same sample long and straight nanowires appeared. Nanowires could be made of carbon as only hydrogen and methane was present in the gas phase, and also the substrate was diamond. The experimental conditions are summarized in Table 4.3 and the SEM observation of this sample is shown in figure 4.39.

Table 4.3. Growth conditions of the nanostructures (with 3 nm Ni layers) shown in figure 4.41.

Total gas pressure	30 Torr
Gas flow rate:	H_2 - 297 sccm; CH_4 - 3 sccm
Microwave power	850 watt
Substrate temperature	1000 °C
Deposition time	1 hour

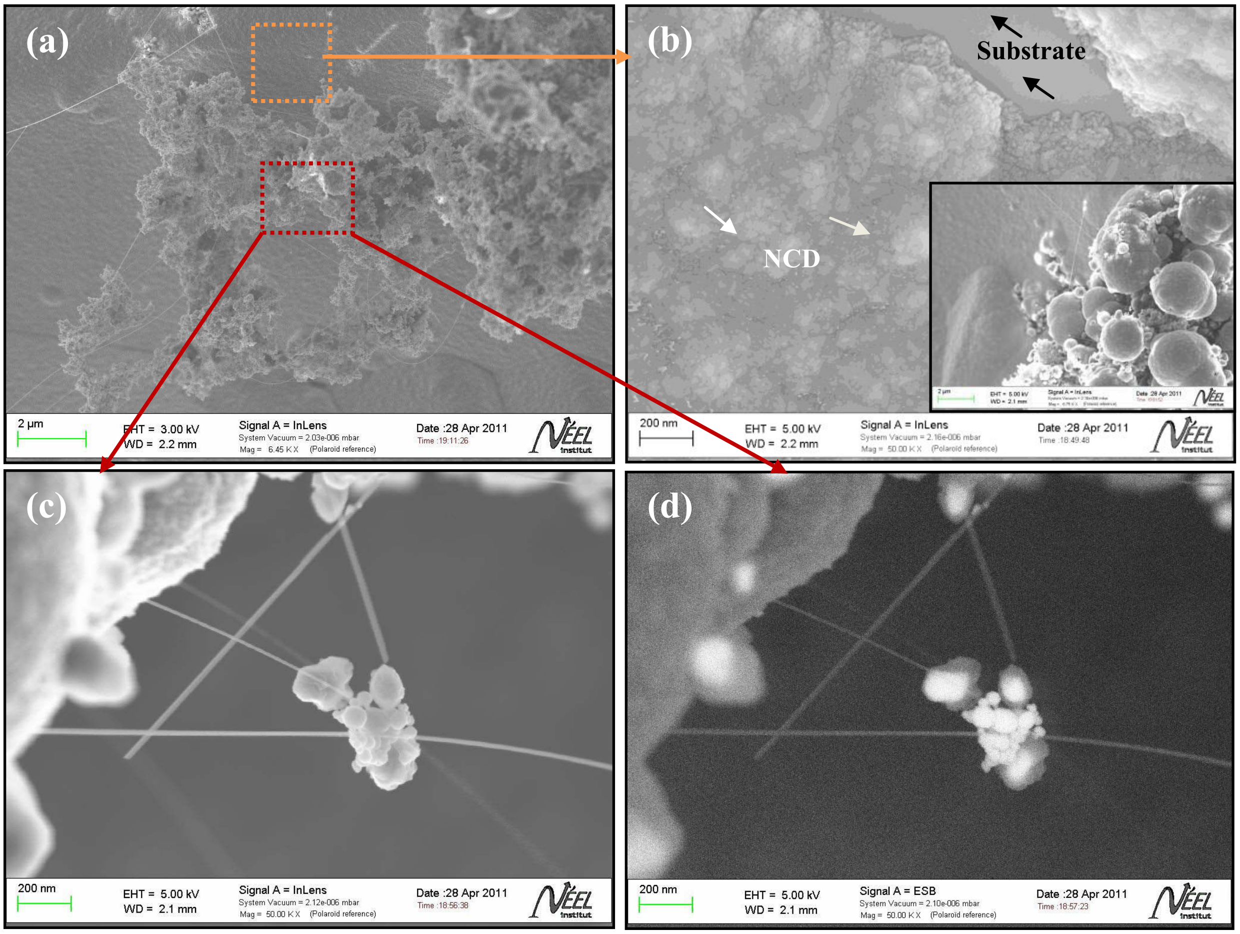

Figure 4.39. SEM images of MPCVD deposited nanostructures on a polycrystalline diamond substrate with 3 nm Ni layers and 1 vol.% CH$_4$ in the gas phase; (a) nanostructures at low magnification, (b) nanocrystalline diamond layer covering the substrate surface, the inset showing the carbonaceous balls formed on few places in the sample, (c) nanowires appeared only near and on the carbonaceous balls and (d) ESB detected SEM image where bright contrast representing the Ni nanoparticles.

Further characterization of these nanowires was not possible because of their very low density on the substrate and poor reproducibility. From the SEM observation it is found that one end of the nanowires are buried either in the nanocrytalline diamond layer or inside the carbonaceous ball and the free end does not show the presence of Ni nanoparticles. The nanoparticles could be present at the buried end but it is not conclusive and thereby it is difficult to say that the VLS process was operative in the nanowire growth. On the other hand, the location of nanowire growth, near and on the carbonaceous balls, suggests that carbon rich region, preferably in *sp*^{2} form, could favor the 1D growth with or without the assistance of metal catalyst. Note that **Bonnot** (**1990**) observed the growth of carbonaceous balls (cauliflower-like) during HFCVD deposition of diamond with 4 vol.% CH_4 and she concluded that these structures could be a mixture of sp^2 and sp^3 carbon.

Under the same deposition conditions (Table 4.3) but with increased CH_4 concentration (2 vol.%) in the gas phase resulted in the growth of carbon nanostructures different than that was observed for 1 vol.% CH_4 (figure 4.39). The morphology of these nanostructures is displayed in the SEM images shown in figure 4.40.

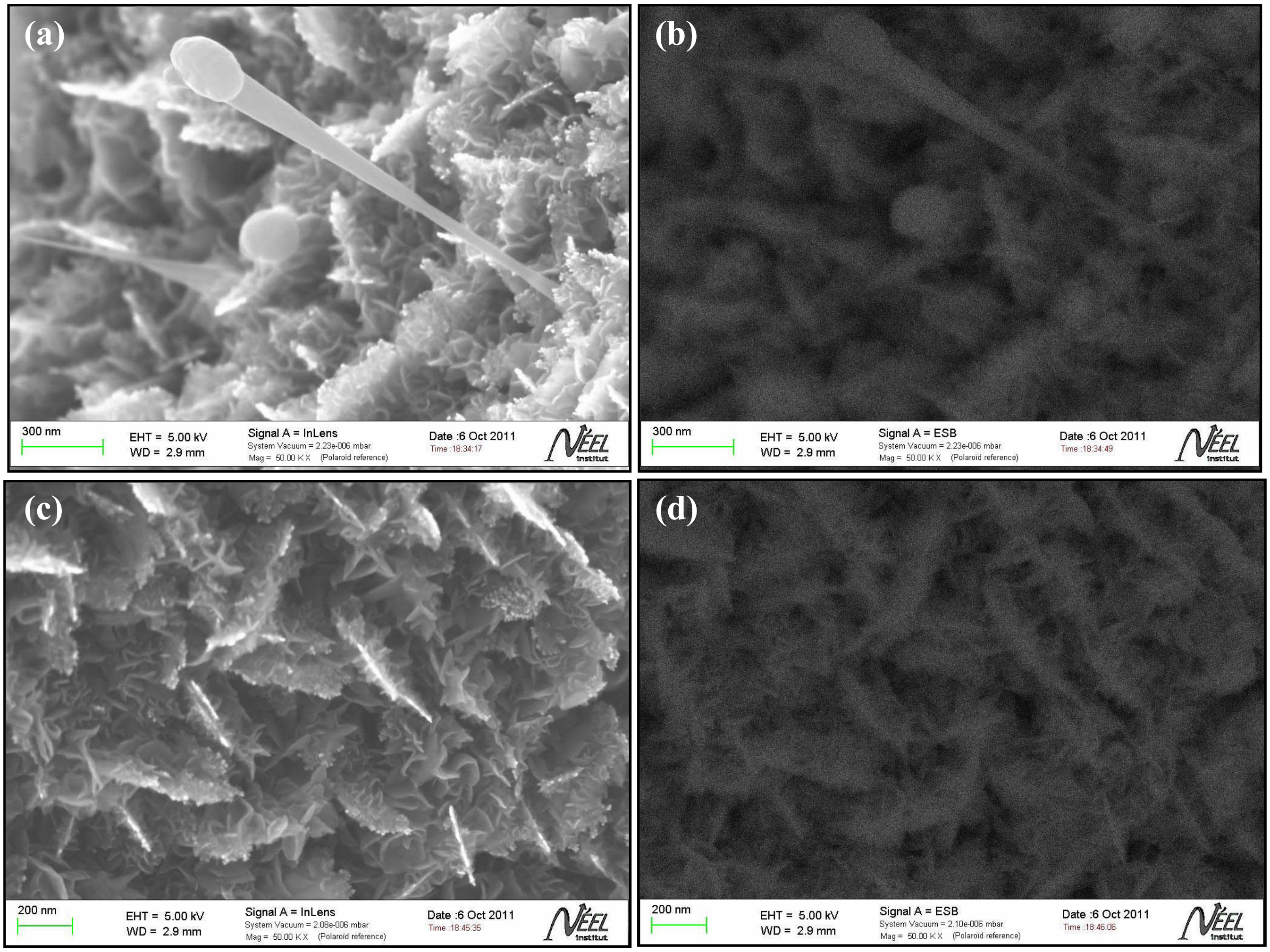

Figure 4.40. SEM images of carbon nanostructures appeared on the diamond substrate under the same deposition conditions, as listed in Table 4.3, but with 2 vol.% CH_4 in the gas phase; (a) nanowire and nanowalls, (b) corresponding ESB detected image showing similar contrast between nanowire and nanowalls, i.e., both nanostructures could be made of same material (carbon), (c) nanowalls and (d) corresponding ESB detected image.

Instead of nanocrystalline diamond layer, growth of uniformly distributed and randomly oriented carbon nanowall (CNW) clusters was observed on the diamond substrate (figure 4.40 (a) and (c)). Each CNW cluster had a “flower-like” shape with CNWs projecting in all directions (figure 4.40 (c)), which is similar to the observations made by **Chuang *et al.*** (**2006**) where CNWs were grown by microwave plasma-enhanced CVD deposition (PECVD) using the growth parameters of carbon nanotube.

“Carbon nanowalls” (CNWs), also referred to as “carbon nanoflakes”, were first discovered by **Wu *et al.*** (**2002**) through PECVD deposition using transition metals as catalysts. CNWs are two-dimensional “graphitic” platelets that are typically oriented vertically on a substrate. An individual CNW has been reported to have a few stacked layers ("graphitic”) with typical lateral dimensions of several micrometers (**Malesevic *et al.* 2008**). There have been a number of studies focused on understanding the CNW growth mechanism and thus targeting control of the growth process (**Hung *et al.* 2009; Wu *et al.* 2002; Shimabukuro *et al.* 2008; Levchenko *et al.* 2007**). While not fully understood, the formation of nanowalls appears to depend on the local electric field in the PECVD system (**Wu *et al.* 2002**). Nevertheless, the sharp edges, vertical orientation and high surface area make CNWs a potential field emission (**Takyo *et al.* 2008**) and a catalyst support material (**Yang *et al.* 2002**).

Together with carbon nanowalls, growth of few nanowires was observed on the diamond substrate (figure 4.40 (a)). They were randomly distributed over the substrate surface and a round object was observed at their tips. ESB detected SEM image (figure 4.40 (b)) shows similar contrast between the nanowire tip and body. This observation suggests that both structures could be made of the same material, carbon, as only hydrogen and methane were present in the gas phase. On the other hand, the SEM images do not show the presence of Ni nanoparticles on the substrate. The nanoparticles could be encapsulated in nanowire tips that are covered by the relatively thick second carbon layer (round object) and thereby they did not appear in the SEM image. Indeed, the nanoparticles could catalyze the growth of these nanowires. This assumption could well be supported by the observation shown in figure 4.41, where Ni nanoparticles were observed as encapsulated in the nanowire tips (figure 4.41 (b)) for 30 min deposition with 2 vol.% CH4 using the conditions listed in Table 4.3. Instead of carbon nanowalls, the susbtrate surface was found to be covered by carbon particle clusters that could form nanowalls for further deposition.

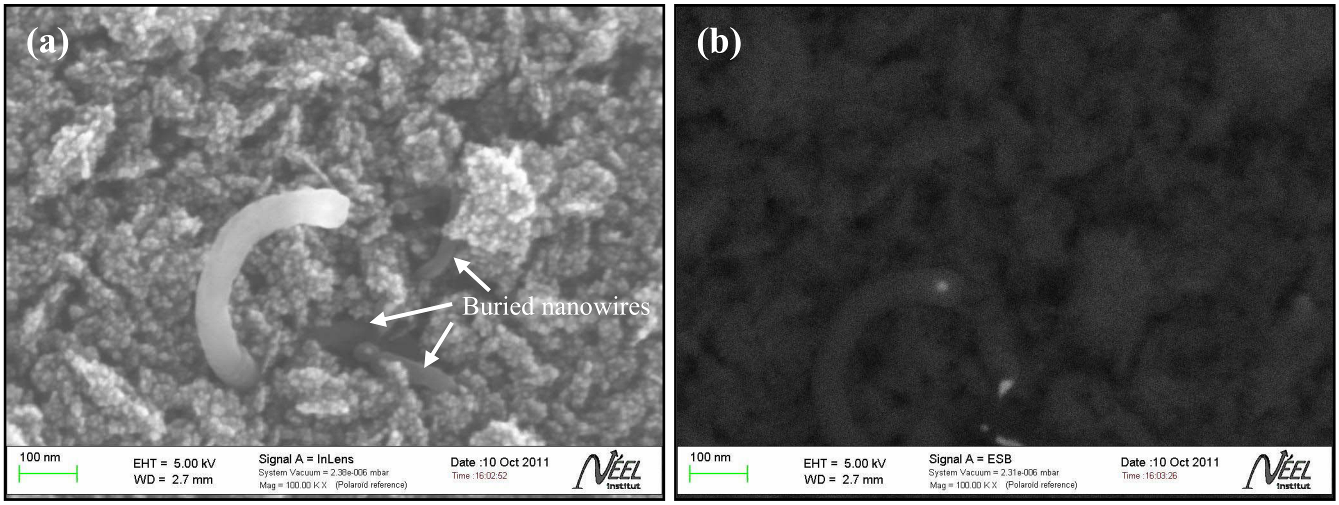

Figure 4.41. (a) SEM image of the nanostructures on the diamond substrate after 30 min deposition with 2 vol.% CH_4 using the conditions listed in Table 4.3 and (b) corresponding ESB detected SEM image showing the presence of Ni nanoparticles (bright contrast) as encapsulated in the nanowire tips.

By using both CH_4 concentrations, 2 vol.% and 1 vol.%, consecutively in a single disposition run, growth of long and highly dense nanowires was observed on the diamond substrate. The deposition process was started with 2 vol.% CH_4 using the conditions shown in Table 4.3. After 1 hour, the CH_4 concentration was adjusted to 1 vol.% and the deposition then continued for 1 hour without changing the other deposition parameters. The sample was then characterized by SEM and Transmission Electron Microscopy (TEM). TEM measurement was carried out in collaboration with Daniel Araujo, Universidad de Cádiz, Spain.

SEM analysis: The morphology of the deposited nanostructures is displayed in the SEM images shown in figure 4.42. The figure shows that nanowires are tangled and randomly oriented over the substrate surface. The average diameter of these nanowires is about 100 nm and the length ranges from a few hundred nanometers to several micrometers based on SEM analysis. No growth of carbon nanowalls was observed and the Ni nanoparticles did not appear in the SEM images. The nanoparticles again could be encapsulated at the nanowire tips that are covered by a second carbon layer, similar to the observation of figures 4.40 and 4.41. The nanowires could therefore have cor-shell structure made of carbon.

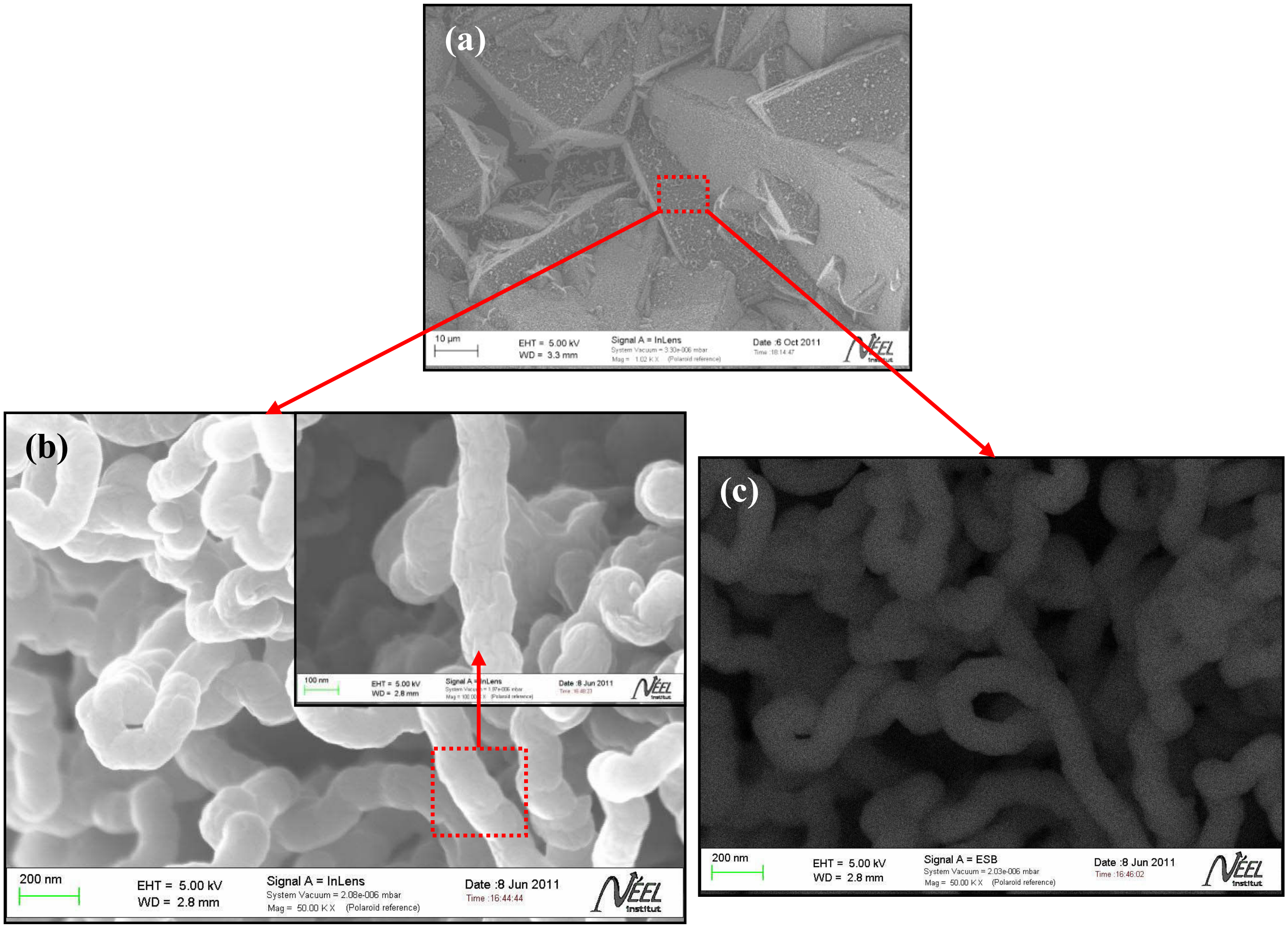

Figure 4.42. SEM images of the deposited nanowires grown using 2 and 1 vol.% CH_4 consecutively in a single deposition; (a) at low magnification, (b) high magnification image showing random orientation (tangled) of the nanowires and (c) SEM image acquired with an EsB detector showing uniform contrast.

TEM results: For TEM analysis, few nanowires were pulled out from the nanowire bundle in the diamond substrate and positioned on a carbon coated Cu TEM mesh grid. A focused ion beam (FIB) and a nanomanipulator whose tip diameter was in the submicron range was used to pull out the nanowires. This process is commonly known as FIB-lift-off technique (**Langford & Rogers, 2008**; **Takeuchi *et al.* 2001**). The nanomanipulator tip is made of tungsten. Once the tip touched the open end of nanowire, a platinum (Pt) deposition (from an organic metal precursor) was made between the tip and the nanowire for adhesion by using an electron beam (5 kV/98 pA e-beam intensity). A strong „pull-out force‟ was then applied to extract the nanowire from the bundle.

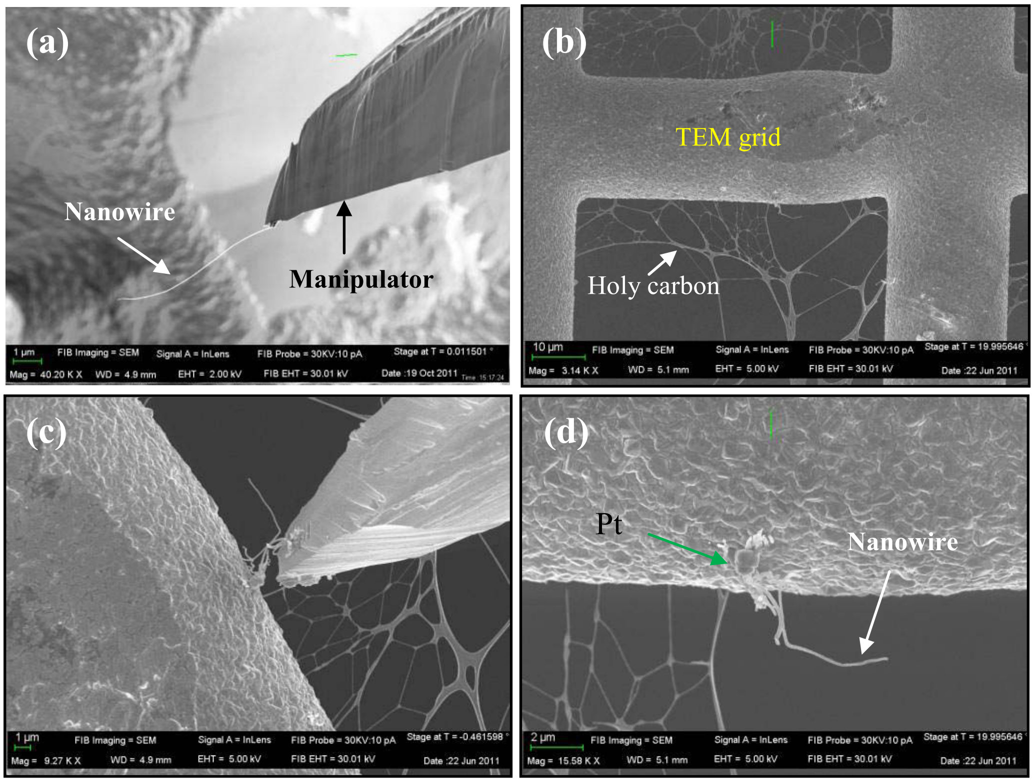

Figure 4.43. SEM images showing nanowire transfer from substrate to TEM grid; (a) an individual nanowire attached to the FIB manipulator, (b) Cu TEM mesh grid, (c) nanowire glued to the grid by Pt metal evaporation and (d) nanowire on the grid glued at one end.

The „pulled“ nanowire was placed and positioned on the TEM grid by the nanomanipulator (figure 4.43). After the nanowire landed in the desired position, the free end of nanowire was adhered to the grid by Pt deposition. The ion beam was used to cut the linkage between the tip and the nanowire made by Pt deposition.

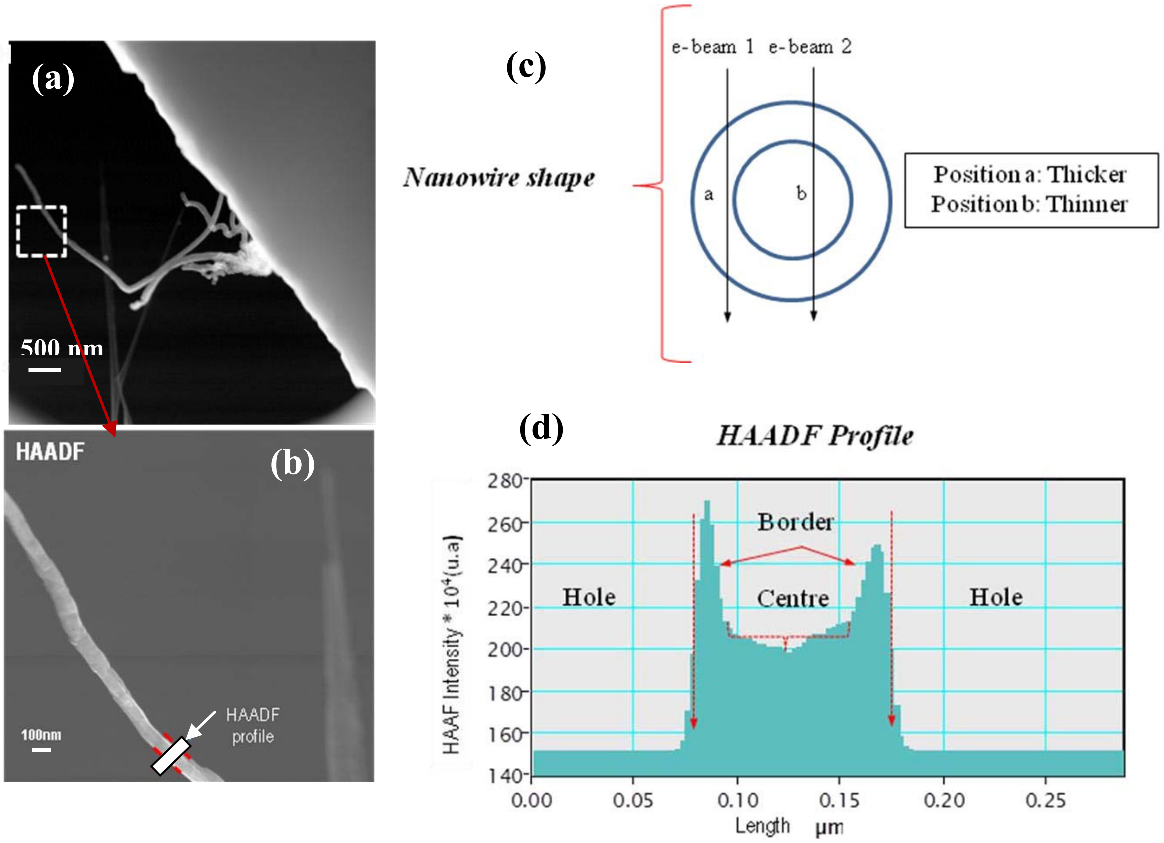

Figure 4.44. (a) HAADF image of the nanowire, (b) high magnification image, white arrow indicates the area from where HAADF was profile obtained, (c) a schematic of the nanowire shape and (d) thickness related profile revealing tubular shape of the nanowire with wall thickness of about 50 nm.

Figure 4.44 shows the high angle angular dark field (HAADF) profile that reveals the tubular shape of the nanowire with wall thickness of about 50 nm. Selected area electron diffraction (SAED) pattern of the nanowire is shown in figure 4.45.

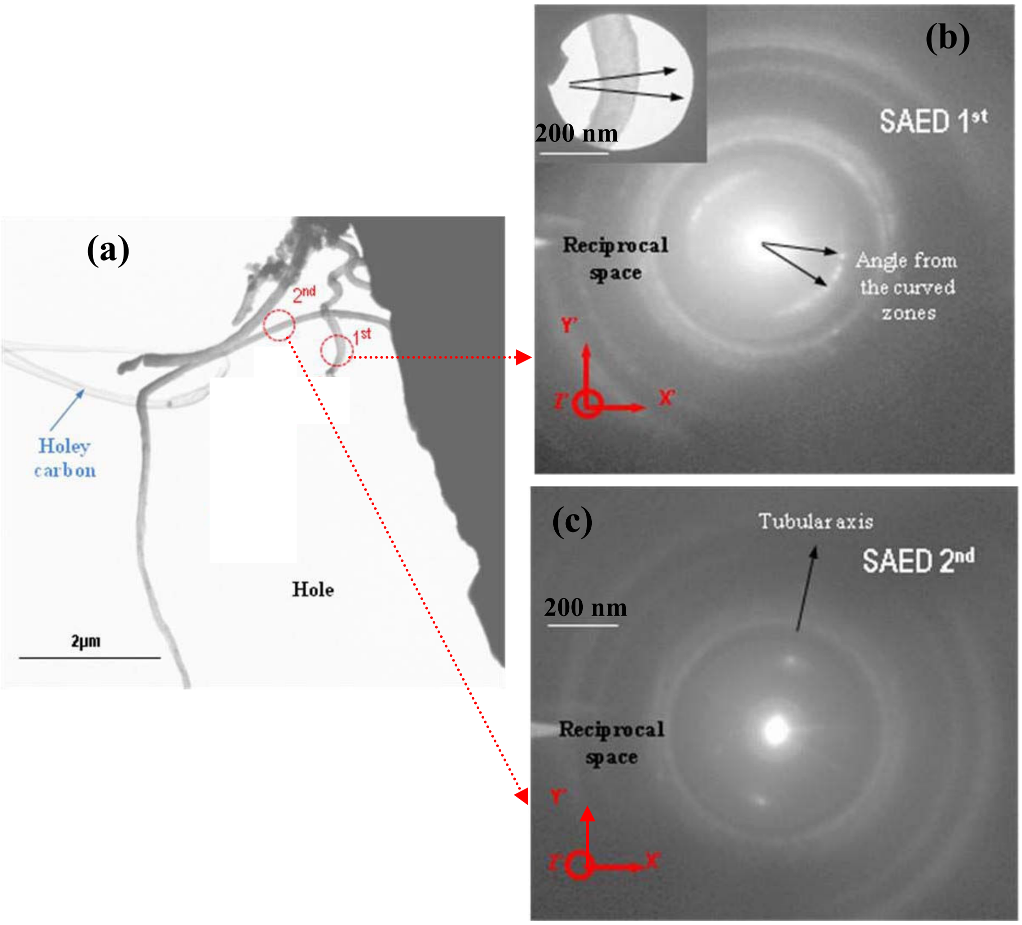

Figure 4.45. (a) TEM micrograph at low magnification; the locaion of the selected area obserervation are indicated by the dashed circles (red color), (b) electron diffraction pattern from the 1st studied zone; the inset shows the corresponding area and (c) electron diffraction pattern from the 2nd studied zone; the inset shows the corresponding area.

Diffraction spots have a spherical shape (figure 4.45 (b)) due to the curved area over which SAED was recoded. Such diffraction pattern is commonly observed for graphitic structure (**Brizoual *et al.* 2007**). The diffraction pattern in figure 4.45 (c) shows the crystallininity of the nanotube in the Y direction and elongated spots in the X direction due to reduced lateral direction of the nanotube.

4.3. Investigation of the Solid-Liquid-Solid (SLS) Mechanism

The Solid-liquid-solid (SLS) growth mechanism shares many similarities with the well known vapor-liquid-solid (VLS) mode, for example, both of them are mediated by nano-scaled catalyst drops with the diameter of the nanowires being determined by the size of catalyst drops. Meanwhile, they differ strikingly in the growth balance conditions and the principles in morphology control. All these differences arise from the solid state precursor in an SLS process, instead of vapor phase precursor.

4.3.1. SLS for SWCNT Growth: Basis of the Investigation

In addition to VLS process, the SLS mechanism has also been investigated for the synthesis of 1D-carbon nanostructures, in particular, single-wall carbon nanotubes (SWCNTs) and nanofibers. It is argued that the SWCNT growth mechanism is a kind of solid-liquid-solid graphitization of amorphous carbon or other imperfect carbon forms catalyzed by molten supersaturated carbon-metal nanoparticles (**Kataura *et al.* 2000**; **Saito *et al.* 1995**; **Bandow *et al.* 1998**; **Gorbunov *et al.* 1999**). This mechanism is illustrated in figure 4.46.

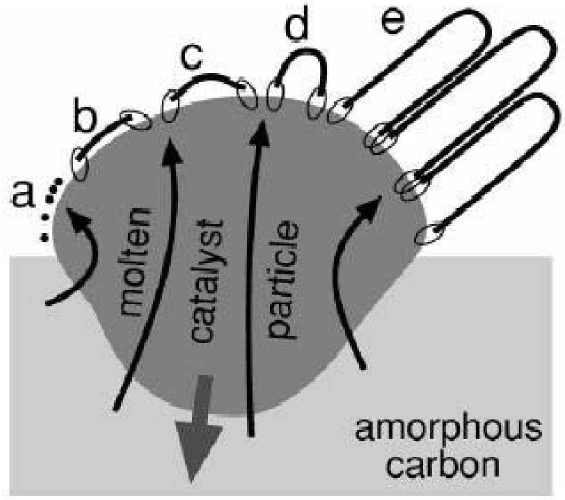

a. Carbon atom precipitation
b. Atom arrangement in a graphene sheet
c. Graphene sheet Buckling
d. SWCNT nucleation
e. SWCNT growth

Figure 4.46. The proposed solid-liquid-solid mechanism of SWCNT ncleation and growth by dissolution-precipitation of amorphous carbon condensed at early stages of the reaction. Ellipses symbolize the overlapping metal-carbon electron orbitals.

A molten catalyst nanoparticle penetrates an amorphous carbon aggregate dissolving it and precipitating carbon atoms (figure 4.46 (a)). These atoms arrange in a graphene sheet (figure 4.46 (b)), whose orientation parallel to metal-carbon melt is not energetically favorable. Any local defect of this graphene sheet will result in its buckling (figure 4.46 (c)) and formation of a SWCNT nucleus (figure 4.46 (d)). Further precipitating carbons incorporate in edges of growing nanotube (figure 4.46 (e)) which are anchored to catalyst nanoparticle by overlapping its unsaturated sp^2 orbitals with the metal orbitals of the catalyst nanoparticles.

The synthesis temperature and the nature of the catalyst metal seem to be the most critical process parameters among the studied ones (**Kataura *et al.* 2000**; **Saito *et al.* 1995**; **Bandow *et al.* 1998**; **Gorbunov *et al.* 1999**). The optimum synthesis temperature is determined by two competing factors. On the one hand, the higher the temperature the more catalytic nanoparticles are molten and able to nucleate SWCNTs and to maintain their growth. On the other hand, the driving force for the amorphous carbon increases with reduction of the synthesis temperature. Experimentally, the optimal synthesis temperature lies 100-200 K below the equilibrium eutectic temperature of the catalyst (**Kataura *et al.* 2000**; **Gorbunov *et al.* 1999**).

In the SLS mechanism, the initial vaporization of the carbon source is not an important condition for the SWCNT formation. A low-temperature transformation of a disordered carbon into SWCNTs was observed (**Chadderton *et al.* 1999**), where nanotubes were grown without involving any deposition from the vapor phase or chemical reactions. The carbon feedstock for the growing SWCNTs is the condensed amorphous and the SWCNT growth is therefore a condensed state transformation of one solid form of carbon into the other. A known condensed state reaction of this kind is the catalytic graphitization. It involves a group VI /and VIII metal dissolving non-graphitic carbon phases and precipitating carbon in form of graphite when cooled, or as a consequence of supersaturation (**Derbyshire *et al.* 1975**; **Fedorov *et al.* 1978**). The metal acts as a transporting medium and the driving force behind the soot reaction is the free energy difference $\Delta G = \Delta H — T\Delta S$ between the initial and the final forms of carbon, where ΔH and ΔS are the corresponding differences in the specific standard enthalpy and entropy of formation.

4.3.2. SLS for Diamond Nanowire: Results and Discussion

In order to investigate the SLS mechanism for diamond nanowire growth, a nanocrystalline diamond film (NCD) with thickness ~ 300 nm and average grain size ~ 100 nm grown on Si substrate (figure 4.29) was used as the only source of carbon (solid state precursor), no other hydrocarbon was added in the gas phase. Ni layers with thickness in the range of 1-3 nm were evaporated on the diamond surface as catalyst. It is commonly known that the grain size of a nanocrystalline diamond film determines the surface to volume ratio, which is in turn the main determining factor in the *sp*^{2} and hydrogen content (**Williams, 2011**). Obviously, smaller grains (≤ 100 nm) result in higher surface areas, which in turn lead to a higher *sp*^{2} and hydrogen content due to the enhanced grain boundary volume (**Williams *et al.* 2008**, **2010**, **Kriele *et al.* 2009**; **Michaelson *et al.* 2010**). During the SLS process, this *sp*^{2} phase could be the potential source of carbon for nanowire growth. It has also been shown that hot Ni particles destroy the crystallinity of diamond at the diamond-Ni interface (**Anton, 2006**). This amorphous carbon might be able to diffuse into and through the Ni and precipitate at the vacuum interface (**Lander *et al.* 1952**; **Clifton & Evans, 1995**).

In this work, the SLS process was investigated in the hot-filament CVD (HFCVD) reactor (chapter 3, figure) under hydrogen environment using the diamond growth temperature (~ 2200 °C) and pressure (~ 20 Torr). Hot-filament and hydrogen atmosphere were used to provide a favorable condition for diamond growth, where hot-filament would produce atomic hydrogen to etch *sp* and *sp*^{2} carbon sites on the growing nanowire converting them to *sp*^{3} carbon (**Butler *et al.* 2009**) and thereby, assisting diamond nanowire growth.

The process used for this work is shown schematically in figure 4.47.

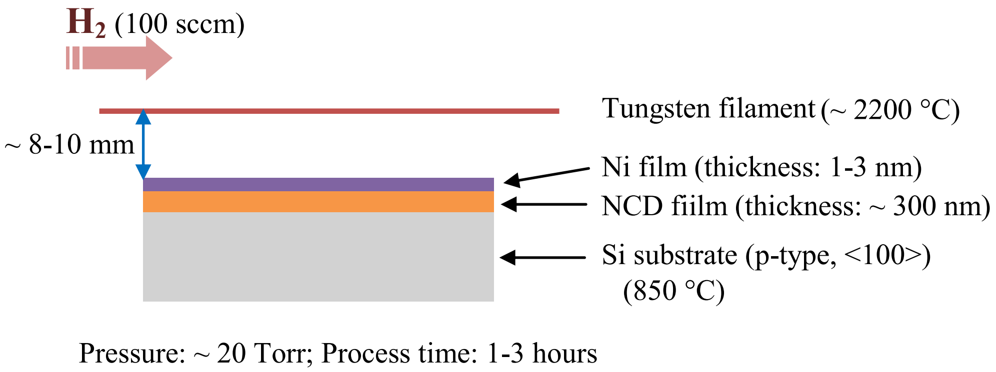

Figure 4.47. Schematic of the experimental process for the investigation of the SLS mechanism.

Figure 4.48 shows the morphology of the processed NCD films with 2 and 3 nm Ni layers for 2 hours.

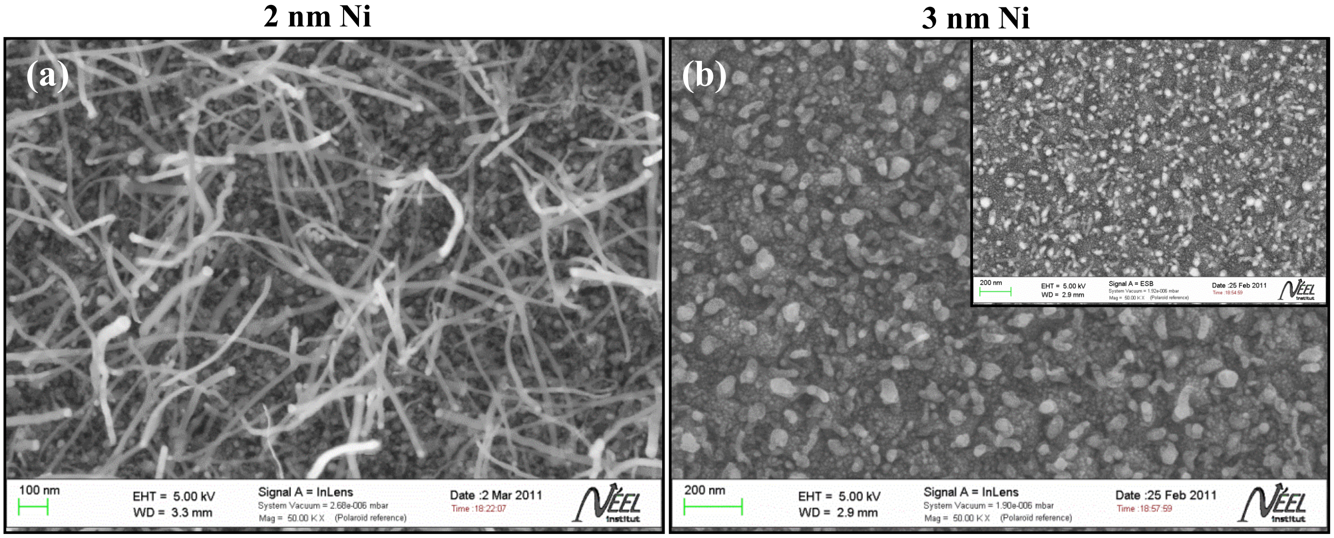

Figure 4.48. SEM images of the processed NCD films with (a) 2 nm and (b) 3 nm Ni layers for 2 hours, (T_f: 2200 °C; T_s: 850 °C; P_{H2}: 20 Torr); the inset of panel (b) is the corresponding EsB detector recorded SEM image.

Nanowire growth was observed for the NCD film processed with 2 nm Ni layers (figure 4.48 (a)), whereas the film processed with 3 nm Ni layers resulted in the formation of Ni nanoparticles and transparent carbon films around the particles (figure 4.48 (b)). Interestingly, the nanowire growth was reproducible only when two NCD films were processed together with different Ni layer thickness, e.g., 2 nm and 3 nm Ni layers (figure 4.48). In some cases, nanowires appeared on the film processed with 3 nm Ni layers instead of 2 nm Ni layers. Note that the NCD film was deposited on a 2 inch Si wafer in a PECVD reactor and the wafer was then broken into small parts that were used for this investigation.

On the other hand, when only one NCD sample was processed with Ni layers of thickness 2 or 3 nm, formation of nanopores was observed in the diamond film. Figure 4.49 (a) shows the nanopore formation with average diameter about 30 nm (based on SEM analysis) in the NCD film after 2 hours processing with 2 nm Ni layers at the filament temperature of 2200 °C.

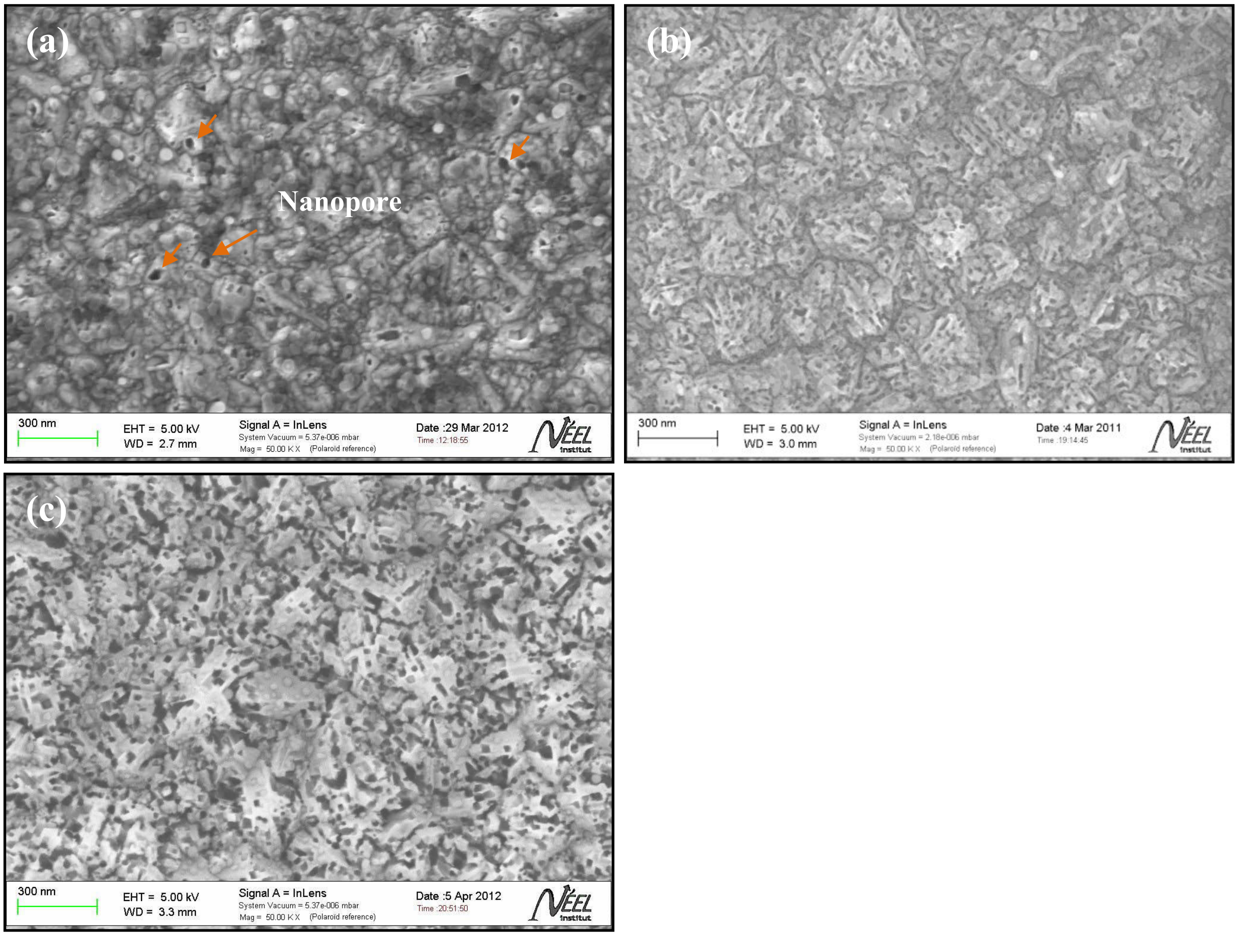

Figure 4.49. SEM images of the processed NCD film with 2 nm Ni layers for 2 hours at (a) 2200 °C, (b) 1200 °C and (c) no filament heating ($T_f = 0$), (T_s: 850 °C, P_{H2}: 20 Torr). In panel (a) few nanopores are indicated by arrows.

A significant increase in the nanopore density was observed when filament activity, production of atomic hydrogen, was reduced, i.e., at low filament temperature (e.g., 1200 °C) (figure 4.90 (b)). On the other hand, nanopore formation was observed even when the filament heating was stopped (T_f = 0), only substrate was heated (T_s = 800 °C) (figure 4.49 (c)).

Similar phenomena occurred when polycrystalline diamond substrate (figure 4.34) was processed with Ni layers under the similar conditions. Figure 4.50 shows the nanopore formation with average diameter about 45 nm (based on SEM analysis) in polycrystalline diamond substrate after 2 hours processing with 3 nm Ni layers at different temperatures.

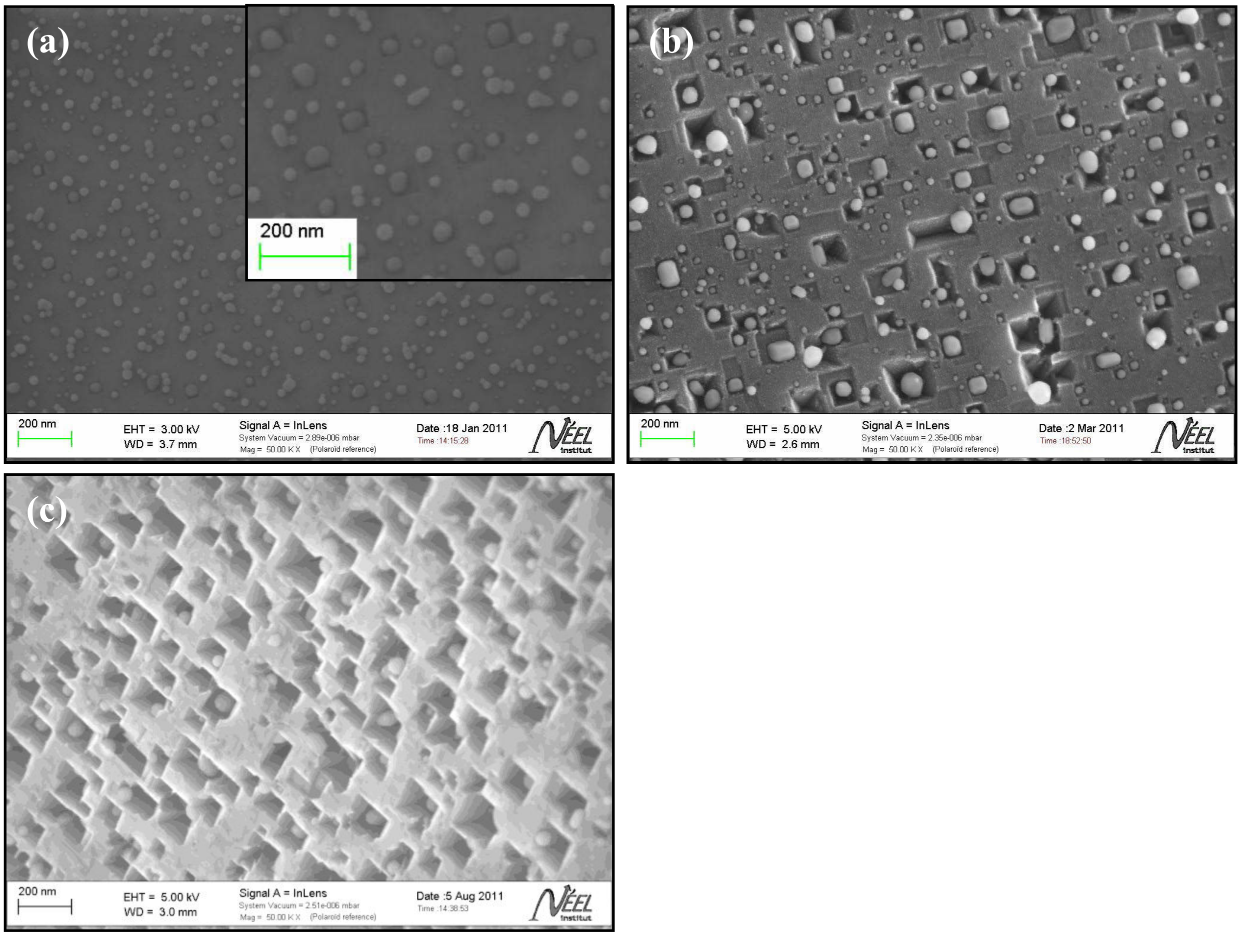

Figure 4.50. SEM images of (100) surface of the processed polycrystalline diamond substrate with 3 nm Ni layers for 2 hours at (a) 2200 °C, (b) 1200 °C and (c) no filament heating ($T_f = 0$), (T_s: 850 °C, P_{H2}: 20 Torr). The inset of panel (a) is the corresponding magnified image.

From figures 4.49 and 4.50, it is obvious that nanopores can be formed in diamond, whatever its microstructure, without any need for a hot-filament process. Ni nanoparticles could play the major role in removing the carbon atoms from the diamond surface and thereby, forming nanopores. As discussed earlier that hot Ni particles destroy the crystallinity of diamond at the diamond-Ni interface (**Anton, 2006**). This amorphous carbon might be able to diffuse into and through the Ni and precipitate at the vacuum interface (**Lander *et al.* 1952**; **Clifton & Evans, 1995**). No growth of carbon materials suggests that the precipitated carbon atoms could be etched away by atomic hydrogen produced by either hot filament or Ni catalyst. Hydrogen could also diffuse into the molten Ni particles and gasifies the dissolved carbon to form hydrocarbons. Similar chemical reactions have been detected also on activated carbon and natural graphite crystals as reported by **Tomita *et al.*** (**1974**). This group observed the formation of etched channels in graphite substrates which were accompanied by the formation of methane.

Since the nanopore formation is associated with the removal of carbon from diamond with the assistance of metal catalyst, the approach could be regarded as a catalytic etching process. Usually etching of diamond, required for device fabrication, is performed almost exclusively with reactive ions with a resolution that is strongly limited to lithographical processes (**Hausmann *et al.* 2010**; **Janssen & Gheeraert, 2011**). As shown here, the catalytic etching process could generate nanopores without any need for a lithograpy process. This process therefore shows the potentialities to be a simple and cost-effective etching method for diamond. In order to optimize the process for the fabrication of nanopores with controlled diameter, depth and density, the process was investigated extensively by studying different process parameters, such as etching temperature, time, atmosphere, catalyst nature and thickness, etc. The investigation is presented in the next chapter, Chapter 5, in detail.

Bibliography

Angus, J. C. & Hayman, C. C. **1998** *Science* 241, 643.

Anton, R ; **2008** *Carbon* 46, 656.

Baker, R. T. K., Harris, P. S. Thomas, R. B. & Waite, R. J. **1973** *J. Catal*. 30, 86.

Bandow S, Asaka S, Saito Y, Rao AM, Grigorian L, Richte E, Eklund PC. **1998** *Phys. Rev. Lett.* 80, 3779.

Behr, M. J., Gaulding, E. A., Mkhoyan, K. A. & Aydil, E. S. **2010** *J. Vac. Sci. Technol. B* 28, 1187.

Berger, H. F., Grosslinger, E. & Rendulic, K. D. **1992** *Surf. Sci.* 261, 313.

Bonnot, A. **1990** *Phys. Rev*. B 41, 6040.

Brizoual, L. Le., Belmahi, M., Chatei, H. & Assouar, M. B. **2007** *Diamond Relat. Mater*. 16, 1244.

Butler, J.E., Mankelevich, Y.A., Cheesman, A., Ma, J. & Ashfold, M.N.R. **2009** *J. Phys.: Condens. Matter* 21, 364201.

Butler, J.E. & Woodin, R.L. **1993** *Phil. Trans. R. Soc. Lond. A* 342, 209.

Chadderton, L. T. & Chen, Y. **1999** *Phys. Lett. A* 263, 401.

Chattopadhyay, A., Sarangi, S. K. & Chattopadhyay, A. K. **2008** *Appl. Surf. Sci.* 255, 1661.

Chen, K. H., Wu, C. T., Hwang, J. S., Wen, C. Y., Chen, L. C. *et al*. **2001** *J. Phys. Chem. Solids* 62, 1561.

Chuang, A. T. H., Boskovic, B. O. & Robertson, J. **2006** *Diamond Relat. Mater.* 15, 1103.

Clifton, P. H. & Evans, S. **1995** *Ind. Diamond Rev.* 55 26.

Derbyshire F., Jagtoyen, M. & Thwaites. M. **1995** In *Carbons: characterizations and applications*. (ed. Jr. W. Patric), 1st ed. United Kingdom.

Ding, F., Bolton, K. & Rose´n, A. **2006** *Comput. Mater. Sci.* 35, 243.

Gamarnik, M. Y. **1996** *Phys. Rev. B* 54, 2150.

Gamarnik, M. Y. **1996** *NanoStruct. Mater.* 7, 651.

Gheeraert, E. **1992** PhD thesis, Université Joseph Fourier, Grenoble, France.

Givargozov, E. I. **1975** *J. Cryst. Growth* 31, 20.

Gladkich, N. T., Niedermayer, R. & Spiegel, K. **1966** *Phys. Status Solidi B* 15, 181.

Gorbunov, A. A., Friedlein, R., Jost, O., Golden, M. S. *et al.* **1999** *Appl. Phys. A* 69, S593.

Gross, A. **1998** *Appl. Phys. A: Mater. Sci. Process.* 67, 627.

Harris, S. J., Weiner, A. M. & Perry, T. A. **1988** *Appl. Phys. Lett*. 53, 1605.

Hausmann, B. M., Khan, M., Zhang, Y., Babinec, T. M., Martinick, K., McCutcheon, M., Hemmer, P. R. & Lončar, M. **2010** *Diamond Relat. Mater.* 19, 621.

Janssen, W. & Gheeraert, E. **2011** *Diamond Relat. Mater.* 20, 389.

Kamins, T. I., Williams, R. I., Basile, D. P., Hesjedal, T. & Harris, J. S. **2001** *J. Appl. Phys*. 89, 1008.

Kanda, H. & Watanabe, K. **1997** *Diamond Relat. Mater*. 6, 708.

Kataura H, Kumazawa, Y., Maniwa, Y., Ohtsuka, Y., Sen, R. *et al.* **2000** *Carbon* 38, 1691.

Kikkawa, J., Ohno, Y. & Takeda, S. **2005** *Appl. Phys. Lett*. 86, 123109.

Kriele, A., Williams, O. A., Wolfer, M., Brink, D., Muller-Sebert, W. & Nebel, C. E. **2009** *Appl. Phys. Lett.* 95, 031905.

Kukovitsky, E. F. L., vov, S. G. & Sainov, N. A. **2000** *Chem. Phys. Lett*. 317, 65.

Lander, J. J., Kern, H. E. & Beach, A. L. **1952** *J. Appl. Phys.* 23, 1305.

Langford, R. M. & Rogers, M. **2008** *Micron* 39, 1325.

Lawson S. C., Kanda, H., Wanatabe, N., Kiflawi, I. & Sato, Y. **1996**. *J. Appl. Phys*. 79, 4348.

Lee, S. T., Wang, N. & Lee, C. S. **2000** *Mater. Sci. Eng. A* 286, 16.

Levchenko, I, Ostrikov, K, Rider, A. E., Tam, E., Vladimirov, S. V. & Xu, S. **2007** *Phys. Plasmas* 14, 063502.

Lew, K. & Redwing, J. M. **2003** *J. Cryst. Growth* 254, 14.

Malesevic A, Kemps, R., Vanhulsel, A., Chowdhury, M. P., Volodin, A. & van Haesendonck, C. **2008** *J. Appl. Phys.* 104, 084301.

May, P. W., Smith, J. A. & Rosser, K. N. **2008** *Diamond Relat. Mater.* 17, 199.

May, P. W., Smith, J. A. & Mankelevich, Yu. A. **2006** *Diam. Relat. Mater*. 15, 345.

May, P. W. 2000 *Philos. Trans. Math., Phys. Eng. Sci*. 358, 473.

Menon, M., Richter, E., Raghavan, P. & Teranishi, K. **2000** *Superlattices Microstruct*. 27, 577.

Michaelson, S., Stacey, A., Orwa, J., Cimmino, A. *et al.* **2010** *J. Appl. Phys.* 107, 093521.

Moustakas, T. D. **1989** *Solid State Ionics* 32–33, 861.

Nørgård, C. & Matthews, A. **1996** *Diam. Relat. Mater*. 5, 332.

Page, A. J., Minami, S., Ohta, Y., Irle, S., Morokuma, K. & Givargozov, E. I. **2010** *Carbon* 48, 3014**.**

Rakha, S. A., Xintai, Z., Zhu, D. & Guojun, Y. **2010** *Curr. Appl. Phys*. 10, 171.

Ruan, J., W. J. Choyke, W. J. & Partlow, W. D. **1991** *Appl. Phys. Lett*. 58**,** 295.

Saito, Y., Okuda, M., Tomita, M. & Hayashi, T. **1995** *Chem. Phys. Lett.* 236, 419.

Shimabukuro, S., Hatakeyama, Y., Takeuchi, M., Itoh, T. & Nonomura, S. **2008** *Thin Solid Films* 516, 710.

Sundaresan, S. G., Albert, V., Davydov, M. D. *et al.* **2007** *Chem. Mater.* 19, 5531.

Sundaresan, S. G., Rao, M. V., Tian, Y. L. *et al.* **2007** *J. Appl. Phys.* 101, 073708.

Takeuchi, D., Watanabe, H., Yamanaka, S., Okushi, H. *et al*. **2001** *Phys. Rev. B* 63, 245328.

Takyo, G., Kono, S., Goto, T., Sasaoka, H. & Nishimura, K. **2008** *Jpn. J. Appl. Phys.* 47, 2241.

Tomita, A., Sato, N. & Tamai, Y. **1974** *Carbon* 12, 143.

Wagner, R. S. & Ellis, W. C. **1964** *Appl. Phys. Lett.* 4, 89.

Wang, L. et al. 1992 *J. Mater. Res.* 7, 148.

Wanka, H. N. & Schubert, M. B. **1997** MRS Proc. 467

Williams, O. A. **2011** *Diamond Relat. Mater*. 20, 621.

Wu, Y., Cui, Y., Huynh, L., Barrelet, C. J. *et al.* **2004** *Nano Lett*. 4, 433.

Wu, Y. H., Yang, B. J., Han, G. C. *et al.* **2002** *Adv. Funct. Mater.* 12, 489.

Wu, Y. H., Qiao, P. W., Chong, T. C. & Shen Z. X. **2002** *Adv. Mater.* 14, 64.

Yang, B. J., Wu, Y. H., Zong, B. Y. & Shen, Z. X. **2002** *Nano Lett.* 2, 751.

Zeiler, E., Schwarz, S., Rosiwal, S. M. & Singer, R. F. **2002** *Mat. Sci. Eng.* A 335, 236.

Chapter 5

Development of a Catalytic Etching Technique for Diamond:

Results and Discussion

Résumé

Ce chapitre traite le second objectif de cette thèse qui était de développer une technique de gravure simple, rapide et rentable pour la fabrication de nanostructures orientées (nanopores) dans les membranes de diamant. Dans ce procédé, un film de diamant est recuit avec des couches métalliques d'une épaisseur de 1 à 15 nm à 800-850 ° C dans une atmosphère d'hydrogène. La couche de métal démouille et des particules auto-assemblées se forment, qui gravent le carbone de l'interface diamant-métal avec l'aide d'une atmosphère d'hydrogène. Par conséquent, les particules pénètrent dans le volume du diamant et génèrent des pyramides inversées, ou des nanopores cylindriques ou coniques, selon l'orientation cristalline et de ce fait, révélent l'anisotropie de gravure en diamant.

Divers types de catalyseurs (Ni, Co, Pd, Pt, Fe et Au) ont été étudiées, de même que les paramètres du procédé tels que la composition du gaz, de l'épaisseur de catalyseur, la pression, la température, la microstructure de diamant ou de l'orientation cristallographique, et la durée processus. Les échantillons de diamants gravés ont été étudiés par différentes techniques, y compris l'analyse chimique de surface et la composition du gaz a été analysée au cours du processus. l'étude nous a conduit à proposer une image claire du processus de gravure et de l'influence des différents paramètres.

Le méthane a été détecté par spectrométrie de masse comme le seul produit du processus de gravure. L'étude attentive des paramètres du procédé montre que des nanopores peuvent être formés dans du diamant polycristallin, nanocristallin ou monocristallin. La taille des pores latérale et en profondeur peut être contrôlée par l'épaisseur du film métallique. Ni a montré la plus forte activité de gravure parmi les métaux étudiés. L'hydrogène a été trouvé à jouer un rôle pour le processus de gravure en aucune gravure s'est produite quand il n'y avait pas d'hydrogène. Pas de changement dans la microstructure de diamant en raison de gravure a été observé. Profondeur nanopore a été observée à augmenter avec l'épaisseur du film métallique ce qui suggère que le procédé de gravure n'est pas limité par la diffusion du carbone dans les particules de métal. Toutefois, le procédé de gravure est arrêté pour des particules de catalyseur situées profondément à l'intérieur du volume de cristal en raison de l'échange de gaz limité entre la surface et la particule, conduisant à la saturation en carbone. Pour expliquer les mécanismes de gravure cinq étapes importantes du processus de gravure ont été identifiés comme suit:

1. Diffusion de l'hydrogène moléculaire à partir de la chambre vers la surface du catalyseur,
2. Un atome d'hydrogène moléculaire est dissocié en catalytiquement par l'hydrogène atomique de nickel,
3. Atomes de carbone de la surface du diamant peut être enlevé par deux moyens différents:
   a. les atomes de carbone se dissolvent dans la goutte de nickel et ensuite diffusent à l'interface métal-gaz où ils réagissent avec les atomes d'hydrogène formant le méthane,
   b. diffuser des atomes d'hydrogène dans le catalyseur pour atteindre l'interface diamant-métal, puis à éliminer le carbone sous forme de méthane
4. Désorption du méthane à partir du catalyseur,
5. exo-diffusion de méthane à partir du voisinage du catalyseur

Dans les deux cas, 3a et 3b, la réaction n'est pas limitée par la diffusion à travers le catalyseur, le taux de gravure ne diminue pas avec l'épaisseur de catalyseur. Le procédé est donc limité par la réaction à l'interface diamant catalyseur. Analyse de la composition de surface des échantillons recuits par XPS n'a révélé aucun élément de carbure à l'interface diamant-métal.

La meilleure compréhension du processus, et en particulier l'étape cinétiquement limitante, nous a permis d'améliorer les conditions de gravure. Des nanopores avec la taille latérale de l'ordre de 15-225 nm et aussi profond que environ 550 nm ont été gravés dans une membrane en diamant. La technique de gravure a été utilisé pour créer des nano-et microstructures dans la membrane en diamant avec un film métallique le film a été fait par photolithographie conventionnelle. Dans le cas de motifs Pd film de l'opération de gravure conduit à une intéressante inverse pyramidaux à microstructures en forme de paroi en quatre [111] orientés plans.

Après l'optimisation, la technique a été utilisée pour explorer certaines applications prometteuses qui sont présentés dans le chapitre 5.

5.1. Motivation

5.1.1. Nanopores in Diamond Membrane

A nanopore is, essentially, a nano-scale hole. This hole may be:

- Biological: formed by a pore-forming protein in a membrane such as a lipid bilayer
- Solid-state: formed in synthetic materials such as silicon nitride or graphene
- Hybrid: formed by a pore-forming protein set in synthetic material

Nnanopores are of general interest because of the potential applications in drug delivery systems, ion exchange membranes for separation of biomacromolecules, antifouling materials with reduced molecular adsorption, biochemical sensors and energy storage (**Wei *et al.* 2012**; **Venkatesan *et al.* 2011**; **Wanunu *et al.* 2010**; **Healy *et al.* 2007**; **Gershow & Golovchenko**, **2007**; **Dekker, 2007**; **Iqbal *et al.* 2007**; **Yamaguchi *et al.* 2004**; **Li *et al.* 2003)**.
In particular, nanopore based sensors are an emerging tool for measuring the structural properties of individual biomolecules, such as DNA. The nanopore sensing concept utilizes chips (typically made in silicon, figure 5.1 (a)) that contain a thin free-standing membrane into which a nanometer-sized aperture (nanopore) is drilled (figure 5.1(b)) (**van den Hout *et al.* 2010**; **Li *et al.* 2001, 2003**, **Storm *et al.* 2003**; **Wanunu *et al.* 2010**). When a nanopore chip is placed in a saline solution and an electric potential is applied across the membrane, the ionic current will be determined by the possibility for ions to move through the nanopore. If a biomolecule, e.g. DNA, RNA, or a protein, moves through the nanopore (**Li *et al.* 2001**), the ionic current will be partially blocked (figure 5.1(c)) (**Kowalczyk *et al.* 2010**; **Li *et al.* 2003; Storm *et al.* 2005)**. In this way, individual molecules can be detected electrically. The concept is commonly used to investigate charged molecules, which can be drawn through the pore electrophoretically by the same electric potential that is used to measure the ionic pore current (**Kowalczyk *et al.* 2010; Li *et al.* 2003; Smeets *et al.* 2006; van den Hout *et al.* 2010; Wanunu *et al.* 2011, 2010)**. Apart from the possibility to detect single molecules, the concept provides information on molecular length, size, and degree of folding through detailed analysis of the magnitude of the current blockade (Δt) and the associated dwell time (t_d)(figure 5.1(d)) (**Storm *et al.* 2005**).

The potential for high-throughput DNA sequencing on large fragments and determining length or size of biomolecules have been the two most dominant driving factors in nanopore research. In both cases, the highest aim is to achieve sub-nanometer spatial resolution on the molecule of interest.

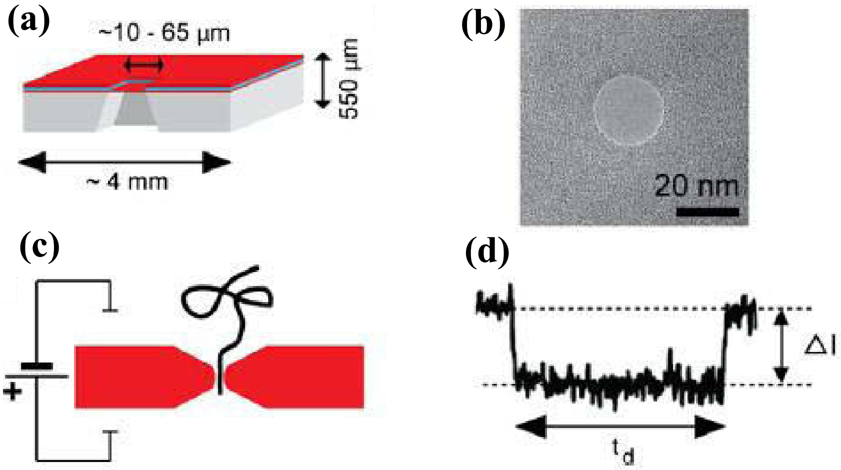

*Figure 5.1. Molecular detection in nanopore experiments. (a) Schematic representation (vertical cross section) of a chip used in solid-state nanopore experiments (**Keyser et al. 2005**; **Li et al. 2003**, **2001**; **Wanunu et al. 2010**). The millimeter-sized silicon chip (gray) contains a micrometer-sized free-standing membrane (bottom red layer) in which a nanometer-sized hole (nanopore) is drilled. The area around the free-standing membrane is coated with insulating layers (top red and blue layer) to minimize electrical noise in the nanopore experiment. (b) Transmission electron microscope (TEM) image of a 20 nm wide nanopore drilled in a 20 nm thick free-standing SiN membrane. (c) Schematic representation of a typical nanopore experiment. The membrane (red) divides a reservoir containing a saline solution into two compartments. Each compartment is equipped with an electrode that allows one to control the electrical potential across the membrane, resulting in an ionic current through the nanopore. (d) When a molecule (black line in panel (c)) passes through the nanopore, the molecule partially blocks the ionic current due to volume exclusion. The depth of the current blockade (1I) and the dwell time (td) are characteristic respectively for the length and the diameter of the molecule (***Storm et al.* 2005**).*

In 1996, Kasianowicz performed the first characterization of DNA molecules in nanopore sensors using α-hemolysin, a 1.5 nm diameter ion channel naturally occurring *Staphylococcus aureus* bacteria (**Kasianowicz *et al.* 1996**). Using a genetically engineered and adapted variant of α-hemolysin, **Clarke *et al.*** (**2009**) demonstrated the ability to use nanopore sensors for single nucleotides discrimination. **Derrington *et al*.** (**2010**) demonstrate a similar ability to discriminate nucleotides in another biological ion channels, MspA. Owing to the selfassembly process which govern their formation, biological ion channels of the same type are chemically and structurally identical, enabling a high degree of repeatability.

However, biological ion channels are extremely sensitive to changes in ionic concentration, *p*H, transmembrane potential, mechanical stresses, and temperature, and thereby prone to failure (**Dekker, 2007**). Furthermore, the range of possible analytes is restricted by the diameter of the biological ion channel, which is rarely larger than a couple of nanometers. These limitations have driven interest in the fabrication of nanopores in inorganic dielectric membranes, often referred to as solid state nanopores.

Notable examples include nanopores in SiO_2 and Si_3N_4 (**Storm *et al.* 2003; Li *et al.* 2001**; **Mitsui *et al.* 2006**) fabricated by using modern silicon technology. For example, **Storm *et al.*** (**2003**) presented a technique to prepare single-nanometer precision silicon oxide pores by anisotropic etching of single crystal Si in KOH and a post treatment with high energy electrons to shrink the holes in the membrane.

Such solid state nanopores possess high stability and can withstand pressure variations and mechanical vibrations and thus give more reproducible results. However, analyzing molecules in harsh conditions such as extreme temperatures, voltages or *p*H conditions could lead to the malfunctioning or in extreme cases to the destruction of sensors. It is therefore important to establish nanopores in a material that is able to sustain such extremes. Diamond is the perfect candidate for this task since it has exceptional properties such as the highest hardness and Young's modulus (1200 GPa) of all known solids, a very high thermal conductivity (20–22 W cm^{-1} K^{-1}) and a low thermal expansion coefficient (**El-Dasher *et al.* 2006**; **Berman, 1979**; **Auciello *et al.* 2004**; **Kriele *et al.* 2009**). It can be used to attach binding sites in order to be able to detect specific molecules (**Lud *et al.* 2006**). Furthermore due to its wide band gap, it is well known, that the background current of diamond is very low and the potential window very wide compared to conventional electrodes made from metals or graphite (**Nebel *et al.* 2007**). This behavior enables detection with low noise over a wide potential range.

5.1.2. Etching of Diamond

Despite all the unique properties, the development of diamond based devices has been slow as the extreme hardness of diamond and its chemical inertness in gases and liquids at room temperature makes the fabrication process very difficult. Usually, in the fabrication process, a etching step is required that is performed almost exclusively by the reactive ion etching (RIE) technique with the help of lithographical processes, lithography being used for mask deposition (**Hausmann *et al.* 2010**; **Janssen & Gheeraert, 2011**; **Janssen *et al.* 2011**).

However, with the RIE, fabrication of very narrow (10 to 50 nm in lateral size) and long (typically longer than 300 nm) pores has become problematic due to the limitation in lithographic resolution and high aspect ratio (ratio of pore depth divided by pore size) etching profiles. In addition, the inevitable involvement of a lithography process (e.g., e-beam lithography) makes the RIE technique costly and time consuming. A simple, fast and cost-effective etching technique therefore needs to be developed.

There have been reported catalytic etching techniques using metals for obtaining high quality polishing and thinning of initially rough diamond films (**Jin *et al.* 1993**), nano-holes /and nano-channels in activated carbon (**Iwazaki *et al.* 2008**; **Khalili *et al.* 2000**; **Tamai *et al.* 1977**), in highly oriented pyrolytic graphite (**Konishi *et al.* 2006**; **Takasu *et al.* 2005**), in pure and doped diamond (**Smirnov *et al.* 2010**; **Ohashi *et al.* 2011a**, **2011b**; **Chepurov *et al.* 2011**, **2000**; **Takasu *et al.* 2006**; **Lee *et al.* 1995**) and for patterning diamond surfaces (**Ralchenko *et al.* 1993**). The ability of carbon to be dissolved in iron at elevated temperatures was a prerequisite for the development of the hot metal lapping technique (**Jin *et al.* 1993**), which provides high quality polishing of initially rough diamond films. However, when the fabrication of high resolution structures is required, the thickness of the metal pattern must be reduced to the nanometre scale. Such thin films would dissolve only a small amount of carbon, and obtaining deep patterns could become problematic. On the other hand, nano-holes /and nano-channels were achieved only in the surface layers of diamond, whereas mostly distorted patterns were obtained in the case of patterning diamond surfaces. The reported catalytic etching technique therefore can not be applied for creating nanopores with controlled diameter and density, in particular high aspect ratio, that are necessary for the applications discussed earlier. Moreover, the exact etching mechanism of diamond remains somewhat unclear. For example, formation of a carbide-like layer containing hydrogen at the diamond-metal interface was suggested for channeling diamonds by metal nanoparticles in a flowing gas mixture of hydrogen and nitrogen (**Takasu *et al.* 2006**). The successive formation of this layer was thought to assist the moving of nanoparticles resulting in the channeling of diamonds. In contrast, **Ralchenko *et al.*** (**1993**) interpreted the etching according to a mechanism involving carbon dissolution in metal, followed by diffusion from the diamond-metal to the metal-gas interface and finally desorption of carbon as hydrocarbons. A systematic investigation of the catalytic etching process is therefore necessary not only to understand the mechanism but also to develop a simple method for the fabrication of nanopores in diamond with controlled density and shape.

5.2. Catalytic Etching of Diamond: The Technique

The etching technique consists of two steps, (i) the deposition of thin metallic layers on a diamond substrate and (ii) the subsequent annealing in a hydrogen atmosphere. A schematic of the technique is shown in figure 5.2.

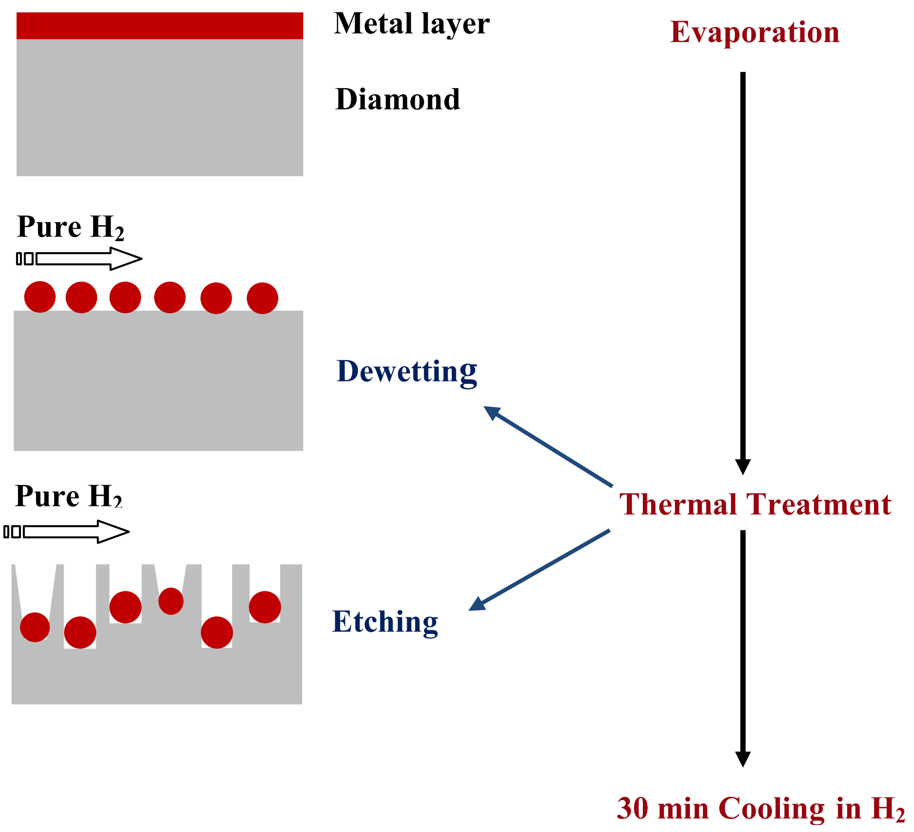

Figure 5.2. A Schematic of the catalytic etching of diamond.

Metals (Ni, Co, Pd, Pt, Fe and Au) with thickness in the range of 1–15 nm were deposited on diamond substrates by e-beam evaporation, the thickness being measured by a quartz crystal oscillator. The annealing step was carried out in a CVD reactor, usually dedicated to diamond growth, at 750–900 °C in 60 Torr flowing hydrogen with 100 sccm (sccm denotes cubic centimeter per minute at STP) for between a few minutes to several hours. The base pressure of the furnace before annealing was $< 10^{-6}$ Torr. The temperature was increased at a rate of 200 °C/min and measured with an infrared pyrometer with a reading precision of ± 10 °C. After the annealing step, the samples were cooled down for 30 min under a continuous hydrogen flow.

Two types of diamond films were used for these experiments, namely polycrystalline diamond with a grain size of typically 50 µm (figure 5.3 (a)) and nanocrystalline diamond (grain size 100 nm) (figure 5.3 (b)). Polycrystalline diamond (dimension of the substrate: 3×3×3 mm^3) was grown by Element Six (electrochemical grade and boron doped CVD diamond). Nanocrystalline diamond (undoped) with thickness in the range of 300 nm–1.5 µm was grown on silicon substrates in a microwave plasma CVD reactor (5200 Seki Technotron MPCVD reactor) using the bias-enhanced nucleation method (**Barrat *et al.* 1998**) with following parameters: 900 °C temperature, 1000 W microwave power, 0.3% methane in hydrogen, and pressure of 30 Torr.

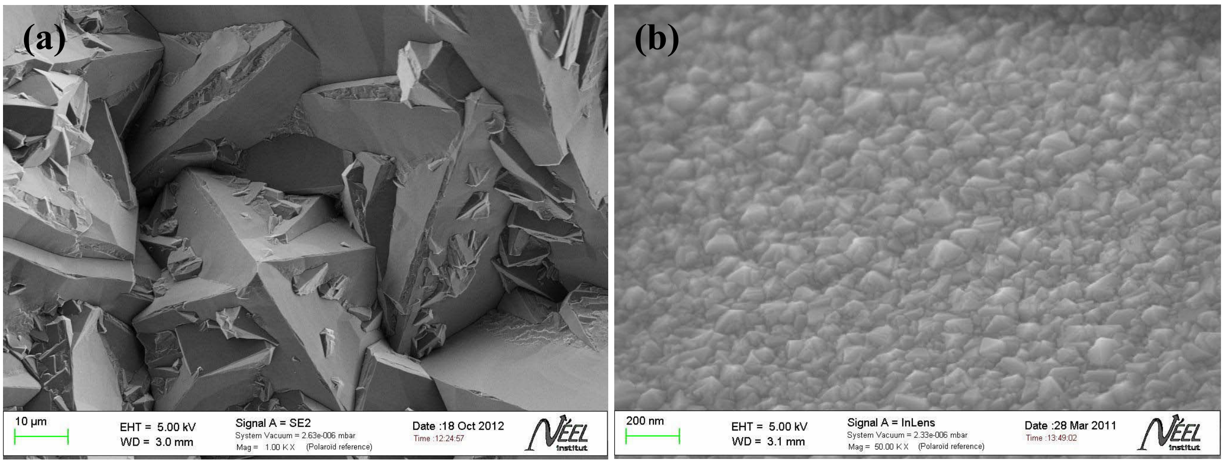

Figure 5.3. SEM images of (a) as-received polycrystalline diamond with average grain size of about 50 µm and (b) nanocrystalline diamond with average grain size of about 100 nm. Polycrystalline diamond substrates are electrochemical grade and boron doped CVD diamond purchased from Element Six.

As shown in figure 5.2, during annealing the metal layer melts and forms self-assembled nanodroplets that remove carbon from the diamond surface with the assistance of hydrogen atmosphere, and consequently the droplets enter the crystal volume forming oriented nanostructures, usually referred to as etch pits or nanopores. The phenomenon that leads to the formation of self-organized nanodroplets from an initially two-dimensional metal film through thermal annealing is known as dewetting and is currently a topic of great interest, due to applicational relevance, e.g., in thin film technology.

5.2.1. Fundamental of Dewetting

Because thin films have a high surface-to-volume ratio, on heating, a thin, solid, continuous film may develop holes and may eventually agglomerate into shapes with a lower surface-to-volume ratio (figure 5.4). This process is known as dewetting and driven by capillary energy minimization and often occurs via surface self-diffusion at temperatures well below the melting temperature of the material (**Srolovitz & Safran, 1986a**; **Jiran & Thompson, 1990**, **1992**). Thinner films have higher capillary driving forces for dewetting, and also reduced kinetic barriers to dewetting (**Srolovitz & Safran, 1986b**; **Jiran & Thompson, 1990**, **1992**). In addition, a thin metal film can melt at a temperature lower than the melting point of its corresponding bulk metal, a process that relates to the melting point lowering effect of thin metal films and hydrogen diffusion into the metal (**Gladkich *et al.* 1966**; **Buffat & Borel, 1976**; **Yang *et al.* 1998**; **Pundt, 2004**). Such unique behavior of thin films further stimulates the dewetting process.

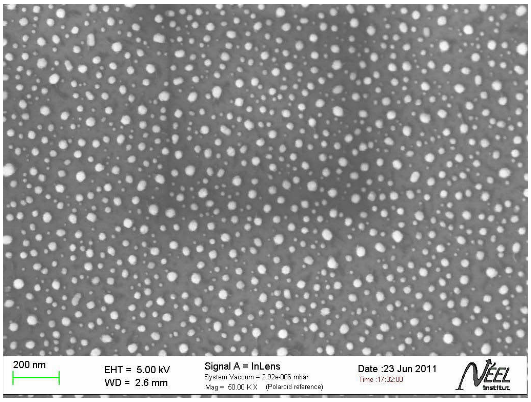

Figure 5.4. SEM image of self-organized Ni nanoparticles on a (100) surface of the polycrystalline diamond resulted from the dewetting of a 3nm continuous Ni film at 750 °C for 10 min under 60 Torr H_2 pressure.

In order to understand the fundamental of dewetting, it is necessary to clarify the distinction among stable, metastable, and unstable films. The effective interface potential $\varphi(h)$ is defined as the excess free energy per unit area necessary to bring two interfaces (solid–liquid and liquid–gas interface) from infinity to a certain distance h. The distance h then defines the thickness of the liquid layer between them. As shown in figure 5.5 (**Seemann *et al.* 2001a**), $h \to \infty$ induces $\varphi(h) \to 0$ indicating stability of a film with infinite film thickness. When $\varphi(h) > 0$ and the global minimum lies at infinite thickness, the film is called stable (curve [1] of figure 5.5). If the second derivative of φ with respect to film thickness is negative, $\varphi''(h_0) < 0$, where h_0 is the initial thickness of a homogeneous film, the system is unstable (curve [2] of figure 5.5), such that capillary waves on the film surface are spontaneously amplified under thermal annealing. The rupture mechanism is termed "spinodal dewetting" (**Vrij, 1966**; **Brochard-Wyart, 1990**; **Xie *et al.* 1998**). In curve [3], the film is unstable for small film thicknesses where $\varphi''(h_0) < 0$, whereas for larger film thicknesses ($\varphi''(h_0) > 0$), the film is metastable. In the metastable case, the system has to overcome a potential barrier in order to reach its state of lowest energy at $h = h^*$. Some kind of nuclei, e.g. dust particles or defects, are required to lower $\varphi(h)$ and can therefore induce rupture of the film, a mechanism called "heterogeneous nucleation" (**Mitlin, 1993**, **1994**).

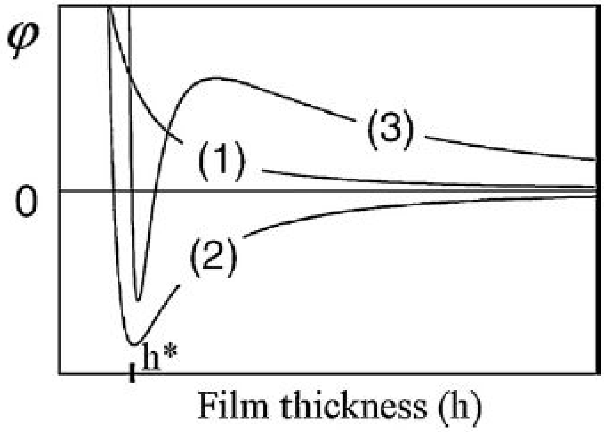

Figure 5.5. Effective interface potential ϕ(h) as a function of film thickness h for stable (1), unstable (2), and metastable (3) films, adapted from ***Seemann et al. 2001a****.*

It is difficult to distinguish metastable and unstable mechanisms experimentally since both nucleation and spinodal dewetting can lead to dewetting in unstable films (**Reiter, 1992**; **Xie *et al.* 1998**; **Thiele *et al.* 1998**; **Thiele & Velarde, 2001**). In case of unstable system, however, there is a certain wavelength λ_s, the amplitude of which grows fastest, leading to a characteristic dewetting pattern of the liquid film (**Seemann *et al.* 2001a**). The wavelength λ_s and $\varphi''(h_0)$ are connected by the following equation:

$$\lambda_s = [-8\pi\gamma/\varphi''(h)]^{1/2} \tag{1}$$

where γ is the surface tension of the liquid film (with respect to air) (**Vrij, 1996**). Numerical simulations indicate that the dewetting pattern is related to the given surface tension, and there may be a cross region between the two mechanisms (**Sharma & Khanna, 1999**; **Reiter *et al.* 1999**). Close to the sign reversal of $\varphi''(h_0)>0$, thermal activation is sufficient to overcome the potential barrier for the nucleation of holes, a process called "thermal nucleation" or "homogeneous nucleation" representing a third dewetting mechanism (**Seemann *et al.* 2001a**, **2001b**). The characteristic feature of homogeneous nucleation is a continuous breakup of holes, whereas heterogeneous nucleation causes holes that emerge only within a narrow time interval (**Jacobs *et al.* 1998**). Thus, the hole opening is most likely to happen at locations having the smallest thickness, which can be caused by fluctuations of the film thickness or elevated regions on the substrate. A stable film, ($\varphi''(h_0) > 0$), may become unstable locally on an elevated heterogeneity if the local thickness decreases below the critical thickness. On a complex substrate comprising both wettable and less wettable (or unwettable) regions, holes generate at the unfavored locations and the wettability contrast drives the liquid flow from the less wettable areas to the more wettable areas, lowering the total energy.

After the hole opening, the classical process includes hole growth, the combination of holes to form ribbons, and the decay of ribbons into droplets (**Reiter, 1992, 1993**). A typical hole shows a circular shape and the round shape remains stable until holes contact one another. It is assumed that hole growth, i.e. the removal of material from the hole border, takes place by film surface diffusion (**Presland *et al.* 1972**). During hole growth a rim of piled-up material is formed around the hole. This rim has to be moved for further void growth, thus a decrease in hole growth rate for increasing hole size is expected if the hole remains circular. **Jiran & Thompson** (**1990**) observed branched hole growth at the edges of thin gold lines and proposed a corrected model for hole growth kinetics which is based on branched growth. The model states that a rim is formed at the sides of the finger shaped hole while at the tip of the hole the material can diffuse away in several directions and no pile-up of material is observed. According to this model hole growth preferably takes place at the tips of holes and no decrease in the void growth rate is expected. **Kan & Wong** (**2005**) have shown that an instability in the rim at the edge of a film exists that leads to the growth of such regularly spaced fingers**. Jiran & Thompson** (**1990, 1992**) also attributed branching to capillary effects and stated that branching is not affected by the presence of grain boundaries; they found that voids grew across grain boundaries and grains alike. In contrast to their observations, several experimental studies have suggested that hole growth is taking place preferably along grain boundaries (**Krietensen *et al.* 1991**; **Presland *et al.* 1972**; **Petersen & Mayr, 2008**).

In the literature, four modes for dewetting of thin films are described: (1) grain boundary mediated dewetting caused by thermal grooving (**Mullins, 1957**; **Luber *et al.* 2010**); (2) heterogeneous nucleation, which initiates from a defect located at the film surface or the film–

substrate interface, (3) homogeneous nucleation, which occurs via a small thermal density fluctuation that acts as a nucleus for hole formation, and (4) spinodal dewetting, which occurs by the amplification of periodic film thickness fluctuations (i.e., capillary wave); such films induce self-correlated dewetting patterns (**Seemann *et al.* 2001a**; **Trice *et al.* 2007**; **Krishna *et al.* 2010**; **Sharma, 2003**; **Vrij, 1966**; **Sarkar & Sharma, 2010**; **Thiele *et al.* 2003**; **Bischof *et al.* 1996**; **Herminghaus *et al.* 1998**). The first three modes are nucleation-dominated mechanisms, whereas spinodal dewetting is driven by thermodynamic system instability. The different modes can be distinguished by their geometrical signatures (**Thiele *et al.* 2003**) and the onset time for the dewetting process: thermal nucleation and thermal grooving have nucleated holes that are randomly distributed in location and time of appearance, whereas holes formed by both heterogeneous nucleation and spinodal dewetting appear at early stages of the dewetting process, can have non-random size distributions, and can display ordered spatial distributions. For thick films (thickness >100 nm), the dewetting evolves via nucleation and growth of a dry spot, while for thin films (thickness <100 nm), spinodal decomposition becomes dominant in the formation of the dewetting. Structures accessible through spinodal dewetting include hemispherical droplets, irregular asymmetric particles, connected polygons, randomly oriented ridge-like structures, and plateaus of continuous film with dispersed holes (**Krishna *et al.* 2010**; **Sarkar & Sharma, 2010**; **Bischof *et al.* 1996**; **Herminghaus *et al.* 1998**; **Trice *et al.* 2008**; **Strobel *et al.* 2010**).

A number of factors play a critical role in the dewetting behavior and subsequent pattern formation such as the underlying substrates (**Alford *et al.* 2003**; **Petersen & Mayr, 2008**; **Ishikawa *et al.* 2003**; **Giermann & Thompson, 2005**), the film thickness (**Alford *et al.* 2002**), and the doping with other atoms (**Hummel *et al.* 1981**; **Lee *et al.* 1987**).

Most thin metallic film deposition methods usually yield polycrystalline films, with grain sizes of the order of the film thickness (**Mullins, 1958**). Thus, for such films the formation of particles in the course of dewetting is relatively fast due to an abundance of hole-nucleation sites and of short-circuit diffusion paths. In addition, due to the lack of symmetry in polycrystalline films, the holes do not propagate in a regular way and it leads to irregular island morphologies. In the case of single-crystal metallic films the situation is quite different and only few, recent works exist (**Jongpil & Thompson, 2010**), owing to the difficulty of producing such films.

An extensive study of the dewetting of different metals on diamond surface could be found in the reference (**Janssen & Gheeraert, 2011**), where the effect of the metal layer type and thickness on surface density, shape and size of the resulting droplets were investigated in order to identify a suitable mask for optimized diamond nanowire fabrication.

5.3. Catalytic Etching of Diamond: Results and Discussion

After the dewetting of thin metallic layers deposited on the diamond surface, the self-organized nanoparticles take part in the etching of diamond depending on their nature of interaction with carbon at the annealing conditions. In this study, the key parameters of the etching process were investigated: type and thickness of the metallic layer; the annealing temperature; the hydrogen pressure; the diamond microstructure and the annealing time. The morphology of all annealed samples was examined with a Zeiss Ultraplus field emission gun scanning electron microscope (FEG-SEM). Raman Spectroscopy was performed on the etched samples using 514 nm laser excitation to investigate any change in the diamond microstructure due to etching. In order to explore the existence of nickel carbide at the catalyst-diamond interface, that could limit the etching process, surface chemistry of the samples was analyzed by X-ray photoelectron spectroscopy (XPS). To get further insights into the etching process, the chemical composition of the gas during etching was measured by a quadrupole mass spectrometer. Finally, based on these investigations, a model for etching diamond with metal nanoparticles was discussed.

5.3.1. Effect of Metal Type on Etching

In order to study the effect of metal type on the etching process, Ni, Co, Pd, Pt, Fe and Au with a thickness of 3 nm were evaporated on polycrystalline diamond and annealed at 800°C for 10 min. Figure 5.6 shows the SEM images of (100) surface of annealed polycrystalline diamond.

Etching was observed for Ni, Co, Pd, Pt, and Fe, figure 5.6 (a)-(e), forming etch pits with flat sidewall faces and sharply defined edges. In contrast, finely dispersed Au nanopartices were formed, figure 5.6 (f) and neither etch pits nor nano-channels were apparently found on diamond surface. Ni nanoparticles showed highest etching activity among the studied metals. The observed difference in etching behaviour among the metals may be caused by the combined effect of the difference in the size and melting point of metallic nanoparticles as well as carbon solubility into the nanoparticles at the temperatures in our experiment. The solubility of carbon into Ni, Co and Pt at 900 ^{o}C estimated from M-C, metal-carbon, phase diagrams is 1 at.%, 0.8 at.%, and 0.04 at.% respectively (**Massalski *et al.* 1990**). On the other

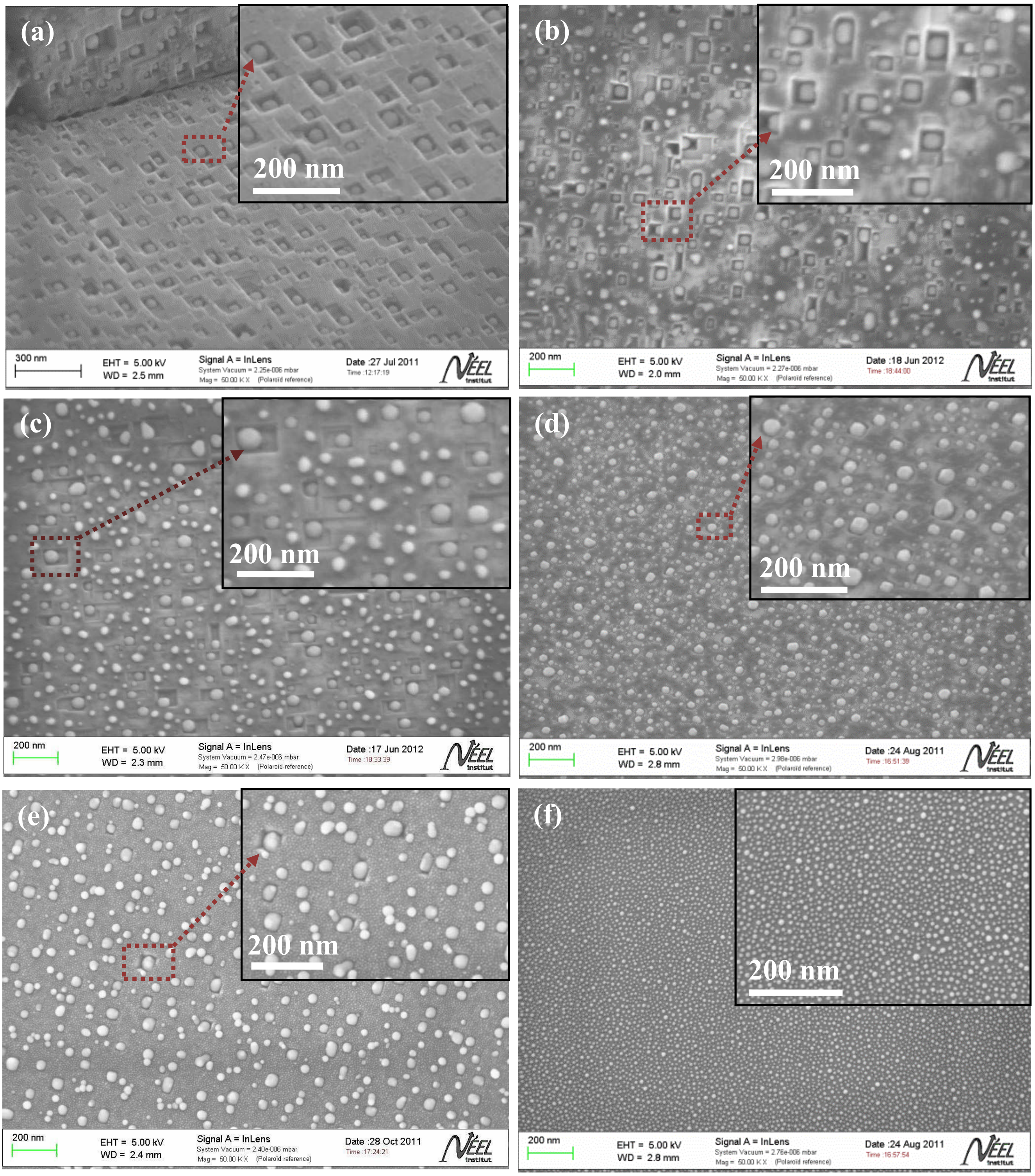

hand, the Fe-C phase diagram is a fairly complex one.

Figure 5.6. SEM images of the (100) surface of polycrystalline diamond after 10 min of annealing with a 3 nm film of (a) Ni, (b) Co, (c) Pd, (d) Pt, (e) Fe and (f) Au, (800 °C, 60 Torr H_2*); the corresponding inset images show etch pits with flat sidewall faces and sharply defined edges for Ni, Co, Pd, Pt, Fe and finely dispersed nanoparticles for Au.*

In the temperature range 800-900 °C, Fe can exist in three different solid phases such as α-ferrite (solid solution of C in BCC Fe), α-ferrite + γ-austenite (solid solution of C in FCC Fe) and γ-austenite + Fe_3C, and each phase has different C solubility (**Massalski *et al.* 1990**). In addition, under the assumption that smaller nanoparticle size would increase the internal (Laplace) pressure, **Harutyunyan *et al.*** (**2007**) concluded that smaller Fe-C nanoparticles display a lower carbon solubility limit. This could be one possible explanation for no etching activity of smaller Fe nanoparticles (figure 5.6 (e)). For other transition metal-carbon systems (e.g., Ni-C), subsurface interstitial sites have been identified as most favorable for carbon incorporation (**Klinke II *et al.* 1998**; **Gracia *et al.* 2005**; **Yazyev & Pasquarello, 2008**; **Moors *et al.* 2009**) on flat surfaces. Assuming that this still holds true for nanoparticles, one could expect the opposite result that carbon solubility increases for smaller nanoparticles of these metals, because a large fraction of C should be expected close to the surface and the surface to volume ratio becomes larger for smaller sizes.

Pd, without any vacancy in its *d*-orbitals and an s-electron, should behave as Cu or Ag with a minimal solubility of carbon. However, this prediction is based on the electronic state of pure Pd metal. When there are carbon atoms around, an electron in the *d*-orbital of Pd may enter the empty *s*-orbital and leaving one *d*-orbital vacant. As a result, Pd has two unfilled orbitals, i.e. *s* and *d* ($5s^1 4d^9$), so it can interact with carbon and dissolve the latter (**Sung & Tai, 1996**).

On the other hand, unlike the iron-group elements (Fe, Ni, Co), the carbon solubility of Au is extremely low (0.018 at.% at 800 °C in bulk phase) (**Massalski *et al.* 1990**). It has recently been reported that when Au particle size becomes several tens of nanometers, it has carbon solubility depending on the nature of the substrate and source of carbon (**Takagi *et al.* 2008**). However, this model of carbon solubility in nanosized Au particles would not be similar to the uptake of carbon from diamond surface.

The observation, effect of metal type on etching, suggests that metals having intermediate interaction with carbon (e.g., Ni) could result in higher etching activity than other metals with strong (e.g., Fe) or very low affinity (e.g., Pt) with carbon. From the pictures (figure 5.6) it is also obvious that the size of the etched structures depends on the size of the initially formed metal nanoparticles. Moreover, the size can be adjusted to a certain extent by the metal layer thickness.

5.3.2. Effect of Metal Film Thickness

Figure 5.7 shows the effect of metal film thickness on the size of etched structures.

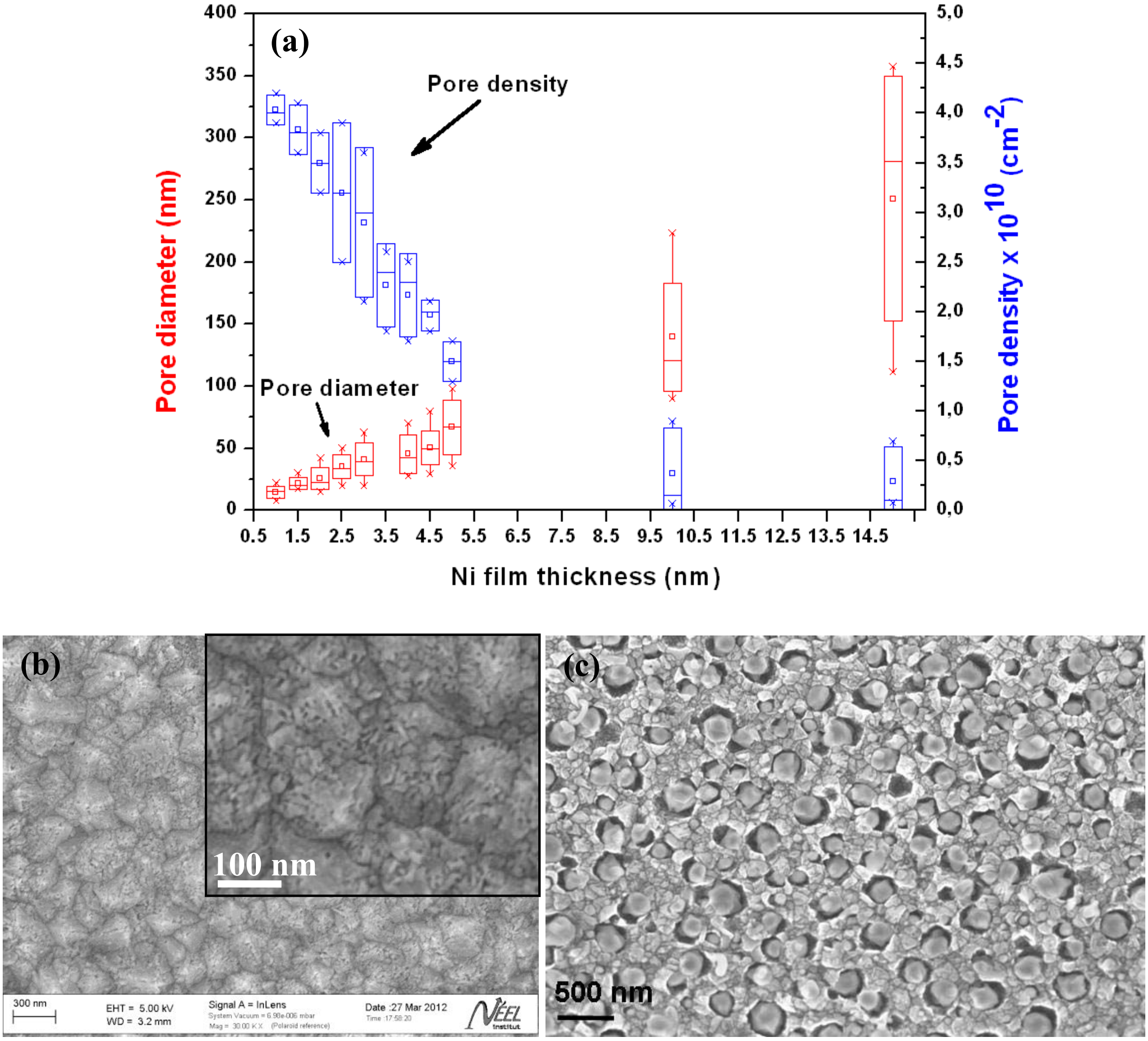

Figure 5.7. (a) Nanopore diameter and density distribution measured for nanocrystalline diamond after 10 min annealing with Ni layers of thickness of 1 to 15 nm, (850 °C, 60 Torr H_2). The box represents standard deviation. The band and square inside refer to median and mean respectively; minimum and maximum values are indicated by the cross. Nanopore diameter and density were estimated by analyzing the SEM images of each processed sample. (b)) corresponding SEM image

showing the smallest pores (~15 nm) obtained in the case of 1 nm Ni layer and (c) the largest pores with mean diameter of 225 nm produced by Ni particles generated from 15 nm Ni layers.

To measure nanopore diameter, a nanocrystalline diamond with thickness of ~ 350 nm was annealed with Ni layers with thickness in the range of 1-15 nm for 10 min at 800 °C. The diameter of the nanopores was then estimated by the analysis of the SEM images. Diameter was considered for the pore size since most of the nanopores had a circular section in first approximation in the case of nanocrystalline diamond. The mean diameter of the nanopores was observed to increase with the Ni layer thickness, figure 5.7 (a). We also calculated the ratio of the mean diameter of nanopores to that of Ni particles to be approximately 1.5:1. In contrast to the diameter distribution, the density of nanopores was decreased, as expected, with the Ni layer thickness, figure 5.7 (a). The density was reduced, for example, by an order of magnitude from 4×10^{10} cm^{-2} for 1 nm to 1×10^{9} cm^{-2} for 15 nm, due to the increased dimensions of the dewetted Ni islands through mass transfer (**Geissler *et al.* 2010; Bower *et al.* 2000**). The SEM image of figure 5.7 (b) shows the smallest nanopores with mean size of about 15 nm were obtained in the case of 1 nm Ni layer, whereas the largest nanopores with mean lateral size of about 225 nm that were achieved by annealing the nanocrystalline diamond with 15 nm Ni layers, figure 5.7 (c).

Figure 5.8 shows the effect of Ni film thickness on nanopore depth. Again, the nanopore depth was measured by SEM on cross sections of each processed sample, as is shown in figure 5.8 (b) for 5 nm Ni. The bright contrast corresponds to Ni nanoparticles that were embedded into the diamond crystal.

From this investigation we observed the increase in nanopore depth with the Ni layer thickness, in particular, for 10 and 15 nm Ni layers. As the carbon atoms etched from the diamond surface have to diffuse through the catalyst particle to reach the gas phase, this increase in depth shows that the etching of diamond is not limited by the diffusion of carbon through the particle. The limitation factor could therefore be the processes occurring at the catalyst-diamond interface, in particular the formation of carbide, or in the gas phase.

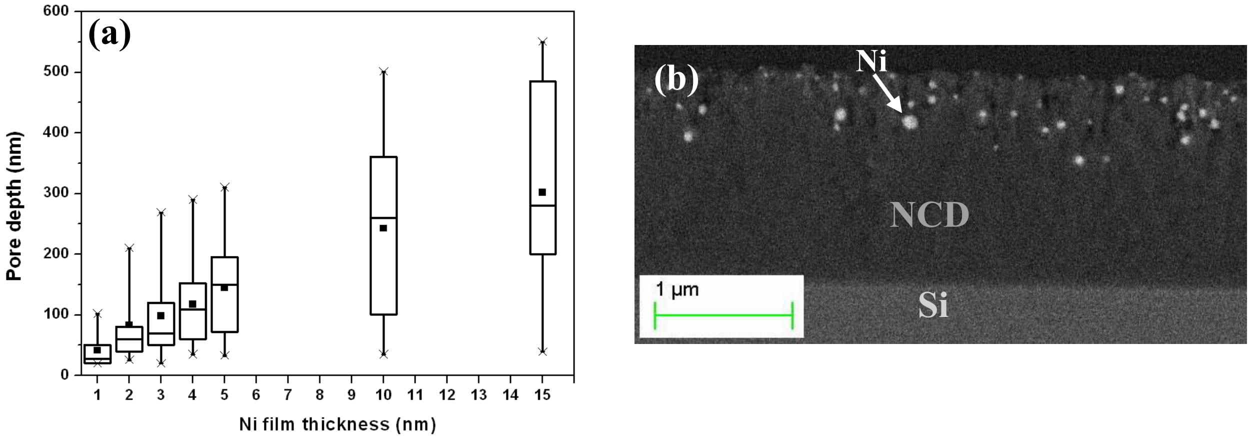

Figure 5.8. (a) Nanopore depth distribution measured for nanocrystalline diamond after 10 min annealing with Ni layers of thickness of 1 to 15 nm, (850 °C, 60 Torr H_2). After annealing cross-sections of each processed sample were observed by SEM and pore depth was estimated by analyzing the images. Bottom and top line of the box represents 25th and 75 th percentile of each data set. The band and square inside refer to median and mean respectively; minimum and maximum values are indicated by the cross. Whiskers refer to standard deviation ± mean. (b) SEM image acquired with a backscattered electron detector (EsB detector), of the cross-section of an etched nanocrystalline diamond after 60 min annealing with 5 nm Ni layers; bright spots correspond to Ni nanoparticles.

5.3.3. Effect of Annealing Temperature

To understand the influence of annealing temperature on the etching process, polycrystalline diamond with a 3 nm film of Ni was annealed at 750 °C, 800 °C, 850 °C and 900 °C in 60 Torr H_2 atmosphere. Figure 5.9 shows the SEM images of (100) surface of polycrystalline diamond after 30 min of annealing. The observation suggests that etching occurs typically in the range of 800-850 °C. No evidence of etching at 750 °C, figure 5.9 (a), could be due to the very low solubility of carbon into Ni at this temperature. On the other hand, density of etched nanostructures was decreased dramatically at 850 °C, figure 5.9 (c). It seems that, at this temperature, some of the particles are not active, in particular the smallest particles. Effect is even stronger at 900°C, where no etching was observed at all, instead particles started to form clusters, figure 5.9 (d). We attribute this to the random nucleation and growth of carbon overlayers on the metal particles and poisoning them at higher temperatures, where the rate of carbon diffusion to the metal-gas interface was the highest. High surface concentration of carbon enhances the probability of nucleation and subsequent growth of inactive carbon layer. In addition, evaporation of Ni could occur during high temperature annealing (850-900 °C) resulting in the generation of smaller particles (**Geissler *et al.* 2010**). While not fully understood, there seems to be a critical particle size below which no etching would occur.

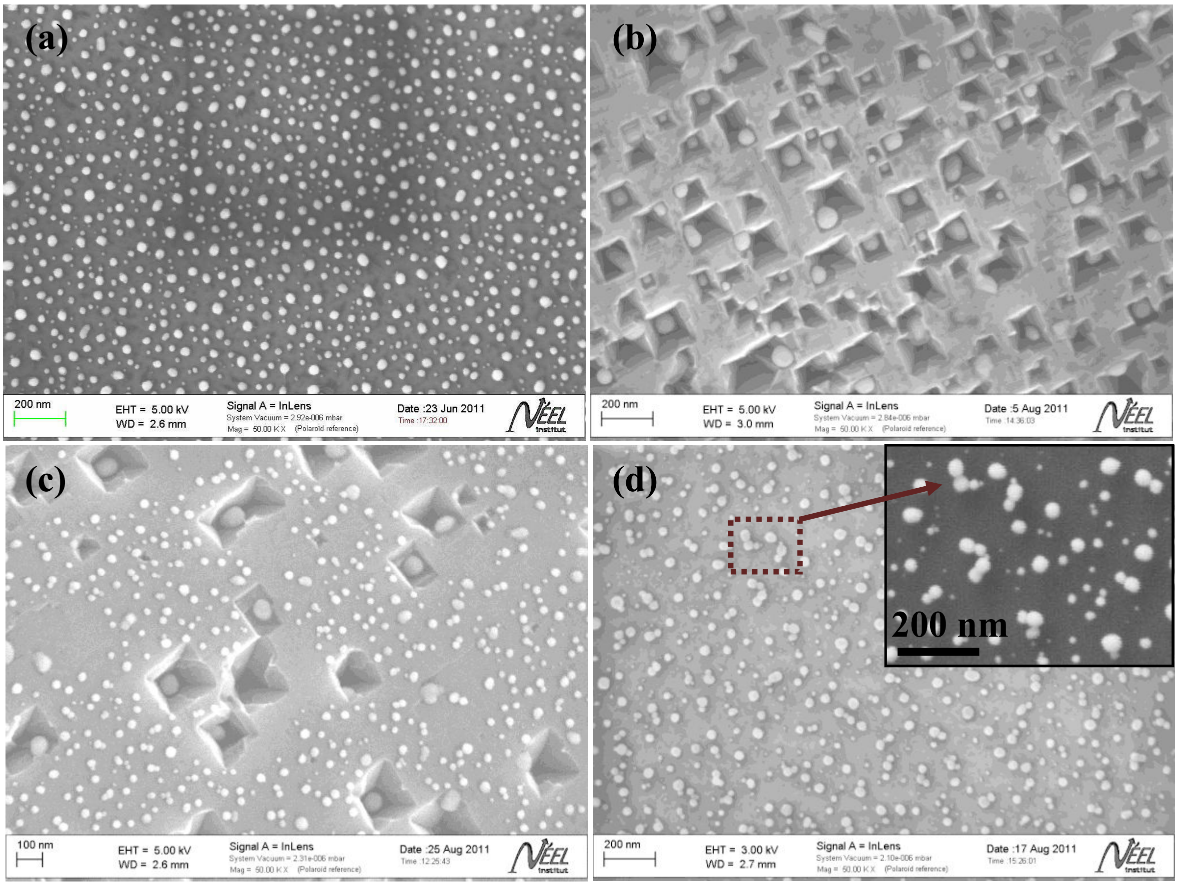

Figure 5.9. SEM images of a (100) surface of polycrystalline diamond after 30 min annealing at (a) 750 °C, (b) 800 °C, (c) 850 °C and (d) 900 °C, (3 nm Ni, 60 Torr H_2). The inset of panel (d) is the corresponding SEM image acquired with a secondary electron detector.

5.3.4. Effect of hydrogen pressure

Figure 5.10 shows SEM micrograph of a (100) surface of polycrystalline diamond annealed with a 3 nm Ni film for 5 min at 800 °C in vacuum, 60 Torr Ar, 60 Torr H_2 and 1 atm H_2.

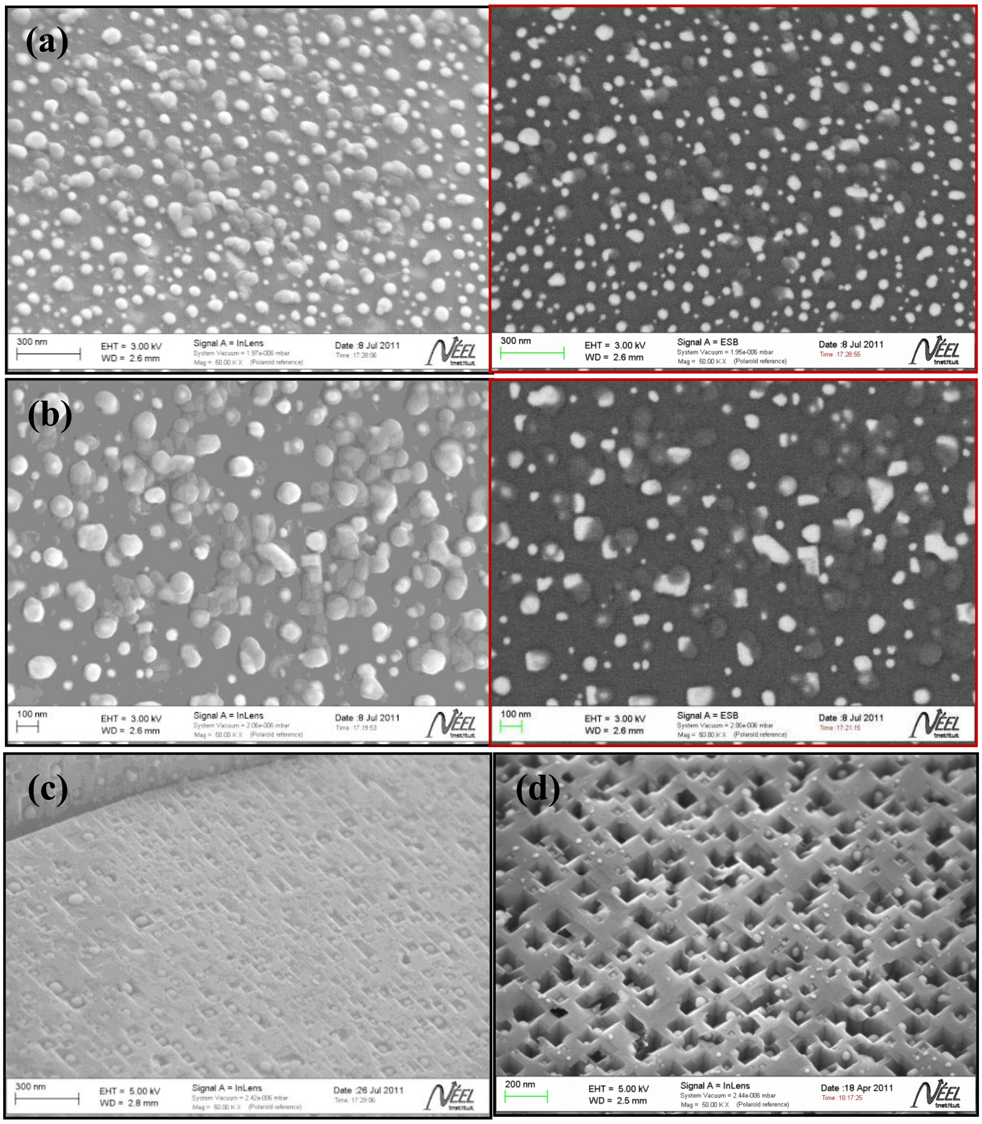

Figure 5.10. SEM images of a (100) surface of polycrystalline diamond after 5 min annealing in (a) vacuum, (b) 60 Torr Ar, (c) 60 Torr H_2 and (d) 1 atm H_2, (3 nm Ni, 800 °C); the right panels of images (a) and (b) are backscattered electron images, showing the presence of carbon overlayers.

Neither etch pits nor nano-channels were apparently found on diamond surface when there was no hydrogen in the furnace, i.e. under vacuum, figure 5.10 (a), and Ar atmosphere, figure 5.10 (b). Moreover, in both cases Ni nanoparticles were covered by overlayers, as appeared in the backscattered electron images (EsB detector), right panels of (a), and (b). The overlayers were confirmed as carbon by energy dispersive X-ray analysis (EDX), and most likely could be amorphous carbon. This observation indicates that when there is no hydrogen, and thereby no desorption, carbon absorbed by the Ni can lead to the nucleation and growth of inactive carbon layers that eventually diminish the catalytic activity of the metal. So, hydrogen is instrumental in the etching process. Moreover, the higher the pressure of hydrogen gas in the furnace, the faster the diamond is etched, figure 5.10 (d). We attributed this to the increased concentration of atomic hydrogen, generated catalytically that, indeed, enhances desorption rate.

5.3.5. Effect of diamond microstructure

Polycrystalline diamond and nanocrystalline diamond were annealed with a 3 nm Ni film at 800 ^{o}C under 60 Torr hydrogen atmosphere. After 30 min of annealing, etching was observed on both microstructures of diamond (figure 5.11). No particular effect related to the grain boundaries was observed. Etch pits with an inverted four sided pyramid were formed on [100] oriented planes of polycrystalline diamond, figure 5.11 (a), whereas a mixture of pyramidal, hexagonal, and trigonal shaped etch pits were observed on nanocrytalline diamond, figure 5.11 (b). Note that the nanocrystalline diamond sample exhibits a mixture of [111] and [100] oriented planes, and the etching behaviour is different depending on the crystallographic orientation.

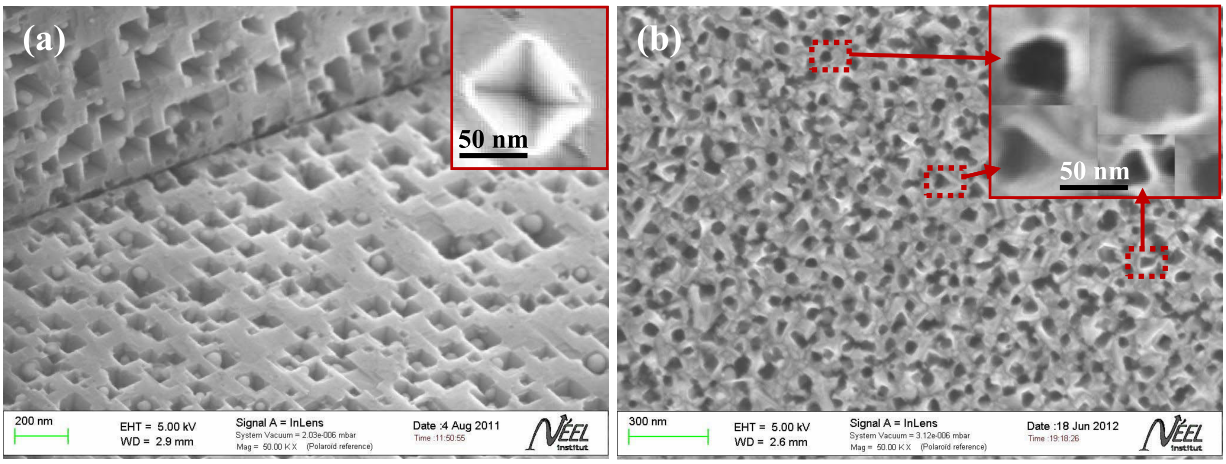

Figure 5.11. SEM images of (a) (100) surface of polycrystalline diamond and (b) nanocrystalline diamond after 30 min annealing with 3 nm Ni film, (800 ^{o}C, 60 Torr H_2), showing the formation of nanopores with no obvious dependence on the diamond microstructure. The inset of panel (a) is a SEM image taken after removal of Ni by aqua rezia (HCL:HNO_3 3:1) showing inverse pyramidal pore walled by four {111} planes, whereas the inset of panel (b) showing trigonal, pentagonal and pyramidal nanopores.

The orientation dependence of diamond etching has already been studied using molten Ce (**Jin *et al.* 1994**), Fe particles (**Sonin *et al.* 2003**), Co nanoparticles (**Konishi *et al.* 2006**), and molten Ni (**Smirnov *et al.* 2010**), as catalysts. It has been shown that Ni assisted diamond etching is slowest for [111] oriented diamond planes and that they act as stopping planes (**Smirnov *et al.* 2010**). Since the uptake of carbon atoms from diamond by the metal nanoparticles occurs from the weakly bonded atoms, the carbon atoms of the closest packing plane, {111} planes, are the most stable against the dissolution of carbon in nanoparticles, as compared to the other crystal planes (**Konishi *et al.* 2006**). As a result, etch pits walled with four {111} planes are formed on the {100} planes whereas {111} show etching pits with equilateral triangles and hexagons (**Smirnov *et al.* 2010**).

5.3.6. Change in Microstructure during Etching

Two diamond samples, [100]-oriented single crystalline (CVD diamond plate, Element Six) and nanocrystalline diamond (1.5 µm thickness, 100 nm grain size), were annealed with 3 nm Ni for 10 min at 800 °C. In order to detect an eventual change in microstructure, such as the appearance of graphitic phases on the surface, both samples were then characterized by Raman spectroscopy using 514 nm laser excitation, and the spectra were compared with those recorded before annealing. Figure 5.12 (a) shows Raman spectra for a [100]-oriented diamond crystal recorded before (red curve) and after (blue curve) annealing. Both spectra show a similar characteristic diamond line at 1332.4 cm^{-1}, and no graphitic component is observed before or after treatment.

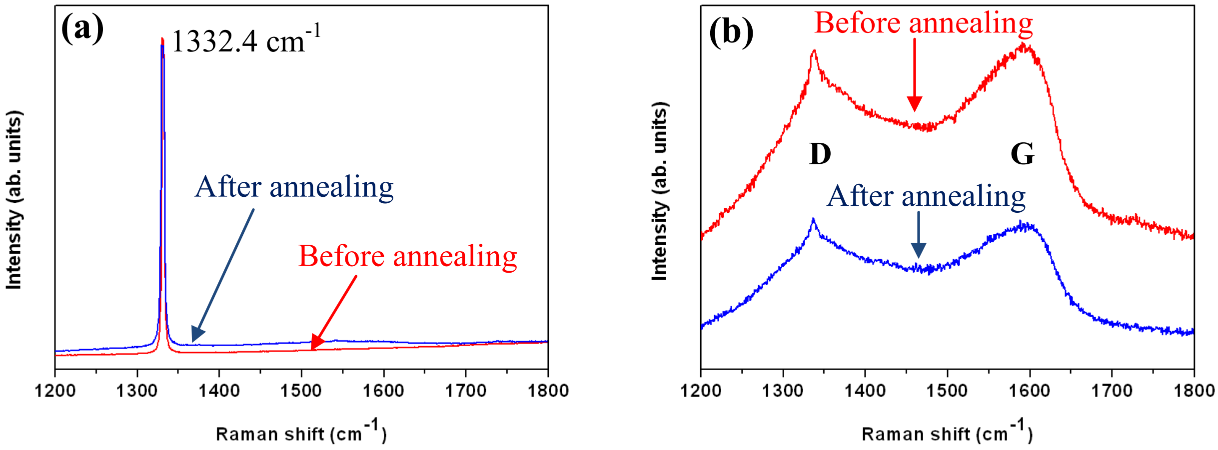

Figure 5.12. Raman spectra of (a) single crystal diamond ([100]-oriented, CVD diamond, Element Six) and (b) nanocrystalline diamond (1.5 µm thickness, 100 nm grain size) taken with 514 nm laser excitation, showing no change in the diamond structure after the catalytic etching by Ni nanoparticles, (3 nm Ni, 800 °C, 10 min, 60 Torr H_2).

On the other hand, D and G peaks, which lie at 1337 and 1590 cm^{-1} respectively, were observed for the nanocrystalline diamond sample, figure 5.12 (b). The band at 1337 cm^{-1} is assigned to the sp^3-bonded carbon in diamond (D band) and the broad peak around 1590 cm^{-1} is attributed to the sp^2-bonded carbon (G band). The peak intensity ratio of the D band to the G band (I_D / I_G) is a measure of the amount of graphitic impurities. The measured I_D / I_G values of the treated and untreated samples were 1.02 and 1.01 respectively. The observation suggests that the diamond structure was maintained for both samples (single crystalline and nanocrystalline diamond) after the catalytic etching by Ni nanoparticles.

5.3.7. Effect of Annealing Time

To study the effect of annealing time in the etching process, both polycrystalline and nanocrystalline diamond were annealed with 3 nm Ni layers at 800 °C from 30 sec to 6 hours. After 30 sec annealing, only self-organized Ni nanoparticles were observed on the diamond surface (figure 5.13 (a)), no nanopore appeared. During annealing the Ni layer melts and dewets resulting in spherically shaped nanoparticles prior to etching in order to minimize the surface energy. This effect is well known and relates to the melting point lowering effect of thin metal films and hydrogen diffusion into the metal (**Pundt, 2004**; **Yang *et al.* 1998**; **Buffat & Borel, 1976**; **Gladkich *et al.* 1966**). Etched structures started to appear after 3 min (figure 5.13 (b)) and nanopores with flat sidewall faces, and sharply defined edges were formed after 10 min of annealing (figure 5.13 (c)). After 6 hours, nanopores lost their previous shape (pyramidal shape) due to the rupture both at edges and sidewall faces (figure 5.13 (d)).

Figure 5.14 (a) shows the pore depth variation with annealing time measured for nanocrystalline diamond, where after every 10 min, the cross section of the sample was observed in SEM and the depth of etch pores was estimated from the observation. Figure 5.14 (b) shows the SEM micrograph, of the cross-section of the etched nanocrystalline diamond after 90 min of annealing acquired with an EsB detector. The white spots correspond to Ni nanoparticles.

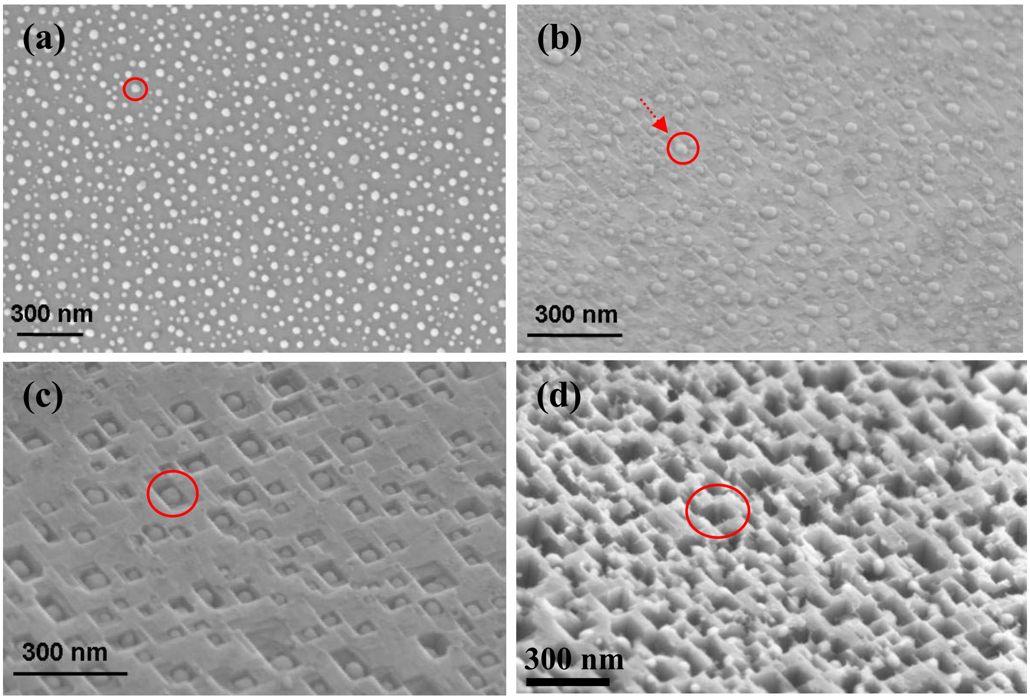

Figure 5.13. SEM images of (100) surface of the annealed polycrystalline diamond with 3 nm Ni layers after (a) 30 sec, (b) 3 min, (c) 10 min and (d) 6 hours annealing, (800 °C, 60 Torr H_2). The red circle identifies a particular particle evolution, and the red arrow indicates the movement of the particle due to gravity prior to etching.

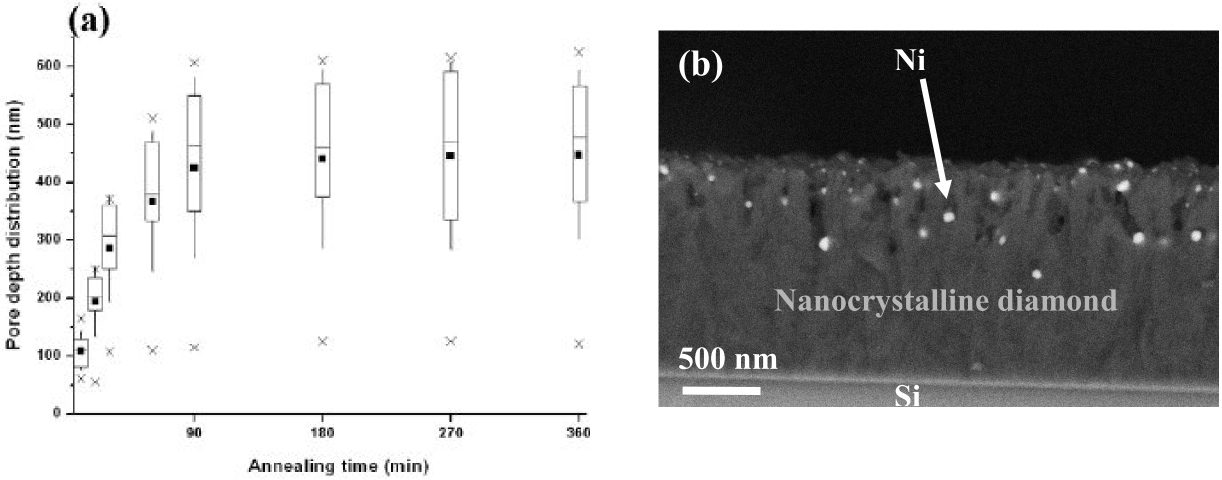

Figure 5.14. (a) Variation of etch depth with annealing time measured for nanocrystalline diamond after 6 hours of annealing with 3 nm Ni film, (800 °C, 60 Torr H_2). Bottom and top line of the box represent the 25th and 75th percentile of each data set. The band and square inside refer to the median and mean respectively; minimum and maximum values are indicated by the cross. Whiskers refer to mean ± standard deviation. After every 10 min the cross section of the etched sample was

observed by SEM and pore depth was estimated from the SEM image. Note that the Ni particles that were present on the diamond surface after annealing were excluded from the depth measurement. (b) Corresponding SEM image acquired with an EsB detector after 90 min, revealing Ni nanoparticles embedded into the crystal volume.

According to figure 5.14 (a), etching proceeded rapidly within first 60 min, then slowed down, and eventually was saturated after 90 min of annealing. After 6 hours of annealing, the mean depth was estimated to be about 520 nm. The observed reduction and saturation of the etching rate for long processing times could be explained by the increase in the distance from the top surface down to the metal nanoparticle. As the Ni nanoparticle moves deeper into the diamond, away from the source of molecular hydrogen, the carbon desorption from the nanoparticle becomes less effective, eventually leading to the saturation of the catalyst with carbon.

5.3.8. Analysis of Annealed Diamond Surfaces by XPS

As shown in figure 5.15 (a), the etching of diamond is not limited by the diffusion of carbon through the particle. The limitation factor could therefore be the processes occurring at the catalyst-diamond interface, in particular the formation of carbide, or in the gas phase. In order to explore the existence of nickel carbide at the catalyst-diamond interface, the surface composition of annealed samples was investigated by XPS.

Two polycrystalline diamond films with 3 nm Ni layers were annealed for 30 sec and 10 min at 800 °C in 60 Torr hydrogen atmosphere. The corresponding SEM images are displayed in figure 5.13 (a) and (c). The samples were then characterized by XPS with a monochromatic Al Kα anode (1486.6 eV) that was calibrated with respect to the Au 4f 7/2 peak located at 84.0 eV. The spectrometer was equipped with an EA 125 hemispherical analyzer. The path energy was 20 eV, corresponding to an absolute energy resolution of 0.6 eV. The detection limit of our XPS setup is estimated to be 0.2 at.%. Areas of XPS core levels were extracted after a Shirley correction of the background and atomic contents were calculated after correction by the photoionized cross-sections.

Table 1 shows quantitative analysis of the surface composition of the annealed samples and reveals the presence of C, Ni, O and Si in the surface layers of diamond where O and Si were contaminants. The Si 2p core level shows that silicon is bonded to oxygen with the oxide component located at 101.5 eV (**Arnault *et al.* 2008**). The silicon atomic % (Table 1) indicates that the major part of detected oxygen comes from this oxide. Samples were only slightly contaminated by oxygen during their handling in the air before /and after the process.

Table 1. Quantitative analysis of the surface composition estimated from XPS measurement of annealed polycrystalline diamond.

Name	Sample[1a] (at.%)	Sample[1b] (at.%)
C 1s	85.4	85.5
Ni 2p	1.2	0.6
Si 2p	3.7	4.0
O 1s	9.7	9.9

[a] 30 sec annealing; [b] 10 min annealing

[1] 3 nm Ni, 800 °C, 50 Torr H_2

Ni concentration was found to decrease after 10 min of annealing. The SEM picture of this sample, figure 5.13 (c), shows that due to etching a significant part of the Ni particles are buried (~ 110 nm deep) into the diamond film, therefore, the particles contributed less to the XPS signal. In contrast, after 30 sec of annealing all the particles were present on the surface of the diamond film, figure 5.13 (a), resulting in the enhanced detection. The XPS spectra of C 1s and Ni 2p core levels are shown in figure 5.15.

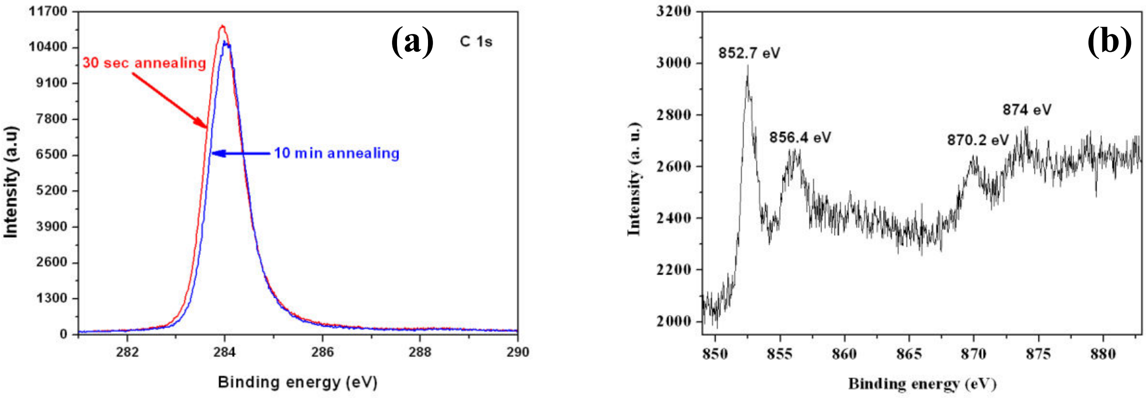

Figure 5.15. XPS spectra of (a) C 1s core level for 30 sec and 10 min annealed polycrystalline diamond with 3 nm Ni layers showing similar peak at 284 eV that is related to the carbon atoms lying at the diamond surface and (b) Ni 2p core level for 10 min annealed polycrystalline diamond showing the signature of metallic Ni at 852 eV (Ni 2p3/2) and oxide (Ni_2O_3) at 856 eV.

The C 1s spectra for 30 sec and 10 min annealed diamond, figure 5.15 (a), show similar carbon peak at 284 eV that is related to the carbon atoms lying at the diamond surface (Arnault *et al.* 2007). Ni 2p core level spectrum, figure 5.15 (b), obtained from 10 min annealed diamond shows the signature of metallic nickel at 852.7 eV (Ni 2p3/2) and nickel oxide (Ni_20_3) at 856.4 eV (**Rey *et al.* 2011**; **Biesinger *et al.* 2009**). Similar spectrum was obtained for 30 sec annealed diamond. For both samples, the spectra of C 1s and Ni 2p core levels did not show carbide component. According to the literature, a component should appear close to 283 eV (**Wiltner & Linsmeier, 2004**; **Rey & Normand, 2010**). Indeed, metallic carbides lead to the presence of an additional component at C1s located at lower binding energy vs diamond one. On the other hand, X-ray energy loss spectra (XEELS) recorded at C 1s core level for 30 sec and 10 min annealed diamond exhibit the characteristic diamond bulk plasmon at +34 eV and surface plasmon at +24 eV from the C1s (**Arnault *et al.* 2007**) (figure 5.16).

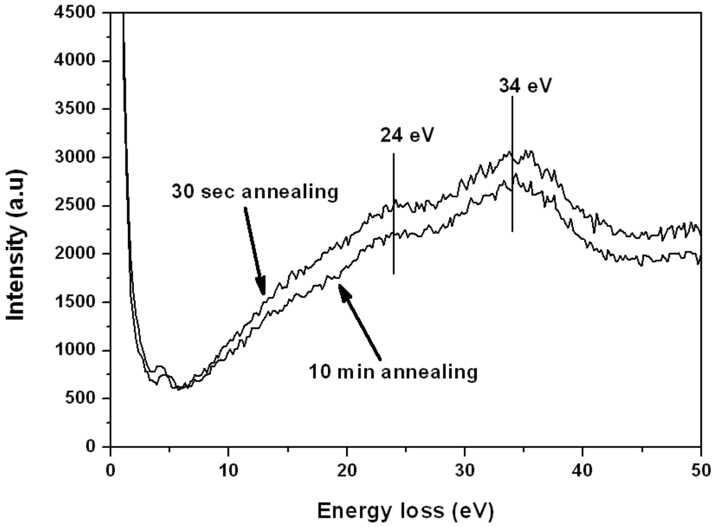

Figure 5.16. ELS spectra recorded at the C 1s core level for 30 sec and 10 min annealed polycrystalline diamond with 3 nm Ni layers showing the characteristic diamond bulk plasmon at +34 eV and surface plasmon at +24 eV and suggesting no change in the diamond structure after catalytic etching by Ni particles.

The result suggests that the diamond structure was maintained after the catalytic etching by Ni nanoparticles.

In a typical XPS measurement, the detection of any component is strongly influenced by the penetration depth of X-ray (probed depth d) that is calculated by the equation: $d = 3\ \lambda\ \cos\theta$, where λ is the mean free path of photoelectrons and θ is the angle between the surface normal and the analyzer direction (for our XPS geometry $\theta = 41°$). Probed depths for C 1s and Ni 2p were estimated to be 7.0 nm and 2.3 nm taking into account λ values of 3.1 nm and 1.0 nm, respectively (**Tanuma *et al.* 1988**). On the other hand, the diameter of spherically shaped Ni nanoparticles generated from the 3 nm Ni layers was estimated to be approximately 45 nm. Any component, e.g., carbide, that might form at the diamond-metal interface or present within the particles below the probe depth was not therefore detectable. We also investigated the interface by XPS after removing Ni particles from the 10 min annealed diamond by aqua regia. The spectra (not shown) again did not show any carbide component. No carbide was therefore detected before or after the removal of the nickel catalyst. However, we can not completely exclude the occurrence of carbide at the interface during the process at 800°C.

There could be a thin layer of carbide at the interface hidden by the nickel, but was etched away together with nickel by aqua regia.

5.3.9. Gas Composition Analysis by Mass Spectrometer

For a better understanding of the etching process, the gas composition in the chamber was analyzed during the process. A quadrupole mass spectrometer gas analyzer (AMETEK Dycor Dymnaxion DM 100) was fitted to the exhaust port of the reaction chamber with an aperture inlet consisting of a 5 µm aperture within a manual valve. The aperture was chosen to reduce the pressure from 50 Torr in the process chamber down to 10^{-5} Torr in the quadrupole. The detection set consisted of a Faraday cup detector, and an electron multiplier was used to amplify the signal by approximately one thousand. The minimum detectable partial pressure for the Faraday cup detector is 5×10^{-12} Torr and that for electron multiplier units is 5×10^{-14} Torr with mass resolution of 0.5 AMU at 10% height.

In order to increase the signal, the process was carried out in the closed chamber (no hydrogen flow) and a 2 inch nanocrystalline diamond was used. Temperature was 800°C and 3 nm Ni layers were deposited on the sample. After one minute of process, methane was detected by the spectrometer (figure 5.17 (b)).

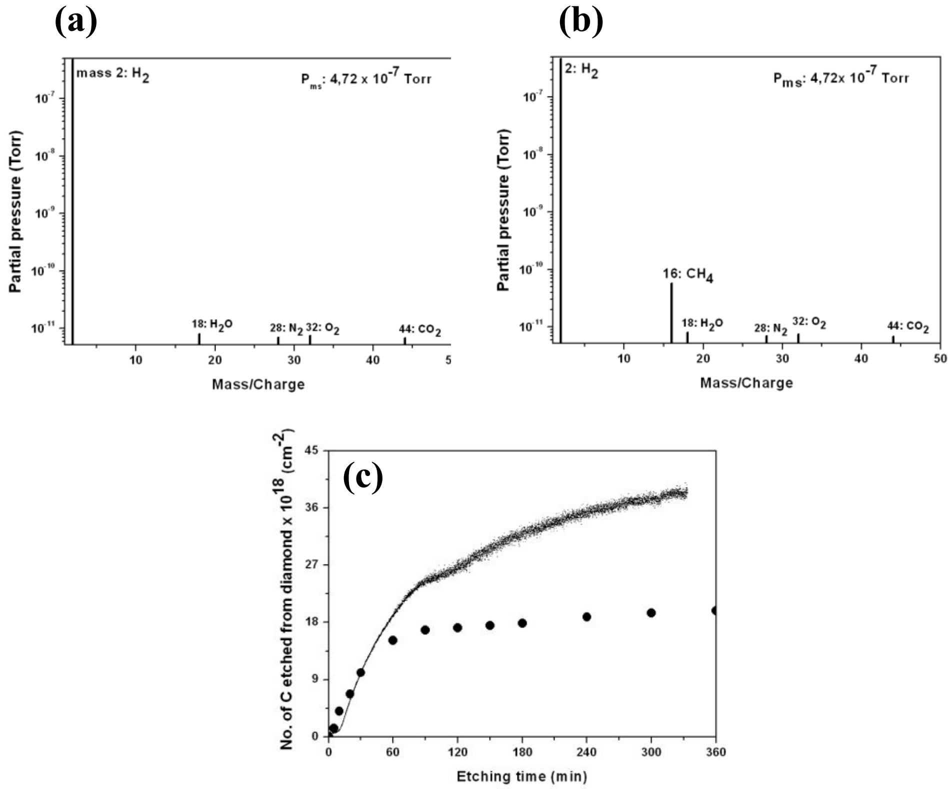

Figure 5.17. Mass spectra (a) before annealing, hydrogen being added in the gas phase, (b) after 1 min of the process revealing the release of carbon atoms from the diamond, (c) number of carbon atoms removed from nanocrystalline diamond during 6 hours of the process, (800 ^{o}C, 3 nm Ni, 50 Torr H_2), solid line represents spectrometer data, whereas the dotted line corresponds to the number of removed carbon atoms calculated from the average depth and diameter of the nanopores; P_{ms} indicates pressure in the spectrometer head.

The process was carried on for 6 hours. Figure 5.17 (c) shows the evolution of the total number of carbon atoms in the gas phase. Two different regimes were observed: rapid etching within first 60 min, then slow etching and eventually saturation after 90 min. In order to compare these results with the SEM observations, the number of carbon atoms removed from the diamond surface during etching was estimated from the average diameter and depth of the nanopores, and shown as dotted line in figure 17 (c). The agreement is quite convincing, confirming that the methane is coming out of the nanopores, and that methane is the main hydrocarbon species carrying etched carbon atoms. The observed behaviour of methane evolution could explain the etching process in the following way:

- for short etching time, before typically 60 min of etching, the process is limited by the kinetics at the catalyst-diamond interface, and the etching rate is roughly constant,

- for long etching time, between 60 and 90 min, the catalyst droplets are already located deep inside the diamond film (300 to 500 nm), the diffusion of hydrogen into the pores, and the out-diffusion of methane from the pores, make the carbon desorption from the nickel catalyst decrease. If the desorption rate is not high enough to remove all the carbon, a graphite-like film can be formed at outer metal surface, causing catalyst deactivation (**Tamai *et al.* 1977**). Those areas which turn out to be covered by carbon films show a slower etch rate.

- for etching time typically longer than 90 min, either the methane around the catalyst droplets is in equilibrium with the carbon at the catalyst surface, or there is no hydrogen anymore near the catalyst, and consequently the etching process is stopped.

The etching depth is therefore limited by gas in- and out-diffusion inside the nanopores. In order to confirm this, a polycrystalline diamond sample was annealed in 60 Torr hydrogen at 800°C with 0.5% methane being added in the gas phase. No etching was observed after 60 min of process, figure 5.18 (a).

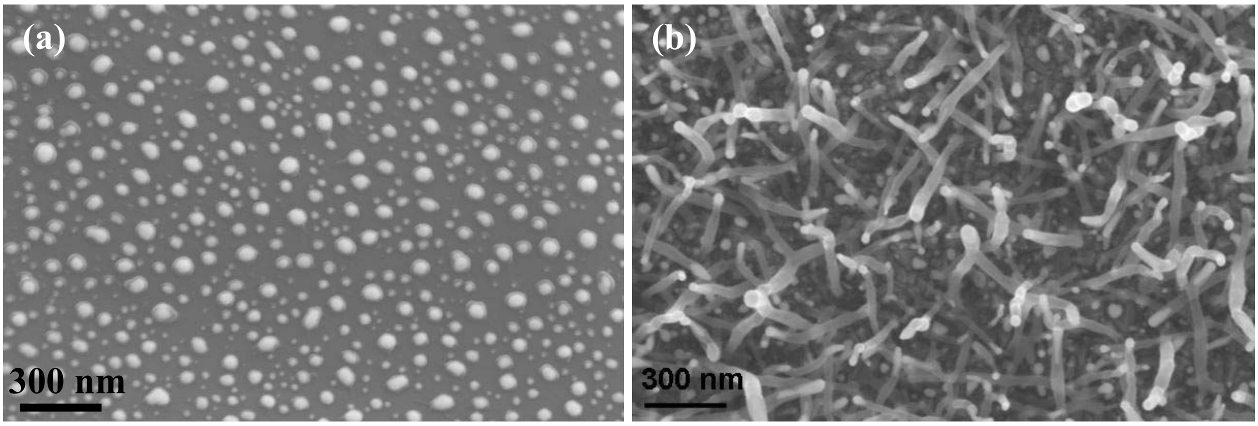

Figure 5.18. SEM images of (a) (100) surface of polycrystalline diamond after 60 min annealing in 60 Torr H_2 and 0.5% CH_4 environment showing the compensation of etching by CH_4 molecules and (b) nanocrystalline diamond after 6 hours annealing in the closed chamber under 60 Torr H_2 demonstrating the growth of carbon nanotubes due to the accumulation of carbon atoms on the catalyst; both samples were processed with 3 nm Ni at 800 ^oC.

In fact, the methane concentration was high enough to stop the carbon desorption from the catalyst, preventing any etching. Interestingly, the increase in carbon concentration around the catalyst could lead, in some particular conditions, to the reverse process: the growth of carbon nanotubes. It was the case, for example, for a nanocrystalline diamond sample annealed in the closed chamber for 4 hours with 3 nm Ni layers at 850°C under 60 Torr hydrogen (without methane added). The nanotubes, figure 5.18 (b), clearly grew after a long etching step, some catalysts being located deep inside the microcrystal.

Similarly, a process performed in vacuum does not lead to any etching, figure 5.10 (a), showing the importance of both hydrogen in-diffusion and methane out-diffusion in the process.

5.3.10. Model for Etching Diamond with Ni

After the formation of catalyst droplets by deweting, five important steps of the process, as shown schematically in figure 5.19, have been identified based on the above investigations:

1. Diffusion of molecular hydrogen from the chamber to the surface of the catalyst
2. Molecular hydrogen is catalytically dissociated into atomic hydrogen by nickel
3. Carbon atoms from the diamond surface can be removed through two different ways:

   a. the carbon atoms dissolve in the nickel droplet and then diffuse to the metal-gas interface where they react with hydrogen atoms forming methane
   b. hydrogen atoms diffuse within the catalyst to reach the diamond-metal interface, then remove carbon in the form of methane
4. Desorption of methane from the catalyst
5. Out-diffusion of methane from the vicinity of the catalyst

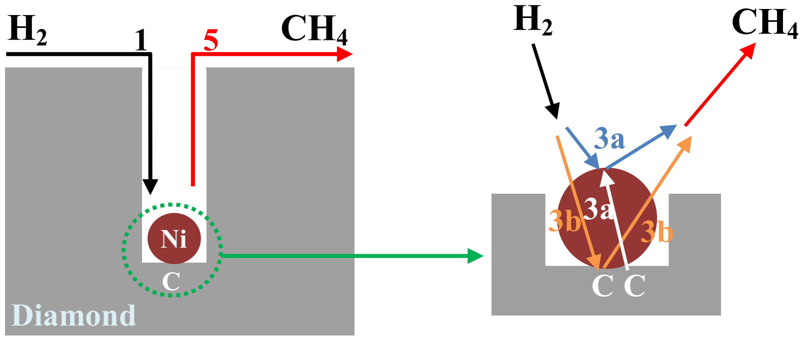

Figure 5.19. Schematic representation of the model for etching diamond with Ni; (1) hydrogen diffusion to the catalyst surface, (3a) carbon diffusion from the metal_diamond interface to metal-gas interface and then desorption as methane, (3b) hydrogen diffusion to the diamond-metal interface and carbon desorption as methane, (5) out-diffusion of methane from the vicinity of the catalyst.

For low etching time, when the catalyst is still located close to the diamond surface, step 3 is limiting the etching process. In both cases, 3a and 3b (figure 5.19), the reaction is not limited by the diffusion through the catalyst, as the etching rate does not decrease with the catalyst thickness. The process is therefore limited by the reaction at the diamond-catalyst interface. The surface study carried out by XPS did not show any evidence of nickel carbide that could have limited the interface reactions.

5.4. Catalytic Etching for Selective Patterning of Diamond Films

Due to their unique properties, diamond thin films have been receiving much attention for potential high-performance electronic devices and microelectromechanical (MEMS) applications (especially in hostile environments, such as high ambient temperatures, reactive environment or extensive wear and friction conditions). Precise patterning of diamond microstructures is a key technology in the application of diamond to microelectronic devices and MEMS. However, due to its extremely high chemical stability, diamond is difficult to be micropatterned by the conventional microfabrication processes, which use chemical etching though a photoresist mask. Several alternative methods have been exploited to solve this problem, such as selective growth (**Masood *et al.* 1991**; **Katsumata *et al.* 1994**; **Avigal *et al.* 1997**; **Sakamoto *et al.* 1998**; **Regel & Wilcox, 1999**), plasma etching with reactive ion (**Dorsch *et al.* 1992**; **Edo *et al.* 1996**; **Deguchi *et al.* 1997**; **Ramesham *et al.* 1998**; **Baik *et al.* 1999**) and direct laser writing (**Ralchenko *et al.* 1995**). However, all of these techniques used previously could not produce the precise diamond lines with steep sidewalls demanded by micromechanical devices mainly due to a low nucleation-selectivity (the nucleation ratio of the desired to the undesired region) in the selective growth technique, low etching-selectivity between the mask material and the diamond films in plasma etching technique, and a rough side-wall surface of the diamond pattern in the laser writing technique. Due to its simplicity and cost-effectiveness the catalytic etching technique could be a potential candidate for precise patterning of diamond microstructures.

5.4.1. Methods and Materials

In order to produce microstructures in polished diamond films the metal films (Ni and Pd) were patterned first by conventional photolithography and then were transferred onto diamond via the catalytic etching process at 850 °C. [100]-oriented single crystalline CVD diamond plates (Element Six) (figure 5.20) with 3 mm thickness were used as substrates.

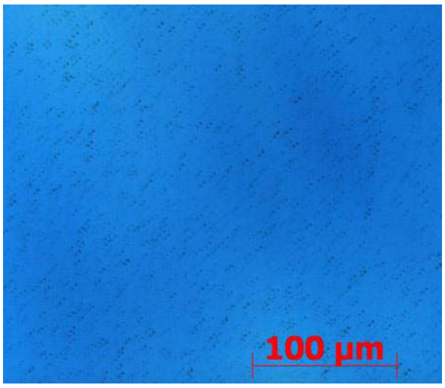

Figure 5.20. Optical microscopy image of a [100]-oriented single crystalline CVD diamond plate (purchased from Element SiX).

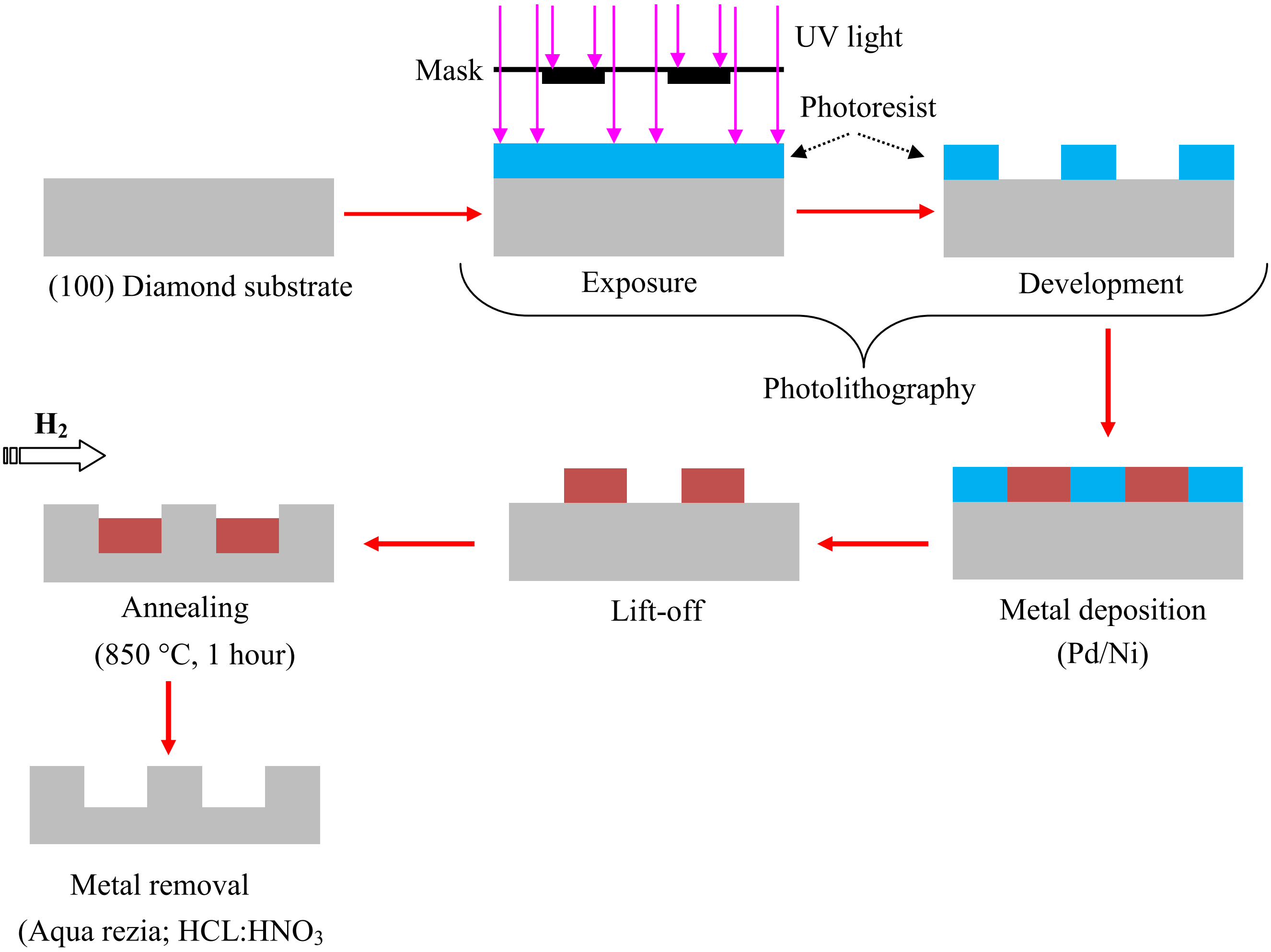

Figure 5.21. Schematic illustration of the fabrication process of microstructures in diamond films by catalytic etching with patterned metal films.

A schematic of patterning metal films and the subsequent etching process is shown in figure 5.21. Prior to photolithography the diamond substrates were cleaned by standard procedures in a clean room. The substrate surface was then spin-coated with a thin film (~2.5 µm thick) of positive photoresist (Microposit 1813). After soft-baking, the film was exposed to UV light through a transparency-based photomask (black ink printed). Two photomasks were used: rectangle and square shaped features; only circular shaped feature. After development, Ni and Pd metal films with thickness in the range of 100-200 nm were deposited on the patterned surface by e-beam evaporation. Lift-off process was then performed to remove the remaining photoresist from the diamond surface and finally the samples were annealed in hydrogen atmosphere at 850 °C for 1 hour.

5.4.2. Results and Discussion

Figure 5.22 shows the morphology of etched microstructures generated after 1 hour of annealing with 100 nm patterned Ni film in the case of photomask with square and rectangle shaped features. The microstructures retain the original feature shape and size except distortion at edges. The SEM images after Ni removal by aqua rezia (HCL: HNO_3 3:1) (righ panels of figure 5.22, as indicated by red border), show step-like features inside the microstructures revealing the inhomogeneities in the etching. Improvement in the etching uniformity was observed for 200 nm patterned Ni film, in particular for square shaped feature (figure 5.23 (a)) and microstructures with more accurate edges were formed.

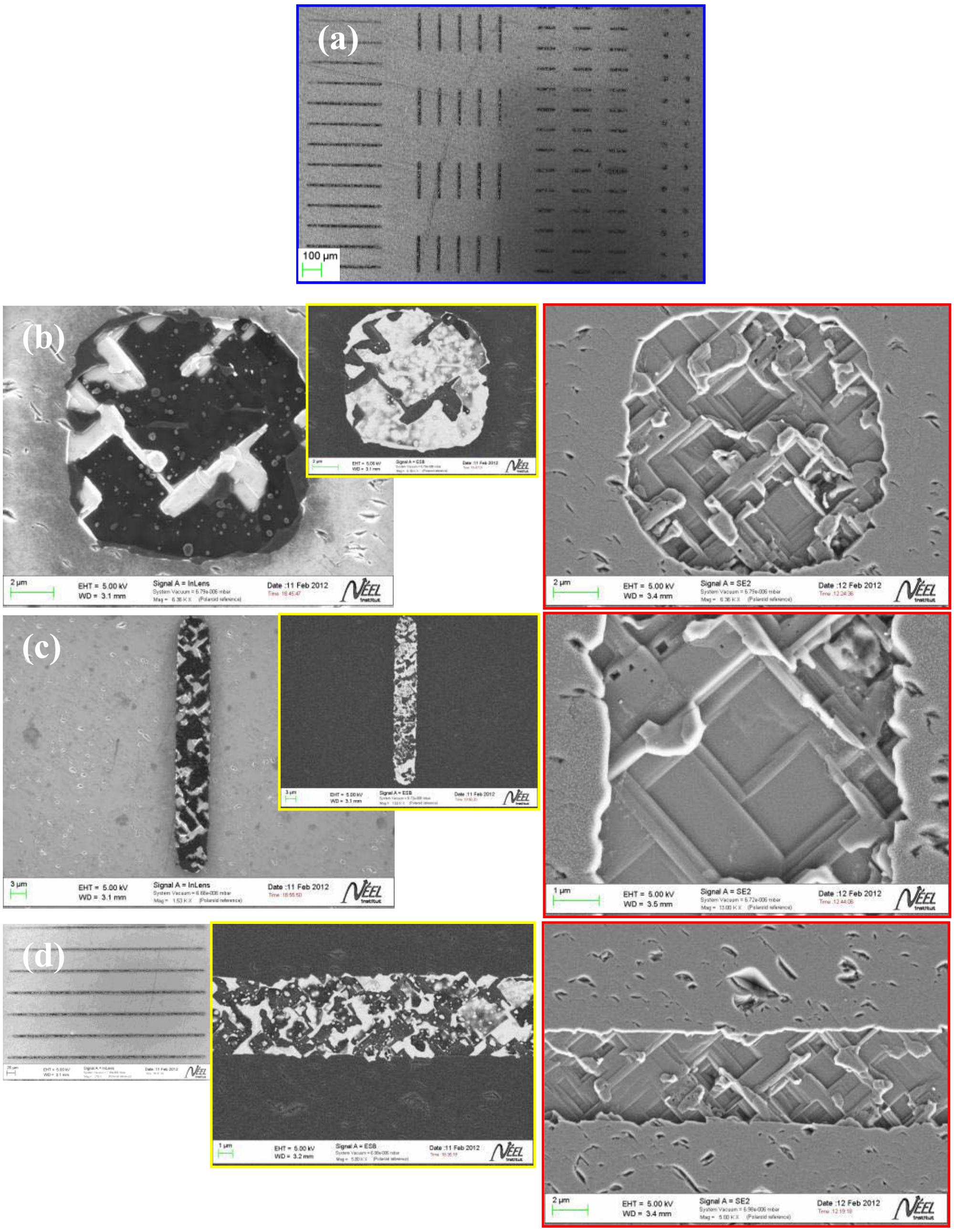

Figure 5.22. The morphology of microstructures in [100]-oriented single crystalline diamond after 1 hour of annealing with 100 nm patterned Ni film, (850 °C, 60 Torr); (a) low magnification SEM image, (b) generated structure of about 10 × 10 μm^2 from square shape feature in the photomask, (c) generated structure of about 50 × 5 μm^2 from rectangle feature and (d) generated structure of about 200 × 5 μm^2 from rectangle feature. The insets of panels (b)-(d), as indicated by yellow border, are SEM images acquired with a backscattered electron detector; the right panels, red border, SEM images acquired with a secondary electron detector after Ni removal with aqua regia revealing the inhomogeneity in etching and distortion at microstructure edges.

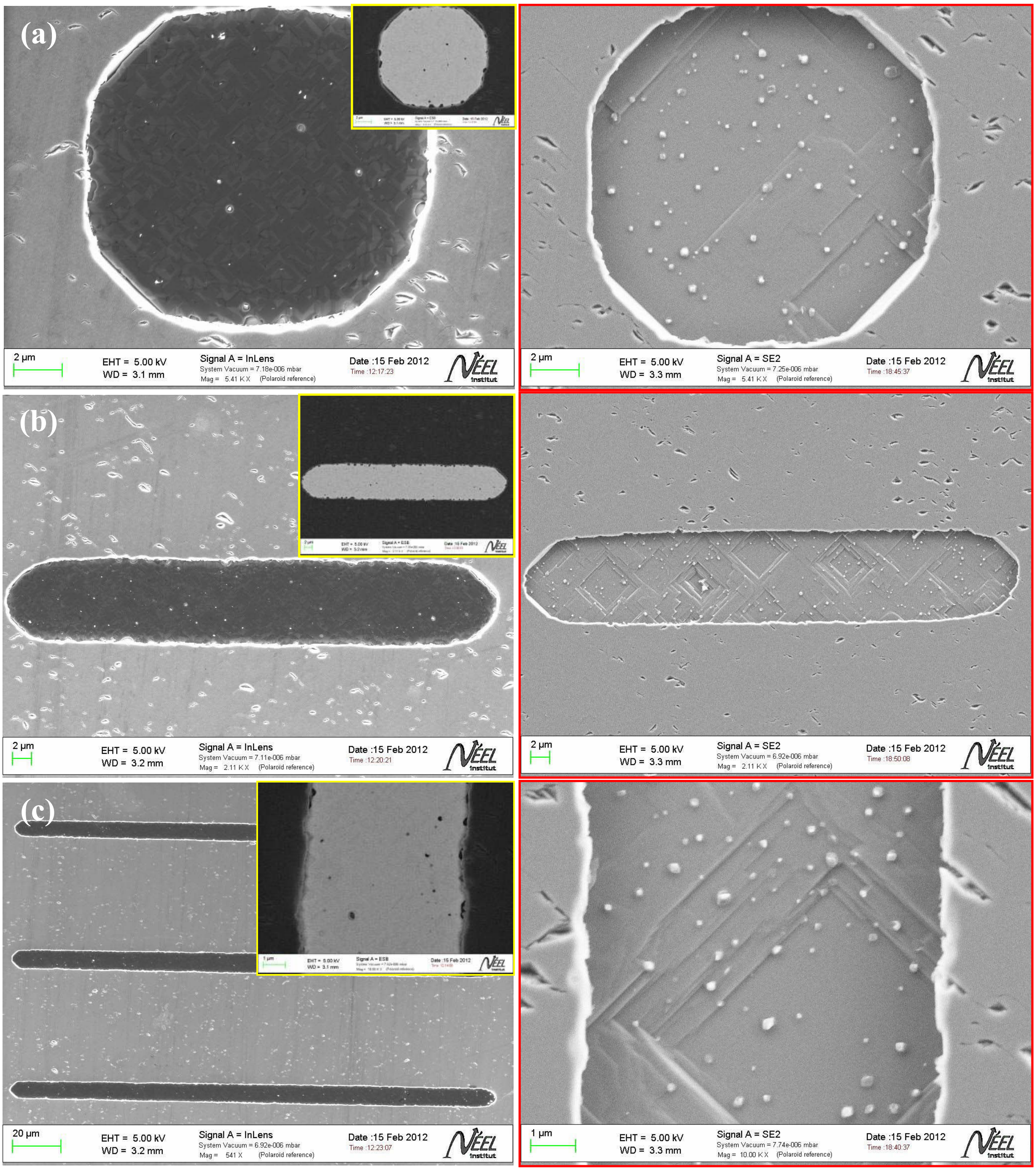

Figure 5.23. The morphology of microstructures in [100]-oriented single crystalline diamond after 1 hour of annealing with 200 nm patterned Ni film, (850 °C, 60 Torr); (a)-(c) SEM images of generated structure of about 10 × 10, 50 × 5, 200 × 5 µm^2 in size repectively. The insets, as indicated by yellow border, are SEM images acquired with a backscattered electron detector; the right panels, red border, SEM images acquired with a secondary electron detector after Ni removal with aqua rezia revealing the less inhomogeneity in etching and microstructures with more accurate edges.

In addition, for the thicker film (200 nm), slight changes in the original feature shape were observed (right panels of figure 5.23), e.g., imperfect octagonal microstructures for square feature. Furthermore, unlike 100 nm film no apparent discontinuity was observed in the surface of 200 nm film after etching (insets of figure 5.23, as indicated by yellow border).

The formation of branched Ni particles (or discontinuity) in the 100 nm film after etching indicate that there might be defects (pinholes /and unevenly deposited areas) in the initially deposited films. Such imperfections could result from any fault in the processes prior to etching (lithography, metal evaporation, lift-off etc.). During annealing these defects could provide effective sites for void nucleation that might propagate in a branched manner which is usually observed in the dewetting of Au thin film on solid substrates and is described as the fractal growth mode (**Kown *et al.* 2003**; **Gadkari *et al.* 2005**). The branching of Ni particle could induce the fabrication of step-like features inside the etched structures and thereby the non-uniformity of etching. In contrast, no dewetting of the 200 nm Ni film was observed suggesting that the film was stable against the thermal annealing at 850 °C.

On the other hand, 1 hour of annealing with 200 nm patterned Pd film resulted in a very interesting microstructure (figure 5.24). Note that a photomask with circular feature of size about 10 μm was used. Big spherically shaped Pd particles were generated upon annealing (figure 5.24 (b)) due to dewetting of the film and high cohesion energy of Pd (**Lee & Kim, 2007**). The morphology of the etched structure after removal of the particle by aqua regia shows the inverse pyramidal-shaped microstructure with sharply defined edges and walled by four {111} planes (figure 5.24 (c)), a characteristic etched feature for [100]-oriented plane, where {111} planes act as etch stopping planes, revealing anisotropy in the diamond etching similar to that was observed for etching with metal nanoparticles. The difference in size and shape between particles and etched structures suggests that the size of the microstructures depends on the initially formed metal particles. The lateral size and depth of the microstructure were estimated by optical profilometer to be about 5×5 μm^2 and 2 μm respectively. Unlike Ni films and the associated photomask (figure 5.23), no discontinuity in the etching and dewetting was observed for Pd. There seems to be a trade-off between the metal film thickness, etch rate and spatial resolution of patterns in diamond. Nevertheless, the inverse pyramidal microstructures could find some potential applications, in particular in the fabrication of diamond based electronic devices where generation of well-oriented {111}

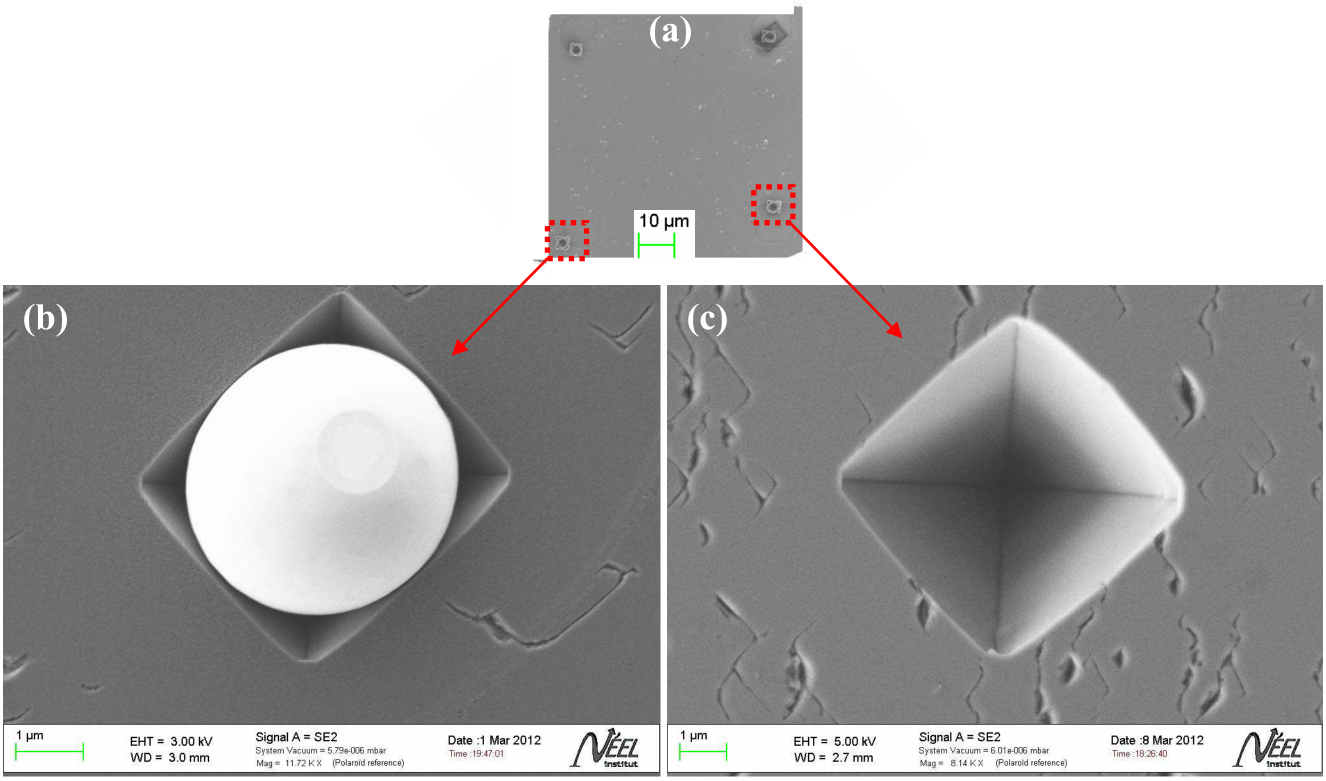

Figure 5.24. The morphology of etched microstructures in [100]-oriented single crystalline diamond after 1 hour of annealing with 200 nm patterned Pd film, (850 °C, 60 Torr); (a) low magnification SEM image showing few ordered microstructures, (b) SEM image acquired with a secondary electron image where spherically shaped particles (bright contrast) corresponds to Pd and (c) secondary electron image after Pd removal by aqua rezia revealing the inverse pyramidal-shape of microstructure walled by four {111} planes.

planes in [100]-oriented diamond crystal might be necessary.

Bibliogrqphy

Alford, T. L., Chen, L. H. & Gadre, K. S. **2003** *Thin Solid Films* 429, 248.

Alford, T. L. & Allee, D. R. **2002** *Appl. Phys. Lett.* 81, 4287.

Auciello, O., Birrell, J., Carlisle, J. A., Gerbi, J. E., Xiao, X. C., Peng, B. & Espinsoa, H. D. **2004** *J. Phys.: Condens. Matter.* 16, R539.

Arnault, J. C., Saada, S., Delclos, S., Intiso, L., Rocha, L., Polini, R., Hoffman, A. & Bergonzo, Ph. **2008** *Chem. Vap. Deposition* 14, 187.

Arnault, J. C., Saada, S., Delclos, S., Intiso, L., Tranchant, N., Polini, R. & Bergonzo, Ph. **2007** *Diamond Relat. Mater.* 16, 690.

Avigal, Y., Glozman, O. & Etsion, I. **1997** *Diam. Relat. Mater.* 6, 381.

Baik, F. S., Baik, Y. J. & Jeon, D. **1999** *Diam. Relat. Mater*. 8, 2169.

Barrat, S., Saada, S., Dieguez, I. & Bauer-Grosse, E. **1998** *J. Appl. Phys.* 84, 1870.

Berman, R. **1979** In *The Properties of diamond (*ed. J E Field) London: Academic.

Biesinger, M. C., Payne, B. P., Lau, Leo. W. M., Gerson, A. & Roger St. C. Smart, R. St. C. **2009** *Surf. Interface Anal.* 41, 324.

Bischof, J., Scherer, D., Herminghaus, S. & Leiderer, P. **1996** *Phys. Rev. Lett.* 77, 1536.

Bower, C., Zhou, O., Zhu, W., Werder, D. J. & Jin, S. **2000** *Appl. Phys.Lett.* 77, 2767.

Brochard-Wyart, F. & Dalliant, J. **1990** *J. Phys*. 68, 1084.

Buffat, P. & Borel, J. P. **1976** *Phys. Rev. A* 13 2287.

Chepurov, A. I., Sonin, V. M., Chepurov, A. A., Zhimulev, E. I., Tolochko, B. P. & Eliseev, V. S. **2011** *Inorg. Mater.* 47, 957.

Chepurov, A. I., Sonin, V. M. & Dereppe, J.-M. **2000** *Diamond Relat. Mater.* 9, 1435.

Clarke, J., Wu, H. C., Jayasinghe, L., Patel, A., Reid, S. & Bayley, H. **2009** *Nat. Nanotechnol*. 4, 265.

Dekker, C. **2007** *Nat. Nanotechnol.* 2, 209.

Deguchi, M., Hase, N. & Kitabake, M. **1997** *Diam. Relat. Mater*. 6, 367.

Derrington, I. M., Butler, T. Z., Collins, M. C., Manrao, E., Pavlenok, M., Niederweis, M. & Gundlach, J. H. **2010** *PNAS* 1-6.

Dorsch, O., Werer, M. & Obsermeier, E. **1992** *Diam. Relat. Mater*. 1, 277.

El-Dasher, B. S., Gray, J. J., Tringe, J. W., Biener, J., Hamza, A. V., Wild, C., Worner, E. & Koidl, P. **2006** Surface *Appl. Phys. Lett.* 88, 241915.

Edo, M., Watnabe, Y. & E. Yonezawa, E. **1996** in: Proceedings of the International Symposium on Microsystems, Intelligent Material and Robotics. pp. 177. Sendai, Japan.

Gadkari, P. R., Waren, A. P., Todi, R. M., Petrova, R. V. & Coffey, K. R. **2005** *J. Vac. Sci. Technol. A* 23, 1152.

Geissler, A., He, M., Benoit, J-C. & Petit, P. **2010** *J. Phys. Chem. C* 114, 89.

Gershow, M. & Golovchenko, J. A. **2007** *Nat. Nanotechnol.* 2, 775.

Giermann, A. L. & Thompson, C. V. **2005** *Appl. Phys. Lett.* 86, 121903.

Gladkich, N. T., Niedermayer, R. & Spiegel, K. **1966** *Phys. Status Solidi B* 15, 181.

Gracia, L., Calatayud, M., Andr`es, J., Minot, C. & Salmeron, M**. 2005** *Phys. Rev. B* 71, 033407.

Harutyunyan, A. R., Mora, E., Tokune, T., Bolton, K., Rosn, A., Jiang, A., Awasthi, N. & Curtarolo, S. **2007** *Appl. Phys. Lett.* 90, 163120.

Healy, K., Schiedt, B. & Morrison, A. P. **2007** *Nanomedicine* 2, 875.

Herminghaus, S., Jacobs, K., Mecke, K., Bischof, J., Fery, A., Ibn-Elhaj, M. & Schlagowski, S. **1998** *Science* 282, 916.

Hummel, R. E., Dehoff, R.T., Matts-Goho, S. & Goho, W. M. **1981** *Thin Solid Films* 78, 1.

Hausmann, B. M., Khan, M., Zhang, Y., Babinec, T. M., Martinick, K., McCutcheon, M., Hemmer, P. R. & Lončar, M. 2010 *Diamond Relat. Mater.* 19, 621.

Iqbal, S. M., Akin, D. & Bashir, R. **2007** *Nat. Nanotechnol.* 2, 243.

Ishikawa, Y., Imai, Y., Ikeda, H. & Tabe, M. **2003** *App. Phys. Lett.* 83, 3162.

Iwazaki, T., Semba, T., Konishi, S., Sezai, T., Murakami, Y., Sugimoto, W. & Takasu, Y. **2008** *Chem. Lett.* 37, 1194.

Jacobs, K., Herminghaus, S. & Mecke, K. R. **1998** *Langmuir* 14, 965.

Janssen, W. & Gheeraert, E. **2011** *Diamond Relat. Mater.* 20, 389.

Janssen, W., Faby, S. & Gheeraert, E. **2011** *Diamond Relat. Mater.* 20, 779.

Jin, S., Zhu, W., Siegrist, T., Tiefel, T. H., Kammlott, G. W., Graebner, J. E. & McCormack, M. **1994** *Appl. Phys. Lett.* 65, 2675.

Jin, S., Graebner, J. E., McCormack, M., Tiefel, T. H., Katz, A. & Dautremont-smith, W. C. **1993** *Nature* 362, 822.

Jin, S., Graebner, J. E., Kammlott, G. M., Tiefel, T. H., Kosinski, S. G., L. H. Chen, L. H. & Fastnacht, R. A. **1992** *Appl. Phys. Lett*. 60, 1948.

Jiran, E. & Thompson, C. V. **1992** *Thin Solid Films* 208, 23.

Jiran, E. & Thompson, C. V. **1990** *J. Electron. Mater*. 19, 1153.

Jongpil, Y. & Thompson, C. V. **2010** *Acta Mater*. 59, 582.

Kan, W. & Wong, H. **2005** *J. Appl. Phys*. 97, 043515.

Karhanek, M., Kemp, J. T., Pourmand, N., Davis, R. W. & Webb, C. D. **2005** *Nano lett.*5, 403.

Kasianowicz, J. J., Brandin, E. & Deamer, D. W. **1996** *Proc. Natl. Acad. Sci. USA* 93, 13770.

Katsumata, S., Oobuchi, Y. & Asano, T. **1994** *Diam. Relat. Mater*. 3, 1296.

Keyser, U. F., Krapf, D., Koeleman, B. N., Smeets, R. M. M., Dekker, N. H. & Dekker, C. **2005** *Nano Lett*. 5, 2253.

Khalili, N. S., Campbell, M., Sandi, G. & Golas, J. **2000** *Carbon* 38, 1905.

Kim, M. J., Wanunu, M., Bell, D. C. & Meller, A. **2006** *Adv. Mater.* 18, 3149.

Klinke II, D. J., Wilke, S. & Broadbelt, L. J. **1998** *J. Catal.* 178, 540-54.

Konishi, S., Ohashi, T., Sugimoto, W. & Takasu, Y. **2006** *Chem. Lett.* 35, 1216.

Kowalczyk, S. W., Hall, A. R. & Dekker, C. **2010** *Nano Lett.* 10, 324.

Kriele, A., Williams, O. A., Wolfer, M., Brink, D., Muller-Serbert, W. & Nebel, C. E. **2009** *Appl. Phys. Lett.* 95, 031905.

Krishna, H., Sachan, R., Strader, J., Favazza, C., Khenner, M. & R. Kalyanaraman, R. **2010** *Nanotechnology* 21, 1.

Kristensen, N., Ericson, F., Schweitz, J. A. & Smith, U. **1991** *Thin Solid Films* 197, 67.

Kwon, J. Y., Yoon, T. S. & Kim, K. B. **2003** *J. Appl. Phys*. 93, 3270.

Lee, Ji-M. & Kim, B-I. **2007** *Mater. Sci. Eng. A* 449–451, 769.

Lee, W-S., Baik, Y-J., Eun, K. Y. & Yoon, D-Y. **1995** *Diamond Relat. Mater.* 4, 989.

Lee, S. Y., Hummel, R. E. & Dehoff, R. T. **1987** *Thin Solid Films* 149, 29.

Li, J., Greshow, M., Stein, D., Brandin, E. & Golovchenko, J. A. **2003** *Nat. Mater.* 2, 611.

Li, J., Stein, D., McMullan, C., Branton, D., Aziz, M. J. & Golovchenko, J. A. **2001** *Nature* 412, 166.

Luber, E. J., Olsen, B. C., Ophus, C. & Mitlin, D. **2010** *Phys. Rev. B* 82, 085407.

Lud, Q., Steenackers, M., Jordan, R., Bruno, P., Gruen, D. M., Feulner, P., Garrido, J. A. & Stutzmann, M. **2006** *J.Am. Chem. Soc.* 128, 16884.

Masood, A., Aslam, M., Tamor, M. A. & Potter, T. J. **1991** *J. Electrochem. Soc.* 138, L67.

Massalski, T. B., Okamoto, H., Subramanian, P. R. & Kacprzak, L. **1990** *Binary Alloy Phase Diagrams.* vol 1. pp. 835. Ohio: ASM International.

Mitlin, V. S. **1993** *J. Colloid Interface Sci.* 156, 491.

Mitlin, V. S. **1994** *Colloids Surf. A* 89, 97.

Mitsui, T., Stein, D., Kim, Y. R., Hoogerheide, D. & Golovchenko, J. A. **2006** *Phys. Rev. Lett.* 96, 036102.

Mullins, W. W. **1957** *J. Appl. Phys*. 28, 333.

Mullins, W. W. **1958** *Acta Metall.* 6, 414.

Moors, M., Amara, H., Visart de Bocarm´e, T., Bichara, C., Ducastelle, F., Kruse, N. & Charlier, J. C. **2009** *ACS Nano* 3, 511.

Nebel, C.E., Rezek, B., Shin, D., Uetsuka, H. & Yang, N. **2007** *J. Phys. D* 40**,** 6443.

Nebel, C. E. & Ristein, J. **1992** *Thin-Film Diamond II*. Elsevier.

Nilsson, J., Lee, J. R. I., Ratto, T. V. & Létant, S. E. **2006** *Adv. Mater.* 18, 427.

Ohashi, T., Sugimoto, W. & Takasu, Y. **2011** *Bull. Chem. Soc. Jpn.* 84, 276.

Petersen, J. & Mayr, S. G. **2008** *J. Appl. Phys*. 103, 023520.

Presland, A. E. B., Price, G. L. & Trimm, D. L. **1972** *Prog. Surf. Sci.* 3, 63.

Pundt, A. **2004** *Adv. Eng. Mater.* 6, 11.

Ralchenko, V. G., Korotushenko, K. G., Smolin, A. A. & Loubnin, E. N. **1995** *Diam. Relat. Mater*. 4, 893.

Ralchenko, V. G., Kononenko, T. V., Pimenov, S. M., Chernenko, N. V., Loubnin, E. N., Armeyev, V. Yu. & Zlobin, A. Yu. **1993** *Diamond Relat. Mater*. 2, 904.

Ramesham, R., Ellis, C. D., Olivas, J. D. & Bolin, S. **1998** *Thin Solid Films* 330, 62.

Regel, L. L. & Wilcox, W. R. **1999** *J. Mater. Sci. Lett.* 18, 427.

Reiter, G., Sharma, A., Khanna, R., Casoli, A. & David, M. **1999** *J. Colloid Interface Sci*. 214, 126.

Reiter, G. **1993** *Langmuir* 9, 1344.

Reiter, G. **1992** *Phys. Rev. Lett.* 68, 75.

Rey, S., Hommet, J., Schmerber, G. & Normand, F. Le. **2011** *Thin Solid Films* 519, 4426.

Rey, S. & F. Le Normand, F. Le. **2010** *Thin Solid Films* 519, 4426.

Sakamoto, Y., Takaya, M., Sugimura, H., Takai, O. & Nakagiri, N. **1998** *Thin Solid Films* 334, 161.

Sarkar, J. & A. Sharma, A. **2010** *Langmuir* 26, 8464.

Seemann, R., Herminghaus, S. & Jacobs, K. **2001a** *J. Phys. Condens. Matter* 13, 4925.

Seemann, R., Herminghaus, S. & Jacobs, K**. 2001b** *Phys. Rev. Lett*. 86, 5534.

Sharma, A. **2003** *Eur. Phys. J. E* 12, 397.

Sharma, A. & Khanna, R. **1999** *J. Chem. Phys*. 110, 4929.

Smeets, R. M. M., Keyser, U. F., Krapf, D., Wu, M. Y., Dekker, N. H. & Dekker, C. **2006** *Nano Lett*. 6, 89.

Smirnov, W., Hees, J. J., Brink, D., Muller-Sebert, W., Kriele, A., Williams, O. A. & Nebel, C. E. **2010** *Appl. Phys. Lett.* 97, 073117.

Sonin, V. M., Chepurov, A. I. & Fedorov, I. I. **2003** *Diamond Relat. Mater.* 12, 1559.

Storm, A. J., Chen, J. H., Zandbergen, H. W. & Dekker, C. 2005 *Phys. Rev. E* 71, 051903.

Storm, A. J., Chen, J. H., Ling, X. S., Zandbergen, H. W. & Dekker, C. **2003** *Nat. Mater.* 2, 537.

Srolovitz, D. J. & Safran, S. A. **1986a** *J. Appl. Phys*. 60, 247.

Srolovitz, D. J. & Safran, S. A. **1986b** *J. Appl. Phys*. 60, 255.

Strobel, S., Kirkendall, C., Chang, J. B. & Berggren, K. K. **2010** *Nanotechnology* 21, 505301.

Sung, C. M. & Tai, M. F. **1997** *Int. J. Refract. Met. Hard Mater.* 15, 237.

Takagi, D., Kobayashi, Y., Hibino, H., Suzuki, S. & Homma, Y. **2008** *Nano Lett.* 8, 832.

Takasu, Y., Konishi, S., Sugimoto, W. & Murakami, Y. **2006** *Electrochem. Solid-State Lett.* 9, C114.

Takasu, Y., Konishi, S., Miyoshi, R., Nukii, K., Matsuse, T., Sugimoto, W. & Murakami, Y. **2005** *Chem. Lett.* 34, 1008.

Tamai, A., Watanabe, H. & Tomita, A. **1977** *Carbon* 15, 103.

Tomita, A. & Tamai, Y. **1974** *J. Phys. Chem.* 78, 2254.

Tomita, A. & Tamai, Y. **1972** *J. Catal.* 27, 293.

Tanuma, S., Powell, C. J. & Penn, D. R. **1988** *Surf. Interfaces Anal*. 11, 577.

Thiele, U., Sharma, A., Kaya, H., Jerome, B. & Jonas, A. M. **2003** *Eur. Phys. J. E* 12, 395.

Thiele. U. & Velarde, M. G. **2001** *Phys. Rev. Lett*. 87, 016104.

Thiele, U., Mertig, M. & Pompe, W. **1998** *Phys. Rev. Lett*. 80, 2869.

Trice, J., Favazza, C., Thomas, D., Garcia, H., Kalyanaraman, R. & Sureshkumar, R. **2008** *Phys. Rev. Lett.* 101, 017802.

Trice, J., Thomas, D., Favazza, C., Sureshkumar, R. & Kalyanaraman, R. **2007** *Phys. Rev. B* 75, 235439.

van den Hout, M., Skinner, G. M., Klijnhout, S., Krudde, V. & Dekker, N. H. **2011** *Small* 7, 2217.

Venkatesan, B. M. & Bashir, R. **2011** *Nat. Nanotechnol.* 6, 615.

Vrij, A. **1966** *Discuss. Farad. Soc*. 42, 23.

Wanunu, M., Dadosh, T., Ray, V., Jin, J., McReynolds, L. & Drndic, M. **2010** *Nat. Nanotechnol.* 5, 807.

Wei, R., Gatterdam, V., Wieneke, R., Tampè, R. & Rant, U. **2012** *Nat. Nanotechnol.* 7**,** 257.

Wiltner, A. & Linsmeier, C. **2004** *Phys. Status Solidi A* 201, 881.

Xie, R., Karim, A., Douglas, J. F., Han, C. C. & Weiss, R. A. **1998** *Phys. Rev. Lett*. 81, 1251.

Yamaguchi, A., Uejo, F., Yoda, T., Uchida, T., Tanamura, Y., Yamashita, T. & Teramae, N. **2004**

Nat. Mater. 3 337.

Yang, P. C., Liu, W., Schlesser, R., Wolden, C. A., Davis, R. F., Prater, J. T. & Sitar, Z. J. **1998** *J. Cryst. Growth* 187, 81.

Yazyev, O. V. **&** Pasquarello, A**. 2008** *Phys. Rev. Lett.* 100, 156102.

CHAPTER 6

Catalytic Etching of Diamond:

Future Perspective

Résumé

Ce chapitre explore deux applications du processus de gravure développé. La première sont des membranes poreuses utilisées comme bio-capteurs. Le défi consiste à fabriquer des pores longs (> 100 nm) et étroit (< 30 nm) dans une membrane de diamant nanocristallin, qui agissent comme un filtre sélectif pour les biomolécules. Comme les techniques de gravure usuelles telles que la gravure ionique réactive ne parvient pas à fabriquer de telles structures de rapport d'aspect élevé, notre nouveau processus est la technologie clé pour le développement de tels capteurs.

La seconde application concerne les neuro-capteurs à base de nanotubes de carbone. La grande réactivité des nanotubes de carbone améliore le signal mesuré, mais la mauvaise adhérence des nanotubes sur le substrat est un sujet de préoccupation pour la reproductibilité et aussi pour des applications in vivo. Après la gravure d'une membrane diamant nanocristallin, les nanoparticules de catalyseur qui restent à l'intérieur du nanopore sont utilisées comme catalyseurs de la croissance de nanotubes de carbone par CVD. Une croissance du type base de nanotube a été observée. Le processus de gravure donc permis d'ancrer les nanotubes de carbone en profondeur dans un substrat de diamant nanocristallin, ce qui conduit à une électrode en carbone à haute résistance mécanique, biocompatibilité élevée et une grande sensibilité. Le développement de ces électrodes, principalement réalisée dans le cadre d'une autre thèse dans notre groupe de recherche, est brièvement présenté pour donner un aperçu du potentiel de la technologie de gravure nouvelle que nous avons développé.

6.1. Porous Nanocrystalline Diamond Membrane

As discussed in chapter 5, by varying the Ni film thickness and the annealing time, the catalytic etching technique can generate nanopores with diameter in the range of 15 to 225 nm and as deep as about 500 nm in diamond membrane without any need for a lithography process. The technique therefore opens up the opportunities for fabricating porous diamond membranes, in particular porous nanocrystalline diamond membranes.

Nanocrystalline diamond (NCD) offers optimal properties because of its smooth surface and excellent, homogeneous mechanical and thermal properties, approaching to the single crystal diamond values (**Mortet *et al.* 2005**). It was demonstrated that NCD provide extreme biocompatibility and stability in physiological media (**Kopecek *et al.* 2008**; **Bergonzo *et al.* 2011**). Thus, porous NCD membranes will most likely offer considerable promise for future applications.

For example, porous diamond electrodes exhibit the highest possible chemical and electrochemical stability (**Kraft, 2007**), a wide electrochemical potential window in aqueous electrolytes (2.5 V (**Honda *et al.* 2000**)) and a high capacitance (16 F g^{-1} (**Honda *et al.* 2000**)), and can be employed to advantage, for instance, in electrochemical capacitor applications. It is expected that porous diamond electrodes can also find use in biofuel cells, because they do not produce an adverse effect on the activity and viability of bacteria (**Moriuchi *et al.* 2008**). Indeed, diamond-based film structures are practically ideal catalyst supports for polymer electrolyte membrane fuel cells (**Shao *et al.* 2009**), because they have a high specific surface, high conductivity and are not oxidized by either dry or wet air. Porous diamond films can be used to advantage in various separation techniques, because they meet most of the demands placed on the stationary phase in chromatography (**Nesterenko & Haddad, 2010**). It is highly predicted that porous ultrananocrystalline diamond films may open new opportunities in implant medicine because of the highest degree of biocompatibility and anti-biofouling, unmatched by other materials (**Shenderova & Gruen, 2006**).

Porous materials are often distinguished based on pore size, size distribution, shape, and order. They are considered uniform if the size distribution is narrow as opposed to a wide pore size distribution (**Adiga *et al.* 2009**). The pores can be cylindrical, conical, slit-like, or irregular in shape. They can be well ordered with a vertical alignment as opposed to a random network of tortuous pores. Some of the key properties that nanoporous membranes are required to possess for many applications specifically in biomedical devices include a well controlled pore size; a narrow pore size distribution in order to achieve high biomolecule selectivity; high porosity as well as low thickness in order to enable high analyte flux; mechanical stability; biocompatibility, biofouling resistance; and chemical stability (**Adiga *et al.* 2009**).

Despite the strong interest, fabrication of porous diamond films still remains a problem of daunting complexity. Membranes with a two-dimensional (2D) ordered porous structure were prepared by etching a polycrystalline diamond film in oxygen plasma through an aluminum oxide mask (**Honda *et al.* 2000**). High porosity, high aspect ratio UNCD membranes were fabricated using e-beam lithography, reactive ion etching and optical lithography (**Makarova *et al.* 2010**). The nanocasting technique, also known as template synthesis (**Lu *et al.* 2009**), is presently an efficient an inexpensive approach that includes preparation of an ordered sacrificial template, impregnation of precursors inside pores, a chemical treatment to yield the goal product and removal of the template. The colloidal template synthesis of bulk porous diamond with a 3D ordered porous structure was described by (**Zakhidov *et al.* 1998**). A very recent paper reported on synthesis by the nanocasting route of bulk porous material consisting of diamond spheres (**Ralchenko *et al.* 2011**).

Although the catalytic etching technique that we developed offers great control over pore density and aspect ratio, the main challenges were in the control of long pores and in the separation of porous NCD membrane from Si substrate, which is necessary for in-depth characterization of the pores. The careful study of the process described in chapter 5 allowed us to tune the fabrication parameters in order to get pores longer than 500 nm in NCD, long enough for membrane applications. An example of processed NCD film is shown figure 6.1, resulting from annealing the NCD film of ~ 250 nm thickness with 3 nm Ni layers at 800 °C for 30 min. It can be seen from the SEM images that few nanopores with tortuous shape are extended to the NCD-Si interface.

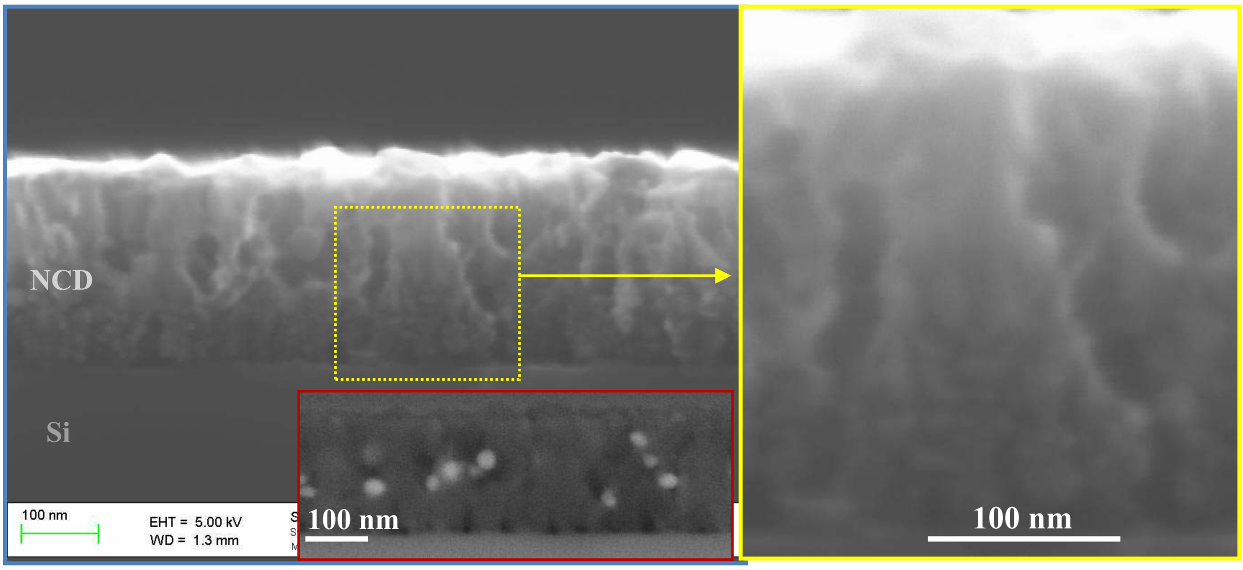

Figure 6.1. SEM images of a cross-section of the etched NCD film of 250 nm thickness, (3 nm Ni, 800 °C, 30 min, 60 Torr H_2); right panel (yellow border) is a magnified view of the marked section showing nanopores with tortuous shape extended to the NCD-Si interface and the inset (red border) is a backscattered electron image where bright contrast corresponds to Ni nanoparticles.

For membrane separation, the approach that is currently in progress can be described as follows: NCD film of about 300 nm thickness is deposited on both sides of a silicon substrate (<100> oriented and ~250 µm thick). From one side of the substrate the diamond film is etched selectively by Inductively Coupled Plasma Reactive Ion Etching (ICP-RIE) with the help of photolithography, the lithography being used for mask deposition (Janssen *et al.* 2011). The exposed Si area is etched wet chemically in KOH. Other side of the substrate is then etched catalytically by Ni nanoparticles resulted from the dewetting of deposited Ni film. A schematic of the membrane separation is shown in figure 6.2.

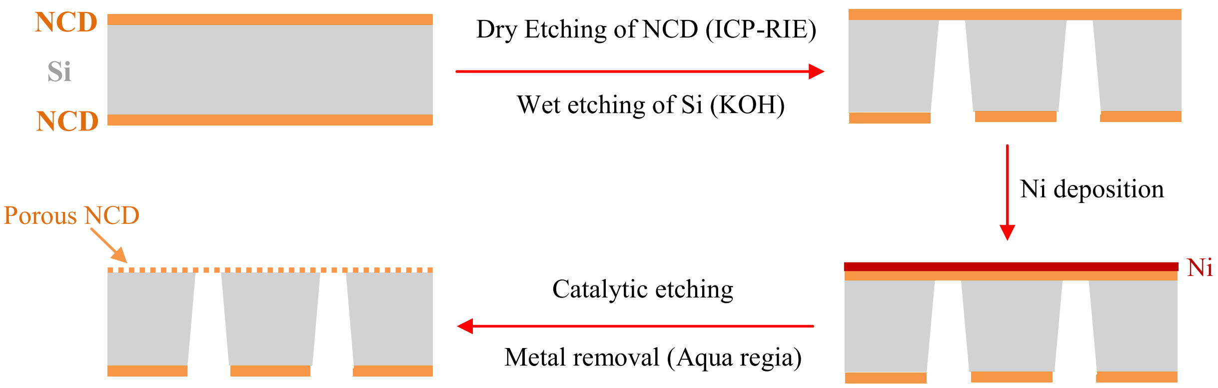

Figure 6.2. A schematic of the membrane separation process.

SEM images (figure 6.3 (a) and (b)) show the morphology of the backside after dry etching (ICP-RIE) of NCD and wet etching (KOH) of Si. After catalytic etching, the Ni nanoparticles generated from the initially evaporated 3 nm Ni film was observed on the backside of the NCD film, as shown in figure 6.3 (d).

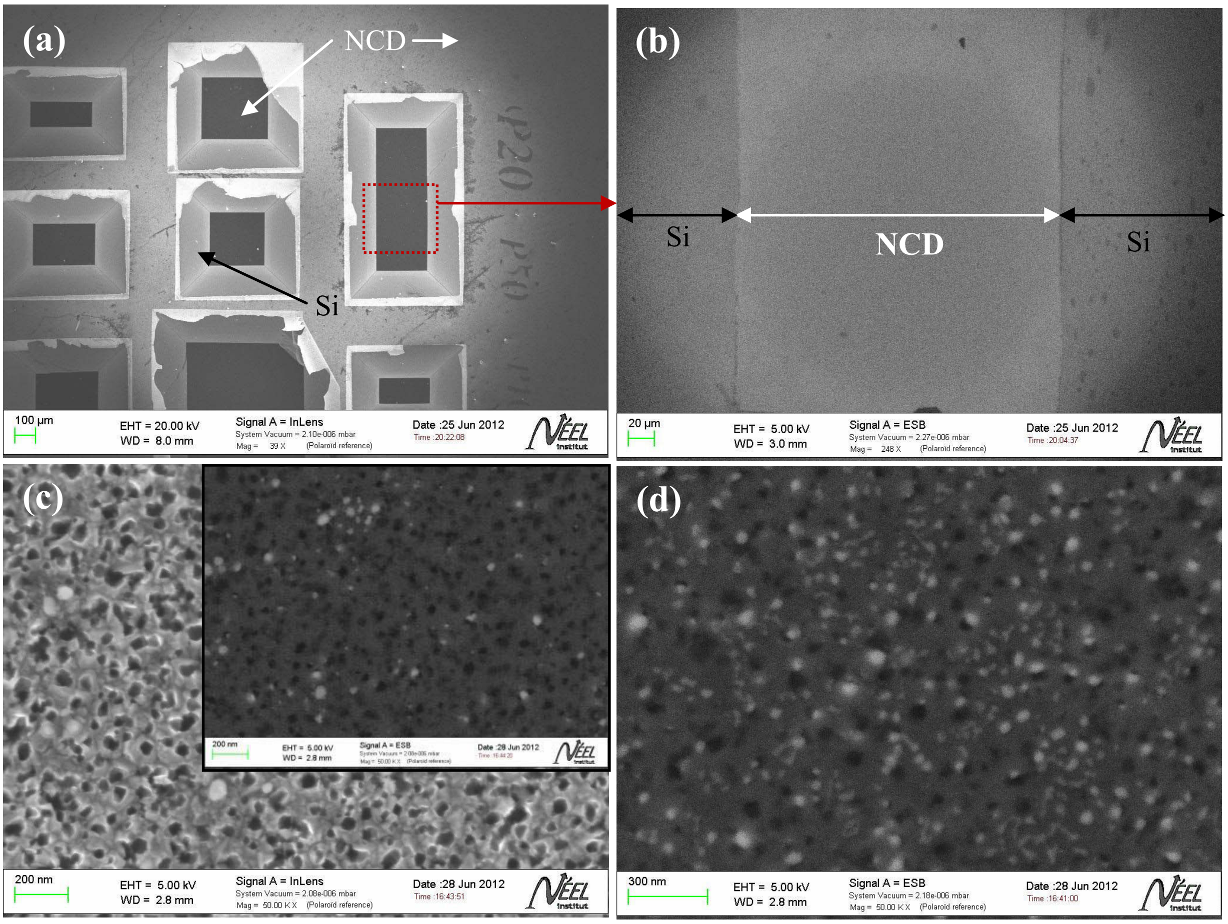

Figure 6.3. SEM images of (a, b) backside of the sample after dry etching of NCD (ICP-RIE) and wet etching of Si (KOH), (c) top side after catalytic etching with Ni particles and (d) backside after catalytic etching acquired with an EsB detector showing the presence Ni particles (bright contrast). The inset of panel (c) is SEM image of the top side recorded by EsB detector.

It is necessary to note that NCD growth on silicon substrate is usually accompanied by a thin silicon carbide layer at the diamond-substrate interface (**Sarrieu *et al.* 2011**). This carbide layer glues the film strongly to the substrate and thereby makes the membrane separation very difficult. In addition, the carbide layer could prevent the Ni nanoparticles to reach to the interface resulting in pore blocking. Growth of NCD film on a zirconia (ZrO_2) substrate is currently considered to be an efficient and simple approach to this problem. Growth of free standing boron-doped microcrystalline diamond film on ZrO_2 has been demonstrated (**Brandao *et al.* 2010**). In this work it has been shown that the diamond film adheres very weakly with the zirconia substrate, and no additional layer (e.g., carbide) appears at the interface. Studies are currently underway that involve preparing and separating high porosity, high aspect ratio porous NCD membranes and their characterization to measure mechanical strength, chemical stability, ion flux and so on. In addition, preparation of ordered porous membranes is also under investigation, where the approach, the catalytic etching with patterned film, will be used. Figure 6.4 shows an array of ordered pores in NCD membrane fabricated by catalytic etching with patterned Ni film of 25 nm thickness.

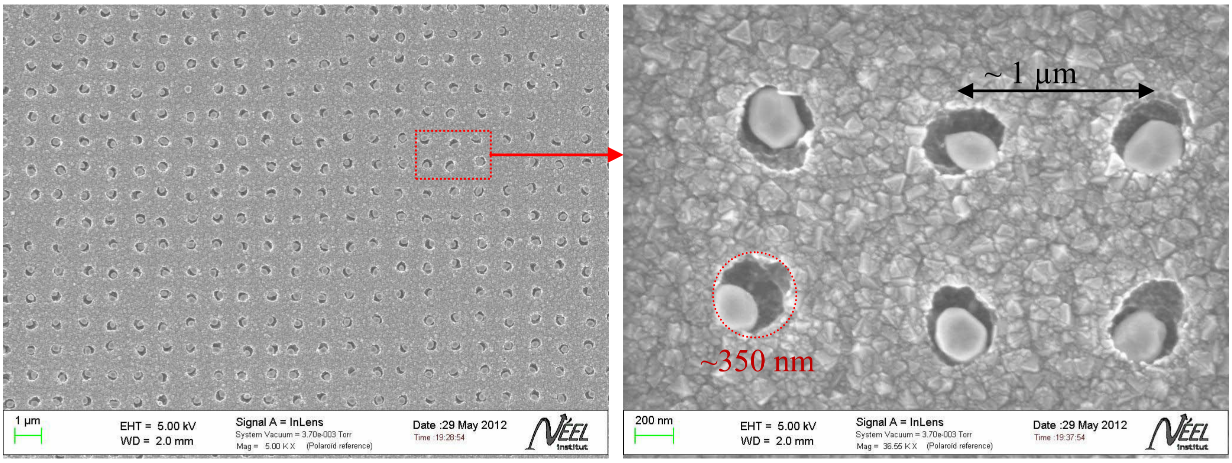

Figure 6.4. SEM images of the etched NCD for 10 min with patterned Ni film of 25 nm thickness showing ordered, cylindrical pores in the membrane, (800 °C, 60 Torr H_2). Ni film was patterned by deep UV lithography where square-shaped feature of size 500 nm × 500 nm was used.

Cylindrical pores with average diameter of about 350 nm were generated after 10 min etching. The pores are separated from one another by ~ 1 µm. Pore size and separation can be controlled by the metal film thickness and feature geometry in the photomask. Reduction of pore size down to 100 nm or more would be difficult by photolithography due to the limited resolution. However, these types of porous nanocrystalline diamond membranes with well-ordered pores could be useful as photonic crystals (**Joannopoulos *et al.* 2008**).

6.2. Carbon Nanotubes Partially Embedded in Diamond film: A New Composite Material

This work was performed in collaboration with Clement Hebert (Institut Néel).

Carbon nanotube coated electrodes are now recognized as a very promising material system for neural interfacing (**Mattson *et al.* 2000**; **Lovat *et al.* 2005**; **Keefer *et al.* 2008**; **Cellot *et al.* 2009**; **Malarkey *et al.* 2010**), thanks to the fascinating properties of carbon nanotubes (CNTs). The main issue that might preclude the development and use of such electrodes is the CNT toxicity (**Poland *et al.* 2008**; **Nagai *et al.* 2010**). **Minnikanti *et al*.** (**2011**) recently has suggested that this issue can be easily overcome by strongly anchoring the individual nanotubes on the electrodes since they are not considered harmful as long as they are not dispersed in single entities. In addition to the electrode application, CNT-based field emission devices are also demanding for very reliable CNT connection (**Zhang *et al.* 2006**; **Lim *et al.* 2006**). Poor adhesion of the nanotube can lead to the covering of the anode or a vacuum breakdown, resulting in a dramatic decrease of the device efficiency. Many methods such as electrophoretic deposition (**Sung *et al.* 2008**), screen printing (**Choi *et al.* 1999**) microwave treatment (**Su *et al.* 2010**) were developed to anchor properly the carbon nanotube to the substrate, but reliable devices are still difficult to obtain. Thus, a new route needs to be developed for a strong adhesion of the nanotubes on their substrates.

Such a strong anchoring implies an important role of the substrate material. Carbon nanotubes can be deposited or directly grown on many substrates, but a few have the necessary properties to be used in the devices mentioned above. Diamond can be a perfect candidate because of its outstanding chemical, mechanical, thermal and biocompatible properties. While diamond is intrinsically insulating, it can be made highly conductive when heavily doped with boron (**Klein *et al.* 2007**). In addition, diamond thin layers can be transferred on polymers to comply with flexible technologies (**Hess *et al.* 2011**); an important feature makes diamond a very special substrate for CNT growth.

To reach this goal, anchoring nanotubes in diamond film, a thin nanocrystalline diamond (NCD) of about 600 nm thickness was first etched catalytically by Ni nanoparticles generated from the initially deposited 3 nm Ni film for 20 min at 800 °C. Not that NCD with average grain size of about 100 nm was grown on a Si substrate in a Microwave Plasma CVD reactor using bias enhanced nucleation approach (**Barrat *et al.* 1998**) with following parameters: 900

°C temperature, 1000 watt microwave power, 0.4 vol.% methane in H_2, 30 Torr pressure, 4 hours deposition.

Figure 6.5 shows the morphology of a cross section of the etched NCD sample displayed in a SEM image acquired with an energy-selective backscattered detector (EsB detector).

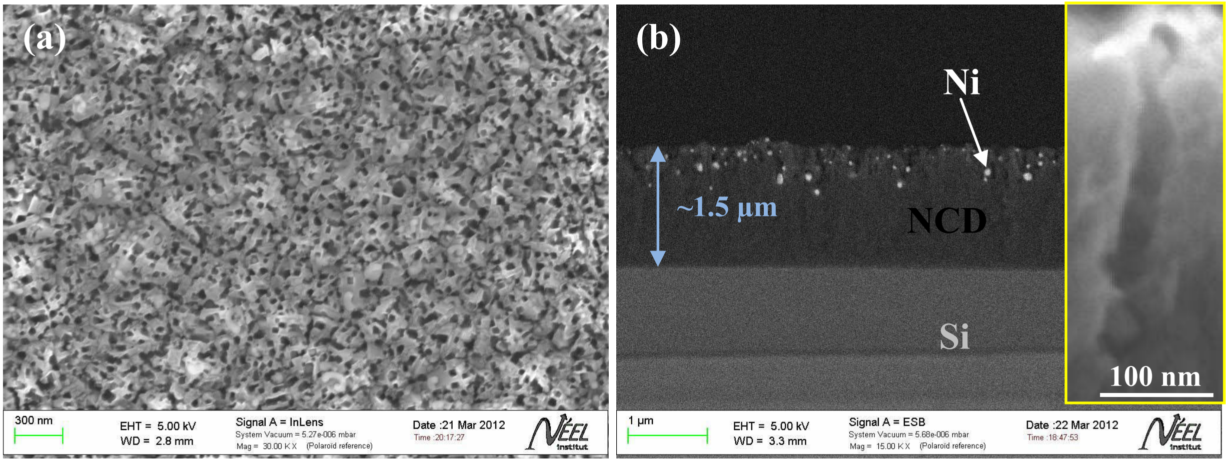

Figure 6.5. SEM images of the etched NCD by Ni nanoparticles generated from the initially evaporated 3 nm Ni film on the diamond surface at 800 °C, (20 min, 30 Torr H_2); (a) top view and (b) cross-sectional image acquired with an EsB detector showing embedded Ni nanoparticles (bright contrast) in NCD. The inset of panel (b) is a cross-sectional image recorded with the in-lens detector representing nanopore shape, "saw-tooth" type.

The pore diameter ranges from 15 to 45 nm and the average depth is about 250 nm based on SEM analysis (figure 6.5). The Ni nanoparticles (mean diameter ~ 10-30 nm) that remained at the bottom of the pores were then used as catalyst for the subsequent CNT growth by HFCVD with following parameters: 1950 °C filament temperature, 800 °C substrate temperature, 8 vol.% methane in H_2, 60 Torr pressure, 10 min deposition. The tungsten filament was placed in parallel at 10 mm above the substrate.

Cross-sectional SEM images of the resulting composite materials (figure 6.6) exhibit a dense carbon nanotube forest. The tube diameters are in the range of 15 to 30 nm, which corresponds to that of nanoparticle diameter. This is in good agreement with the typical catalyst-assisted CNT growth where tube diameter is controlled by catalyst diameter (**Kukovitsy *et al.* 2002**; **Nasibulin *et al.* 2005**). The observation clearly emphasizes that the catalytic properties of nickel were not impaired during the etching process. In addition, from SEM images (figure 6.6 (c) and (d)) acquired with an EsB detector, it can be clearly seen that the nanoparticles remain at the bottom of the tubes, about 220 nm deep inside the diamond, prevailing the base growth mechanism of CNTs (**Song *et al.* 2004**).

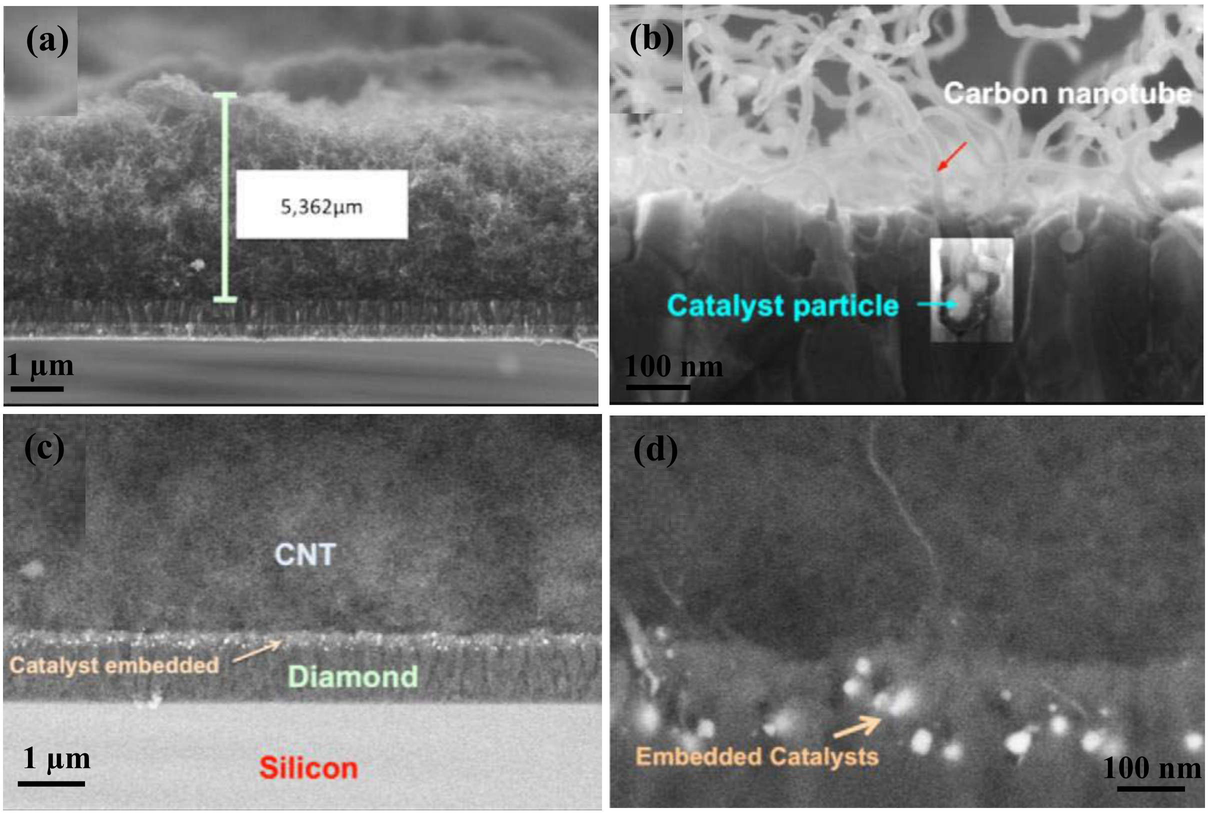

*Figure 6.6. SEM images of a cross-section of the CNT forest partially embedded in diamond acquired with (a, b) an in-lens detector and (c, d) an EsB detector showing the base growth mode of the CNTs (**Hebert et al. 2013**).*

The base growth mechanism may contribute to prevent the interaction of any biological medium with the metal nanoparticles, thus reducing toxicity issues. As CNTs are embedded in the diamond substrate, the resistance to tube tearing from the substrate should be increased as compared to that of CNTs directly grown on the substrate surface. The pore shape, "saw-tooth", (inset in figure 6.5) could also improve both mechanical and electrical contacts as a result of larger area of contact between the CNTs and the pores. However, extensive structural defects in the CNTs could impair their mechanical properties and thereby reduce the lateral force necessary to tear out the tubes from the substrate. Further study of this composite material will enable preparation of a macro-electrode system.

6.3. All Diamond Microelectrode Arrays Coated with CNTs

Using the process of anchoring carbon nanotubes in diamond film (section 6.2), an array of diamond microelectrodes (MEA) coated with CNTs on Si substrates was prepared. In the fabrication process, first an insulating and a heavily boron-doped (BDD) (concentration ~ 10^{21} cm^{-3}) nanocrystalline diamond layers were successively deposited on a silicon substrate. The boron-doped layer was then patterned to form a 121-microelectrode array with wire to connect each electrode separately. The diamond wires were insulated using a selective insulating diamond growth. An optical profile of the microelectrode array and a SEM image of an electrode are shown in figure 6.7 (a) and (b). After the electrode preparation, 3 nm Ni film was deposited on the BBD layer with the help of direct laser writing lithography and the sample was then annealed at 800 °C. Nanopores were formed in the doped electrode after 20 min of annealing (figure 6.7 (c)). Finally CNTs were grown in a HFCVD reactor using the Ni nanopaticles as catalyst (figure 6.7 (d)).].

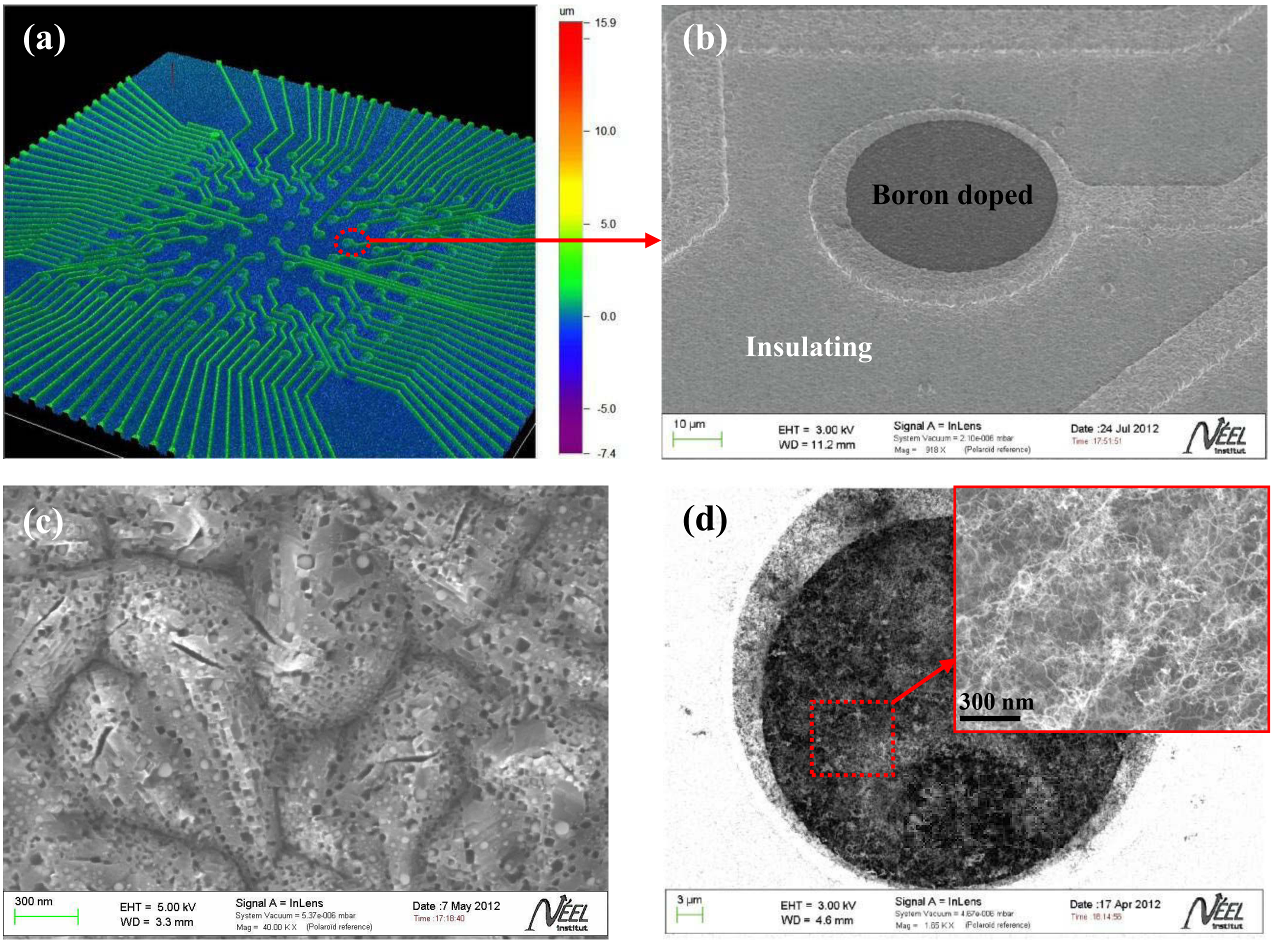

Figure 6.7. (a) Optical profile of an array of diamond microelectrodes, SEM images of (b) of an electrode showing the BBD and insulating diamond layer, (c) etched BBD layer after 20 nm annealing with patterned 3 nm Ni film, (800 °C, 60 Torr H_2), direct laser writing lithography was used for patterning and (d) CNTs in BBD grown in a HFCVD reactor using Ni nanoparticles remained inside the pores as catalyst.

The advantage of using MEAs over macro-electrodes is expected to be improved due to their unique properties resulting from geometrical characteristics with the excellent electrochemical properties of BDD materials (**Pagels *et al.* 2005**; **Kiran *et al.* 2012**). Preparation of MEAs was performed in collaboration with Clement Hebert. Current studies that are underway involve the characterization of the interface between the carbon nanotubes and the diamond substrates by ultrasonic treatment, lateral force microscopy, cyclic voltammetry and electrochemical impedance spectroscopy. The quality of the CNTs will be assessed by scanning electron microscopy and multiwavelength Raman Spectroscopy.

Bibliography

Adiga, S. P., Jin, C., Curtiss, L. A., *et al.* **2009** *Nanoporous membranes for medical and biological applications*. Wiley.

Sarrieu, C., Bauer-Grosse, E. & Barrat, S. **2011** *Diamond Relat. Mater.* 20, 1246.

Barrat, S., Saada, S., Dieguez, I. & Bauer-Grosse, E. **1998** *J. Appl. Phys.* 84, 1870.

Bergonzo, P., Bongrain, A., Scorsone, E. *et al*. **2011** *IRBM* 32, 91.

Brandao, L. E. V. S., Pires, R. F. & Balzaretti, N. M. **2010** *Diamond Relat. Mater*. 54, 84.

Cellot, G., Cilia, E., Cipollone, S., Rancic, V., Sucapane, A. *et al.* **2009** *Nat. Nanotechnol*. 4, 126.

Choi, W. B., Chung, D. S., Kang, J. H., Kim, H. Y., Jin, Y. W. & Han, I. T. **1999** *Appl. Phys. Lett.*75, 3129.

Hebert, C., Ruffinatto, S., Eon, D., Mermoux, M. *et al.* **2013** Carbon 52, 408-417.

Hess, A. E, Sabens, D. M., Martin, H. B. & Zorman, C. A. **2011** *J. Microelectromech. Syst.* 20, 867.

Honda, K., Rao, T. N., Tryk, D. A., Fujishima, A. *et al.* **2000** *J. Electrochem. Soc.* 147, 659

Joannopoulos, J. D., Johnson, S. G., Winn, J. N. & Meade, R. D. **2008** *Photonic Crystals: Molding the Flow of Light.* 2nd edn. NJ: Princeton University Press.

Keefer, E. W., Botterman, B. R., Romero, M. I., Rossi, A. F. & Gross, G. W. **2008** *Nat. Nanotechnol*. 3, 434.

Kiran, R., Rousseau, L., Lissorgue, G., Scorsone, E. *et al*. **2012** *Sensors* 12, 7669.

Klein, T., Achatz, P., Kacmarcik, J., Marcenat, C. *et al*. **2007** *Phys. Rev. B* 75, 165313.

Kopecek, M., Bacakova, L., Vacik, J., Fendrych, F. *et al*. **2008** *Phys. Status Solidi A* 205, 2146.

Kraft, A. **2007** *Int. J. Electrochem. Sci.* 2, 355.

Kromka, A., Grausova, L., Bacakova, L. *et al.* **2010** *Diam. Relat. Mater.* 19, 190.

Kukovitsy, E. F., L'vov, S. G., Sainov, N. A. *et al.* **2002** *Chem. Phys. Lett.* 355, 497.

Lim, S., Choi, H., Jeong, H., Song, Y. *et al.* **2006** *Carbon* 44, 2809.

Lovat, V., Pantarotto, D., Lagostena, L. *et al.* **2005** *Nano Lett*. 5, 1107.

Lu, A-H., Zhao, D. & Wan, Y. **2009** *Nanocasting: A Versatile Strategy for Creating Nanostructured Porous Materials.* Cambridge: RSC Publishing.

Makarova, O. V., Divan, R., Moldovan, N. & Tang, C-M. **2010** *NSTI-Nanotech* vol 1.

Malarkey, E. B. & Parpura, V. **2010** *Acta Neurochir. Suppl*. 106, 337.

Mattson, M. P., Haddon, R. C. & Rao, A. M. **2000** *J. Mol. Neurosci*. 14, 175–82.

Minnikanti, S. & Peixoto, N. **2011** In *Carbon nanotube applications on electron devices*. (ed. Marulanda JM). pp. 143. Rejika: InTech.

Moriuchi, T., Morishima, K. & Furukawa, Y. **2008** *CIRP Ann.-Manuf. Technol.* 57, 571

Mortet, V., D'Haen, J., Potmesil, J. *et al.* **2005** *Diamond Relat. Mater.* 14, 393.

Nagai, H. & Toyokuni, S. **2010** *Arch. Biochem. Biophys*. 502, 1.

Nasibulin, A. G., Pikhista, P. V., Jiang, H. & Kauppinen, E. I. **2005** *Carbon* 43, 2251.

Nesterenko, P. N. & Haddad, P. R. **2010** *Anal. Bioanal. Chem.* 396, 205

Pagels, M., Hall, C.E., Lawrence, N.S. *et al*. **2005** *Anal. Chem*. 77, 3705.

Poland, C. A., Duffin, R., Kinloch, I., Maynard, A. *et al*. **2008** *Nat. Nanotechnol*. 3, 423.

Ralchenko, V. G., Sovyk, D. N., Bolshakov, A. P. *et al.* **2011** *Phys. Solid State* 53, 1131.

Shao, Y., Liu, J., Wang, Y. & Lin, Y. **2009** *J. Mater. Chem.* 19**,** 46.

Song, I. K., Choi, Y. S., Park, J. B. & Kim, D. J. **2004** *Diamond Relat. Mater.* 13, 1210.

Stulik, K., Amatore, C., Holub, K., Marecek, V. & Kutner, W. **2000** *Pure Appl. Chem*. 72, 1483.

Su, H. C., Chen, C. H., Chen, Y. C. *et al*. **2010** *Carbon* 48, 805.

Sung, W., Lee, S., Kim, W. *et al*. **2008** *Diamond Relat. Mater*. 17, 1003.

Shenderova, O. A. & Gruen, D. M. **2006** *Ultrananocrystaline diamond*. Norwich: William Andrew.

Zhang, J.,Wang, X., Yang, W., Yu, W. *et al.* **2006** *Carbon* 44, 418.

Zakhidov, A. A., Baughman, R. H., Iqbal, Z. *et al.* **1998** *Science* 282, 897

Conclusion and outlook

The first objective of this PhD work was to grow diamond nanowires starting from the growth process proposed by Sun *et al.* in 2005 for diamond nanowire growth by hydrogen plasma post-treatment of mutiwalled carbon nanotubes without any metal catalyst. In order to promote diamond nucleation on the nanotubes, our goal was to use conditions that induce a weak or negligible etching of nanotubes, i.e., conditions for which the nanotube growth is balanced with the etching of sp^2 forms of carbon by atomic hydrogen. This enhances the activated carbon concentration at the surface of nanotubes and promotes nucleation of carbon clusters. During treatment the nucleation of sp^2 carbon would be suppressed by atomic hydrogen, and the etching of nanotubes would be reduced by the appropriate experimental conditions, allowing slow nucleation of diamond to occur. In order to reduce spontaneous nucleation no methane was added; adsorbed carbon would have to come from the nanotube itself.

For the investigation, commercial purified carbon nanotubes were dispersed on silicon substrates and then, their stability under hot-filament as well as plasma environment was studied extensively. Experiments were performed under hydrogen atmosphere in a Hot-Filament assisted CVD and a Microwave Plasma assisted CVD system using conventional diamond growth temperature and pressure. From the hot-filament study, a window of stability for nanotubes was identified depending on the filament temperature (T_f):

- T_f = 1900-2000 °C: Very high etching of nanotubes; almost all nanotubes disappeared from the substrate after 1 hour of treatment,
- 2000°C < $T_f \leq$ 2200°C: Low or no etching of nanotubes,
- 2300 °C-2400°C: Very high tendency of nanotube conversion to polycrystalline material.

The etching behavior of nanotubes in microwave plasma was more or less similar to that in hot filament treatment: low temperature (700-800 °C), higher etching and vice versa. Further investigation in the temperature range, T_f: 2100-2200 °C, resulted in the growth of several nano-objects on /and from nanotubes, such as nanocrystals, nanowires and nanospikes. The extremely poor reproducibility and very low density of these nano-objects made their characterization very difficult and therefore, their exact nature and origin was not possible to identify. Moreover, a round shaped object was observed at the nanowire tips suggesting catalyst-assisted growth of the nanowires. As no metal catalyst was added in the process, the source of this catalyst could be the contaminants present in the commercial nanotubes or the tungsten filament used during the process. We therefore focused on catalyst-assisted treatment of nanotubes, where a thin Ni film was deposited intentionally on nanotubes, and it resulted in the growth of nanowires. However, Raman analysis showed only characteristic peaks of Si materials suggesting Si contamination in the process. Hot-filament treatment of nanotubes in a Si free environment, nanotubes being dispersed on bulk diamond substrates, showed no nanowire growth suggesting that Si contamination could play an important role in nanowire growth.

In order to promote the growth of diamond nanowires, methane was added during the process with nickel catalyst on diamond in a silicon-free environment, creating the conditions for a Vapor-Liquid-Solid growth mechanism. With the most favorable conditions, using 2 vol.% and 1 vol.% CH_4 consecutively in a single disposition run, growth of long, tangled and highly dense nanowires was observed on the diamond substrate. Transmission electron microscopy shows tubular shape of the nanowires with wall thickness of about 50 nm, and selected area electron diffraction patterns reveal the graphitic structure of the nanowires.

The routes that have been explored for diamond nanowire growth can be summarized as follows:

1. Hot-filament and plasma treatment of dispersed carbon nanotubes
2. Hot-filament treatment of dispersed carbon nanotubes with catalyst
3. Investigation of Vapor-Liquid-Solid growth mechanism using methane as carbon precursor and Ni as catalyst
4. Investigation of Solid-Liquid-Solid growth mechanism using bulk diamond substrates as the only source of carbon and Ni as catalyst.

No crystalline diamond phase was observed, even if part of the nanowires were identified as sp^3 bonded carbon. The conclusion is that under the experimental conditions, explored with or without catalyst, no diamond nanowire could be grown. We did not succeed in the reproduction of the process proposed by Sun *et al.* in 2005, as no other research group did either.

If conditions for the diamond nanowire growth exist, which direction should be explored? Because of poor control of the local environment and possible contamination, dispersed carbon nanotubes and hot-filament process are not the most appropriate technique to pursue for diamond nanowire growth. The most promising technique would be the Vapor-Liquid-Solid process where one can achieve better control over the local carbon concentration than that of treatment with dispersed carbon nanotubes. High pressure combined with high temperature (substrate temperature 900-1100 °C) and high-pressure effect induced by the nano-sized catalyst, could promote the nucleation of sp^3 phase during the nanowire growth. Therefore, the investigation should be carried out by atmospheric pressure CVD, without any plasma; the diamond stability would be promoted by the high pressure inside the catalyst. Smaller droplets, typically 1 to 5 nm in diameter, could generate high pressure. Such droplets could be obtained by either dewetting of a thin film or drying out a solution containing a low concentration of metal catalyst.

On the other hand, when no methane was added in the gas phase, etching of diamond by metal nanoparticles generated from the initially evaporated metal film was observed. The second objective of this work was then to explore this interesting etching phenomenon in order to develop a simple, fast and cost-effective etching technique for the fabrication of oriented nanostructures (nanopores) in the diamond membranes. In this process, a diamond film is annealed with metal layers with thickness of 1 to 15 nm at 800-850 °C in hydrogen atmosphere. The metal layers dewet and form self-assembled nanoparticles that assist carbon removal from the diamond-metal interface by the help of hydrogen atmosphere. Consequently, the particles enter the diamond volume generating inverse pyramidal, cylindrical or conical nanopores depending on the crystalline orientation and thereby, revealing the anisotropy in diamond etching. Methane was detected by mass spectrometer as the only product of the etching process. The careful study of the process parameters shows that nanopores can be formed in diamond, whatever its microstructure. The pore lateral size and depth can be controlled by the metal film thickness. Ni showed the highest etching activity among the studied metals (Co, Pt, Fe, Pd and Au). Hydrogen was found to be instrumental for the etching process as no etching occurred when there was no hydrogen. No change in the diamond microstructure due to etching was observed. Nanopore depth was observed to increase with the metal film thickness suggesting that the etching process is not limited by carbon diffusion through the metal particles.

However, the etching process is stopped for catalyst particles located deep inside the crystal volume due to limited gas exchange between the surface and the particle, leading to carbon saturation. To explain the etching mechanism five important steps of the etching process have been identified as follows:

1. Diffusion of molecular hydrogen from the chamber to the surface of the catalyst
2. Molecular hydrogen is catalytically dissociated into atomic hydrogen by nickel
3. Carbon atoms from the diamond surface can be removed through two different ways:
    a. the carbon atoms dissolve in the nickel droplet and then diffuse to the metal-gas interface where they react with hydrogen atoms forming methane
    b. hydrogen atoms diffuse within the catalyst to reach the diamond-metal interface, then remove carbon in the form of methane
4. Desorption of methane from the catalyst
5. Out-diffusion of methane from the vicinity of the catalyst

In both cases, 3a and 3b, the reaction is not limited by the diffusion through the catalyst, as the etching rate does not decrease with the catalyst thickness. The process is therefore limited by the reaction at the diamond-catalyst interface. Surface composition analysis of the annealed samples by XPS did not reveal any carbide component at the diamond-metal interface.

The better understanding of the process, and in particular the rate limiting step, allowed us to improve the etching conditions. Nanopores with lateral size in the range of 15-225 nm and as deep as about 550 nm were etched in the diamond membrane. The etching technique was employed to create ordered nano- and microstructures in diamond membrane using patterned metal film; the film was patterned by conventional photolithography. In the case of patterned Pd film the etching process resulted in an interesting inverse-pyramidal shaped microstructures walled by four [111]-oriented planes.

Extensive study of the process parameters of the catalytic etching technique enabled us to optimize the etching process and to understand the etching mechanism. Despite the limitation to nanopore depth, the technique is ready to be used in various applications such as the fabrication of porous nanocrystalline diamond membranes suitable for sensor applications.

Conclusion et Perspectives

Le premier objectif de cette thèse était de développer des nanofils de diamant à partir du processus proposé par Sun *et al.* en 2005 pour la croissance des nanofils de diamant par post-traitement de nanotubes de carbone sans catalyseur métallique. Afin de promouvoir la nucléation du diamant sur les nanotubes, notre objectif était d'utiliser des conditions qui induisent une gravure faible, voire négligeable de nanotubes, c'est à dire, les conditions pour lesquelles la croissance de nanotubes est équilibrée avec la gravure de formes de carbone sp^2 par l'hydrogène atomique. Cela améliore la concentration de carbone activé à la surface des nanotubes et favorise la nucléation. Pendant le traitement, la nucléation des sp^2 carbone serait supprimée par l'hydrogène atomique, et la gravure de nanotubes serait réduite par le choix de conditions expérimentales appropriées, ce qui permet à la nucléation du diamant de se produire. Afin de réduire nucléation spontanée pas de méthane a été ajouté; carbone adsorbé devrait venir du nanotube lui-même.

Cans cette étude, des nanotubes de carbone purifiés commerciaux ont été dispersés sur silicium et leur stabilité sous filament chaud ou plasma ont été étudiés. Des expériences ont été réalisées sous atmosphère d'hydrogène dans un réacteur CVD soit assisté par filament chaud soit assisté par plasma micro-ondes, des les conditions usuelles de croissance du diamant. De l'étude filament chaud, une fenêtre de stabilité des nanotubes a été identifiée en fonction de la température du filament (T_f):

- T_f = 1900-2000 ° C: gravure très élevée des nanotubes, presque tous les nanotubes disparu à partir du substrat après 1 heure de traitement,
- 2000 ° C $<T_f \leq$ 2200 ° C: gravure Peu ou pas de nanotubes,
- 2300 ° C-2400 ° C: tendance très élevé de conversion de nanotubes à polycristallin matériau.

Le comportement de gravure de nanotubes de plasma micro-ondes était plus ou moins similaire à celle de traitement à chaud de filaments: basse température (700-800 ° C) gravure importante. Dans la plage de température, T_f: 2100-2200 ° C, croissance de plusieurs nano-objets sur / à partir de nanotubes, tels que les nanocristaux, nanofils et nanospikes. La faible reproductibilité et de très faible densité de ces nano-objets ont rendu leur caractérisation très difficile et, par conséquent, leur nature exacte et origine n'a pas été identifiée. En outre, un objet de forme ronde a été observée au bout de nanofils suggérant la croissance de nanofils assistée par catalyseur. En l'absence de catalyseur métallique ajouté volontairement dans le processus, la source de ce catalyseur peut être induite par des contaminants présents dans les nanotubes, ou les filament de tungstène utilisé au cours du processus. Nous avons donc mis l'accent sur catalyseur traitement assisté par des nanotubes, où un film mince de Ni a été déposé intentionnellement sur les nanotubes, et il en résulta la croissance de nanofils. Cependant, l'analyse Raman a montré que les pics caractéristiques de Si suggérant une contamination des matériaux de Si dans le processus. Traitement à chaud de filaments de nanotubes dans une Si milieu libre, les nanotubes sont dispersées sur des substrats de diamant en vrac, n'ont montré aucune croissance des nanofils ce qui suggère que la contamination Si pourrait jouer un rôle important dans le nanofil croissance.

Afin de promouvoir la croissance des nanofils de diamant, le méthane a été ajouté au cours du processus avec un catalyseur au nickel sur le diamant dans un environnement exempt de silium, ce qui crée les conditions d'un mécanisme de croissance de type phase vapeur-liquide-solide. Avec les conditions les plus favorables, en utilisant 2% vol. et 1 vol.% CH_4 consécutivement à une course unique disposition, la croissance de long, emmêlés et très nanofils denses a été observé sur le substrat de diamant. Microscopie électronique à transmission montre une forme tubulaire avec des nanofils épaisseur de paroi d'environ 50 nm, et la zone sélectionnée spectres de diffraction électronique révèle la structure graphitique des nanofils. Les voies qui ont été explorées pour la croissance des nanofils de diamant peuvent être résumées comme suit:

1. Traitement à chaud de filaments de plasma et de nanotubes de carbone dispersés,
2. Traitement à chaud de filaments de nanotubes de carbone dispersés de catalyseur,
3. Enquête de croissance mécanisme vapeur-liquide-solide utilisant le méthane sous forme de carbone précurseur et Ni comme catalyseur,
4. Enquête sur les mécanismes de croissance solide-liquide-solide en utilisant des substrats de diamant en vrac comme seule source de carbone et Ni comme catalyseur.

Aucune phase cristalline du diamant a été observée, même si une partie des nanofils ont été identifiés comme sp^3 carbone lié. La conclusion est que dans les conditions expérimentales, a exploré avec ou sans catalyseur, sans nanofil diamant pourrait être cultivé. Nous n'avons pas réussi à l' reproduction de la démarche proposée par Sun et al. en 2005, car aucun autre groupe de recherche a supporté.

Si les conditions pour la croissance du diamant nanofil existent, dans quelle direction devraient être explorées?

Parce que d'un mauvais contrôle de l'environnement local et la contamination possible, la dispersion nanotubes de carbone et la croissance par CVD assistée par filament chaud ne sont pas les techniques les plus appropriées pour poursuivre pour la croissance de nanofils de diamant. La technique la plus prometteuse serait la vapeur-liquide-solide où l'on peut obtenir un meilleur contrôle de la concentration en carbone local que le traitement avec des nanotubes de carbone dispersés. Haute pression combinée avec des influence de la température (température de substrat 900-1100 ° C) et haute pression induite par l'effet de taille nanométrique catalyseur, pourrait favoriser la nucléation de la phase sp^3 pendant la croissance des nanofils. Par conséquent, l'étude devrait être menée par CVD sous pression atmosphérique, sans aucune plasma, la stabilité du diamant serait favorisée par la forte pression à l'intérieur du catalyseur. Gouttelettes plus petites, typiquement de 1 à 5 nm de diamètre, pourrait générer une pression élevée. De telles gouttelettes pourraient être obtenues soit par démouillage d'un film mince ou sécher une solution contenant une faible concentration du catalyseur métallique.

D'autre part, en l'absence de méthane ajouté dans la phase gazeuse, la gravure du diamant par nanoparticules générées par le film métallique évaporé a été observée. Le deuxième objectif de ce travail était alors d'explorer ce phénomène de gravure intéressant pour développer une technique de gravure simple, rapide et rentable pour la fabrication d'orientation nanostructures (nanopores) dans les membranes de diamant. Dans ce processus, un film de diamant est recuit des couches métalliques d'une épaisseur de 1 à 15 nm à 800-850 ° C atmosphère d'hydrogène. Le démouillage des couches métalliques forme des nanoparticules auto-assemblées qui gravent l'interface diamant-métal à l'aide d'une atmosphère d'hydrogène. Par conséquent, les particules pénètrent dans le volume du diamant formant des pyramides inversées, des nanopores cylindriques ou coniques, selon l'orientation cristalline. Cela révéle l'anisotropie de gravure du diamant. Le méthane a été détecté par spectrométrie de masse comme le seul produit du processus de gravure. L'étude attentive des paramètres du procédé montre que les nanopores ne peut être formé en diamant, quelle que soit sa microstructure. La taille des pores latéraux et la profondeur peuvent être contrôlées par l'épaisseur du film métallique. Ni a montré la plus grande gravure activité parmi les métaux étudiés (Co, Pt, Fe, Pd et Au). L'hydrogène a été jugée instrumentale pour le processus de gravure en aucune gravure s'est produite quand il n'y avait pas d'hydrogène. Aucun changement de la microstructure diamant en raison de gravure a été observée. Le procédé de gravure ne semble pas limité par la diffusion du carbone dans les particules de métal.

Cependant, le processus de gravure est arrêté pour des particules de catalyseur situés profondément à l'intérieur du volume du cristal due à l'échange de gaz limité entre la surface et la particule, conduisant à du une saturation en carbone. Pour expliquer le mécanisme de gravure cinq étapes importantes du processus de gravure ont été identifiées comme suit:

1. Diffusion de l'hydrogène moléculaire à partir de la chambre à la surface du catalyseur,
2. Un atome d'hydrogène moléculaire est dissocié en catalytiquement par l'hydrogène atomique de nickel,
3. Atomes de carbone de la surface du diamant peut être enlevé par deux moyens différents:
   a. les atomes de carbone se dissolvent dans la goutte de nickel et ensuite diffusent vers l'interface où ils réagissent avec les atomes d'hydrogène formant le méthane,
   b. diffusion des atomes d'hydrogène dans le catalyseur pour atteindre l'interface diamant-métal, puis évacuation du carbone sous forme de méthane,
4. Désorption du méthane à partir du catalyseur,
5. exo-diffusion de méthane à partir du voisinage du catalyseur

Dans les deux cas, 3a et 3b, la réaction n'est pas limitée par la diffusion à travers le catalyseur, comme la vitesse d'attaque ne diminue pas avec l'épaisseur de catalyseur. Le procédé est donc limité par la réaction à l'interface diamant-catalyseur. L'analyse par XPS de la composition de la surface d'échantillons recuits n'a révélé aucun élément de carbure à l'interface.

La meilleure compréhension du processus, et en particulier l'étape cinétiquement limitante, nous a permis d'améliorer les conditions de gravure. Des nanopores avec une taille latérale de l'ordre de 15 à 225 nm et une profondeur d'environ 550 nm ont été gravés dans une membrane diamant. Dans le cas de motifs réalisés avec du Pd, le procédé de gravure donné lieu à une intéressante inverse de forme pyramidale microstructures par quatre paroies orientées selon les plans [111]..